Hydrogen Electrochemistry in Room Temperature Ionic Liquids

Yao Meng

St. Edmund Hall College

University of Oxford

DPhil Thesis

Michaelmas Term, 2012

Physical and Theoretical Chemistry

Abstract

Hydrogen Electrochemistry in Room Temperature Ionic Liquids

A Thesis submitted for the Degree of DPhil in Chemistry by Yao Meng

St. Edmund hall college, Michaelmas Term, 2012

This thesis primarily focuses on the electrochemical properties of the H_2 / H^+ redox couple, at various metallic electrodes in room temperature ionic liquids. Initially, a comprehensive overview of room temperature ionic liquids (RTILs) compared to conventional organic solvents is presented which identifies their favourable properties and applications, followed by a second chapter describing the basic theory of electrochemistry. A third chapter presents the general experimental reagents, instruments and measurements used in this thesis. The results presented in this thesis are summarized in six further chapters and shown as follows.

(1) Hydrogenolysis: hydrogen loaded palladium electrodes by electrolysis of H[NTf_2] in a RTIL [C_2mim][NTf_2].
(2) Palladium nanoparticle-modified carbon nanotubes for electrochemical hydrogenolysis in RTILs.
(3) Electrochemistry of hydrogen in the RTIL [C_2mim][NTf_2]: dissolved hydrogen 'lubricates' diffusional transport.
(4) The hydrogen evolution reaction in a room temperature ionic liquid: mechanism and electrocatalyst trends.
(5) The formal potentials and electrode kinetics of the proton/hydrogen couple in various room temperature ionic liquids.
(6) The electroreduction of benzoic acid: voltammetric observation of adsorbed hydrogen at a Platinum microelectrode in room temperature ionic liquids.

The first two studies show electrochemically formed adsorbed H atoms at a metallic Pt or Pd surface can be used for clean, efficient, safe electrochemical hydrogenolysis of organic compounds in RTIL media. The next study shows the physicochemical changes of RTIL

properties, arising from dissolved hydrogen gas. The last three studies looked at the electrochemical properties of H_2 / H^+ redox couple at various metallic electrodes over a range of RTILs vs a stable Ag / Ag^+ reference couple, using H[NTf_2] and benzoic acid as proton sources. The kinetic and thermodynamic mechanisms of some reactions or processes are the same in RTILs as in conventional organic or aqueous solvents, but other remarkably different behaviours are presented. Most importantly significant constants are seen for platinum, gold and molybdenum electrodes in term of the mechanism of proton reduction to form hydrogen.

Table of Contents

Glossary

Table 1 List of symbols used throughout this thesis

Symbol	Definition
η	dynamic viscosity or overpotential
ρ	density
κ	conductivity
ν	scan rate
γ	chemical activity coefficent
μ	potential
α / β	heterogeneous charge transfer coefficient
τ	dimensionless time parameter
Φ	work function
A	area
$[A]_{bulk}$	bulk concentration of species A
C	homogeneous chemical reaction step
C_O	concentration of species O at the electrode surface
C_R	concentration of species R at the electrode surface
C	capacitance
C_{dl}	double layer capacitance
c	concentration
$\partial C/\partial x$	concentration gradient
$\partial C/\partial t$	Variation in concentration with time
D	diffusion coefficient
D_∞	hypothetical diffusion coefficient at infinite temperature
e	electronic charge
e^-	electron
E	heterogeneous electron transfer step
E_f^0	formal potential
E^0	standard potential of half-cell
dE/dt	differetial of potential versus time
E_A / E_a	activation energy

$E_{a,D}$	diffusional activation energy
E_i	initial potential
E_r	inversion potential
E_p	peak potential
$E_{p/2}$	half peak potential
E_{pp}	peak-to-peak potential
$E_{½}$	half wave ptential
E_b	binding energy of the electron
E_k	measured kinetic energy of the electron
F	Faraday constant
ΔG	Gibbs energy
ΔG^0	standard Gibbs energy
H	enthalpy
i	current
i_p	peak current
j	current density
J_d	diffusive flux
k_B	Boltzmann constant
k_H	henry's law constant
k_0	standard heterogeneous rate constant
k_f	forward rate constant
k_b	backward rate constant
K	equilibrium constant
M	molecular weight
n	number of electrons
n_{rds}	number of electron transfer before the rate determining step
O	species prone to undergoing a reduction
p	gas partial pressure
Q	electricity
R	species prone to undergoing a oxidation
r	radius
r_d	radius of electrode
S	entropy
T	absolute temperature
T_0	absolute temperature where the conductivity extrapolates to zero

t	time
dt	small time
Δt / δt	time interval
U	internal energy
u	mobility
V / v	volume
dx^2	small area
δ*x*	distance
d*x*	width
z_i	the magnitude of its charge

Table 2 List of abbreviations used throughout this thesis

Abbreviation	Full name
aq.	aqueous solubtion
ADI	alternating direct implicit method
BBD	boron doped diamond
BZA	benzoic acid
Co / Co^+	cobaltocene / cobaltocenium hexafluorophosphate
CV	cyclic voltammetry
CRT	cathode ray tube
CNTs	carbon nanotubes
DSSCs	dye-sensitized solar cells
DMF	dimethylformamide
EW	electrochemical window
Fc / Fc^+	ferrocene / ferrocenium
fcc	face-centered cubic
GC	glassy carbon
GC-MS	gas chromatography–mass spectrometry
HER	hydrogen evolution reation
HA	proton solvated by solvent anion
hr	hour
IHP	Inner Helmoholtz Layer
IL	ionic liquid
MeCN	acetonitrile
min	minute
RTIL	room temperature ionic liquid
TBAP	tetrabutylammonium perchlorate
THF	tetrahydrofuran
TMPD	N,N,N′,N′-tetramethyl p-phenylenediamine
RHE	reversible hydrogen electrode
SEM	scanning electron microscope
SHE	standard hydrogen electrode
SCE	saturated calomel electrode
rds	rate determining step
OHP	Outer Helmoholtz Layer

OPD H or H_{OPD}	over-potential deposition of hydrogen atom
PC	personal computer
UPD H or H_{UPD}	under-potential deposition of hydrogen atom
UV light	ultraviolet light
WE	working electrode
XPS	X-Ray photoelectron spectroscopy

Table 3 List of Units used throughout this thesis

Unit	Definition
cP	centipoise
K	Kelvin
g	gram
m	meter
cm	centimeter
mm	millimeter
µm	micrometer
nm	nanometer
V	Volt
kV	kilo Volt
eV	electron Volt
mS	mill Siemens
A	ampere
nA	nano-ampere
M	Molar mass
mM	millimolar
s	second
atm	atmospheric pressure
C	coulombic
wt	weight
ppm	parts per million
Å	ångström
µF	microfarad
Ω	Ohm
Hz	Hertz
W	Watt
mL	milliliter
µL	microliter
kJ	kilo Joule

Acknowledgements

First and foremost, I would like to take this chance to express my deepest gratitude to my supervisor Professor Richard G. Compton for welcoming me into his research group, for his patience with my poor English and weak communication, for his support and guidance over the past three years. I am very pleasure to work with such a great supervisor, and give thanks to all the opportunities he has given me. I appreciate these valuable discussions and interesting communications, from which I have learned a lot, both on the academic and life level. I appreciate his in-depth review of every manuscript and my thesis word by word in his busy schedule. I also appreciate his care and encouragement in my everyday life at Oxford. Despite many frustrations over last three years, I had a wonderful time with my respectable supervisor in this historic university. Thanks!

I would like to thank all members of the Compton group, past and present, for their support and sharing the enjoyable life. Special mentions go to Dr. Leigh Aldous for his careful and patient guidance to a fresh electrochemical research, for his review of most manuscripts, for the XPS measurements; Dr. Neil Rees for his funny and academic guidance; Stephen R. Belding for his simulation programs accompanied with three-year research career and the skilled chess; Sven Ernst for his helpful discussion and careful maintenance of laboratory equipments. Thanks to my best partners in this family for their support and encouragement for making my life enjoyable. (Edmund; Christopher; Eduardo; Rahamt; Xingjiu Huang; Yige Zhou; Yijun Wang; Jane; Qian Li; Xiong; Ben *et al.*)

My research involved much collaboration. I prefer taking this opportunity to express my great appreciation. To Prof. Christopher Hardacre at Queen's University Belfast for providing all room temperature ionic liquids throughout this thesis. To Prof. Timothy J. Donohoe and Mr. Ben S. Pilgrim in Chemistry Research Laboratory (Oxford University) for carrying out the

NMR spectroscopy to characterise my products. To Mr. Junyu Sun in Department of material (Oxford University) for the SEM measurements.

Finally, I would like to thank my family and in particular, my girlfriend Chen, for all their care and encouragement over the last few years. Also, the financial supporting from a China Scholarship Council is gratefully acknowledged. I am looking forward to a great successful viva as a perfect ending of my D.Phil.

Chapter 1 Room Temperature Ionic Liquids

Room Temperature Ionic Liquids (RTILs) exist in the liquid state at room temperature, and are composed entirely of cations and anions. They have several characteristic properties, such as low volatility, high thermal stability, wide electrochemical potential windows and intrinsic conductivity. RTILs are the subject of intensive investigation relating to various fields such as gas sensors, synthesis and catalysis, electrodeposition, batteries, solar cells and so on.

This chapter focuses on the physical, chemical and electrochemical properties of RTILs, as well as some industrial applications compared with the traditional molecular solvents, such as acetonitrile or acetone.

1.1 The development of RTILs

The term room temperature ionic liquid is used to describe one kind of material which consists solely of ions and exists in the liquid form at normal temperature and pressure[1] where the comparable molten salts are solid state, such as NaCl, KCl. Therefore, RTIL characteristically possess high lattice enthalpies and relatively weak Coulombic interactions to significantly decrease the relative melting point. In comparison, the melting point of ionic crystals is commonly higher than 1000 K.

Ionic liquids were first found in 1914,[2] but drew little attention until 1982. Ionic liquids were based on the haloaluminate anion ($[AlCl_4]^-$) were reported in several publications,[3-5] but the synthesized ionic liquids were highly sensitive to air and moisture and required maintaining under anhydrous conditions; these are defined as the first generation of ionic liquids. It is well known that this first generation is not of general applicable use, due to their very high sensitivity to air and moisture. Ionic liquids based on some specific cations and anions, such as tetrafluorobarate ($[BF_4]^-$) or more hydrophobic bis(trifluoromethylsulfonyl)imide ($[NTf_2]^-$) were explored to improve the stability toward water although they still absorbed some

Cations

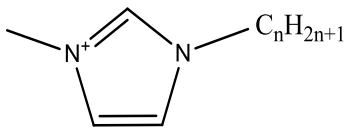

methylimidazolium, $[C_nmim]^+$

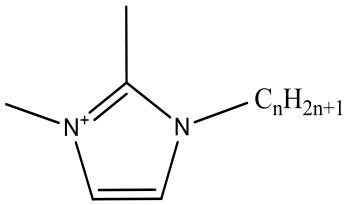

dimethylimidazolium, $[C_ndmim]^+$

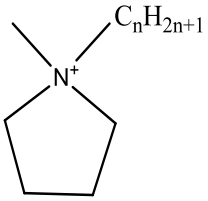

Pyrrolidinium, $[C_nmpyrr]^+$

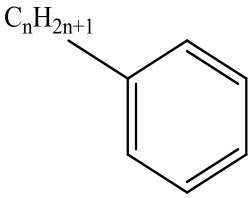

Pyridinium, $[C_npy]^+$

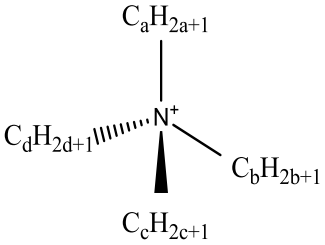

Tetraalylammonium, $[N_{a,b,c,d}]_+$

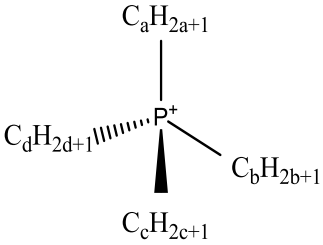

Tetraalylphosphonium, $[P_{a,b,c,d}]_+$

Anions

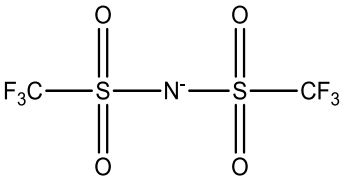

Bis(trifluoromethylsufonyl)imide, $[NTf_2]^-$

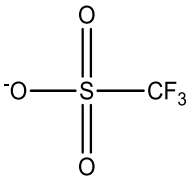

Trifluoromethylsulfonate, $[OTf]^-$

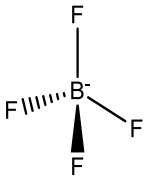

Tetrfluoroborate, $[BF_4]^-$

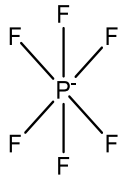

Hexafluorophosphate, $[PF_6]^-$

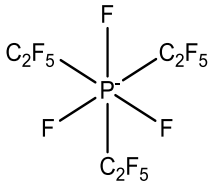

Trifluorotrisphosphate, $[FAP]^-$

Figure 1.1 Molecular structures of some commonly used cations and anions employed in RTILs in this thesis.

moisture. These are the second generation of ionic liquids showing the favourable physical and chemical properties. Figure 1.1 shows the structures of some commonly used cations and anions which make up non-haloaluminate RTILs. Their properties are listed in table 1.1.

So called third generation of ionic liquids, or 'task-specific' ILs, usually exploits the unique tunability in refinement of cations and anions in the design of novel structures which enables particular desired purposes to be realised. Prof. James G. Davis[6, 7]has reviewed a huge number of possible cations and anions for 'task-specific' ILs to accommodate specific requirements, such as extraction, gas separation, molecular absorption, dissolution of inorganic salts and special electrolyte. The Henni group[8] predicted the gas solubility for CO_2 as a function of temperature from amongest 73 cations and 37 anions where the anions based on [EtOHmim] and [choline] gave the highest CO_2 solubility. Also, imidazolium cations functionalized with amine groups[9]were more likely to separate CO_2 from the gaseous mixture due to the high CO_2 solubility. Kimizuka and Nakashima[10, 11] have simultaneously predicted and reported an excellent capability of biomass (carbohydrates and protein) dissolution in [MeOMe-MIM]Br and [MeOEt-MiM]Br, as well as [MeOEt-MiM][BF_4]. In general, a typical approach to the synthesis of 'task-specific' ILs is to add functional chains, such as ethers, alcohol groups or carboxyl groups, to common cations and anions. [12, 13]

1.2 Physical and Chemical Properties of RTILs

It is necessary to appreciate the various physical and chemical properties of RTILs before the consideration of their uses in the design of electrochemical reactions. A huge number of papers reveal several advantageous properties of RTILs employed in different conditions and experimental systems, such as high intrinsic conductivity, wide electrochemical window, high thermal stability, low toxicity and high polarities. The following sections examine each property in detail.

Table 1.1 The physical and electrochemical parameters for some commonly used RTILs and conventional molecular solvents, including viscosity (η), density (ρ), conductivity (κ) at 293K and electrochemical window (EW) at a platinum electrode with a platinum *quasi* reference electrode.

Ionic Liquids	η / cP	ρ / K / g cm^{-3}	κ / mS cm^{-1}	EW$^{\&}$ / V
[C_2mim][NTf_2]	34[15]	1.53[16]	8.8[15]	4.3
[C_4mim][NTf_2]	52[15]	1.44[16]	3.9[15]	4.8
[C_8mim][NTf_2]	74[17]	1.33[16]	-	5.0
[C_4dmim][NTf_2]	105[18]	1.42[16]	2.0[19]	5.2
[C_4mpyrr][NTf_2]	89[18]	1.40[16]	2.2[20]	5.2
[$N_{6,2,2,2}$][NTf_2]	167[21]	1.27[21]	0.67[20]	5.4
[$P_{14,6,6,6}$][NTf_2]	450[22]	1.07[16]	-	5.0
[C_4mim][OTf]	90[15]	1.30[15]	3.7[15]	4.9
[C_4mim][BF_4]	112[18]	1.21[23]	1.7[24]	4.7
[C_4mim][PF_6]	371[23]	1.37[23]	1.5[24]	4.7
[C_6mim][FAP]	74[25]	1.56[16]	1.3[25]	5.3
[C_4mim]Cl	7453[25]	1.05[16]	-	3.2
[C_4mim]I	1110[26]	1.49[16]	-	2.1
Acetonitrile*	0.34[27]	0.79[27]	7.6[27]	5.0[28]
Dichloromethane*	0.44[27]	1.33[27]	-	3.5[28]
N, N-Dimethylformamide*	0.92[27]	0.94[27]	4.0[27]	4.3[28]
Dimethylsulfoxide*	1.99[27]	1.10[27]	2.7[27]	4.4[28]

* containing 0.1 M TBAP as the supporting electrolyte at 295K

$^{\&}$defined by the voltage range where the measured current is about 1nA, using a 10 μm diameter Pt working electrode and Pt *quasi*-reference electrode

1.2.1 Viscosity

Viscosity is an important physical concept that describes a fluid's inherent resistance to flow. The viscosity of organic solvents typically range from 0.2 to 10 cP,[29] whereas the viscosity of the RTILs are two or three order of magnitude higher, in the range of *ca.* 20 - 7500 cP[15] at normal temperature and pressure. These viscosity values for some common RTILs and molecular solvents are shown in the second column of table 1.1. The high viscosity slows down mass transport of electroactive species, significantly influencing the rate of diffusion controlled reactions.[30] Therefore, lowering their viscosity needs to be carefully considered for each RTIL studied in order to possibly eliminate this unfavourable influence. One way[31] is to add a small amount of organic solvents to weaken the Coulombic interactions, yet retain the favourable properties.

It is well known that Coulombic interactions play an important role in dictating the viscosity of ionic liquids, as well as van der Waals forces and hydrogen bonding.[32, 33] Thus, the influences on viscosity have widely investigated, mainly focusing on the molecular structure of cations and anions. Taking $[C_nmim]^+$ as an example, increasing the length of carbon chain on the imidazolium cation(n=2,4,8…) will cause the viscosity to increase due to the influence of Van der Waals forces; however, the longer the carbon chain is present, the weaker Coulombic interactions (the major contribution to viscosity) exists. So overall the viscosity decreases. Also, hydrogen bonds introduced into RTILs results in their increased viscosity, for example, as in adding a fluoride functional group to an imidazolium carbon chain.[30, 34]

It is evident that the nature of anions has a stronger influence on the viscosity than that of cations.[35] Therefore, it is not difficult to conclude that RTILs based on $[NTf_2]^-$ anions have lower viscosity since the negative charge is delocalised over the sulfoxide group. In comparison, RTILs based on halide anions often give very high viscosity due to the

concentrated charges and the relatively small anion radius. Additionally, hydrogen bonds need to be considered in some cases, such as H---F, or H---O bonds.[36, 37]

Many different methods based on 'group contributions' have been used to estimate RTIL viscosity.[38-43] The Orrick-Erbar[38] approach is an example, considering the equation below

$$In\frac{\eta}{\rho M} = A + \frac{B}{T} \tag{1.1}$$

where η is the fluid's viscosity, ρ is the relative density, M is the molecular weight, T is the absolute temperature and A, B are experimental parameters, which has been obtained by employing a group contribution technique with a temperature variation proposed by De Guzman.[44]

The temperature dependent viscosity of RTILs typically show a 20% change over a 5 K jump around the ambient temperature.[45] The Arrhenius relationship commonly describes a temperature-dependent parameter, and the effectiveness has been proved by Okoturo and VanderNoot[18] over a study of 23 RTILs at ambient temperatures (283-343 K).

1.2.2 Density

Various estimation methods[46-49] have been developed to parameterise the temperature-dependent density of RTILs. *e.g.*. the Ye and Shreeve method [46] The calculated RTIL's densities are over a range of 1 to 1.6 g cm^{-3}, the values of which are listed in the third column of Table 1.1 and are slightly larger than those of organic solvents. The densities of the RTILs commonly decrease with the bulk increase of cations, such as the imidazolium RTILs. Change of anions leads to a more obvious density change of the corresponding RTILs due to the larger molecular density. A approximate trend for the common anions can be summarized as $[BF_4]^-$<$[OTf]^-$<$[NTf_2]^-$<$[FAP]^-$. Approximately linear relationships are proposed between the RTIL density and the inverse of the temperature. The volume expansion coefficient is

about *ca.* 5×10^{-4} K^{-1},[50, 51] significantly lower than that in organic solvents, typically *ca.* 1×10^{-3} K^{-1}.

1.2.3 Conductivity

As solvents in electrochemical experiments, RTIL conductivity is one of most important parameters, generally depending on the number of charge carriers, and their mobilities. Since there exists few charge carriers in conventional organic solvents, a supporting electrolyte, such as tetrabutylammonium perchlorate, TBAP, is required to compensate the relatively low conductivity in most electrochemical processes. Typically a concentration 100 times larger than the concentration of the studied solute is needed.

It must be noted that the conductivity of solvent cannot increase infinitely by increasing the concentration of charge carriers: ionic atmosphere effects limit the conductivity. Ionic liquids never lack charge carriers, but actually do not reach the desired high-conductivity. The reason mainly comes from two aspects: ion-pairing effect exists in a solvent with an extremely high concentration of charge carriers, reducing the effective number of charge carriers.[52, 53] Second, the high viscosity of RTILs (compared to the conventional organic solvents in table 1.1, second column) limits the actual conductivity due to the effect on ion mobility. In general, the conductivities of RTILs are seen to be approximately inversely proportional to their viscosities.

Increased temperature prompts the mobility to increase, resulting in the increase of conductivity. RTILs with symmetric cations and anions (including any functional group) are available to be described by the Vogel-Tammann-Fulcher equation:[54-56]

$$\kappa = A\sqrt{T}e^{-B(T-T_0)} \qquad (1.2)$$

where κ is conductivity, A and B are empirical constants obtained from experiments, and T_0 is the temperature where the conductivity extrapolates to zero. The equation is applicable to

the temperature-dependent conductivity of RTILs with a high level of precision.[20, 50, 57, 58] The conductivity is less dependent on anion size. Vila *et al*. reported that the conductivity of imidazolium based RTILs slightly decreases as the length of the alkyl chain on the cations increases.[58]

In order to obtain higher conductivity, the syntheses of 'task specific' RTILs with specific functional groups have been reported, which are described by the formula $[C_nmin][F(HF)_m]$, (where m=2, 3)[59, 60] giving the conductivities ranging from 12 to 110 mS cm^{-1}.

1.2.4 Electrochemical Windows

Electrochemical potential window is an effective voltage range of a solvent for an electrochemical process on a particular conducting surface, which is decided by the potentials for anodic and cathodic decompositions of the relevant molecules or ions.[28, 61] In general, aqueous solutions show a relatively narrow electrochemical window of about 1.5 V. Organic solvents with relatively concentrated supporting electrolytes show a wider electrochemical window, *e.g.* 5.0 V for acetonitrile and 4.4V for dimethylsulfoxide. RTILs are widely recognized to be in the range of *ca.* 4.0-5.5V.[3]

It is well known that electrochemical window of RTIL is dependent on the nature of its constituent cations and anions. Table 1.1 shows the electrochemical windows for some common cations and anions at a Pt electrode, as well as some conventional aprotic solvents. $[P_{14,6,6,6}][FAP]$ RTIL gives the widest electrochemical window. RTILs based on the imidazolium cation are easiest to be reduced among various cations, due to the reduction of the proton linked with the carbon ring between the two heteroatoms.[15] Indeed, if the electroactive proton is replaced with a methyl group to form the $[C_ndmim]^+$ cation, the corresponding electrochemical window was observed to expand.[37] Meanwhile, extended electrochemical windows are realised by increasing the alkyl chain length on the imidazolium ring, but they are likely to be narrowed if replaced by some functional groups, such as an alkyl-ether, and

thus bringing about the degradation at a less negative potential.[62] Pyridinium, tetraalkylammonium and tetraalkylphosphonium cations show wide electrochemical windows.

The most stable anion can be assigned to be $[FAP]^-$. The RTIL $[N_{4,4,4,4}][FAP]$ shows a very wide electrochemical potential window of *ca.* 7.0 V.[61] $[NTf_2]^-$, $[BF_4]^-$, $[PF_6]^-$ and $[OTf]^-$ anions show similar contributions for electrochemical windows of the corresponding RTILs, being of the order 0-300mV voltage difference. In addition, halide anions, such as Cl^- and I^- will give narrower electrochemical windows due to their lower oxidation potentials.

It is noted that the measured electrochemical windows of RTILs in the literature slightly differ from one to another. These differences arise from different definitions of the window, various degrees and types of impurities, which can alter the electrochemical window, or the different electrode metals used in their measurements. The influences of impurities are detailed in section 1.3. The choice of a stable reference electrode or a stable reference couple does not cause the change of absolute value of electrochemical window, but a stable reference is necessary to characterize both the cathodic and anodic processes.

In general, a Pt or Ag wire is used as a *quasi*-reference electrode, but the accuracy of this cannot be guaranteed due to the inevitable experimental error. The choice of a stable reference couple gives comparable experimental conditions, and this is of the importance to all electrochemical processes. Both ferrocene and cobaltocenium hexafluorophosphate are widely used as the internal probes, [63] independent of electrode materials, concentration gradients and scan rates. However, it has been demonstrated that ferrocene reacts with the protons and that the cobaltocenium reduction wave can overlap with the voltammetry of interest.[64] Therefore, a stable reference electrode in the RTIL system is developed in this thesis.

1.2.5 RTILs as solvents

The concept of polarity is very commonly used to describe the dissolving power of molecular solvents and solutes. A general rule is that a polar solvent is capable of dissolving any polar solute, rather than a non-polar solute.[65] The magnitude of polarity is quantified by the physical parameter, the dielectric constant. In comparison, RTILs are difficult to be classified as either polar or non-polar molecules. Moreover diverse features may exist in any one RTIL structure, showing some particular interactions, such as hydrogen bonding, Coulombic interactions or electron donating / accepting properties.[66] Take RTILs based on imidazolium as an example, the polarity is mainly determined by the carbon ring, whereas the alkyl chain shows nonpolar properties. Therefore, most RTILs show an excellent solvating property for both polar and non-polar solutes.[67] It is noted that high ion concentration does not in itself mean high polarity.[68] In fact, the measured 'polarity' values are usually fairly low differing from one laboratory to another due to different experimental methods and the accuracy of the experimental processes.

The solubility, solvation capacity of a solvent, depends on its polarity, as well as temperature and pressure. The solubility represents the maximum concentration of dissolved species in a particular solvent. Gas solubility in RTILs is widely studied to encourage the development of gas sensors. Gases, such as carbon dioxide and sulphur dioxide, are exceptionally soluble;[69] carbon monoxide with weak polarity is less soluble; and non-polar oxygen and hydrogen show a small solublity.[70, 71]

Gas solubility is commonly characterized using the Henry's law constant in molecular solvents and most RTILs. It is directly proportional to the gas partial pressure above the solvent.[28] The relationship is described as:

$$p = k_H c \qquad (1.3)$$

where k_H is the temperature-dependent constant (Henry's law constant), p is the gas partial pressure and c is the concentration of dissolved gas in the solvent. The temperature-dependent Henry's law constant of each gas in a particular RTIL is determined by the van't Hoff isochore over a range of temperatures where one of the Henry's Law constant at a special temperature and the enthalpy of the reaction is required to be known. The van't Hoff isochore[28] is written as:

$$\ln\left(\frac{k_{H1}}{k_{H2}}\right) = \left(\frac{\Delta H}{R}\right)\left(\frac{1}{T_1} - \frac{1}{T_2}\right) \quad (1.4)$$

where k_{H1} is Henry's law constant at T_1 (K), as well as k_{H2} at T_2, R is universal gas constant (8.31 J / mol) and ΔH is enthalpy of the dissolution. In fact, beside temperature affecting the Henry's law constant, other important factors also include the pH of solutions, compound hydration, the presence of dissolved salts and so on.[72] It should be noted that Henry's law is a limiting condition that only applies for sufficiently dilute solutions where the dissolved gas does not chemically react with the solvent.

This thesis focuses primarily on dissolved hydrogen in a range of RTILs. The choice of chronoamperometry is made to allow accurate measurement of gas solubility when the radius of a microelectrode and diffusion coefficient of dissolved gas are known at a particular temperature. It is worth mentioning that solubility of some particular gases, such as H_2 and CO_2,[36, 73] are comparable between different RTILs solvents, suggesting that these RTILs have a similar polarity, as proved by Carmichael and Seddon.[74]

In contrast, there are only a few articles on the solubilities of solids and liquids in RTILs, which also obey the similar trend to gas solubilities in RTILs. It is found that aliphatic compounds are sparingly soluble,[32] but aldehyde compounds are completely miscible in RTILs.[75] In addition, it is of importance to characterize the dissolution properties of ferrocene

and cobaltocenium in RTILs,[63] which usually act as a stable reference couple, or as standard intermediates to allow the extraction of parameters in electrochemical processes.

1.2.6 Thermal stability

The thermal stability of a RTIL is an important physical property giving an upper working temperature when using RTIL at very high temperatures. The strength of the heteroatom-carbon and heteroatom-hydrogen bonds is thought as the main influence on the stability of the solvents.[32] For RTILs, it is believed that thermal stability of RTIL is primarily dependent on the size of cations and anions, e.g. Cl^-‹ $[BF_4]^-$‹ $[NTf_2]^-$‹ $[PF_6]^-$.[51, 76]

Purely from the chemical concept, decomposition temperatures of most RTILs in the literature fall into the range 573-674 K, whilst some thermally stable RTILs survive up to 725 K.[26] In fact, such upper working temperatures for each RTIL only represent an ambiguous beginning of the rapid decomposition, but some decomposition also exists when using a RTIL at relatively low (elevated) temperature. The literature reports that RTILs exposed to temperatures above *ca.* 473 K for a long time will inevitably result in decomposition.[33, 77] Besides, other factors affecting these decomposition temperatures involve impurities in the RTIL and the applied experimental methods. This is why the measured decomposition temperatures of each RTIL in different literature reports differ from each other. Therefore, for most applications of RTILs, the actual temperatures used are far away from their decomposition temperatures. The thesis does not refer to such high temperature; rather it normally lies in the range of 273 K to 323 K.

1.2.7 Environmental friendliness

In earlier studies of RTILs, they were optimistically thought as ‘green’ solvents to replace traditional molecular solvents in the field of synthesis and catalysis because of their low volatility, chemical stability and good reproducibility. Moreover, the relatively low toxicity of RTILs is also suitable for large-scale industrial applications. But with further study in

recent years, at least one major problem has been arisen with regard to their electrochemical degradations and the resulting hazardous products. Therefore, some RTILs are unworthy of the name of 'green' solvent. For example, $[BF_4]^-$ and $[PF_6]^-$ anions are likely to degrade to form the hazardous hydrogen fluoride, HF.[78] Also, the $[NO_3]^-$ anion is proven to decompose under acidic conditions.[79] The choice of an experimental RTIL not only ideally shows an environmental friendly property, but also guarantees a favourable pathway for the electrochemical reaction. In addition, it is noted that the hazardous by-products are inevitable when undergoing the synthesis processes of RTILs.

1.3 Influence of major impurities

Even though exposure to vacuum has been proven to effectively remove most impurities from RTILs, in air the presence of impurities are inevitable at least at low concentrations, and can cause undesirable electrochemical properties and interfere with analysis under certain conditions. Therefore, it is necessary to identify the nature of every major impurity individually in order to minimize and distinguish these influences in electrochemical measurements.

1.3.1 Water

To illustrate the effect of impurities, $[C_2mim][NTf_2]$ RTIL was evacuated under vacuum for four hours, then the non-electroactive nitrogen gas was used to carry purified water through the RTIL surface before the recording of voltammograms. Figure 1.2 shows the effect of water in $[C_4mim][NTf_2]$ on the voltammogram vs the time exposed to water. It shows that the cathodic potential window is continuously decreased where RTIL is exposed to moist nitrogen for some time. The decreasing trend probably stops when a saturated-water RTIL solvent is formed. A similar study of the water effect was performed on both cathodic and anodic features in $[C_4mim][PF_6]$ by Schrőder *et al.*,[80] and also showed a nearly two fold

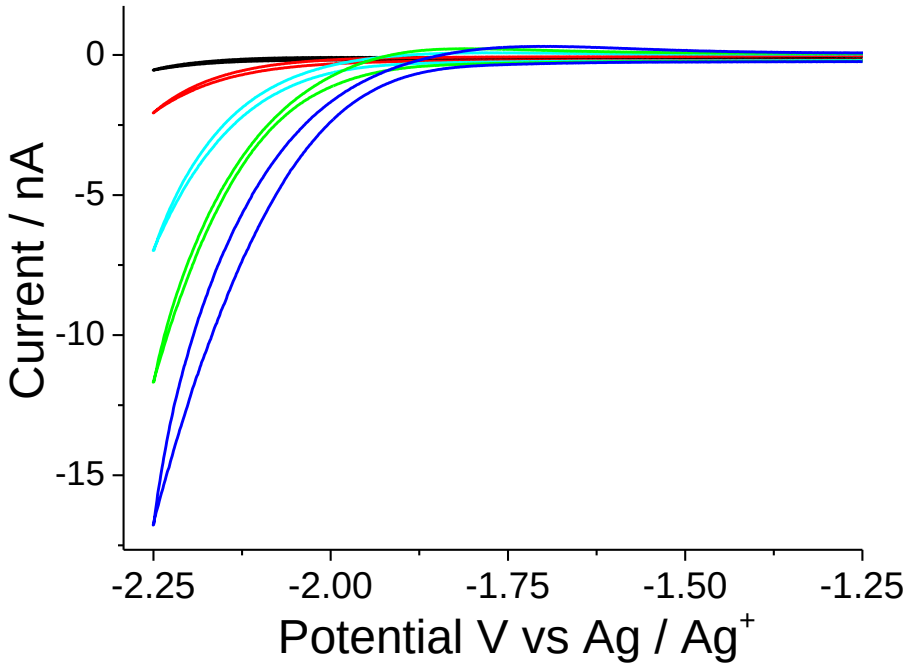

Figure 1.2 My study of water effect in dried [C_4mim][NTf_2] RTIL at a Pt electrode vs Ag / Ag^+ reference couple at 298 K, showing the cathodic features with the increased time exposed to water flux : 0, 15, 30, 45 and 60 minutes.

increase of the diffusion coefficient of electroactive species in the presence of 5 wt.%.of water.

It can be inferred that water impurity in RTIL leads to a decreased viscosity, increased conductivity and a significantly decreased electrochemical window, which are all important factors when employing RTILs as electrochemical solvents.[26, 80-82]

In order to show reproducibility, the study of RTIL needs to be carried out under anhydrous conditions in all electrochemical experiments. It is understood that a small amount of water is nevertheless inevitable, even if the best vacuum technique is applied for a sufficiently long time. Therefore, the electrochemical property of the resident water needs to be approximately negligible, compared with that of the electroactive species. Table 1.2 shows water contents

Table 1.2: The measured water content of some common RTILs, under the long-term exposed to air and vacuum dried for 24h at 333 K, using the Karl Fischer titration method.[83]

Ionic liquids	Water content / ppm (Long-term exposed to air)	Water content / ppm (Vacuum dried)
$[C_2mim][NTf_2]$	3,385	105
$[C_4mim][NTf_2]$	491	144
$[C_4dmim][NTf_2]$	504	295
$[C_4mpyrr][NTf_2]$	406	133
$[N_{6,2,2,2}][NTf_2]$	1,150	167
$[C_4mim][OTf]$	15,227	250
$[C_4mim][BF_4]$	5,083	119
$[C_4mim][PF_6]$	2,119	268
$[C_4mim]I$	11,349	1,050
$[C_4mim]Cl$	61,049	2,231

over a range of RTILs under the air-equilibrated and vacuum dried conditions, as found using the Karl Fischer titration method.[83] It is seen from the table that even the 'hydrophobic' RTILs absorb water to some extent under exposure to air, but the water contents can be significantly decreased after being vacuum dried for 24 hour at 333K. The final content is mainly dependent on the vacuum technique and the nature of the RTIL.

Some affinity between every RTIL and water is well known under all conditions. Most 'hydrophobic' RTILs appear to have a relatively low water contents in contrast to the halide RTIL being most hydrophilic. RTILs based on $[NTf_2]^-$ anion is a good 'hydrophobic' example to show a saturated water content of less than 2%.[15, 21] Nevertheless, the change of $[C_4mim][OTf]$ RTIL better reflects the real value of the vacuum technique.

1.3.2 Oxygen

Another important consideration is the interference of dissolved gases (such as oxygen, nitrogen, carbon dioxide and so on) when using RTILs as solvents in chemical or electrochemical reactions. Dissolved oxygen is able to interfere with the electrochemical performance of the hydrogen evolution reaction at different metals. It has been reported that the oxygen voltammogram generally consists of two reductive waves, being of oxygen to superoxide, and superoxide to peroxide.[84] Therefore, the electrochemical window of any RTIL is significantly reduced in the present of oxygen. In addition, there is potential that oxidizing the electrode surface with oxygen could significantly change the original electrochemical behaviour, seriously deviating from the aim of the study. Therefore, before the measurement of every electrochemical experiment, it is necessary to degas the RTIL, using either vacuum techniques or purging with an inert gas, such as nitrogen or argon.

1.3.3 Halides

Halide impurities are introduced during the synthesis methods used in the production of most RTILs, and cannot be efficiently removed using the common vacuum techniques. However, most commercial available RTILs are pure. Several methods exist to quantify the halide in RTILs, such as chronomatography,[85] capillary electrophoresis[86] and electrochemistry.[87]

In terms of the properties of RTILs based on halide anions, it is well known that the halide anion is much easier to be oxidized than most common anions which make up the non-haloluminate RTILs. Therefore, a decreased electrochemical window is displayed. This inference was shown by Seddon *et al.* in RTILs based on imidazolium cations, also showing the effect of an increased viscosity.[88]

It is noteworthy that some unpredictable reactions can be induced by a small amount of halide impurities left over in RTILs. For example, Aldous *et al.* reported the electrochemical

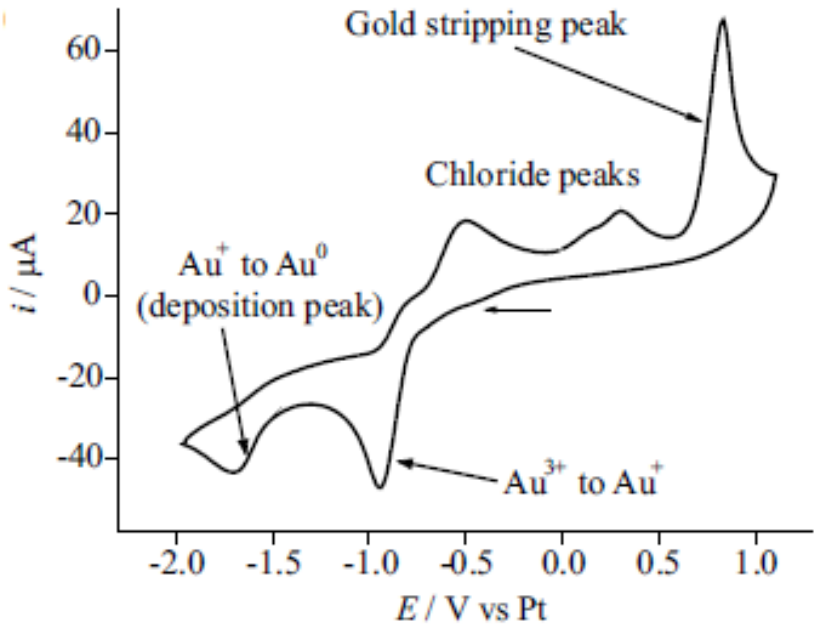

Figure 1.3 the voltammogram for the reduction of *ca.* 5mM $HAuCl_4$ in $[C_4mim][NTf_2]$ on a BDD electrode vs a platinum *quasi* reference at 100 mV s^{-1}.[89]

studies of gold and chloride obtained on a boron doped diamond (BBD) electrode in $[C_4mim][NTf_2]$. (see figure 1.3) A gold stripping wave or electrodissolution of bulk gold was observed, induced by the presence of Cl_3^- and Cl^-, forming Au(I) and Au(III) species. On the reverse sweep, the reductive waves at ca. -0.9V and -1.7V (vs Pt reference) correspond to the reduction of Au(III) to Au(I), and Au(I) to Au(0), respectively.[89] A similar electrochemical behavior was found for a pure RTIL on a gold electrode due to a small amount of chloride impurity attached to the gold surface.[90] In addition, trace amounts of halide impurities in RTILs cause a certain inhibition or deactivation of some catalytic reactions on the transition metals, such as hydrogenolysis and hydrogenation, greatly reducing the yield of the desired synthesis.[91]

1.3.4 Coloured RTILs

The formation of color (typically yellow or orange) frequently appears when using RTILs. It is attributed to either the colored impurities left over from colored starting materials, or side

reactions induced by excessive heat during the synthesis, or potential degradation of species when the RTIL is exposed to air or sunshine.[92] However, it is widely reported that highly pure RTILs should be colorless, based on a large number of experimental results and reports, It is advised to avoid using colored RTILs due to the potential changes of the electrochemical properties during the electrochemical reactions. Adsorbents, such as activated charcoal, have been proposed to remove the color impurities in order to use high quality RTIL in various studies.[92, 93]

1.4 Applications of RTILs

The physical, chemical and electrochemical properties of RTILs, discussed above, reflect many unique advantages allowing the replacement or improvement of many traditional solvents, such as in catalysis, synthesis, biosensors, electrodeposition and electrochemical devices such as solar cells, fuel cells, lithium ion batteries and supercapacitors. The scopes for RTIL commercial applications are extensively recognized. Some favourable applications are introduced in the following sections.

1.4.1 Synthesis and Catalysis

The label of 'green' solvents for RTILs was commonly found in early research papers due to their low volatility and high (chemical and electrochemical) stability. However, it is evident that some RTILs probably undergo degradations to produce toxic materials and these can cause side reactions.[78] But a large number of RTIL papers have been published to exemplify favourable properties as solvents on synthesis and catalysis.[32, 65, 94-96]

Room temperature is merely required to achieve high selectivity and outcome of a Diels-Alder reaction when using an imidazolium-based RTIL rather than the low temperatures (such as *ca.*195 K, high experimental cost), being commonly used in molecular solvents to get the same goal.[97] The Rh-catalyzed hydrogenation of cyclohexene c was successfully investigated in [Bmim][SbF_6] by using a biphasic reaction system. Since a five times

difference of solubility is present for cyclohexadiene to cyclohexene, it was found that 98% selectivity of the latter was obtained at 96% conversion, and the hydrogenation rate was five times faster than the comparable rate in acetone. All the ionic liquids used showed a favourable recycling property accompanied with negligible loss of the Rh catalyst.[98]

In order to simplify the product separation and obtain a high outcome rate, a biphasic reaction is proposed for applications in which the starting material including catalyst and the product are separately isolated in different phases. The possibility of adjusting the solubility properties of the reactants and products by selecting different cation / anion combinations prompts the biphasic reaction to be systematically optimized, such as to realise the selectivity of reaction path, or the purification of products. Another important consideration is the possibility of RTIL recycling to reduce long-term cost.[99, 100]

Besides the techniques discussed above, RTIL studies of synthesis and catalysis have been extended to the biochemical field, in which enzyme catalysis is widely recognized as one of most important branches. In general, traditional enzyme catalysis is performed in aqueous / buffered solution accompanied with many additional requirements to overcome the inherent harsh conditions, such as the undesirably low solubility of hydrophobic biomass, enzymes, and deactivated processes of enzymes. Therefore, many additional biocatalytic processes are proposed to improve solubility properties and retain the enzyme activity.

As a favourable alternative to traditional molecular solvents, ionic liquids show many noticeable advantages on enzyme-catalyzed reactions, as reported in a large number of papers.[101-107] van Rantwijk and Sheldon gave a comprehensive overview.[108] First of all, RTILs have the ability to stabilize enzymes with high activity, strongly affecting the catalytic route and the product yield. However, some enzymes are weakly soluble or insoluble in most RTILs. Adding a small amount of water promotes the enzyme solubility in RTIL and helps to retain their bioactivity. For example, cytochrome dissolved in RTIL with 20 wt % water

maintains its stability and activity for six months, as opposed to 1 week in a buffered aqueous solution.[109] Another important advantage is that a higher possibility for biotransformation reactions of highly polar species exists in RTIL. This is due to their high polarity property to overcome the extremely low solubility of highly polar species, such as amino acids, in traditional molecular solvents, and to shift the equilibrium of catalyzed synthesis, such as those involving polysaccharides. Meanwhile, a high selectivity of the catalyzed route and the recycling property are successfully retained when extending the RTIL solvent to the biochemical field.[110]

Despite all the advantages mentioned above, the disadvantages of using RTIL replacing traditional solvents have also to be taken into account. It was reported that RTILs can potentially alter reaction rates, catalytic activity and form by-products in many synthesises. An extensive explanation of the reactivity of RTILs was given by Chowdhury *et al.* in the context of the research directions for the RTIL applications in any synthetic and catalytic areas. [111] Similarly, RTILs need be carefully selected as solvents for biocatalytic processes. For example, $[NTf_2]^-$, $[BF_4]^-$ and $[PF_6]^-$ anions are beneficial to retain the activity of the lipase enzyme, whereas it is deactivated when employing Cl^-, $[OTf]^-$ and $[NO_3]^-$ anions.[112] It should be noted that it is quite difficult to extract non-volatile products from RTILs.

1.4.2 Electrochemical storage devices

The short lifetime, arising from the low stability and conductivity of solvent, is a limiting factor in obtaining high performance electrochemical storage based on traditional molecular solvents, such as aqueous, gel or polymer electrolytes. Due to their favorable properties, such as high conductivity, wide electrochemical windows, high thermal stability and low volatility, it is reported that RTIL appear to be an attractive alternative electrolytes for many high performance electrochemical storage devices, such as fuel cells,[113, 114] dye-sensitized solar

cells,[115] lithium ion batteries,[116] supercapacitors,[117] channel field effect transistors[118] and light-emitting electrochemical cells.[119]

For the dye-sensitized solar cells (DSSCs), capture of a photon by the organic dye causes an electronic transition to an excited state. This unstable state releases the excess energy in the form of electron donation to a conductive substrate, such as TiO_2, and the oxidised dye is reduced by a charge carrier within the electrolyte, typically the I^- / I_3^- redox couple. The complete circuit is realised with the migration of electrons and ionic charge carriers. It is well known that the durability of the DSSCs is improved when using RTIL as the electrolyte, but the mass transport has been highlighted as a limiting factor for high performance. Kawano and Wanatabe reported that RTILs resulted in fast charge transport.[120] Bai *et al*. used mixtures of IL cations and anions to reduce the viscosity and thus improve the charge transport.[121] 'Task specific' ILs represent a path to lower viscosity, with substantial improvements in durability: Notably, it is unnecessary to sacrifice the most favorable properties to simply lower the RTIL viscosity.

As a good alternative to traditional fuel cell electrolytes, ionic liquids can behave as proton conductors, typically those formed through the reaction of a strong acid with a base. The overall efficiency of a fuel cell is strongly dependent on the properties of the cation / anion combinations, for example, a 67% efficiency is seen, using $[C_4mim][BF_4]$ as a supporting electrolyte for commercially available alkaline fuel cells with air and hydrogen at atmospheric pressure, as opposed to only a 28% efficiency in $[C_4mim][PF_6]$ at normal temperature and pressure.[122] That is because the performance of the fuel cell might degrade in the present of impurities, such as water or halide anions. Another challenge is that of the relatively high operating temperature of fuel cells, typically over 373 K. There is slow loss

Table 1.3 Solubility of various gases in RTILs and water (298K and 1atm. pressure)

Solvent	H_2 / mM	O_2 / mM	H_2S / mM	SO_2 / mM
$[C_2mim][NTf_2]$	4.2[125]	10.8[126]	530[127]	230[128]
$[C_4mim][BF_4]$	5.2[125]	3.7[129]	-	1,600[128]
$[C_4mim][PF_6]$	5.1[125]	3.6[129]	230[127]	250[128]
H_2O	0.8[130]	16[126]	&74[131]	1,470[132]

& tested at 313K

of RTIL electrolytes due to the small amount of volatile neutral acid and base produced by reversion of proton transfer. To avoid this, very strong acids or bases are recommended.[123, 124]

1.4.3 Gas sensors

The lifetime of gas sensors, which employ traditional electrolytes, typically H_2SO_4 / H_2O mixtures cannot survive harsh conditions, such as drastic temperatures, extreme dry or humid conditions, where the electrolytes are quickly dried out, and even show slow loss under normal temperatures and pressures. Due to their ability to maintain physically and chemically unchanged over a wide temperature range, and to give high intrinsic conductivities and wide potential windows, RTILs have been used to replace conventional solvents for use in stable and robust electrochemical gas sensors. The electrochemical properties of gases, such as hydrogen,[125, 133] oxygen,[126, 129, 134] ammonia,[135] carbon dioxide,[136] hydrogen sulfide[127, 137] and sulfur dioxide,[128] have been extensively studied in various common RTILs for the development of electrochemical gas sensors. Meanwhile, gas solubilities (table 1.3) in RTILs have been provided by the use of electrochemical methods. A clear trend shows that non-polar gases, such as hydrogen and oxygen have relatively lower solubility than that of polar gases, such as hydrogen sulfide and sulfur dioxide, and the polar gases are much more soluble in RTILs, compared to other solvents. It is also important to mention that the gas

solubilities are strongly dependent on the nature of RTIL anion.[69] It is necessary to take this into account when choosing a RTIL for use in an electrochemical gas sensor.

Besides their overall favourable properties, some less attractive symptoms need be taken into consideration when choosing a RTIL as an electrolyte, such as their high viscosity slowing down mass transport, and their high sensitivity to moisture.

1.4.4 Biofuels

It is well known that a huge amount of non-food biomasses (such as corn stalks and softwood) in the form of lignocelluose are produced every year, and such biomasses are widely recognized as an important and potential of biofuel source to cope with the energy crisis. Biofuel represents a potentially sustainable, carbon-neutral transportation fuel source, such as ethanol, butanol or biodiesel.

Lignocellulose consists of the carbohydrate polymers cellulose, hemicellulose and phenolic polymer lignin in the form of a very sturdy matrix-network including covalent and hydrogen bonds. In conventional solvents, the lignocellulose is impossible or difficult to break down into the components used as the starting materials for biofuel production, under mild conditions. Fortunately, it has been found that many anions, such as carboxylates and halide, which make up ionic liquids, behave as a favourable hydrogen-bond acceptors, and such RTILs are available to dissolve the 'insoluble' cellulose and lignocellulose by destroying their sturdy networks of intramolecular hydrogen bonds.[138, 139] Meanwhile, when adding water into a suitable RTIL, these dissolved cellulose-anion bonds can break down to a structurally disrupted form, which may facilitate the biomass catalysis with a particular enzyme, for example, the production of ethanol from the fermentable sugars.[140] It is also important to note that natural biopolymers, such as silk, can be dissolved into RTILs, and this can be beneficial for their functional modification processes.[141]

1.4.5 Electrodeposition

It is well known that the attractive electrochemical windows of the RTILs are generally much wider than those of conventional solvents, allowing a wider range for metal or semiconductor electrodepositions which are normally deposited out of the potential range of conventional solvents, and a morphology control to generate high quality deposition due to the absence of the hydrogen evolution process, which occurs in water.[142] However, in addition to viscosity and conductivity concerns, impurities such as water, halides and organic compound have proved to be the major drawbacks when employing RTILs as electrodeposition media. Glove box or the vacuum techniques are used to minimize this negative effect. Several papers, reviews and handbooks has been published to show the studies of electrodeposition of a range of metals including gold, zinc, tin, palladium, copper and aluminium, semiconductors involving silicon and germanium, and aluminium alloys in various RTILs.[142 143-145]

1.5 The aims of this thesis

The experiments reported in this thesis have three main parts. The aim of the first part is the investigation of fast hydrogenation and hydrogenolysis of organic compounds in RTILs on a palladium microelectrode, as well as palladium nanoparticle-modified carbon nanotubes under mild conditions, using the high active adsorbed hydrogen atoms which arise from the reduction of H^+ in RTILs. This is demonstrated both voltammetrically, and by the isolation, identification and quantification of the hydrogenolysis products obtained in the IL environment. Palladium nanoparticle-modified carbon nanotubes also showed a high surface area which is highly active for electrochemical hydrogenolysis, and which is fully characterised. The second part provides new insights into the solvation of H_2 in $[C_2mim][NTf_2]$ RTIL, as well as the corresponding changes that result in the structure of the ionic liquid itself. The significant influence of H_2 gas on the diffusion coefficient of dissolved protons and ferrocene, as well as its influence on the viscosity of the RTIL is quantified. The

third part has the most important position in this thesis and reports the investigation of the H^+/H_2 redox couple at various electrocatalytic metals (platinum, gold, molybdenum, nickel and titanium) over a range of RTILs vs Ag / Ag^+ reference electrode. The latter was newly developed as part of the research. Both the mechanism and kinetics of the process were quantitatively investigated, and compared and contrasted with the existing literature of hydrogen evolution reaction at various transition metals available for aqueous systems. The influence of the interaction between protons and anions are shown, and changes in both kinetic and thermodynamic parameters are seen. Finally, a quantitative investigation of the hydrogen evolution reaction arising from the weakly acidic benzoic acid (rather than strongly acidic $H[NTf_2]$)as the proton source was carried out at a Pt electrode over a range of RTILs, giving the voltammetic characteristics of benzoic acid to be seen, as well as adsorption /desorption processes of hydrogen atoms.

References

1 N. V. Plechkova, K. R. Seddon, *Chemical Society Reviews* 2008, *37*, 123-150.

2 P. Walden, *Bull. Acad. Sci. St. Petersburg* 1914, *1*.

3 J. S. Wilkes, J. A. Levisky, R. A. Wilson, C. L. Hussey, *Inorganic Chemistry* 1982, *21*, 1263-1264.

4 C. L. Hussey, *Pure and Applied Chemistry* 1988, *60*, 1763-1772.

5 F. H. Hurley, T. P. Wier, *Journal of the Electrochemical Society* 1951, *98*, 207-212.

6 J. H. Davis, *Chemistry Letters* 2004, *33*, 1072-1077.

7 J. H. Davis, *'Synthesis of Task-Specific Ionic Liquids' in Ionic Liquids in Synthesis, John Wiley and Sons: New York, USA* 2003.

8 K. Z. Sumon, A. Henni, *Fluid Phase Equilibria* 2011, *310*, 39-55.

9 E. D. Bates, R. D. Mayton, I. Ntai, J. H. Davis, *Journal of the American Chemical Society* 2002, *124*, 926-927.

10 N. Kimizuka, T. Nakashima, *Langmuir* 2001, *17*, 6759-6761.

11 S. Park, R. J. Kazlauskas, *Journal of Organic Chemistry* 2001, *66*, 8395-8401.

12 S. H. Yeon, K. S. Kim, S. Choi, H. Lee, H. S. Kim, H. Kim, *Electrochimica Acta* 2005, *50*, 5399-5407.

13 S. H. Fang, Z. X. Zhang, Y. D. Jin, L. Yang, S. Hirano, K. Tachibana, S. Katayama, *Journal of Power Sources* 2011, *196*, 5637-5644.

14 S. K. Tang, G. A. Baker, H. Zhao, *Chemical Society Reviews* 2012, *41*, 4030-4066.

15 P. Bonhote, A. P. Dias, N. Papageorgiou, K. Kalyanasundaram, M. Gratzel, *Inorganic Chemistry* 1996, *35*, 1168-1178.

16 Online, *http: //ildb.merck.de/ionicliquids/en/startpage.htm*.

17 S. V. Dzyuba, R. A. Bartsch, *Chemphyschem* 2002, *3*, 161.

18 O. O. Okoturo, T. J. VanderNoot, *Journal of Electroanalytical Chemistry* 2004, *568*, 167-181.

19 Y. D. Wang, K. Zaghib, A. Guerfi, F. F. C. Bazito, R. M. Torresi, J. R. Dahn, *Electrochimica Acta* 2007, *52*, 6346-6352.

20 D. R. MacFarlane, J. Sun, J. Golding, P. Meakin, M. Forsyth, *Electrochimica Acta* 2000, *45*, 1271-1278.

21 J. Sun, M. Forsyth, D. R. MacFarlane, *Journal of Physical Chemistry B* 1998, *102*, 8858-8864.

22 R. E. Del Sesto, C. Corley, A. Robertson, J. S. Wilkes, *Journal of Organometallic Chemistry* 2005, *690*, 2536-2542.

23 K. R. Seddon, A. Stark, M. J. Torres, *Clean Solvents* 2002, *819*, 34-49.

24 H. a. M. Olivier-Bourbigou, L., *J. Mol. Catal. A* 2002, *182183*, 419-437.

25 N. V. Ignat'ev, U. Welz-Biermann, A. Kucheryna, G. Bissky, H. Willner, *Journal of Fluorine Chemistry* 2005, *126*, 1150-1159.

26 J. G. Huddleston, A. E. Visser, W. M. Reichert, H. D. Willauer, G. A. Broker, R. D. Rogers, *Green Chemistry* 2001, *3*, 156-164.

27 D. R. Lide, *Handbook of Chemistry and Physics: 76th Edition, CRC Press, Boca Raton, USA* 1996.

28 A. J. Bard, L. R. Faulkner, *Electrochemical Methods: Fundamentals and Applications, 2nd ed., John Wiley and Sons: New York, USA* 2001.

29 D. R. Lide, *Ed. Handbook of Chemistry and Physics: 76th Edition, CRC Press, Bocaraton, USA* 1996.

30 H. Weingartner, P. Sasisanker, C. Daguenet, P. J. Dyson, I. Krossing, J. M. Slattery, T. Schubert, *Journal of Physical Chemistry B* 2007, *111*, 4775-4780.

31 J. J. Wang, Y. Tian, Y. Zhao, K. Zhuo, *Green Chemistry* 2003, *5*, 618-622.

32 P. Wasserscheid, W. Keim, *Angewandte Chemie-International Edition* 2000, *39*, 3772-3789.

33 F. Endres, S. Z. El Abedin, *Physical Chemistry Chemical Physics* 2006, *8*, 2101-2116.

34 A. E. Visser, R. P. Swatloski, W. M. Reichert, R. Mayton, S. Sheff, A. Wierzbicki, J. H. Davis, R. D. Rogers, *Environmental Science & Technology* 2002, *36*, 2523-2529.

35 A. Ahosseini, A. M. Scurto, *International Journal of Thermophysics* 2008, *29*, 1222-1243.

36 Y. Meng, L. Aldous, S. R. Belding, R. G. Compton, *Chemical Communications* 2012, *48*, 5572-5574.

37 L. E. Barrosse-Antle, A. M. Bond, R. G. Compton, A. M. O'Mahony, E. I. Rogers, D. S. Silvester, *Chemistry-an Asian Journal* 2010, *5*, 202-230.

38 J. M. P. R.C. Reid, T.K. Sherwood, *The Properties of Gases and Liquids, 4rd ed., McGraw-Hill, New York* 1987.

39 A. K. Mehrotra, W. D. Monnery, W. Y. Svrcek, *Fluid Phase Equilibria* 1996, *117*, 344-355.

40 M. J. Assael, N. K. Dalaouti, I. Metaxa, *Fluid Phase Equilibria* 2002, *199*, 237-247.

41 J. W. Przezdziecki, T. Sridhar, *Aiche Journal* 1985, *31*, 333-335.

42 A. S. Teja, P. Rice, *Chemical Engineering Science* 1981, *36*, 7-10.

43 A. S. Teja, P. Rice, *Industrial & Engineering Chemistry Fundamentals* 1981, *20*, 77-81.

44 E. N. D. C. ANDRADE, *Nature* 1930, *125*, 309–310.

45 A. B. McEwen, H. L. Ngo, K. LeCompte, J. L. Goldman, *Journal of the Electrochemical Society* 1999, *146*, 1687-1695.

46 C. F. Ye, J. M. Shreeve, *Journal of Physical Chemistry A* 2007, *111*, 1456-1461.

47 L. P. N. Rebelo, J. N. C. Lopes, J. M. S. S. Esperanca, H. J. R. Guedes, J. Lachwa, V. Najdanovic-Visak, Z. P. Visak, *Accounts of Chemical Research* 2007, *40*, 1114-1121.

48 H. D. B. Jenkins, H. K. Roobottom, J. Passmore, L. Glasser, *Inorganic Chemistry* 1999, *38*, 3609-3620.

49 H. L. Ammon, *Structural Chemistry* 2001, *12*, 205-212.

50 C. Nanjundiah, S. F. McDevitt, V. R. Koch, *Journal of the Electrochemical Society* 1997, *144*, 3392-3397.

51 C. P. Fredlake, J. M. Crosthwaite, D. G. Hert, S. N. V. K. Aki, J. F. Brennecke, *Journal of Chemical and Engineering Data* 2004, *49*, 954-964.

52 Y. Marcus, G. Hefter, *Chem Rev* 2006, *106*, 4585-621.

53 J. M. Saveant, *Journal of Physical Chemistry* 1988, *92*, 4526-4532.

54 H. Vogel, *Physik. Z. 22*, 645-646.

55 G. T. a. G. Z. Veszi, *Anorg. Allgem. Chem.* 1926, *150*, 355-380.

56 G. S. Fulcher, *J. Am. Ceram. Soc.* 1925, *8*, 339-355.

57 J. Vila, P. Gines, J. M. Pico, C. Franjo, E. Jimenez, L. M. Varela, O. Cabeza, *Fluid Phase Equilibria* 2006, *242*, 141-146.

58 J. Vila, L. M. Varela, O. CDOI 10.1016/j.electacta.2007.06.044.

59 K. Matsumoto, R. Hagiwara, Y. Ito, *Electrochemical and Solid State Letters* 2004, *7*, E41-E44.

60 R. Hagiwara, K. Matsumoto, Y. Nakamori, T. Tsuda, Y. Ito, H. Matsumoto, K. Momota, *Journal of the Electrochemical Society* 2003, *150*, D195-D199.

61 M. C. Buzzeo, C. Hardacre, R. G. Compton, *Chemphyschem* 2006, *7*, 176-180.

62 R. K. Donato, M. V. Migliorini, M. A. Benvegnu, J. Dupont, R. S. Goncalves, H. S. Schrekker, *Journal of Solid State Electrochemistry* 2007, *11*, 1481-1487.

63 E. I. Rogers, D. S. Silvester, D. L. Poole, L. Aldous, C. Hardacre, R. G. Compton, *Journal of Physical Chemistry C* 2008, *112*, 2729-2735.

64 R. Wibowo, L. Aldous, S. E. W. Jones, R. G. Compton, *Chemical Physics Letters* 2010, *492*, 276-280.

65 T. Welton, *Chemical Reviews* 1999, *99*, 2071-2083.

66 C. Chiappe, D. Pieraccini, *Journal of Physical Organic Chemistry* 2005, *18*, 275-297.

67 C. Reichardt, *Green Chemistry* 2005, *7*, 339-351.

68 M. Deetlefs, K. R. Seddon, *Chimica Oggi-Chemistry Today* 2006, *24*, 16.

69 C. Cadena, J. L. Anthony, J. K. Shah, T. I. Morrow, J. F. Brennecke, E. J. Maginn, *Journal of the American Chemical Society* 2004, *126*, 5300-5308.

70 J. Jacquemin, M. F. C. Gomes, P. Husson, V. Majer, *Journal of Chemical Thermodynamics* 2006, *38*, 490-502.

71 J. Jacquemin, P. Husson, A. A. H. Padua, V. Majer, *Green Chemistry* 2006, *8*, 172-180.

72 J. Staudinger, P. V. Roberts, *Critical Reviews in Environmental Science and Technology* 1996, *26*, 205-297.

73 R. E. Baltus, B. H. Culbertson, S. Dai, H. M. Luo, D. W. DePaoli, *Journal of Physical Chemistry B* 2004, *108*, 721-727.

74 A. J. Carmichael, K. R. Seddon, *Journal of Physical Organic Chemistry* 2000, *13*, 591-595.

75 G. Y. Zhao, T. Jiang, H. X. Gao, B. X. Han, J. Huang, D. H. Sun, *Green Chemistry* 2004, *6*, 75-77.

76 H. L. Ngo, K. LeCompte, L. Hargens, A. B. McEwen, *Thermochimica Acta* 2000, *357*, 97-102.

77 M. Kosmulski, J. Gustafsson, J. B. Rosenholm, *Thermochimica Acta* 2004, *412*, 47-53.

78 R. P. Swatloski, J. D. Holbrey, R. D. Rogers, *Green Chemistry* 2003, *5*, 361-363.

79 J. Roziere, M. T. Rozierebories, J. M. Williams, *Inorganic Chemistry* 1976, *15*, 2490-2494.

80 U. Schroder, J. D. Wadhawan, R. G. Compton, F. Marken, P. A. Z. Suarez, C. S. Consorti, R. F. de Souza, J. Dupont, *New Journal of Chemistry* 2000, *24*, 1009-1015.

81 J. A. Widegren, A. Laesecke, J. W. Magee, *Chemical Communications* 2005, 1610-1612.

82 J. A. Widegren, E. M. Saurer, K. N. Marsh, J. W. Magee, *Journal of Chemical Thermodynamics* 2005, *37*, 569-575.

83 A. M. O'Mahony, D. S. Silvester, L. Aldous, C. Hardacre, R. G. Compton, *Journal of Chemical and Engineering Data* 2008, *53*, 2884-2891.

84 R. G. Evans, O. V. Klymenko, S. A. Saddoughi, C. Hardacre, R. G. Compton, *Journal of Physical Chemistry B* 2004, *108*, 7878-7886.

85 C. Villagran, M. Deetlefs, W. R. Pitner, C. Hardacre, *Analytical Chemistry* 2004, *76*, 2118-2123.

86 D. Berthier, A. Varenne, P. Gareil, M. Digne, C. P. Lienemann, L. Magna, H. Olivier-Bourbigou, *Analyst* 2004, *129*, 1257-1261.

87 C. Villagran, C. E. Banks, C. Hardacre, R. G. Compton, *Analytical Chemistry* 2004, *76*, 1998-2003.

88 K. R. Seddon, A. Stark, M. J. Torres, *Pure and Applied Chemistry* 2000, *72*, 2275-2287.

89 L. Aldous, D. S. Silvester, C. Villagran, W. R. Pitner, R. G. Compton, M. C. Lagunas, C. Hardacre, *New Journal of Chemistry* 2006, *30*, 1576-1583.

90 M. Kavanoz, H. Gulce, A. Yildiz, *Turkish Journal of Chemistry* 2004, *28*, 287-297.

91 P. J. Dyson, D. J. Ellis, D. G. Parker, T. Welton, *Chemical Communications* 1999, 25-26.

92 V. Farmer, T. Welton, *Green Chemistry* 2002, *4*, 97-102.

93 M. J. Earle, C. M. Gordon, N. V. Plechkova, K. R. Seddon, T. Welton, *Analytical Chemistry* 2007, *79*, 758-764.

94 M. P. Narayan, S. S. Kumar, A. S. Arunrao, P. Karthikeyan, B. P. Rambhau, *Research Journal of Chemistry and Environment* 2011, *15*, 92-103.

95 C. B. Yue, D. Fang, L. Liu, T. F. Yi, *Journal of Molecular Liquids* 2011, *163*, 99-121.

96 J. P. Hallett, T. Welton, *Chemical Reviews* 2011, *111*, 3508-3576 Doi 10.1021/Cr1003248.

97 I. Meracz, T. Oh, *Tetrahedron Letters* 2003, *44*, 6465-6468.

98 Y. Chauvin, L. Mussmann, H. Olivier, *Angewandte Chemie-International Edition* 1995, *34*, 2698-2700.

99 H. Olivier, P. Laurent-Gerot, *Journal of Molecular Catalysis a-Chemical* 1999, *148*, 43-48.

100 P. A. Z. Suarez, J. E. L. Dullius, S. Einloft, R. F. deSouza, J. Dupont, *Inorganica Chimica Acta* 1997, *255*, 207-209.

101 Z. Yang, Y. J. Yue, W. C. Huang, X. M. Zhuang, Z. T. Chen, M. Xing, *Journal of Biochemistry* 2009, *145*, 355-364.

102 S. H. Ha, Y. M. Koo, *Korean Journal of Chemical Engineering* 2011, *28*, 2095-2101 DOI 10.1007/s11814-011-0268-1.

103 F. Fischer, J. Mutschler, D. Zufferey, *Journal of Industrial Microbiology & Biotechnology* 2011, *38*, 477-487.

104 M. Moniruzzaman, N. Kamiya, M. Goto, *Organic & Biomolecular Chemistry* 2010, *8*, 2887-2899.

105 H. Zhao, *Journal of Molecular Catalysis B-Enzymatic* 2005, *37*, 16-25.

106 S. H. Schofer, N. Kaftzik, P. Wasserscheid, U. Kragl, *Chemical Communications* 2001, 425-426.

107 U. Kragl, M. Eckstein, N. Kaftzik, *Current Opinion in Biotechnology* 2002, *13*, 565-571.

108 F. van Rantwijk, R. A. Sheldon, *Chemical Reviews* 2007, *107*, 2757-2785.

109 K. Fujita, M. Forsyth, D. R. MacFarlane, R. W. Reid, G. D. EIliott, *Biotechnology and Bioengineering* 2006, *94*, 1209-1213.

110 C. M. Gordon, *Applied Catalysis a-General* 2001, *222*, 101-117.

111 S. Chowdhury, R. S. Mohan, J. L. Scott, *Tetrahedron* 2007, *63*, 2363-2389.

112 J. L. Kaar, A. M. Jesionowski, J. A. Berberich, R. Moulton, A. J. Russell, *Journal of the American Chemical Society* 2003, *125*, 4125-4131.

113 J. Gao, J. G. Liu, W. M. Liu, B. Li, Y. C. Xin, Y. Yin, Jungu, Z. G. Zou, *International Journal of Electrochemical Science* 2011, *6*, 6115-6122.

114 M. L. Guo, J. Fang, H. K. Xu, W. Li, X. H. Lu, C. H. Lan, K. Y. Li, *Journal of Membrane Science* 2010, *362*, 97-104 DOI 10.1016/j.memsci.2010.06.026.

115 X. Pan, S. Y. Dai, K. J. Wang, C. W. Shi, L. Guo, *Acta Physico-Chimica Sinica* 2005, *21*, 697-702.

116 N. Salem, L. Nicodemou, Y. Abu-Lebdeh, I. J. Davidson, *Journal of the Electrochemical Society* 2012, *159*, A172-A176.

117 C. P. Fu, Y. F. Kuang, Z. Y. Huang, X. Wang, Y. F. Yin, J. H. Chen, H. H. Zhou, *Journal of Solid State Electrochemistry* 2011, *15*, 2581-2585.

118 S. A. Gajar, M. W. Geis, *Ieee Transactions on Electron Devices* 1992, *39*, 2649-2650.

119 C. H. Yang, Q. J. Sun, J. Qiao, Y. F. Li, *Journal of Physical Chemistry B* 2003, *107*, 12981-12988.

120 R. Kawano, M. Watanabe, *Chemical Communications* 2005, 2107-2109.

121 Y. Bai, Y. M. Cao, J. Zhang, M. Wang, R. Z. Li, P. Wang, S. M. Zakeeruddin, M. Gratzel, *Nature Materials* 2008, *7*, 626-630.

122 R. F. de Souza, J. C. Padilha, R. S. Goncalves, J. Dupont, *Electrochemistry Communications* 2003, *5*, 728-731.

123 D. S. Silvester, K. R. Ward, L. Aldous, C. Hardacre, R. G. Compton, *Journal of Electroanalytical Chemistry* 2008, *618*, 53-60.

124 M. C. Buzzeo, C. Hardacre, R. G. Compton, *Analytical Chemistry* 2004, *76*, 4583-4588.

125 A. M. O'Mahony, D. S. Silvester, L. Aldous, C. Hardacre, R. G. Compton, *Journal of Physical Chemistry C* 2008, *112*, 7725-7730.

126 L. E. Barrosse-Antle, D. S. Silvester, L. Aldous, C. Hardacre, R. G. Compton, *Journal of Physical Chemistry C* 2008, *112*, 3398-3404.

127 X. J. Huang, E. I. Rogers, C. Hardacre, R. G. Compton, *Journal of Physical Chemistry B* 2009, *113*, 8953-8959.

128 W. C. Barrette, Jr., H. W. Johnson, Jr., D. T. Sawyer, *Analytical Chemistry* 1984, *56*, 1890-8.

129 G. Kuranov, B. Rumpf, N. A. Smirnova, G. Maurer, *Industrial & Engineering Chemistry Research* 1996, *35*, 1959-1966.

130 A. Douabul, J. Riley, *Journal of Chemical and Engineering Data* 1979, *24*, 274-276.

131 M. Yoshizawa, W. Xu, C. A. Angell, *Journal of the American Chemical Society* 2003, *125*, 15411-15419.

132 H. M. Luo, G. A. Baker, J. S. Lee, R. M. Pagni, S. Dai, *Journal of Physical Chemistry B* 2009, *113*, 4181-4183.

133 Y. Meng, L. Aldous, S. R. Belding, R. G. Compton, *Physical Chemistry Chemical Physics* 2012, *14*, 5222-5228.

134 E. I. Rogers, X. J. Huang, E. J. F. Dickinson, C. Hardacre, R. G. Compton, *Journal of Physical Chemistry C* 2009, *113*, 17811-17823.

135 X. B. Ji, D. S. Silvester, L. Aldous, C. Hardacre, R. G. Compton, *Journal of Physical Chemistry C* 2007, *111*, 9562-9572.

136 M. C. Buzzeo, E. V. Klymenko, J. D. Wadhawan, C. Hardacre, K. R. Seddon, R. G. Compton, *Journal of Physical Chemistry B* 2004, *108*, 3947-3954.

137 A. M. O'Mahony, E. J. F. Dickinson, L. Aldous, C. Hardacre, R. G. Compton, *Journal of Physical Chemistry C* 2009, *113*, 10997-11002.

138 R. C. Remsing, G. Hernandez, R. P. Swatloski, W. W. Massefski, R. D. Rogers, G. Moyna, *Journal of Physical Chemistry B* 2008, *112*, 11071-11078.

139 S. D. Zhu, Y. X. Wu, Q. M. Chen, Z. N. Yu, C. W. Wang, S. W. Jin, Y. G. Ding, G. Wu, *Green Chemistry* 2006, *8*, 325-327.

140 A. P. Dadi, C. A. Schall, S. Varanasi, *Applied Biochemistry and Biotechnology* 2007, *137*, 407-421.

141 R. A. Mantz, D. M. Fox, J. M. Green, P. A. Fylstra, H. C. De Long, P. C. Trulove, *Zeitschrift Fur Naturforschung Section a-a Journal of Physical Sciences* 2007, *62*, 275-280.

142 F. Endres, *Chemphyschem* 2002, *3*, 144.

143 S. Ahmad, M. Deepa, V. Sen, S. Kazim, S. K. Agarwal, *Polymer Engineering and Science* 2011, *51*, 1513-1518.

144 A. Lisenkov, M. L. Zheludkevich, M. G. S. Ferreira, *Electrochemistry Communications* 2010, *12*, 729-732.

145 A. Safavi, N. Maleki, F. Tajabadi, E. Farjami, *Electrochemistry Communications* 2007, *9*, 1963-1968.

Chapter 2 Fundamentals of Electrochemistry

2.1 Electrochemistry

Electrochemistry is a branch of chemistry and takes place at an interface between an electron conductor (such as metal, semiconductor and alloy) and an ionic conductor (electrolyte). It is driven and controlled by an external power (applied potential) to achieve electron transfer and drive a reaction associated with oxidation or reduction.

Generally speaking, in the late 18th century, the discovery of *animal electricity* was believed to be the birth of electrochemistry by establishing a link between chemical reaction and *animal electricity*. Soon after, the English chemist William Nicholson and Johann Wilhelm Ritter succeeded in decomposing water into hydrogen and oxygen by electrolysis and the process of electroplating was discovered. In 1832, Michael Faraday developed two important laws of electrochemistry which are the theoretical basic of quantitative study. In the late 19th century, the German chemist Walther Hermann Nernst developed the theory of electromotive force and produced the most important relationship between the concentration of electroactive species and electrode potential, known as the Nernst equation. In 1923, the Brønsted-Lowry acid-base theory was published promoting the development of electrochemical theory and the experimental method. After 1940, a series of novel techniques, such as transient techniques, surface studies and nano-technology, have been introduced to solve the mechanism of many rapid and complicated electrochemical reactions, and corresponding technologies have been carried out in the industry. [1, 2]

It is necessary to divide the electrochemical processes into three main distinct categories. The first one relates to equilibrium processes. The current densities for oxidation and reduction are the same which induce the no net current passing through the external circuit and the corresponding potential is given by the Nernst equation. Therefore, such measurements can yield a wealth of thermodynamic information involving Gibbs energy, entropy changes,

enthalpy changes, equilibrium constant and pHs of solution. The second relates to processes under kinetic control and occur when the applied potential falls into a small range near the equillbrium potential. The current density as a function of applied potential under this condition is depicted by the famous Butler-Volmer equation. The third relates to mass transport controlled processes which are strongly influenced by the size of electrode and the nature of solvent and diffusion coefficient.

The oxidation of ferrocene[3] is thought as a simplest electrochemical process, only involving a mass transport of a reactant to the electrode surface, heterogeneous electron transfer without any adsorbed process and a mass transport of the product to the bulk solution. In other processes a series of complex reactions, such as adsorption, desorption, crystallization, electrotrodeposition, protonation, parallel paths or branching mechanism, accompany the electrochemical reaction. The magnitude of current density is controlled by the step in which the reaction has the slowest rate, the rate determining step.

This thesis is concerned with all the individual types of processes. The rest of this chapter provides an introduction to the fundamental electrochemical principles, concepts and methods. A more detailed description is given in several Electrochemistry textbooks.[4-8]

2.2 The solid / liquid interface

The solid / liquid interface is of the heart of electrochemistry study. It is well known that two types of current responses are present when potential is applied to the interface between an electrode and an electrolyte. It is necessary to reveal their derivation and the relationship to the potential.

2.2.1 Faradaic and NonFaradaic current

The measurement current consists of two types of current responses at the interfacial region.[9] One is named as the 'Faradaic current', and arises from electron transfer between the electrode and electroactive species in the electrolyte when oxidation or reduction occurs. It is known that the amount of reaction associated with the flowing current is proportional to the amount of charge passed, the Faraday's law. The magnitude of Faradaic current is mainly dependence on the kinetic constant (heterogeneous electron transfer at the interface), diffusion coefficient of interest (mass transport) and the rate of any homogeneous chemical reaction or heterogeneous electrochemical reaction which might exist before or after the main electrochemical process. These factors are the important and fundamental structures of electrochemical analysis, which are elaborated as required in the whole thesis.

The relatively low currents are observed in the voltammogram where no Faradaic current occur. This current response is caused by any adsorption / desorption processes and the structure change of the double layer, termed as the nonFaradaic current. Charge transfer occurs across the interface, this type of charging current is behaves as a capacitor as a function of applied potential.

$$i_c = AC\frac{dE}{dt} = AC\nu \tag{2.1}$$

where A is the area of electrode, *C* is the double layer capacitance, $\frac{dE}{dt}$ is differetial of potential versus time and *v* is scan rate.

Both faradaic and nonFaradaic current contribute to the total current density all electrochemical reactions. In general, only the faradaic response is an experimental aim as a function of electroactive species. Accordingly, minimizing the nonFaradaic response is a common requirement and achieved by using the supporting electrolyte in the solution. Indeed, two situations which occur in the thesis cannot neglect the influence of nonFaradaic current.

One is an extremely low concentration of interest in the absence of any excess supporting electrolyte and the other is at high scan rates, where the charging current can be larger than the Faradaic current caused by the oxidation or reduction of interest.

2.2.2 The description of the electrical double layer

According to the discussion of NonFaradaic current, the behaviour of electrode / electrolyte interface is analogous to that of a capacitor. When potential is applied to the electrode, a donor or acceptor of electrons is present at the electrode. An electrical field gradient will arise across the interface and it leads to the charge separation and rearrangement of ions in the vicinity of the solution in an effort to maintain the electroneutrality. As a result, the region where ions of opposite charge are attracted to the direction of electrode surface and the others are repelled toward the bulk solution is named the electrical double layer.

Various models have been proposed to depict the real and complicated structure of the double layer. A simple model acting as the behaviour of a parallel plate capacitor was proposed first by Helmholtz[10] where two rigid planar layers are established at each side of electrode / electrolyte interface in the presence of equal quantities of electrical charge and the opposite charge. A more realistic model was established by Gouy[11] and Chapman[12], which proposed that the approximate exponential distribution of opposite ions is governed by the magnitude of electrical field at any space and time with the ions treated as the simple points, and known as the diffuse layer. However, this model did not provide a good explanation for the accumulation of the innermost ions toward the electrode surface. Stern[13] then developed a novel model on the basis of the two earlier models. The model was comprised of two parts: one is a rigid layer with opposite charges, similar to the Helmholtz model, but it did not require the equal quantity of electrical charge. The rest of opposite charge was assigned to the

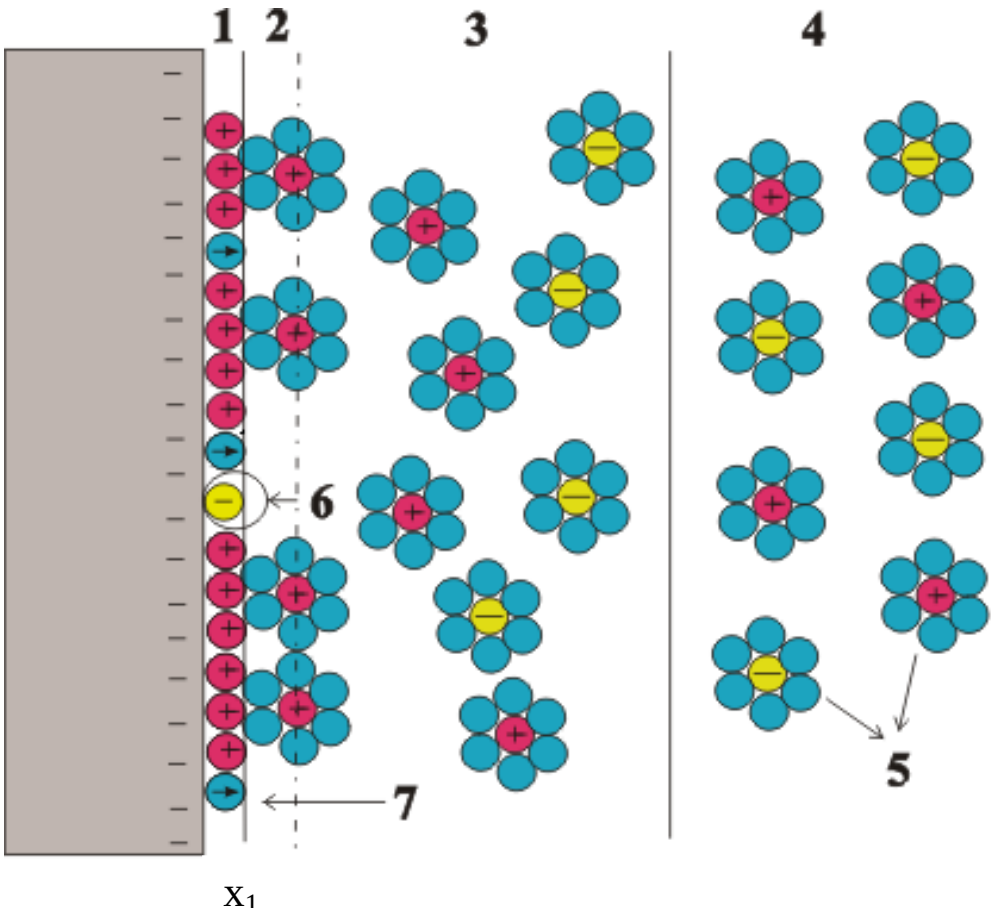

Figure 2.1 the scheme of an electrical double layer, (Gouy-Chapman-Stern model[14])

1. IHP, Inner Helmoholtz Layer
2. OHP, Outer Helmoholtz Layer
3. Diffuse Layer
4. Bulk solution
5. Solvated ions
6. Speculiar adsorptive ions
7. Solvent molecule

second part, the diffuse layer, which is following the approximate exponential distribution. Additionally, the ions were treated as the spheres with a realistic volume in order to reflect steric effects on the electrode surface.

Figure 2.1shows a comprehensive model to distinguish the behaviour of different adsorbed species. The inner rigid layer can be divided into two distinct layers, known as the inner Helmholtz plane (IHP) and the outer Helmholtz plane (OHP), respectively. The IHP consists of the 'naked' adsorbed ions, the locus of which occupies the nearest space at a distance x_1. In contrast, the OHP involves a series of solvated ions with a larger size, the locus of which lay at a relatively more distant location, forming an OHP. Long range coulumbic force contributes to the solvated ions and electrode surface, so this interaction is largely independent of the chemical properties of the solvated ion. The diffuse layer inherits the characteristics of the previous model, the thickness of which depends on a concentration of ions (less than 300Å, using the concentration greater than 0.02 M). The potential drop is approximately linear through the IHP and OHP, with an exponential decrease over the range of diffuse layer. In these models, the interfacial region is still regarded as a homogeneous charge distribution with a stable three-dimensional structure, which is strongly affected by the electrode itself.[15] A non-local electrostatic approach has been used to describe the double layer to give a more accurate diffuse boundary rather than a sharp boundary.[16, 17]

In addition, the model shows a capacitance unlike real capacitor and is a function of the applied potential, typically[4] in the range of 10 to 40μF / cm^2.

2.3 Mass transport

Electron transfer at the interface and mass transport of new electroactive species to the reactive surface are the main factors to the electrochemical dynamics. In this part, the thesis focuses on mass transport only, focusing on mass transport controlled reactions. Mass transport represents the movement of material in the solution, causing the replenishment of the reactant and the release of the product on the reactive surface. Three modes have been taken into account accompanied with mathematical models, arising from the chemical,

electrical, and physical difference from one location to another, known as diffusion, migration and convection, respectively.

2.3.1 Diffusion

The reduction or oxidation of interest leads to a low reactant concentration near the electrode surface, forming concentration gradients of reactant and product, which force the materials to move from the high concentration to low concentration. Therefore, these movements under the influence of the concentration gradient are defined as diffusion. This mode of mass transport has been described by Fick's first law,[8] revealing the relationship between the diffusive flux and concentration, as well as the direction of flux under the assumption of steady state. Consider the case of a linear dimension *x*:

$$J_d(x,t) = D\frac{\partial C_0(x,t)}{\partial x} \tag{2.2}$$

where J_d is the diffusive flux, measuring the amount of interest which passes through the small area (dx^2) at the small time (dt). $\frac{\partial C_0(x,t)}{\partial x}$ is the concentration gradient of interest and negative sign of equation implies that the diffusive flux tend to the inverse direction of concentration increase at the axis of *x*. D is the diffusion coefficient of interest and it represents the rate of diffusing species along the opposite concentration gradient in the specific electrolyte, the value of which is given by

$$D = \frac{(\delta x)^2}{\delta t} \tag{2.3}$$

where δx is a distance at which an assumption of unit moves and δt is the time interval for the movement. In practice, it is useful to explore the influence of diffusion coefficient in term of hydrodynamic theory. It is necessary to consider the Stokes-Einstein relationship[18] that for a simple diffusing species, There is expected to be a linear relationship between the diffusion coefficient of solute (D) and the inverse of solvent viscosity.

$$D = \frac{k_B T}{6\eta\pi\alpha} \tag{2.4}$$

where k_B is the Boltzmann constant, T is the temperature and α is the hydrodynamic radius of the diffusing species.

Actually, the temperature is one of most important variable for the whole electrochemical field. The influence of the temperature on a diffusion coefficient cannot be ignored and a simple mathematic model has been given by the Arrhenius relationship[4]:

$$D = D_\infty exp(\frac{-E_{a.D}}{RT}) \tag{2.5}$$

where D_∞ is a hypothetical diffusion coefficient at infinite temperature, R is the universal gas constant and $E_{a,D}$ is the diffusional activation energy of the electroactive species.

The Fick's second law, the second-order differential equation, shows the variation of concentration at any time and space.

$$\frac{\partial C_0(x,t)}{\partial t} = D_0 \nabla^2 C_0(x,t) \tag{2.6}$$

The equation has been written for a three-dimensional system. It can be simplified for a one dimensional system or transformed into various coordinate systems:

Table 2.1 Fick's law under different coordinate systems

geometry	Variable	∇^2
linear	x	$\partial^2/\partial x^2$
cubic	x, y, z	$\partial^2/\partial x^2 + \partial^2/\partial y^2 + \partial^2/\partial z^2$
spherical	r	$\partial^2/\partial r^2 + (2/r)(\partial/\partial r)$
cylindrical	r	$\partial^2/\partial r^2 + (1/r)(\partial/\partial r)$

In order to analyze the behaviour of diffusion, differential equations have been established under each the coordinate system, but they require initial conditions and boundary conditions to give suitable solutions.

2.3.2 Convection

Convection is the movement of species due to the mechanical movement, which can be divided into two categories: one is natural convection, caused by thermal or density fluctuation. The other one is forced convection, which arises from external forces, such as gas bubbling, stirring and motion of the electrode. In general, the magnitude of forced convection is several order greater than that of natural convection, so natural convection can be negligible in the presence of forced convection. The controllability of forced convection is useful to provide reliability and reproducibility in the experimental environment and increase the transport rate of interest. Regular convections, such as stirring and motion of the electrode,[8] have been extensively investigated by the researchers accompanied by the appropriate mathematic model, but the influence of convection is absence, using suitable experimental design to eliminate the seed

2.3.3 Migration

Migration is the movement of a charged species under the influence of an electrical field.[7] In the present of an electrical field, all charged species will possess a part of contribution for the migratory flux. For any species *i*, the migratory component of flux, J_i can be described by a mathematic expression[6]:

$$J_i = u_i c_i \frac{\partial \emptyset}{\partial x} \tag{2.7}$$

where u_i is the mobility of ion *i*, c_i is the concentration of species *i*, and Φ is the applied electrode potential. The mobility is the limiting migration velocity of the charged species under the unit strength of electric field, which is given by the Einstein relationship:[4]

$$u_i = \frac{|z_i|e}{6\pi\eta r} \tag{2.8}$$

where z_i is the magnitude of its charge, e is the electronic charge, r is the radius of the charged species *i* and η is the viscosity of the electrolyte. The total current in bulk solution is the sum of every fraction which is contributed by every charged species.

The fraction of migration as a function of potential is unpredictable or has a very complicated expression for the most electrochemical measurements, causing complication of electro-chemical analysis. A useful and convenient method is used to overcome this uncontrolled factor where a large excess chemically and electrochemically inert electrolyte is introduced into the solution as the supporting electrolyte. In experimental application, the concentration of the supporting electrolyte should be at least 30 times greater than that of interest. The application of excess electrolyte in the solution can be considered from several aspects. First, the existence of excess electrolyte at the interfacial region leads to the compression of double layer in a small range where the electric field is mainly distributed and stable during electrolysis, facilitating electron transfer due to the quantum tunnelling mechanism. Secondly, the increase of conductivity in the presence of the supporting electrolyte results in the decrease of Ohmic drop, which can share a part of potential drop and distort the ideal potential-current relationship of electrochemical process. Thirdly, the presence of the activity coefficient in Nernst equation is undesirable. The excess of supporting electrolyte provides an excellent experimental environment to fix the activity coefficient of electroactive species, correcting the Nernst relationship at the interfacial region.

2.4 The introduction of electrochemical thermodynamics

2.4.1 Reversibility

Electrochemical thermodynamics show the behaviour of a system at equilibrium and the concept of reversibility is an essential and important factor to analyze real process.

(a) Chemical reversibility

Generally speaking, a spontaneous reaction can take place when the two electrodes of the electrochemical cell are shorted together. If an output of energy source, such as the battery, is added to this external circuit in order to reverse the trend of the previous reaction and back out the cell voltage, and the evolution of the reaction is strictly and merely reversed without any new reaction, this cell is named chemically reversibility.

(b) Thermodynamic reversibility

Thermodynamic reversibility is an ideal process where a reaction can reverse its direction due to an infinitesimal perturbation acting as a driving force, while the reversible path requires maintaining a continuous series of the equilibrium states. Hence the state must be always at equilibrium. According to the definition, this condition cannot occur due to the limited reaction rates and hysteresis effects in any real electrochemical system.

It is noted that chemical reversibility is a necessary condition for thermodynamic reversibility rather than sufficient condition in the electrochemical system.

(c) Practical reversibility

Practical reversibility is an approximation to strict thermodynamic reversibility, as considering the finite rate. Hence, this approximation applies to any desired accuracy the experiment requires. Under these circumstances, the system has passed through a series of *quasi*-reversible states, arising from relatively high rate of reaction. It depends on the time

scale of measurements, the change rate of the electrochemical system with respect to the perturbation and the speed for rebuilding up the equilibrium state.

The Nernst equation[8] behaves as an efficient method to judge whether a process appears reversible or not, providing a relationship between electrode potential and the concentration of interests for a specific electrochemical process.

$$E = E^0 + ln(\frac{(C_O)(\gamma_O)}{(C_R)(\gamma_R)}) \quad (2.9)$$

where, E^0 is standard potential of half-cell, C_O and C_R are the concentration of oxidized and reduced anticipants, and γ_O and γ_R is the corresponding chemical activity for the relevant species. The Nernst equation is one of most fundamental and important expression for the modern electrochemical analysis, which reveals a series of linkages among the thermodynamic behaviour (more detailed will be introduced in Section 2.4.2). In simple terms, if the electrochemical cell obeys the Nernst equation, the electrode process can be called as reversible.

It is noteworthy that the reversibility condition does not apply for a particular redox couple. A given redox system can show the reversibility or not for different conditions.

2.4.2 Gibbs energy

Gibbs energy is an important thermodynamic parameter relating to the system at constant temperature and pressure, the change in which is the maximum non-expansion work can be measured from a closed system. The thermodynamic definition of Gibbs energy is:[4]

$$G = H - TS = U + pV - TS \quad (2.10)$$

where U is the internal energy, p is the pressure of system, V is the volume of electrochemical cell, T is the temperature, S is the entropy and H is the enthalpy. The change

of Gibbs free energy (ΔG) is useful to thermodynamic analysis under fixed temperature and pressure. It is noticed if the calculated ΔG_0 ($\Delta G_0 = G_{final} - G_{initial}$) is a negative value, the electrochemical cell behaves to release the Gibbs energy, resulting in a spontaneous reaction. In contrast for a positive value of ΔG^0, the system needs to absorb the energy from the external source, such as a battery in an external circuit. Thus two inferences appear in: one is when ΔG^0 equal to zero, the system remain at equilibrium (Neither the forward nor the backward reaction can dominate), another is that the minimum of Gibbs energy is a necessary and sufficient condition for any equilibrium closed system in relation to the lowest point of potential curve. These analyses reveal a linkage between ΔG and equilibrium constant (*K*), which is formulated by

$$\Delta G = \Delta G^0 - RT ln\, K \qquad (2.11)$$

where ΔG^0 is the standard Gibbs energy. In an electrochemical system, the maximum value of ΔG can be realized as the total energy contribution in a completely reversible system when the system (electrode potential) changes from one state to another, equalling to the work exchanged in the external circuit. The Gibbs energy is given by

$$\Delta G^0 = -nFE^0 \qquad (2.12)$$

where n is the amount of electrons transfer versus per reacted atom or molecule, and F is the Faraday constant, related to the electrical quantity of charge on a mole of electrons. E^0 is called the standard *emf* of the cell reaction. Therefore, the equation of ΔG *vs* K is another specific form of Nernst equation, and K has been given a specific chemical form.

2.4.3 Electrochemical potential

The electrochemical potential is a thermodynamic measure combined with the concept of inherent energy for every electrochemical process. The redox couple on a electrode metal can be governed by two aspects: first, the energy state of anticipants (molecule or ion) in any

location (electrode metal or solution) depends on the chemical environment, such as adsorption, solvation. Secondly, energy of charge species arises from the potential at the corresponding space. In general for electrochemical measurements, it is very difficult to obtain an accurate value of any single component, but combining the contribution of the two components and makes them possible to be formulated in term of thermodynamic theory. Butler and Guggenheim[19, 20] have developed the following mathematic form of electrochemical potential, $\overline{\mu}_i^{\alpha}$, and referred these two aspects of concept:

$$\overline{\mu}_i^{\alpha} = \mu_i^{\alpha} + z_i F \phi^{\alpha} \tag{2.13}$$

The component μ_i^{α} is termed as chemical potential, which is related to the chemical environment of interest.

$$\mu_i^{\alpha} = (\frac{\partial G}{\partial n_i})_{T,P,n_{j\neq i}} \tag{2.14}$$

The other part can be assigned to the electrical environment at any location.

Simplifying the form of electrochemical potential for some special substance is helpful to the application of this concept.

1. For uncharged species: $\overline{\mu}_i^{\alpha} = \mu_i^{\alpha}$
2. For equilibrium of species *i* between phases α and β: $\overline{\mu}_i^{\alpha} = \overline{\mu}_i^{\beta}$
3. For any substance, the chemical potential consist of the standard chemical potential and the activity of species *i* in α phase. $\mu_c = \mu_c^0 + RTln\ K$

The most important application of the electrochemical potential is to establish the Nernst equation for any equilibrium process. The method can be found in any electrochemical textbook.[4, 7, 8]

2.4.4 Formal potential

Dealing with the activity coefficient in the Nernst equation is usually very complicated and inconvenient for the electrochemical analysis of a half cell process. Actually, since the ionic strength strongly affects the magnitude of the activity coefficient, it is noted that the standard potential cannot remain constant when the redox couple is used in different solutions or the same electrochemical process arises from different donated species. (e.g. the reduction of H^+ from HCl, $HNTf_2$, H_2SO_4).

In order to sidestep the complicate competitive equilibra, the formal potential, E_f^0, has been proposed when the ratio of γ_O / γ_R is unit or the concentration of other species are given, incorporating the standard potential and all of activity coefficients.

$$E = E^0 + \frac{RT}{nF} ln\left(\frac{(C_O)(\gamma_O)}{(C_R)(\gamma_R)}\right) = E_f^0 + \frac{RT}{nF} ln\left(\frac{C_O}{C_R}\right) \quad (2.15)$$

where

$$E_f^0 = E^0 + \frac{RT}{nF} ln\left(\frac{\gamma_O}{\gamma_R}\right) \quad (2.16)$$

2.5 Electrode kinetics

Thermodynamics merely focuses on the state of equilibrium, but has nothing to discuss the mechanism of establish or re-establish equilibrium. The purpose of this section is to develop the theory and mathematic expressions which can quantitatively study the behaviour of electrode kinetics as a function of parameters such as concentration, temperature and electrode potential. Considering a simple one-electron process (reduction) is convenient to analyze the kinetic behaviour, and the species, O, is reduced to R where k_f and k_b represent the forward and backward kinetic constant.

$$O + e^- \underset{k_b}{\overset{k_f}{\rightleftarrows}} R \quad (2.17)$$

2.5.1 The Butler Volmer theory

Figure 2.2 displays the typical configuration of Gibbs energy during the reduction process. The electron transfer needs to rise from one minimum, surmount an energy barrier, known as the activation energy, E_A, and fall into another minimum along the reaction coordinate. The exponential function is proposed to express the possibility of surmounting the energy barrier with respect to the Arrhenius Law.[4]

$$k = Ae^{-E_A/RT} \tag{2.18}$$

where A is a constant, relating to the frequency factor. In order to connect the thermodynamic behaviour with activation energy, transition state theory facilitates a linkage to Gibbs energy, ΔG*.

$$k = Be^{-\Delta G^*/RT} \tag{2.19}$$

It is well known that Gibbs energy is an electrode potential dependent factor, thus the equation can be expanded for both forward and backward process:

$$k_f = k_0 \exp(-\frac{\alpha F(E - E_f^0)}{RT}) \tag{2.20}$$

$$k_b = k_0 \exp(\frac{(1-\alpha)F(E - E_f^0)}{RT}) \tag{2.21}$$

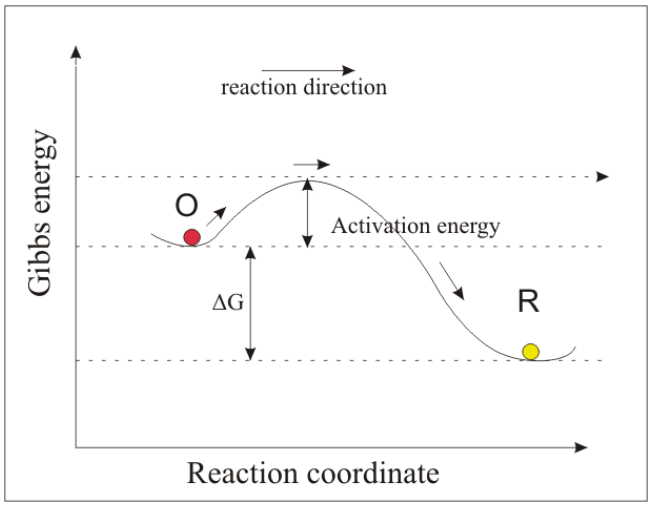

Figure 2.2 the configuration of Gibbs energy during a reduction

where k_0 is the standard kinetic constant, E_f^0 is the formal potential of redox couple and α is the transfer coefficient.

The most widely accepted expression for the kinetic behaviour was proposed by Butler and Volmer[21].

$$i = FAk_0[C_0^R \exp(\frac{(1-\alpha)F(E-E_f^0)}{RT}) - C_0^O(-\frac{\alpha F(E-E_f^0)}{RT})] \qquad (2.22)$$

A critical condition need be mentioned here: ΔG* is not governed directly by the electrode potential. Actually, ΔG^0 reflects the intersection of the configuration in figure 2.2 in relation to the reactant and product energy. If the electrode potential is changed, the electrical potential well of species O will ascend or descend along the vertical direction, the change of ΔG^0 reflects the shift of the potential dependent intersection, but the magnitude of the shift could be very small with respect to the perturbation of electrode potential. A potential independent transfer coefficient (α) is used to reflect the contribution of such change rather than chemical energy.

2.5.2 Transfer coefficient

The transfer coefficient, α, is a parameter to describe the geometric detail of the potential dependent energy barrier. Consider the intersection relationship of the potential curves which arise from the species O and R. In a simple way, the curve can be approximated as linear at the small intersection region, as shown in figure 2.3. Hence, the value of α is formulated by the angle of θ and Φ:

$$\alpha = \frac{\tan\theta}{\tan\phi + \tan\theta} \qquad (2.23)$$

The value of transfer coefficient falls into the range of 0 to 1. If α is close to zero, the transition state matchs with the potential dependent behaviour of species O, otherwise it is

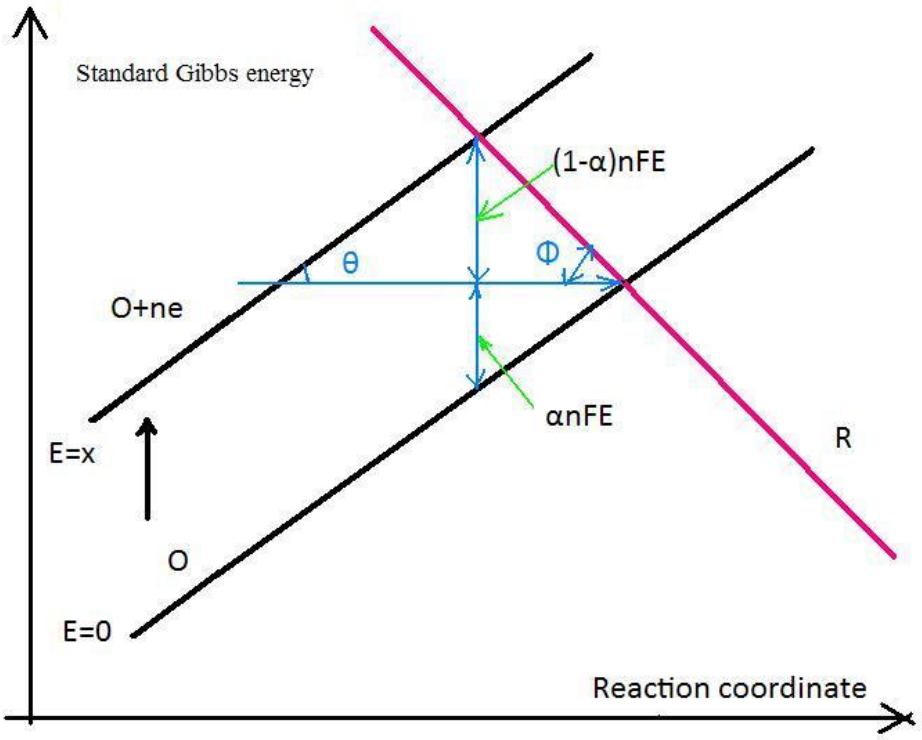

Figure 2.3. Relationship of the transfer coefficient to the angle of intersection of potential dependent Gibbs energy curve

close to the behaviour of species R when α is 1. Thus the transfer coefficient reflects the sensitivity of the transition state to the change of electrode potential at the interface of metal / solution. In other word, it reveals the trend of activation energy as a function of the electrode potential.

Tafel equation is a relatively successful model of electrode kinetic and gives the linkage of current to overpotential.:[4, 5]

$$ln\, i = lni_0 \pm \frac{\alpha R}{RT}\eta \qquad (2.24)$$

The equation shows how to measure α value experimentally, from the slope of plot of the logarithm of current versus potential. It is well known that the Tafel equation is a special case of Butler-Volmer equation where the overpotential is far away from the formal potential of

redox couple. Hence, for example, the current component arises from one reduction process, the oxidation is vanishingly small.

2.6 Multiple processes

In the discussion of a simple one electron transfer process so far it has been assumed that the product of electrochemical reaction is chemically stable (inert). But the generated species from a real electrochemical reaction usually possess a high chemical activity. Therefore, further reaction might appear on the timescale of voltammetry, forming a more complex mechanism of electrolysis. It is necessary to illustrate the common mechanisms of electrochemical system and the corresponding voltammetric responses. A notation proposed by Testa and Reinmuth[22] has been adopted to describe the steps of an electrolysis mechanism: an electrochemical step (heterogeneous electron transfer) at the electrode is termed as an 'E' step and a chemical reaction (homogeneous chemical reaction) in the solution is denoted as a 'C' step. In this section, illustrated reactions are introduced briefly. In particular, the CE, EC and ECE mechanisms.

2.6.1 CE mechanism

The starting species needs to undergo a homogeneous chemical reaction in the solution to form the species B as below.

$$A \xrightarrow{k_c} B(aq) \qquad \text{C}$$

before electron transfer

$$B(aq) \pm e^- \xrightarrow{k_E} C(aq) \qquad \text{E}$$

Typical C processes are the dissociation of metal complexs,[23, 24] the dehydration of carbonyl compounds[25, 26] or the dissociation of acids / bases,[27, 28] which have been widely investigated. The formation of B of higher electrochemical activity, therefore, can maintain the subsequent

process at the electrode surface. An example of this type of mechanism is the reduction of benzoic acid in RTILs. (See chapter 9).

2.6.2 EC mechanism

Analogously if a chemically unstable species B is formed from an E process at the electrode and it is lost through a homogeneous reaction, the electrode process is termed as an EC mechanism.[29, 30] The typical process can be written as

$$A(aq) \pm e^{-} \xrightarrow{k_E} B(aq) \qquad \text{E}$$

$$B(aq) \xrightarrow{k_C} C \qquad \text{C}$$

The observed cyclic voltammograms reflect the subsequent chemical step. Figure 2.4 shows the influence of a chemical step on the observed EC behaviour. The forward voltammetric sweep arises from the oxidation of species A, which is similar to that seen for the general and stable reversible voltammogram. However, the backward wave, corresponding to the reduction of B to A, has been differentiated by the kinetics rate of chemical step, k_c or the stability of species B in the solution. For the situation where k_c.is very slow, a stable

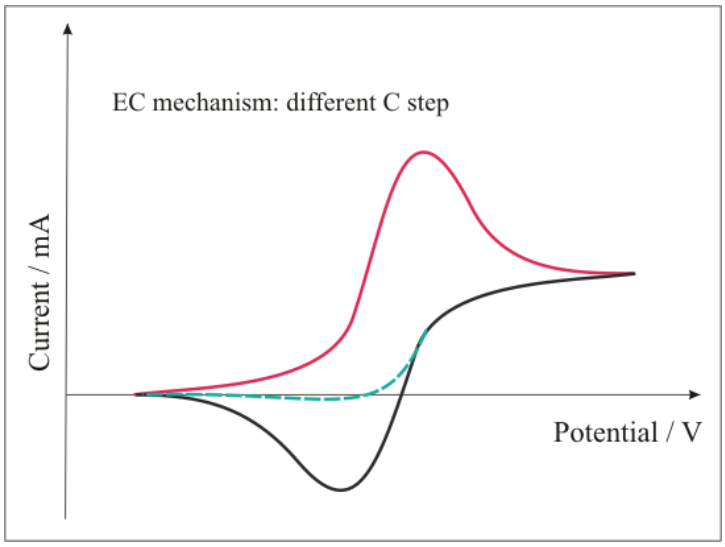

Figure 2.4. shows the influence of chemical step on the observed EC behaviour

reversible voltammogram is detected due to no significant depletion of species B. This is equivalent to a single E process. In comparison, fast k_c leads to the fading of the backward peak. Therefore, the faster the chemical kinetic rate is, the smaller the backward wave is seen

In addition, any analysis of an EC mechanism must account for the potential scan rate, and the relative heights of the backward wave can be used to estimate the kinetic rate of C step. If the potential scan rate is increased; the time for species B to decay and diffuse away from the electrode surface is decreased, leading to a more reversible voltammogram. An example of an EC mechanism is the oxidation of 1,4-aminophenol in acidic aqueous solution.[8]

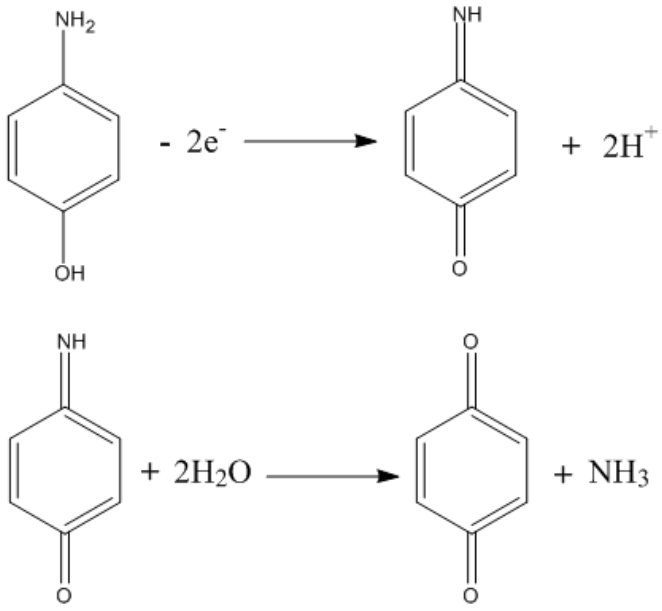

2.6.3 ECE mechanism

The ECE mechanism is an extension of the EC process:

$$A(aq) \pm e^- \xrightarrow{k_E} B(aq) \qquad \text{E1}$$

$$B(aq) \xrightarrow{k_C} C(aq) \qquad \text{C}$$

$$C(aq) \pm e^- \xrightarrow{k_E} D(aq) \qquad \text{E2}$$

The initial E and C steps are identical to the EC mechanism, but the product C(aq) formed by the C step is electroactive and lead to the subsequent E step to form the stable species D.

It is of interest to consider the potential of the second E step, and explore two distinct cases. The case where the species C is more difficult to reduce than the species A is signalled by two separate voltammetric waves.[31] On the forward sweep, the peak detected at the more positive potential corresponds to the reduction of A to B, and the further wave at more negative potential is governed by the reduction of C to D, the magnitude of which is dependent on potential scan rate and the kinetic rate constant, k_C. It is noted that the height of second wave is unlikely to exceed that of first wave. The pattern A in figure 2.5 reflects this case, but other analysis, sepecially seen voltammetric effects, need be taken in account to differ ECE from the simple EE mechanism, or even EEC mechanism. On the contrary, the case where the species C is easier to reduce than the species A is recorded by one potential wave.[32] But at the theoretical level, it must be recognised that this single potential wave actually consists of two overlapping waves associated with two serial electrochemical steps, (figure 3.5, pattern B). The magnitude of this wave is dependent on both potential scan rate and homogeneous rate constant, because the current contribution of C to D is decided by the rate of C formation.

An example of an ECE mechanism is the reduction of 3-bromo benzophenone, RBr in DMF using a 3mm GC electrode.

$$R - Br + e^- \rightleftarrows [R - Br]^{\cdot -}$$

$$[R - Br]^{\cdot -} \rightarrow R^{\cdot} + Br^-$$

$$R^{\cdot} + HS \rightarrow RH + S^{\cdot}$$

$$RH + e^- \rightleftarrows [RH]^{\cdot -}$$

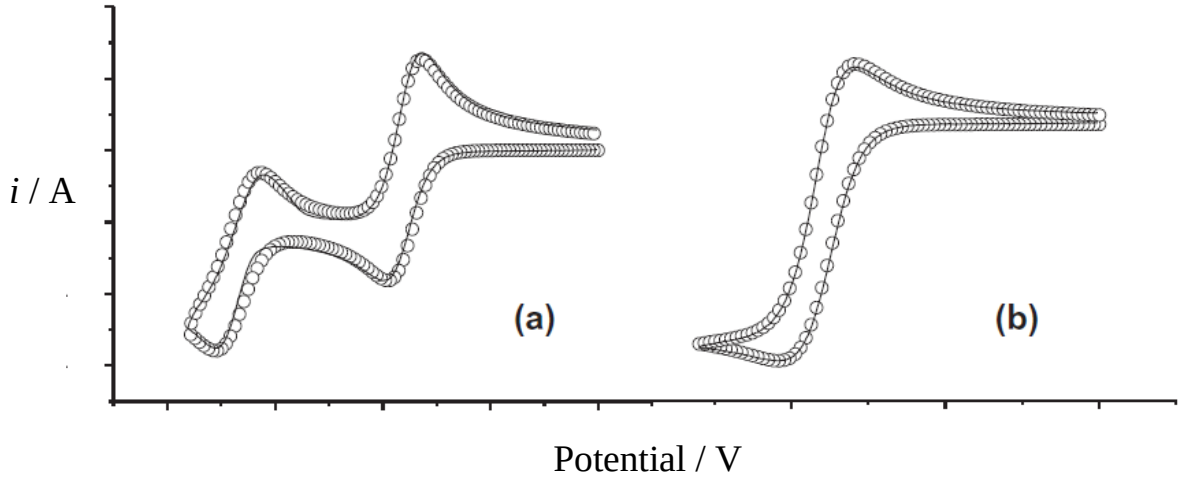

Figure 2.5. Two different voltammetric feature of the ECE mechanism

2.7 Hydrogen evolution reaction on metals

2.7.1 The adsorption of hydrogen atoms[33]

Generally speaking, physisorption of gaseous H_2 molecules[34] is attributed to weak interaction of the van der Waals' nature when the H_2 approaches a metallic surface at very low temperatures (from 5 to 20 K). In the case of chemisorptions, a stronger interaction appears at higher temperature and it is known to proceed by two distinct ways: (i) the release of the enthalpy of adsorption leading to dissociation of H_2 molecule into atomic H and instantaneous formation of a chemical bond with substrate; (ii) The dissociation of hydrogen molecule take places after they surmount an activated barrier, after which is formed the chemical bond. The same energy derives from the different pathways of chemisorptive processes and fall into the range, namely $E_{M\text{-}Hchem}$=250-300 kJ mol^{-1}, which is not dependent on the nature of transition state and the geometric structure of surface, as expressed by

$$E_{M-Hchem} = 0.5D_{H_2} - \Delta H^0_{ads}(H_{chem}) \qquad (2 \quad (2.25)$$

In comparison, electrochemically adsorbed hydrogen reveals two distinct reactive pathways reflecting the different sites of the substrate. One is the under-potential deposition of H (UPD H), and another is the over-potential deposition of H (OPD H). The UPD H can be observed

above the thermodynamic reversible potential of HER on all kinds of surface, on which the HER can occur but the visual properties of the UPD H are merely seen on some noble metals, such as Pt, Pd, Rh and Ir.[35-37] It is noted that the electrochemical behaviour of UPD H can overlap with the anion adsorption on the corresponding potential range in a voltammogram.[38] Relatively complete studies of UPD H in the aqueous solution were carried out in the last century to elaborate that (a) the nature of the M-H_{UPD} and M-H_{chem} bond, are similar, (b) the electrolyte and the applied potential have little influence on the nature of UPD H, (c) the UPD possesses is embedded in the lattice hollow of co-surface, thus it occupies multi-fold adsorption sites.[39-42]

Take Pt fc (111) and fc(100) surface as example, the literature reports that the UPD H atom is preferably bound in octahedral / tetrahedral sites. In comparison, the UPD H favours the octahedral site rather than the tetrahedral site in term of the theoretical calculation of binding

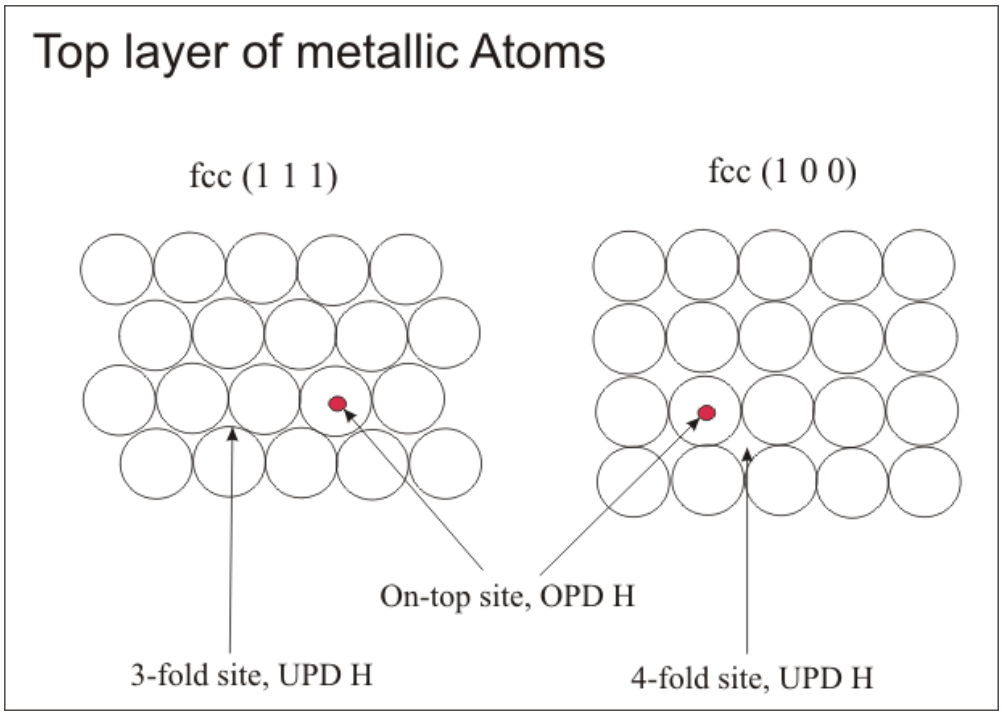

Figure 2.6. Adsorption sites of H_{UPD} and H_{OPD} on the fcc(111) and fcc(100) of platinum surface. [32]

energy. On the other hand, for a reduction of H^+, the OPD H is commonly formed at more negative potentials of the formal potential of the HER, and it is an intermediate of the HER and occupies the mono-coordinated (on-top) site.

2.7.2 The absorption of hydrogen atom

Beside the adsorption behaviour of hydrogen atom appears on the surface of electrode metals, the phenomena that hydrogen can undergo electroabsorption into bulk metals is frequently observed on a part of electrode metals, such as Pd, Fe, Ti, Zr, Ir and the Pd alloy[43-48] based on these metals. It is evident that both OPD H and UPD H can undergo interfacial transfer from the corresponding adsorbed sites to the sub-layer, then diffusing into the bulk metal.

In my thesis, the palladium electrode /nanostructure will engage in the hydrogen evolution reaction in RTILs. The three possible mechanistic pathways of hydrogen absorption are summarized based on the existing literatures. Figure 2.7 is the diagram of these mechanisms

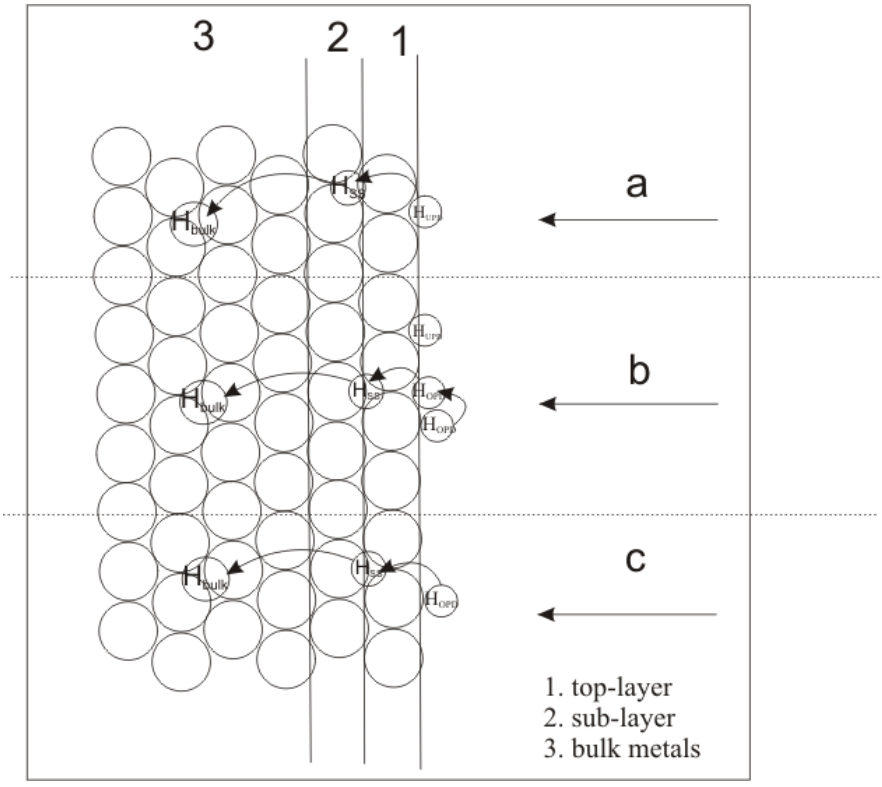

Figure 2.7 the configuration of three distinct pathways of hydrogen absorption into fcc (111) Pd metals.

at the fcc (111) Pd metal, which reveals the linkage among UPD H, OPD H, Sub-surface H and Absorbed H.

(a) UPD H occupying the octahedral sites of surface undergoes interfacial transfer to the subsurface site of Pd lattice, and subsequently diffuses into the interstices of bulk metals. Becoming H_{ads}(adsorbed H atom).

(b) UPD H remains at the previous adsorbed sites (the octahedral site), but OPD H occupying the on-top site of Pd surface can move to the surface vacancies (the tetrahedral site) in the form of self-diffusion, and subsequent undergoes the process of interfacial transfer and inner diffusion to an interstice of the bulk metal.

(c) OPD H occupying the on-top site of Pd surface is tend to the direct process of interfacial transfer to the subsurface site rather than the movement to a tetrahedral site, and following the subsequent diffusion to an interstice of bulk metal.

The mechanism (a) and (b) apply to Pd material which reveals the generation of H_{UPD} and H_{OPD} by subsequent interfacial transfer process with respect to the particular pathways. The mechanism (c) seem to be unavailable for most cases of absorbed behaviour, but when certain adsorbates (poisoning species), such as S and H_2S,[49, 50] occupying the adsorbed sites of metal surface and acting as site blocking species, will promote directly absorption into the host of bulk metal (mechanism (c)). Lots of literature is essential to elaborate on this action caused by the strong chemisorbed species. The competition of adsorbed H and poisoning species can affect the configuration of Gibbs free energy of H atom, thus to cause the possible addition driving force to dredge the third pathways for H entry into the host and restrain the process of interfacial transfer of adsorbed H.

2.7.3 Hydrogen evolution reaction

It is of general interest to explore the hydrogen evolution reaction due to its importance in fuel cells among other applications. The mechanism of the hydrogen evolution reaction has

been extensively studied on different electrode metals in aqueous solution, defined as the behaviour of electrode sensitive. Thus three limiting cases can be identified by the value of the measured transfer coefficient.

Jerkiewicz[33] has pointed out that depending on the nature of metallic electrode and the applied potential, two distinct electroadsorbed species, underpotential deposition of hydrogen ion (H_{UPD}) and overpotential deposition of hydrogen ion (H_{OPD}), can be formed occupying different surface sites, whilst the reaction mechanism is concluded more complicated on some active metal, such as palladium. In general, a reduction is

$$H^+(aq) + e^-(m) + M_s \Rightarrow MH_{(ads,UPD)} \quad (2.26)$$

$$H^+(aq) + e^-(m) + M_s \Rightarrow MH_{(ads,OPD)} \ (Volmer\ reaction) \quad (2.27)$$

where $MH_{ads,UPD}$ and $MH_{ads,OPD}$ are the adsorbed hydrogen ion through under-potential deposition and over-potential deposition, respectively. M_s is a surface metal atom.

Case A. The first electron transfer is rate determining step, related to the slow reaction rate of Volmer reaction. This is characterized by transfer coefficient (α) of, or close to, 0.5.

Case B. The second electron transfer is rate determining step, where transfer coefficients of 1.5 are observed. However, Only H_{OPD}, adsorbed hydrogen atom, could be observed during hydrogen evolution reaction at the interface of RTIL and polycrystalline metal, the mechanism is thought to be

$$H^+(aq) + e^-(m) + MH_{(ads,OPD)} \overset{slow}{\Longrightarrow} M_s + H_2 \ (Heyrovsky\ pathway) \quad (2.28)$$

The transition property can be observed on parts of electrode metal, such as La, Ti and Pd, where it describes the transition of adsorbed hydrogen into absorbed hydrogen. In especial,

Case C applies to palladium electrode, related to the high rate of transition, where tafel plots giving α ~ 2 are observed. This is consistent with the following mechanism.

$$2MH_{(ads,OPD)} \overset{slow}{\Longrightarrow} 2M_s + H_2 \cdot \qquad (2.29)$$

The Volcano plot[2, 51-54] (see Figure 2.8) is a well-known summary of hydrogen electrocatalysis, relating to the electrocatalytic ability of certain substrates, by correlating the current density for the catalysed process with some physical property of the electrocatalytic system.

The interpretation of the electrochemical volcano plot focuses on the adsorbed species, acting as an intermediate of hydrogen evolution reaction. Here if the enthalpy of adsorption was lowin relation to the metals observed on the left side of volcano plot, the intermediate was weakly adsorbed on the surface and the corresponding surface coverage was very low, thus to cause the first electron transfer process as rate determining step. As the enthalpy of adsorption increased, the relatively stronger chemical bond promoted a higher surface

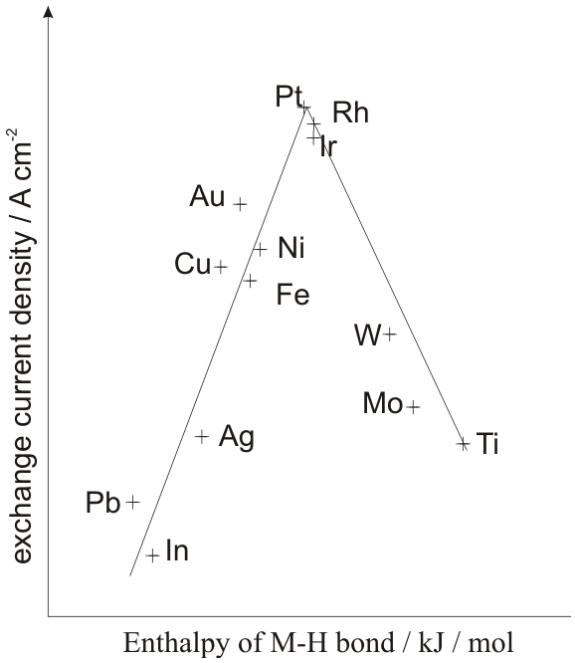

Figure 2.8*:* A Volcano plot displaying exchange current density during H_2 evolution as a function of the electrocatalysts M-H bond enthalpy [2, 51-54]

coverage of adsorbed hydrogen atom. However, it must be recognized that too large enthalpy (on the right side of volcano plot) is replaced as a terrible factor for subsequent process of hydrogen evolution reaction. Because the species (reactant or product) strongly interacted with the metal surface might block the adsorbed site and restrain the refreshment of new H_{OPU}. Thus, the highest exchange current density should be derived from the condition that the enthalpy of adsorption is high enough to guarantee the high surface coverage of H_{OPU}, yet low enough to favour the desorption of products, where Pt is good example for electrocatalyst. Upon the elaborate demonstration of volcano plot, the electrocatalyst activity of the electrode metals has been justified for the hydrogen evolution reaction.

2.8 The establishment of electrochemical simulation

Electrochemical simulation is often employed as a versatile analytical tool to excavate a wealth of theoretical information on thermodynamic and electrode kinetic. It is well known that The Nernst equation or Butler-Volmer equation can be used to describe the electron transfer at the interfacial region, so do Fick's laws for mass transport of electroactive species. But the problem is that the calculation the computer program provides the dispersion function rather than continuous function. It is noted that the actual experimental curve is a dispersion function, consisting of collected points with tiny intervals or steps. Therefore, the constitution of this program is based on the Implicit Finite Difference method,[55] using the commercially software package DigiSim®.

The Implicit Finite Difference method is an approximate method that the continuous space and time can be replaced by discrete units (points) associated with the corresponding variables, forming a grid where the time and space are divided into the tiny step Δt and Δx on the relative coordinate. Solving the partial differential equation generates a net of concentration profile, as well as a total of the time-dependent current immediately near the electrode surface.

The visible and variable parameters, such as potential scan rate, potential range, concentration of electroactive species, diffusion coefficient, radius of electrode, kinetic constant and transfer coefficient, are added into the program as the control panel. The optimised results can be calculated by minimizing the difference between the experimental and theoretical results, using the Least Squares Method.

The following reaction is considered through the whole thesis:

$$H^+ + e^- \Leftrightarrow \frac{1}{2} H_2 \qquad (2.30)$$

Specifically, we consider the case of cyclic voltammetry. This technique is simulated by solving the following mass transport equations:

$$\frac{\partial c_A}{\partial t} = D_A \left(\frac{\partial^2 c_A}{\partial r^2} + \frac{1}{r}\frac{\partial c_A}{\partial r} + \frac{\partial^2 c_A}{\partial z^2}\right) \qquad (2.31)$$

where A= H^+ , and

$$\frac{\partial c_B}{\partial t} = D_B \left(\frac{\partial^2 c_B}{\partial r^2} + \frac{1}{r}\frac{\partial c_B}{\partial r} + \frac{\partial^2 c_B}{\partial z^2}\right) \qquad (2.32)$$

where B= H_2

In cyclic voltammetry, when t > 0, z = 0 and r ≤ re, the boundary condition are the Butler-Volmer conditions (eq. 2.33) describing species A and conservation of mass for species B:

$$D_A \frac{\partial c_A}{\partial z} = k_c^0 c_{A,0} \exp[-\alpha \frac{F(E - E_f^0)}{RT}] - k_a^0 c_{B,0} \exp[\frac{\beta F(E - E_f^0)}{RT}] \qquad (2.33)$$

$$D_A \left(\frac{\partial c_A}{\partial z}\right)_0 = -2D_B \left(\frac{\partial c_B}{\partial z}\right)_0 \qquad (2.34)$$

Note that in the above, first order kinetics have been assumed for both A and B; this corresponds to the best fit of the experimental data as discussed later in this paper. Other kinetic/mechanistic possibilities were considered, notably those giving a rate law which was

second order in A, but were found to be incompatible with the experimental data. In the following it will be shown that the above equations fit the experimental data well for the case where the first electron transfer to H^+ is rate-determining. Accordingly the coverage of adsorbed hydrogen is assumed not to approach significant values due to the rapid discharge of H_2. Similarly although Mo and Ti electrodes can form oxide films in air, the oxide coverage was not observed to be significant following immersion in the extremely strong acid solutions used in the experiments reported.

The remaining boundary conditions are:

t = 0, all r, all z	$c_A = c_A^*$	$c_B = 0$
t > 0, r > r_e, z = 0	$\frac{\partial c_A}{\partial z} = 0$	$\frac{\partial c_B}{\partial z} = 0$
t > 0, all r, z → ∞	$\frac{\partial c_A}{\partial z} = 0$	$\frac{\partial c_B}{\partial z} = 0$
t > 0, r → ∞, all z	$\frac{\partial c_A}{\partial r} = 0$	$\frac{\partial c_B}{\partial r} = 0$
t > 0, r = 0, all z	$\frac{\partial c_A}{\partial r} = 0$	$\frac{\partial c_B}{\partial r} = 0$

In the cyclic voltammetry experiment, the applied potential, E, varies as a function of time, t, according to:

$$E = | -\nu t + E_{start} - E_{vertex} | + E_{vertex} \qquad (2.34)$$

where E_{start} and E_{vertex} are the starting and vertex potentials respectively.

The current at the electrode surface is calculated by

$$i = 2\pi F \int j_A r dr \qquad (2.35)$$

References

1 Online: http://en.wikipedia.org/wiki/History_of_electrochemistry.

2 S. Trasatti, *Chimica & L Industria* 1971, *53*, 364-&.

3 M. C. Lagunas, W. R. Pitner, J. A. van den Berg, K. R. Seddon, *Ionic Liquids as Green Solvents: Progress and Prospects* 2003, *856*, 421-438.

4 A. J. Bard, L. R. Faulkner, *Electrochemical Methods: Fundamentals and Applications, 2nd ed. John Wiley and Sons: New Year* 2001.

5 R. G. a. S. Compton, G. H. W., *Electrode Potentials, Oxford University Press, Oxford, UK* 1998.

6 A. C. Fisher, *Electrode Dynamics, Oxford University Press, Oxford, UK* 1998.

7 P. H. Rieger, *Electrochemistry, 2nd, ed., Chapman and Hall, Inc. New York, USA* 1994.

8 R. G. Compton, and C. E. Banks, *Understanding Voltammetry, Imperial College Press, London, UK* 2010.

9 G. C. Barker, A. W. Gardner, *Journal of Electroanalytical Chemistry* 1979, *100*, 641-656.

10 H. L. F. von Helmholtz, *Ann. Physik* 1853, *165*, 211-233.

11 G. Gouy, *Compt. Rend.* 1910, *149*.

12 D. L. Chapman, *Phil. Mag.* 1913, *25*.

13 O. Stern, *Z. Elektrochem. Angew. Phys. Chem* 1924, *30*, 508-516.

14 P. Delahay, *Double Layer and Electrode Kinetic, Interscience, New York* 1965.

15 O. K. Rice, *Phys. Rev.* 1928, *31*.

16 J. P. Badiali, M. L. Rosinberg, J. Goodisman, *Journal of Electroanalytical Chemistry* 1983, *150*, 25-31.

17 J. P. Badiali, M. L. Rosinberg, J. Goodisman, *Journal of Electroanalytical Chemistry* 1983, *143*, 73-88.

18 A. Einstein, *Investigation on the Theory of Brownian Motion. Dover, New York* 1956.

19 E. A. Guggenheim, *J. Phys. Chem* 1929, *33*.

20 E. A. Guggenheim, *J. Phys. Chem* 1930, *34*.

21 J. A. V. Butler, *J. Trans. Faraday Soc* 1924, *19*, 729-733.

22 A. C. Testa, W. H. Reinmuth, *Analytical Chemistry* 1961, *33*, 1320-&.

23 J. Galceran, J. Puy, J. Salvador, J. Cecilia, H. P. van Leeuwen, *Journal of Electroanalytical Chemistry* 2001, *505*, 85-94.

24 H. P. van Leeuwen, J. P. Pinheiro, *Journal of Electroanalytical Chemistry* 1999, *471*, 55-61.

25 Y. I. Tur'yan, M. Lovric, *Journal of Electroanalytical Chemistry* 2002, *531*, 147-154.

26 T. F. Otero, J. Rodriguez, *Electrochimica Acta* 1994, *39*, 245-253.

27 M. Fleischmann, F. Lasserre, J. Robinson, D. Swan, *Journal of Electroanalytical Chemistry* 1984, *177*, 97-114.

28 D. S. Silvester, W. S. He, L. Aldous, C. Hardacre, R. G. Compton, *Journal of Physical Chemistry C* 2008, *112*, 12966-12973.

29 M. Thompson, R. G. Compton, *Journal of Electroanalytical Chemistry* 2006, *587*, 186-192.

30 K. R. Ward, N. S. Lawrence, R. S. Hartshorne, R. G. Compton, *Journal of Physical Chemistry C* 2011, *115*, 11204-11215.

31 P. Sanecki, K. Kaczmarski, *Journal of Electroanalytical Chemistry* 1999, *471*, 14-25.

32 E. O. Barnes, Y. J. Wang, J. G. Limon-Petersen, S. R. Belding, R. G. Compton, *Journal of Electroanalytical Chemistry* 2011, *659*, 25-35.

33 G. Jerkiewicz, *Progress in Surface Science* 1998, *57*, 137-186.

34 M. G. Nijkamp, J. E. M. J. Raaymakers, A. J. van Dillen, K. P. de Jong, *Applied Physics a-Materials Science & Processing* 2001, *72*, 619-623.

35 F. G. Will, C. A. Knorr, *Zeitschrift Fur Elektrochemie* 1960, *64*, 270-275.

36 G. Jerkiewicz, *Electrocatalysis* 2010, *1*, 179-199.

37 P. Kowalczyk, S. Savard, A. Lasia, *Journal of Electroanalytical Chemistry* 2004, *574*, 41-47.

38 A. Zolfaghari, M. Chayer, G. Jerkiewicz, *Journal of the Electrochemical Society* 1997, *144*, 3034-3041.

39 G. Jerkiewicz, A. Zolfaghari, *Journal of the Electrochemical Society* 1996, *143*, 1240-1248.

40 E. Protopopoff, P. Marcus, *Journal of the Electrochemical Society* 1988, *135*, 3073-3075.

41 A. Bewick, J. W. Russell, *Journal of Electroanalytical Chemistry* 1982, *142*, 337-343.

42 A. Bewick, J. W. Russell, *Journal of Electroanalytical Chemistry* 1982, *132*, 329-344.

43 H. Suzuki, H. Taniguchi, N. Hanada, K. Takai, Y. Hagihara, *Journal of Alloys and Compounds* 2011, *509*, S759-S762.

44 M. Lukaszewski, K. Hubkowska, A. Czerwinski, *Physical Chemistry Chemical Physics* 2010, *12*, 14567-14572.

45 H. Duncan, A. Lasia, *Electrochimica Acta* 2008, *53*, 6845-6850.

46 M. H. Martin, A. Lasia, *Electrochimica Acta* 2008, *53*, 6317-6322.

47 W. E. Triaca, H. A. Peretti, H. L. Corso, A. Bonesi, A. Visintin, *Journal of Power Sources* 2003, *113*, 151-156.

48 L. Birry, A. Lasia, *Electrochimica Acta* 2006, *51*, 3356-3364.

49 S. Y. Qian, B. E. Conway, G. Jerkiewicz, *International Journal of Hydrogen Energy* 2000, *25*, 539-550.

50 A. Czerwinski, *Journal of Electroanalytical Chemistry* 1994, *379*, 487-493.

51 S. Harinipriya, M. V. Sangaranarayanan, *Journal of Physical Chemistry B* 2002, *106*, 8681-8688.

52 S. Trasatti, *Journal of Electroanalytical Chemistry* 1971, *33*, 351-&.

53 S. Trasatti, *Chimica & L Industria* 1971, *53*, 559-&.

54 S. Trasatti, *Journal of Electroanalytical Chemistry* 1972, *39*, 163-&.

55 M. Rudolph, *Journal of Electroanalytical Chemistry* 1991, *314*, 13-22.

Chapter 3 General experimental reagents, instruments and measurements used in this thesis.

3.1 Chemical Reagents

All the chemical reagents used throughout this thesis are summarized in Table 3.1, along with their formulas, the corresponding purities and suppliers. $HNTf_2$ was kept under an argon atmosphere during and after use. Silver epoxy was stored in the fridge and Ag[OTf] was kept in the dark to avoid decomposition. THF and CH_2Cl_2 were dried by purification through two activated alumina purification columns. All molecule solutions were prepared using purified water from Vivendi UHQ grade water system with a resistivity of not less than 18.2 MΩ cm (298 K).

Since the mainstream material manufacturing industries provided only a few fabricated microelectrodes due to the limited demand, such as platinum and glassy carbon electrodes, most of microelectrodes used in this thesis have been fabricated by the auther. The corresponding metallic microwires were listed in table 3.2, giving the commercial sources and specific parameters (purity and diameter). The detail of fabrication procedures and associated measurements is discussed later (section 3.2).

Table 3.3 lists all the RTILs used through this thesis with a reference to show how they were synthesized. Several bis(trifluoromethylsulfonyl)imide RTILs were synthesized by the group of Professor Christopher Hardacre at the School of Chemistry and Chemical Engineering (QUILL, Queen's University Belfast)[1] and the rest of the ionic liquids were kindly donated by Merck KGaA. The RTILs were purified by the colleagues, Dr. Debbie S. Silvester and Dr. Leigh Aldous, when they are received. The RTILs were selected visually in term of the colour. A transparent and colourless nature was priority, but a small amount of yellow

Table 3.1. Chemical reagents use in this thesis, along with their formulas, their purities and the suppliers.

Name	Formula	Purities	Supplier
Ferrocene	$Fe(C_5H_5)_2$ /Fc	98%	Aldrich
Tetra-n-butylammonium perchlorate	TBAP	>99 %	Aldrich
Acetonitrile	MeCN	>99.99 %	Fisher Sci.
Cobaltocenium hexafluorophosphate	$Co(C_5H_5)_2PF_6$ / Cc^+	98%	Acros Org.
Perchloric Acid	$HClO_4$	70%	Aldrich
Nitric acid	HNO_3	70%	Aldrich
Palladium (II) Chloride	$PdCl_2$	>99.9%	Aldrich
Sodium borohydride	$NaBH_4$	98%	Lancaster
Tetrahydrofuran	$(CH_2)_4O$ / THF	>99.9%	Aldrich
Dichloromethane	CH_2Cl_2	>99.8%	Aldrich
N,N'-Bis(benzyloxycarbonyl)-L-lysine	Z-lys(Z)-OH	>98.0 %	Aldrich
Hydrogen bis(trifluoromethylsulfonyl)imide	$HNTf_2$	>95 %	Fluka
Benzoic acid	C_6H_5COOH / BZA	99.5%	BDH
Silver epoxy			Aldrich
Silver trifluoromethanesulfonate	Ag[OTf]	> 99.95 %	Aldrich
Nitrogen	N_2	99.99 %	BOC gases
Hydrogen	H_2	99.995 %	BOC gases
Argon	Ar	99.99 %	BOC gases
Oxygen	O_2	99.5 %	BOC gases

Table 3.2. Purchased electrodes, micro-wires and other conductors. Their characteristics and commercial sources

Name	Supplier	Characteristics
Bamboo-like multi-walled carbon nanotubes (CNTs)	NanoLab, USA	diameter 30 ± 10 nm, length 5-20 μm, purity <95%
Glassy Carbon electrode	BASi, USA	diameter 3 mm
Palladium wire	Goodfellow	diameter 0.01 mm, purity > 99.9 %
Platinum wire	Goodfellow	diameter 0.01 mm, purity > 99.99 %
Gold wire	Goodfellow	diameter 0.01 mm, purity > 99.99 %
Molybdenum wire	Goodfellow	diameter 0.01 mm, purity > 99.8 %
Nickel wire	Goodfellow	diameter 0.1 mm, purity > 99.98 %
Titanium wire	Goodfellow	diameter 0.05 mm, purity > 99.8 %
Silver wire	Goodfellow	diameter 0.5 mm, purity > 99.99 %

Table 3.3. Room temperature ionic liquids and the corresponding synthesis procedures with respect to the literature

Chemical Name	Formula	Reference of synthesis
1-Ethyl-3-methylimidazolium bis(trifluoromethylsulfonyl)imide	$[C_2mim][NTf_2]$	Bonhôte et al[2]
1-Butyl-3-methylimidazolium bis(trifluoromethylsulfonyl)imide	$[C_4mim][NTf_2]$	Bonhôte et al[2]
1-Butyl-2,3-dimethylimidazolium bis(trifluoromethylsulfonyl)imide	$[C_4dmim][NTf_2]$	Bonhôte et al[2]
N-Butyl-N-methylpyrrolidinium bis(trifluoromethylsulfonyl)imide	$[C_4mpyrr][NTf_2]$	MacFarlane et al[3]
1-Butyl-3-methylimidazolium tetrafluoroborate	$[C_4mim][BF_4]$	donated by Merck KGaA
1-Butyl-3-methylimidazolium trifluoromethylsulfonate	$[C_4mim][OTf]$	donated by Merck KGaA

was also acceptable. All selected RTILs need a 24 h vacuum to remove volatile impurities efficiently. Finally, the electrochemical technique (cyclic voltammetry) is used to test the purification of every RTIL at a Pt electrode. The RTILs in which the excess peak of voltammograms is not seen over a range of potential window can be assigned as a suitable solvent for the further experiments.

3.2 Apparatus

3.2.1 The experimental T-cell

A glass T-cell instrument was specially designed to satisfy the requirements of routine electrochemical experiments using RTILs.[4] Due to the dissolution of oxygen and water impurities[5, 6] in RTILs when they have been exposed to air, the function of T-cell design has been proven effective in removing these species. At the same time, both horizontal arms of the cell have followed the requirement of the gas passage. The working electrode slots the bottom of the cell, while the reference electrode and counter electrode slot into the top to satisfy a three-electrode design, as shown in Figure 3.1. Additionally, high vacuum grease is used on every connection of T-cell to prohibit the possibility of leakage.

All the electrochemical experiments were performed using a computer-controlled μ-Autolab potentiostat (Eco-Chemie, Netherlands), which was interfaced with a PC using GPES (version 4.9) software for windows. In most electrochemical experiments, the micro-disk working electrode was polished on soft lapping pads (Buehler Illinois) with alumina slurry of size 3 μm, 1 μm and 0.3 μm respectively. Sample of 40-80 μL of RTILs, into which solutes were dissolved if necessary, were placed into the section of disposable micropipette tip on the top of working electrode and a platinum wire and a platinum ring are used as the reference electrode and the counter electrode, respectively. Ionic liquid was purged under vacuum for ca. 120 min in order to remove detrimental residual water and dissolved gases. This system

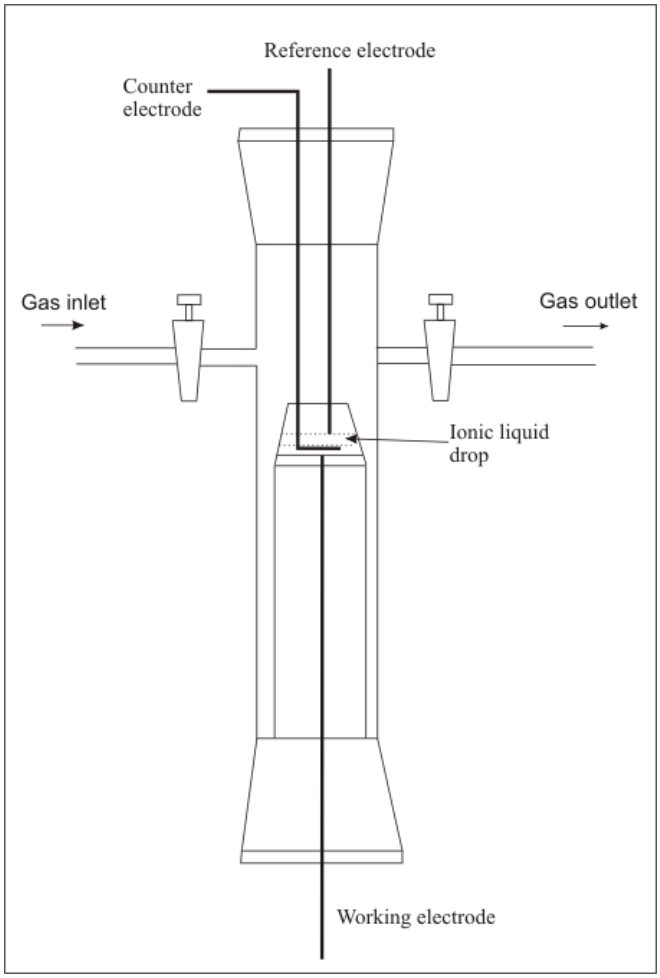

Figure 3.1. The designed T-cell used in all the electrochemical experiments reported in this thesis

has been demonstrated to minimize the electrochemical features (accelerated mass transport and decrease of the electrochemical windows[7]) of ionic liquids caused by water or gas contamination. It is of importance to temperature control all the electrochemical experiments (accurate to ±0.5 K). They were performed in a thermostated box which is also functioned as a Faraday cage.[8]

For experiments involving dissolved gases, the voltammetric experiments were first performed under vacuum and then the vacuum was replaced with a desired constantly flowing gas, being allowed to equilibrate for at least 40 min as evidenced by stable Faradaic currents.

3.2.2 Electrochemical cell and water content

All experiments were performed in a previously reported electrochemical cell, which has been specially designed to work under ultra-high vacuum or with a constant flow of gas[9] under thermostatic conditions.[10] Before each experiment *ca.* 20 µL or 40 µL ionic liquid was placed under vacuum in the electrochemical cell for *ca.* 120 min; voltammetric experiments were then performed under vacuum or after breaking the vacuum with the desired constantly flowing gas mixture, before being allowed to equilibrate for at least 40 min. The small volumes of ionic liquid precluded Karl Fischer titration but facilitated removal of dissolved gases and moisture. This system has been demonstrated to remove electrochemical features associated with water contamination of ionic liquids such as accelerated diffusion and decreased electrochemical windows, indicating negligible water content when treated in this manner.[9, 11]

3.2.3 Microelectrodes and Macroelectrodes

Microdisk and macrodisk electrode show two distinct diffusion patterns as illustrated graphically in Figure 3.2.

The diffusion pattern in figure 3.2 (a) is termed planar diffusion which usually takes place at the macrodisk. It is seen that the larger two-dimensional scale leads to a higher overall absolute current and offers ratio of signal to noise. Theoretically, it is useful to simplify the diffusion at macroelectrode as being of one dimensional form.

Generally speaking, when the scale at any dimension drop to less than *ca.* 50µm, it can be defined as an ultramicroelectrode where convergent diffusion dominates and planar diffusion

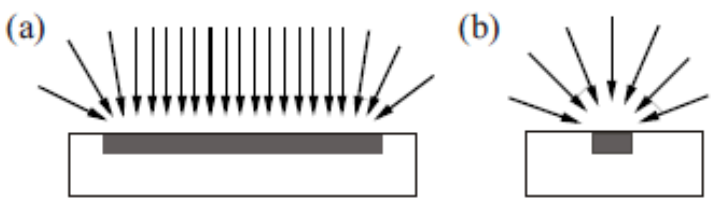

Figure 3.2. Comparison of diffusion near the (a) macrodisk and (b) microdisk electrode

is negligible at conventional scan rates. Figure 3.2 (b) depicts this three dimensional diffusion, showing a hemispherical diffusion layer. The smaller the disk, the greater the current density, the lower additional capacitance and Ohmic drop and the faster mass transport to the electrode surface.

It is easily found that the determination of the diffusion form can be inferred from a comparison of the diffusion layer thickness and the radius of disk electrode. The exact diffusion layer thickness can be described by solving the Fick's second law of diffusion at the disk electrode, however, qualitatively it suffices to use the approximate equation of diffusion distance. The relevant mathematical inequalities[12] are given by:

Planar diffusion

$$\sqrt{2Dt} \ll r_d \qquad (3.1)$$

Convergent diffusion

$$\sqrt{2Dt} \gg r_d \qquad (3.2)$$

where D is the diffusion coefficient of interest, t is the time of the diffusion and r_d is the radius of disk electrode.

3.3 Fabrication of the working microelectrode

During the electrochemical reactions, a working microelectrode acts as a source or acceptor of electrons for exchange with targets in the interfacial region. It must also be electrochemically inert over a range the applied potential window. Thus, platinum, palladium, gold and glassy carbon have commonly been used as electrode materials. Other available materials in table 3.2 were also used for electrodes. The details of fabrication are given in the following paragraph.

A glass tube, cut to *ca.* 8cm in length, was threaded with an appropriate micro-wire (Pd, Pt, Au, Ni, Mo and Ti). Silver epoxy was used to seal one side of the glass tube, and the system was placed under vacuum to remove the active atmosphere molecules. The unsealed side of the glass tube was carefully placed at the centre of an electrode furnace and gradually heated to its softening point. The softening process was allowed to proceed until the fusion of glass and metal wire at 140º C. The electrode was allowed to cool down gradually to room temperature and polished down on alternating hard and soft lapping pads until the metal could be observed with a mirror surface under the microscope.

The cyclic voltammetry of 2 mM solution of ferrocene in acetonitrile with 0.1 M TBAP electrolyte supporting was carried out to size the microelectrode. The precise radius of microelectrode was calibrated using the chronoamperometric experiments, adopting a value of 2.3×10^{-5} cm^2s^{-1} for the ferrocene diffusion coefficient at 298 K. (More detail of measurement is given in section 3.5) The following sizes were measured: 5.25 µm platinum electrode, 4.7 µm palladium electrode, 6.5 µm molybdenum electrodes, 4.6 µm gold electrode, 50 µm nickel electrode and 25 µm titanium electrode were used throughout this thesis.

Additionally, it is well known that Ti metal grows layers of oxide films easily in air and/or in the presence of moisture at room temperature so it was likely that a thin film of TiO_2 will be present on the surface of the Ti microelectrodes.[13]

3.4 Fabrication of the micro-Ag/Ag+ Reference Electrode

A micro-Ag/Ag^+ Reference Electrode was specially designed for the experiments reported and consisted of a disposable micropipette tip, into which a 3 Å molecular sieve was placed, and the tip melted to ensure a good seal. The length of the molecular sieve was then reduced to 2 mm, as otherwise a significant *iR* drop was present. After soaking in $[C_2mim][NTf_2]$, the interior IL was removed and replaced with $[C_2mim][NTf_2]$ containing 10 mM silver triflate.

Into this was immersed an Ag wire (cleaned with dilute HNO_3 and copious water), and the top of the reference electrode was plugged with glass wool, in order to prevent IL loss when placed under vacuum. For studies involving H_2 gas the reference electrode was sealed to be gas tight with black wax due to H_2-induced potential shifts. The reference electrode was tested *vs.* solutions of Fc in $[C_2mim][NTf_2]$, and the E_f^0 of Fc was found to be -0.273 ± 0.003 V at 298 K. The reference electrode was checked in between every experiment, and if the $E_{1/2}$ of ferrocene shifted more than 5 mV then the reference electrode was disposed of and a fresh electrode prepared (typically every 1 – 3 weeks, if stored in the dark). This reference electrode was employed as it was moderately easier to construct than Huber and Roling's[14] glass capillary-based micro-Ag/Ag^+ ionic liquid reference electrode, yet sufficiently robust for the conditions required.

3.5 Voltammetric Measurements

In this thesis, series of measurements have been carried, involving the current response of working electrodes with a specific potential. In the following, Focus on a simple electrode process

$$A \pm e^- \rightleftarrows B$$

where both A and B are electroactive species.

3.5.1 Cyclic voltammetry[12]

Cyclic voltammetry is a very versatile measurement which allows investigation of the mechanism of electron transfer and mass transport properties of interest in a specific solution. A three electrode arrangement has been used through this thesis whereby the potential relative to some *reference* electrode is scanned at a *working* electrode while the resulting

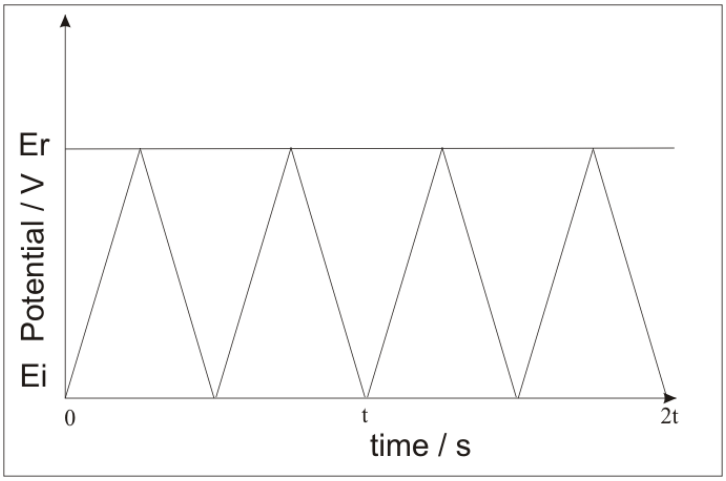

Figure 3.3 The potential ramp used in cyclic voltammetry, showing the trend of applied potential with time

currents flow through a *counter* (or *auxiliary*). The applied potential sweeps following the angle between the two extremes in Figure 3.3.

The working potential is varied linearly from a selected value, E_i, at which the electroactive species does not initially react, to the inversion potential, E_r. Then the potential sweeps back to the initial potential. The potential range usually contains an oxidation or reduction process of interest. The time of a single ramp is controlled by the scan rate (ν), a vital parameter for this technique. Therefore, cyclic voltammetry can be thought as the current response to the ramped potential. The output plot shows the relationship between the current and the applied potential, the profile of which is sensitive to the mass transport and bulk concentration of electroactive species, as well as the morphology and nature of the electrode. As a result, it is necessary to elaborate the characteristic voltammetry seen under different conditions.

3.5.1.1 Simple voltammetry at a macroelectrode

The waveshapes in Figure 3.4 displays three typical characteristic voltammetries where planar diffusion dominates. They are termed as ‘reversible’, ‘quasi-reversible’ and ‘irreversible’ electron transfer processes with the same formal potential, E_f^0, corresponding to ‘fast’, ‘medium’ and ‘slow’ electrode kinetics respectively.

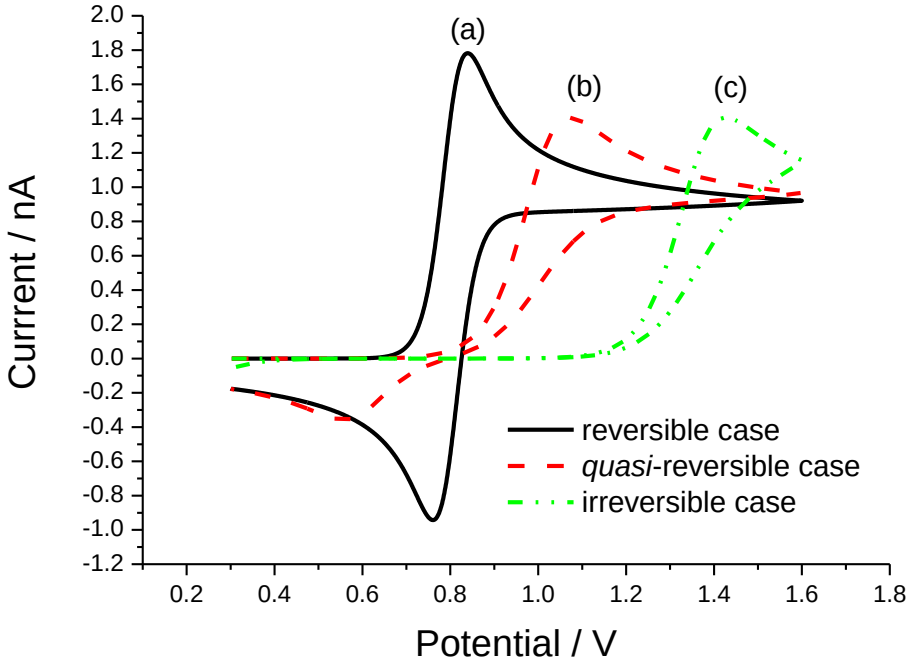

Figure 3.4 A comparison of three typical voltammetries associated with different kinetic processes at macro-electrodes

The shape of the curve for the forward scan of three typical voltammetries is notable. It can be defined as comprising three observed zones, ascent, vertex and descent. For A-e → B, at relatively negative potentials, the applied potential is insufficient to induce electron transfer in relative with no Faradiac current flow. As the sweep goes positively, the trend of the current is to rise till the vertex accompanied with the oxidation of interest of A to B, the rate of which is dependent on the electrode kinetics which get faster as the potential increases. At yet more positive potential, the current passes through a maximum and falls off due to the limit of mass transport at the electrode. That is to say, the occurrence of vertex can be assigned to a relatively slow mass transport of interest A to reactive surface in relation with the rate of electron transfer, causing the exhaustion of A and the accumulation of B near the surface, in a zone which is termed a diffusion layer. As the potential is swept more positively, current response falls as A has been depleted and there is an increase of diffusion layer

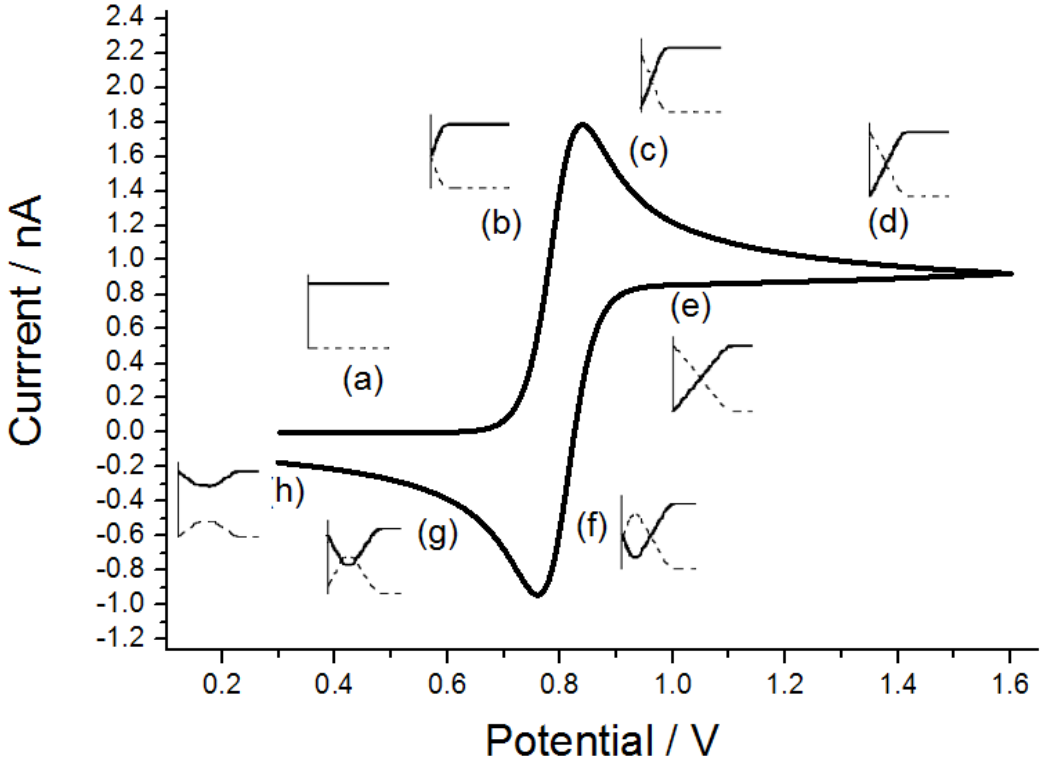

Figure 3.5 Simulated diagrams for concentration–distance profiles near the electrode surface with respective to the various zones of the corresponding voltammogram shown in Fig. 3.4 (a), the solid lines is related to the concentration of species A and the dash lines to that of species B

thickness. Such concentration–distance profiles near the electrode surface with respective to the zones of the corresponding voltammogram are illustrated in figure 3.5, using a reversible case as example. Simultaneously, the product B will diffuse away or enter the subsequent chemical / electrochemical reaction, the details are discussed in electrochemical multiple processes (see Section 2.6).

(a) The reversible case

When the potential is inverted, the accumulated species B starts to be reduced back to A and also the current response of the cathodic process obeys the balance of electron transfer and surface concentration of B to give a peak current.

The peak-to- peak potential separation maintains a value of approximately 57 mV at 298K, independent of scan rate. The fast electrode kinetics implies that the concentration of A and B at the electrode surface obey the Nernst equation through the voltammogram.

The peak current of interest can be calibrated in term of the Randles-Sevčik equation[15, 16]:

$$i_p = 2.69 \times 10^5 n^{\frac{3}{2}} A D^{\frac{1}{2}} [A]_{bulk} v^{\frac{1}{2}} \quad (3.3)$$

where n is the number of electrons, A is the surface area of microelectrode, D is diffusion coefficient of interest, $[A]_{bulk}$ is the bulk concentration of interest and ν is the potential scan rate.

Additionally, the forward reversible peak can be characterised by means of the fixed voltage difference between the potential E_P, related to the peak current, and the potential $E_{P/2}$, related to the half peak current at the ascent zone, giving the relationship:

$$\left|E_P - E_{P/2}\right| = 2.218 \frac{RT}{F} \quad (3.4)$$

For multi-electron-transfer (reversible) processes, the cyclic voltammogram might consist of several distinct peaks, but the number of peaks is likely to be less than the number of redox couples due to overlapping formal potentials for different couples.

For a n-electron reversible transfer

$$| E_P^{ox} - E_P^{red} | = 2.218 \frac{RT}{nF} \quad (3.5)$$

$$| E_P^{ox} - E_{P/2}^{red} | = 2.218 \frac{RT}{F} \quad (3.6)$$

(b) The *quasi*-reversible case

In this case, the electrode kinetics are not fast enough to maintain a Nernst equilibrium and this causes the increase of peak-to-peak separation. Eventually, as the kinetics slows the peak

current is also smaller than that for the fully reversible case and it is not quite proportional to the square root of scan rate.

(c) The irreversible case

In this case, the electron transfer requires a higher overpotential and the forward wave is shifted to much more positive potentials due to the very slow kinetic process. The peak-to-peak separation further increases with respect to *quasi*-reversible case, such that the backward wave cannot be observed owing to the finite potential window of the solution. It is noteworthy that the voltammogram of the irreversible case is similar to some EC processes and experiments are required to clarify the mechanism of the reaction.

The peak current also can be described at 298K by

$$i_p = 2.99 \times 10^5 n(\alpha+n_{rds})^{\frac{1}{2}} A D^{\frac{1}{2}} [A]_{bulk} v^{\frac{1}{2}} \qquad (3.7)$$

where α is the heterogeneous charge transfer coefficient at the rate-determining step and n_{rds} is the number of electron transfer before the rate determining step. The shift of the peak potential has been quantified with scan rate:

$$E_p = E_f^0 - (RT/\alpha + n_{rds}F)[0.78 - In\left[k^0/\sqrt{D}\right] + 0.5In(\alpha + n_{rds}Fv/RT \quad (3.8)$$

where all the parameters has been defined before.In comparison, the relationship between E_P and $E_{P/2}$ at the forward scan becomes

$$\left|E_P - E_{P/2}\right| = 1.857\frac{RT}{\alpha F} \qquad (3.9)$$

Eventually, the concept of reversible or irreversible for any redox couple is a relative rather than absolute one, since the sweep of the peak reflects the competition between electron transfer and mass transport. If the scan rate is sufficiently fast, then all reactions will tend to

be irreversible. Combining together the effect of scan rate and kinetic constant k_0, Matsuda and Ayabe have given a general classification

Reversible:

$$k_0 \geq 0.3\, v^{\frac{1}{2}}\, cm\, s^{-1}$$

Quasi-reversible:

$$0.3v^{\frac{1}{2}} > k_0 > 2 \times 10^{-5} v^{\frac{1}{2}}\, cm\, s^{-1}$$

Irreversible:

$$k_0 \leq 2 \times 10^{-5}\, v^{\frac{1}{2}}\, cm\, s^{-1}$$

3.5.1.2 Voltammetry at microelectrodes

In terms of section 3.2.2 and 3.4.1.1, it is well known that the descending zone of a cyclic voltammogram at a macrodisk arises from the competition between electron transfer and mass transport of interest, that is to say, the supply of electroactive species is seriously insufficient. But higher mass transport rates take place at microdisk electrode, thus the rising current reaches a limiting current plateau, which is named as steady state current, in contrast to the conventional peak shaped voltammogram. It represents a kind of dynamic balance between the reaction of the species (electrode transfer) and the replenishment of the species (mass transport). Typical steady state voltammetry is shown in Figure 3.6.

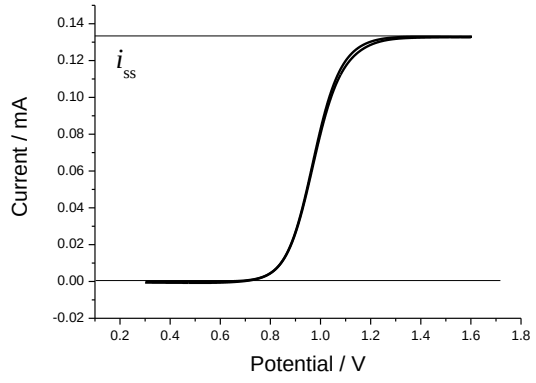

Figure 3.6 Steady state voltammetry at a microdisk electrode

In this case, the steady state current, independent of the applied potential, can be calculated by the equation below:

$$i_{ss} = -4nFDcr_d \qquad (3.10)$$

where F is the Faraday constant, c is the bulk concentration of interest, D is the corresponding diffusion coefficient and r_d is the disk radius. The concentration profile under the steady state is independence of time. The half wave potential $E_{½}$ is close to the formal potential of a reversible couple, but shifts to the positive/negative potential (oxidation / reduction) in the presence of quasi-reversible or irreversible kinetics.

3.5.2 Chronoamperometry

Chronoamperometry[12] is a potential step technique where the current response is recorded with time under potentiostatic controlled, which is often used to determine the diffusion coefficient of reactive species. The potential is stepped from a potential, corresponding to zero faradaic current, to a chosen potential, corresponding to the diffusion controlled zone, as depicted in Figure 3.7. A large current is initially seen at the working electrode, but the current will fall steadily with time due to the depletion of the electroactive species. As we have been discussed planar diffusion and convergent diffusion lead to the transient behaviour and steady state behaviour in the voltammetric technique, respectively. Therefore, for the process where planar diffusion dominates, the limiting current tends to zero associated with the rapid increase of the diffusion layer, but in the present of convergent diffusion, the limiting current leads to a stable value due to a balance between electron transfer and mass transport.

The Cottrell equation[17] gives a general solution of the diffusion equation under planar diffusion (macrodisk electrode). It is necessary to note the boundary conditions of this

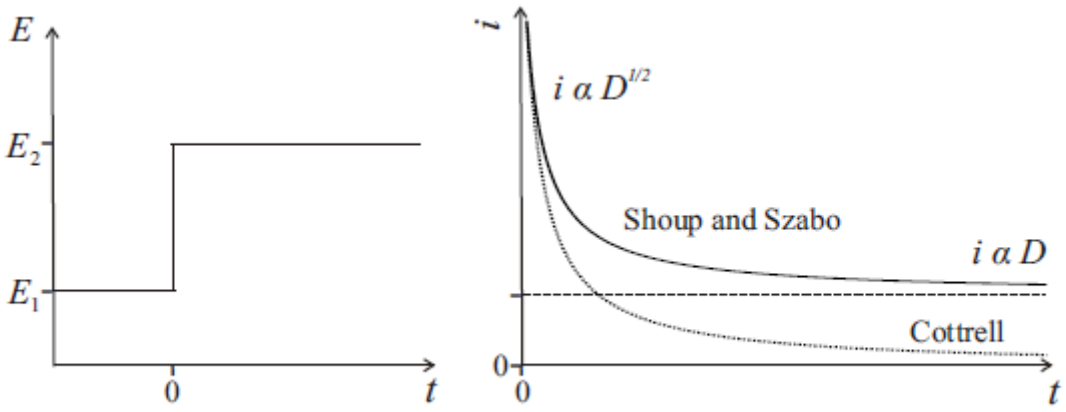

Figure 3.7 The left graph shows a step potential waveform during the chronoamperometry. The right graph shows the corresponding current respond with time at macrodisk and microdisk, obeying Cottrell equation and Shoup and Szabo expression, respectively

equation: (a) only one species exists initially; (b) the bulk concentration is constant regardless of the reactive time; (c) the electron transfer process is very rapid relative to mass transport.

$$i = \frac{nFAD^{\frac{1}{2}}c}{\pi^{\frac{1}{2}}t^{\frac{1}{2}}} \qquad (3.11)$$

where n is the number of electron transfer, F is Faraday's constant, A is electrode surface area, c is concentration of the initial species and t is reactive time. In theory, the diffusion coefficient can be calculated by the slope of a linear plot of *i* versus $t^{-0.5}$, but the unknown concentration can be a barrier to determine the diffusion coefficient of interest. When the measurement is carried out at microdisk electrode, the current response becomes more complex, and as such is necessary to be considered in two parts. At the short time, the Cottrell equation is valid where planar diffusion dominates and the thickness of diffusion layer is smaller than the scale of microdisk, but at the long time, the current tends to a steady state value, caused by the convergent diffusion. In this case, the current scales with the square root of D at the short time, whereas at the long time the current scales with D, as opposed to Cottrellian decay to zero at macrodisk.

The current transient at microdisk is given by

$$I = -4nFDcr_d f(\tau) \tag{3.12}$$

where

$$\tau = \frac{4Dt}{r_d^2} \tag{3.13}$$

Here, the parameters follow the definition in the Cottrell equation and r_d is the radius of microdisk. In terms of the consideration of two different zones, Aoki and Osteryoung[18] used two expressions for $f(\tau)$. At short times when τ is less than 1.44

$$f(\tau) = \sqrt{\frac{\pi}{4\tau}} + \frac{\pi}{4} + 0.094\sqrt{\tau} \tag{3.14}$$

whereas at longer time when τ is longer than 0.82

$$f(\tau) = 1 + 0.71835\tau^{-\frac{1}{2}} + 0.05626\tau^{-\frac{3}{2}} - 0.00646\tau^{-\frac{5}{2}} \tag{3.15}$$

However, these two expressions are only approximate in the intermediate time zone and insufficient to describe the entire current response. The equation proposed by Shoup and Szabo[19] on the basis of rigorous simulations was used to successfully model the $f(\tau)$, which allows a best-fit of chronoamperometric transient with a maximum error of less than 0.6%.

$$f(\tau) = 0.7854 + 0.8863\tau^{-\frac{1}{2}} + 0.2146\exp(-0.7823\tau^{-\frac{1}{2}}) \tag{3.16}$$

The equation allows optimizing the fit between the experimental and theoretical data to obtain the value for D and (nc) given a known value of the electrode radius.

The technique can be extended to embrace two-steps where the potential is stepped from E_1 to E_2, then back to E_1, and the current decay is recorded for both processes. This is called double potential step chronoamperometry. In my thesis, this method is used to measure the

diffusion coefficient and concentration of products formed at microdisk electrodes. The first decay follows the Shoup and Szabo expression[19], and the second wave can be analyzed by the work from Klymenko et al.[20]

3.5.3 Scanning electron microscope (SEM)

SEM is a kind of electron microscope in which a source of high energetic electrons is emitted and bombards the surface layer of the tested sample. Then the electronic transition of the tested elements lead to an emission of electrons or photons from or through the surface, a fraction of which can be collected by an appropriate detector and displayed on a cathode ray tube (CRT monitor). Since the different materials or substrates have various energy bands associated with the different energy electrons or photons emitted, this technique can yield information about the surface features of the sample, the shape and size of particles, and the corresponding composition analysis in the form of the brightness pattern.

Several parameters can be adjusted to obtain the clear image: (a) the incident angle of electron beam; (b) the incident angle of CRT monitor; (c) the transmit power on a voltage between 2 to 50kV; (d) the diameter of electronic beam; (e) the raster's length to the sample; (f) the raster's length to CRT monitor.

Generally speaking, the bombardment of the electronic beam lead to three types of images with respect to different transmission powers, involving secondary electron images, backscattered electron images and elemental X-ray maps. As the applied energy of emitted electron is larger than 50eV throughout this thesis, backscattered electron images are measured to depict the sharp and size of particles and structures. It is noted that conductivity of the sample is an essential requirement for SEM technique.

3.5.4 X-Ray photoelectron spectroscopy (XPS)[21]

X-Ray Photoelectron Spectroscopy is a surface analysis technique in which a beam of X-ray is irradiated onto the top of sample (generally producing the top 1 to 10nm) and the kinetic energy and the number of the escaped electrons are measured by the electron detector to calculate the binding energy of the photoelectron:

$$E_b = E_p - (E_k + \phi) \qquad (3.17)$$

where E_b is the binding energy of the electron, E_p is the energy of the applied X-ray photon, E_k is the measured kinetic energy of the electron and Φ is the work function of the spectrometer. Comparing the binding energy and intensity of a photoelectron peak with a database can provide information of the element identity, chemical state and the quantity of an element on the surface.

References

1 Online: http://quill.qub.ac.uk/.

2 P. Bonhote, A. P. Dias, N. Papageorgiou, K. Kalyanasundaram, M. Gratzel, *Inorganic Chemistry* 1996, *35*, 1168-1178.

3 D. R. MacFarlane, P. Meakin, J. Sun, N. Amini, M. Forsyth, *Journal of Physical Chemistry B* 1999, *103*, 4164-4170.

4 U. Schröder, J. D. Wadhawan, R. G. Compton, F. Marken, P. A. Z. Suarez, C. S. Consorti, R. F. de Souza, J. Dupont, *New Journal of Chemistry* 2000, *24*, 1009-1015.

5 R. G. Evans, O. V. Klymenko, C. Hardacre, K. R. Seddon, R. G. Compton, *Journal of Electroanalytical Chemistry* 2003, *556*, 179-188.

6 L. E. Barrosse-Antle, A. M. Bond, R. G. Compton, A. M. O'Mahony, E. I. Rogers, D. S. Silvester, *Chemistry-an Asian Journal* 2010, *5*, 202-230.

7 A. M. O'Mahony, D. S. Silvester, L. Aldous, C. Hardacre, R. G. Compton, *Journal of Chemical and Engineering Data* 2008, *53*, 2884-2891.

8 R. G. Evans, O. V. Klymenko, P. D. Price, S. G. Davies, C. Hardacre, R. G. Compton, *Chemphyschem* 2005, *6*, 526-533.

9 U. Schroder, J. D. Wadhawan, R. G. Compton, F. Marken, P. A. Z. Suarez, C. S. Consorti, R. F. de Souza, J. Dupont, *New Journal of Chemistry* 2000, *24*, 1009-1015.

10 R. G. Evans, O. V. Klymenko, P. D. Price, S. G. Davies, C. Hardacre, R. G. Compton, *Chemphyschem* 2005, *6*, 526-533.

11 A. M. O'Mahony, D. S. Silvester, L. Aldous, C. Hardacre, R. G. Compton, *Journal of Chemical and Engineering Data* 2008, *53*, 2884-2891.

12 A. J. Bard, L. R. Faulkner., *Electrochemical Methods: Fundamentals and Applications, 2nd ed., John Wiley and Sons: New York* 2001.

13 V. S. R. Morrison., *Electrochemistry at semiconductor and oxidized metal electrodes, Plenum Press, New York* 1980.

14 B. Huber, B. Roling, *Electrochimica Acta* 2011, *56*, 6569-6572.

15 J. E. B. Randles, *Transactions of the Faraday Society* 1948, *44*, 327-&.

16 A. Sevčik, *Chem. Commun* 1948, *13*, 349-377.

17 F. G. Cottrell, *Z. Physik. Chem.* 1903, *42*, 385-431.

18 K. Aoki, J. Osteryoung, *Journal of Electroanalytical Chemistry* 1981, *122*, 19-35.

19 D. Shoup, A. Szabo, *Journal of Electroanalytical Chemistry* 1982, *140*, 237-245.

20 O. V. Klymenko, R. G. Evans, C. Hardacre, I. B. Svir, R. G. Compton, *Journal of Electroanalytical Chemistry* 2004, *571*, 211-221.

21 D. Briggs, M. P.Seah, Eds, *Practical Surface Analysis, Vol 1: Auger and X-Ray Photoelectron Spectroscopy, John Wiley and Sons: Chichester, UK* 1994.

22 S. H. Chung, R. Lopato, S. G. Greenbaum, H. Shirota, E. W. Castner, J. F. Wishart, *Journal of Physical Chemistry B* 2007, *111*, 4885-4893.

Chapter 4 Hydrogenolysis: Hydrogen Loaded Palladium Electrodes by Electrolysis of $H[NTf_2]$ in a RTIL $[C_2mim][NTf_2]$

In this chapter, Electrochemical hydrogenolysis is demonstrated in a room temperature ionic liquid (RTIL) for the first time. Reduction of $H[NTf_2]$ at a Pd microelectrode in the RTIL 1-ethyl-3-methylimidazolium bis(trifluoromethanesulfonyl)imide ($[C_2mim][NTf_2]$) leads to the reversible formation of adsorbed and absorbed hydrogen (Pd/H). Hydrogenation of N,N'-bis(benzyloxycarbonyl)-L-lysine was observed to proceed rapidly, monitored by the consumption of Pd/H. In addition, the electrolysis of adventitious H_2O to form Pd/H is noted.

This work presented in this chapter was carried out with the collaborator of Dr. Leigh Aldous, and has been published in the Journal of Green Chemistry.[1]

4.1 Introduction

Hydrogenation and hydrogenolysis reactions have extensive and diverse applications, and catalytic hydrogenation reactions have been extensively investigated and reviewed in Room Temperature Ionic Liquids (RTILs).[2, 3] Typically such reactions involve the use of H_2 gas in pressurised vessels in conjunction with a suitable catalyst. Alternatively, transfer-hydrogenation involves the introduction of an additional species that decomposes to produce hydrogen on contact with the catalyst.

Electrochemical hydrogenation or hydrogenolysis offers a means of *in-situ* hydrogen generation (such as *via* the electrochemical reduction of a labile proton) thus bypassing both the use of large quantities of potentially explosive H_2 gas, and the generation of a stoichiometric equivalent of waste commonly found in transfer-hydrogenation reactions. Surprisingly, to the best of our knowledge such electrochemical techniques have not been previously demonstrated in an RTIL.

RTILs are of extensive interest to electrochemists, as all RTILs possess inherent conductivity, and other properties such as high thermal and chemical stability, extremely

low vapour pressure, high solubility and tuneable physical properties are widely available.[4] Due to these characteristics they can, in principle, be extensively recycled without producing atmospheric pollution.

Certain RTILs can also dissolve extensive quantities of a wide variety of biomass materials, which makes them promising solvents for the processing of these renewable materials.[5] Hydrogenolysis of cellulose[6] and biomass derivatives[7] in RTILs using H_2 gas and Ru catalysts has recently been reported. The electrochemical hydrogenolysis of biomass compounds[8] is one possible green, clean and safe route to convert these macromolecular compounds into useful chemical feedstocks.

As proof-of-concept, the hydrogenolysis of N,N'-bis(benzyloxycarbonyl)-L-lysine was investigated. By employing a Pd microelectrode, the experiments were carried out under well defined conditions, and also corresponded to the first investigation of such reactions at a microelectrode. A labile proton was reduced at the Pd electrode and hydrogenolysis of N,N'-bis(benzyloxycarbonyl)-L-lysine proceeded rapidly at room temperature, displaying proof of concept that RTILs can be used for such processes.

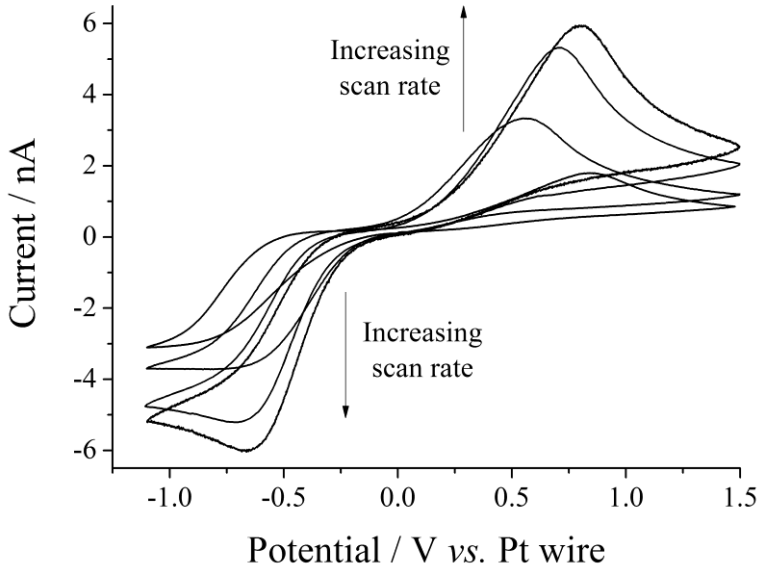

Figure 4.1 Scan rate study (10, 100, 500 and 1000 mV s^{-1}) for the reduction and oxidation of 100 mM H[NTf_2] at a 4.7 µm radius Pd microelectrode in [C_2mim][NTf_2], *in vacuo*.

4.2 Results and Discussion

Initially the electrochemistry of a Pd microelectrode was investigated in the presence of a labile proton source in the IL $[C_2mim][NTf_2]$. Figure 4.1 displays a scan rate study for scans recorded in the presence of 100 mM $H[NTf_2]$ in $[C_2mim][NTf_2]$. With the introduction of $H[NTf_2]$ a reduction wave is clearly observed, corresponding to the reduction of H^+ and concurrent absorption/adsorption of H onto and into the Pd matrix. On the reverse sweep the oxidation of the absorbed/adsorbed H is observed with release of H^+ back into solution. The electrochemistry of $H[NTf_2]$ has previously been investigated in $[C_nmim][NTf_2]$ RTILs at Pt, Au and GC electrodes,[9, 10] and a diffusion coefficient of 3.2×10^{-11} m^2 s^{-1} was determined for $H[NTf_2]$ in $[C_2mim][NTf_2]$.[10] The limiting current displayed in Figure 4.1 corresponds to *ca.* 50 % of that expected for the known D value. This is partially due to the nature of the reduction process, where kinetic limitations can also apply due to the gradual saturation of the palladium lattice, as demonstrated in Figure 4.1 by the broadness of the reduction wave after the sweep is reversed at *ca.* -1.1 V. Partial volatilisation (*in vacuo*) of the $H[NTf_2]$ prior to the experiment is also a possibility, although CVs recorded as a function of time demonstrated that this contribution was minimal (< 10 %) within the first 8 hours.

The removal of *O*- and *N*-benzyl protection groups is frequently performed using Pd/C and H_2 gas.[11] Due to the low solubility of H_2 this process often takes a number of hours to go to completion. Mandal and McMurray[12] have reported the transfer-hydrogenation of a wide variety of compounds by the addition of triethylsilane to Pd/C, resulting in the *in-situ* generation of molecular hydrogen. This included the rapid quantitative or near quantitative hydrogenolysis of benzyloxycarbonyl-protected ((Z)-protected) species in 10–50 min. It should be noted that while this method bypasses the use of H_2, triethylsilane is water-sensitive, highly flammable, has a flashpoint of 269 K, and generates a stoichiometric equivalent of waste.

Reduction of the $H[NTf_2]$ at the Pd microelectrode will result in the formation of reactive Pd/H. If hydrogenolysis occurs on the timescale of the CV, hydrogen will be consumed from the Pd/H resulting in a corresponding decrease in the size of the oxidation peak on the reverse scan. Figure 4.2 displays scans recorded for 200 mM $H[NTf_2]$ in the presence of various concentrations of N,N'-bis(benzyloxycarbonyl)-L-lysine (Z-lys(Z)-OH). Solutions of $H[NTf_2]$ and Z-lys(Z)-OH were tested over a number of days and no change in voltammetry was observed, demonstrating no prior decomposition of the starting material. Slight shifts in the position of each peak are related to slight changes in the *quasi*-reference potential. As the concentration of Z-lys(Z)-OH is increased the limiting current for proton reduction decreased. This is due to the two ester groups present in Z-lys(Z)-OH, which become protonated in the presence of $H[NTf_2]$ and thus decrease the available concentration of protons. In addition the oxidation peak on the reverse scan also decreases, though it decreases in size relatively more rapidly than that of the proton reduction wave.

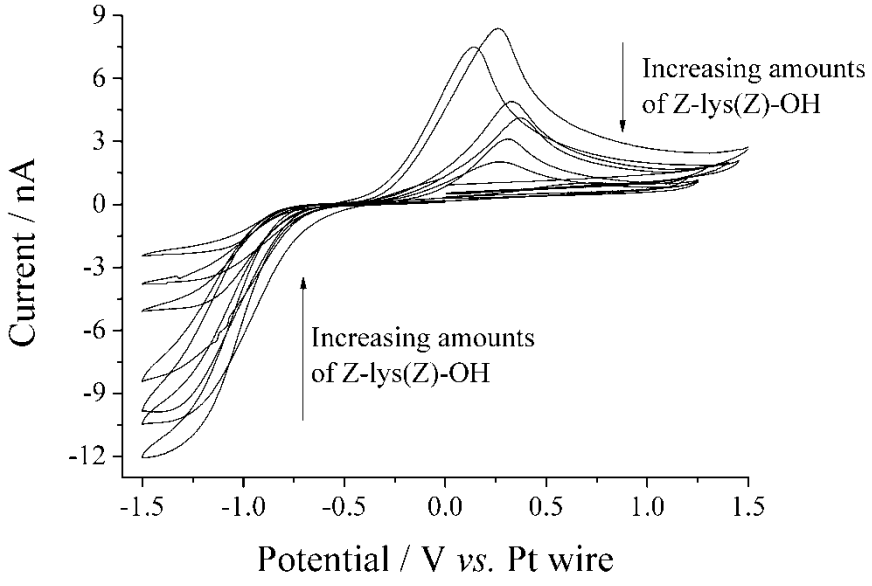

Figure 4.2 Scans recorded for various concentrations of Z-lys(Z)-OH (0 to 80 mM) in the presence of 200 mM $H[NTf_2]$ in $[C_2mim][NTf_2]$ at a 4.7 µm Pd microelectrode, at 100 mV/s and *in vacuo*.

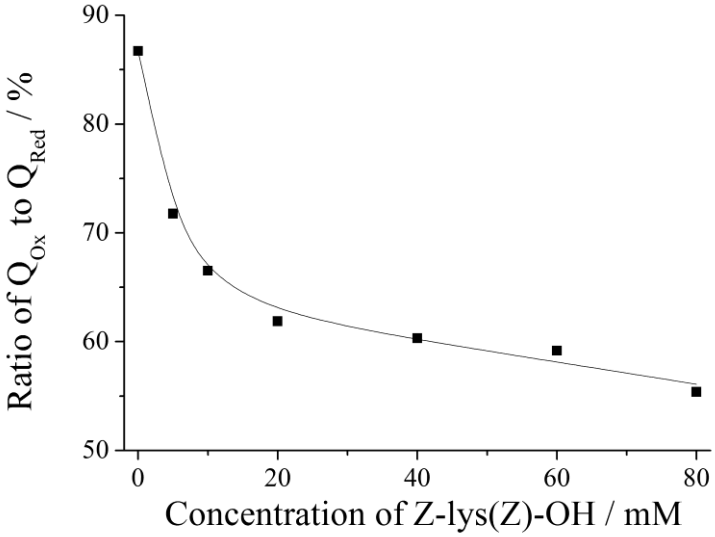

Figure 4.3 Plot of the ratio of oxidation charge to reduction charge (corresponding to formation and removal of Pd/H) for various concentrations of Z-lys(Z)-OH (0 to 80 mM) for the CVs shown in Fig. 4.2.

The relative changes in the two peaks were quantified by integration of both processes, followed by dividing the oxidation charge by the reduction charge in order to obtain the corresponding ratio. Figure 4.3 plots the change in the ratio with the concentration of Z-lys(Z)-OH, demonstrating that as the concentration of Z-lys(Z)-OH increases, progressively less Pd/H is remaining on the reverse scan. This is attributed to the relatively rapid hydrogenolysis of the Z-lys(Z)-OH, Scheme 4.1 displays the expected hydrogenolysis reaction. However, the Pd/H is not completely consumed on the time scale of the scan as the proton is expected to diffuse relatively more rapidly than the bulky Z-lys(Z)-OH molecule, resulting in relatively more H[NTf_2] reaching the electrode than Z-lys(Z)-OH. Figure 4.4 plots a scan rate study for 200 mM H[NTf_2] and 40 mM Z-lys(Z)-OH, the inset plots the change in ratio in the oxidation and reduction charges, and clearly demonstrates that as the scan rate increases relatively less Pd/H is consumed, as would be expected.

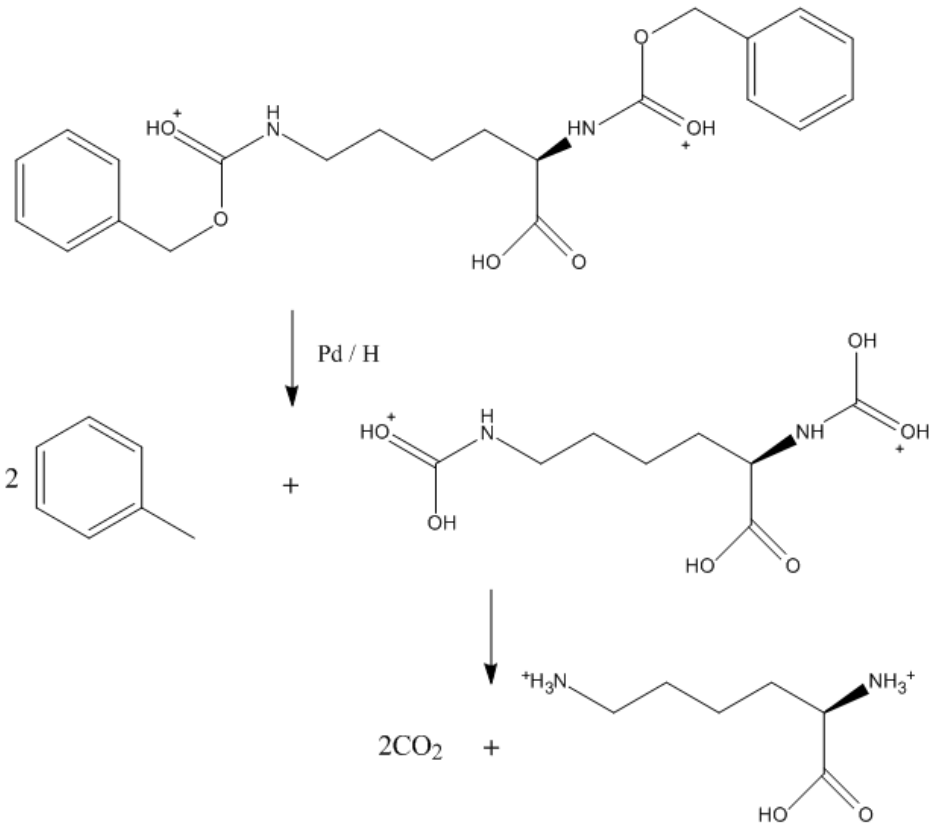

Scheme 4.1 Reaction scheme of the hydrogenolysis of Z-lys(Z)-OH with Pd/H

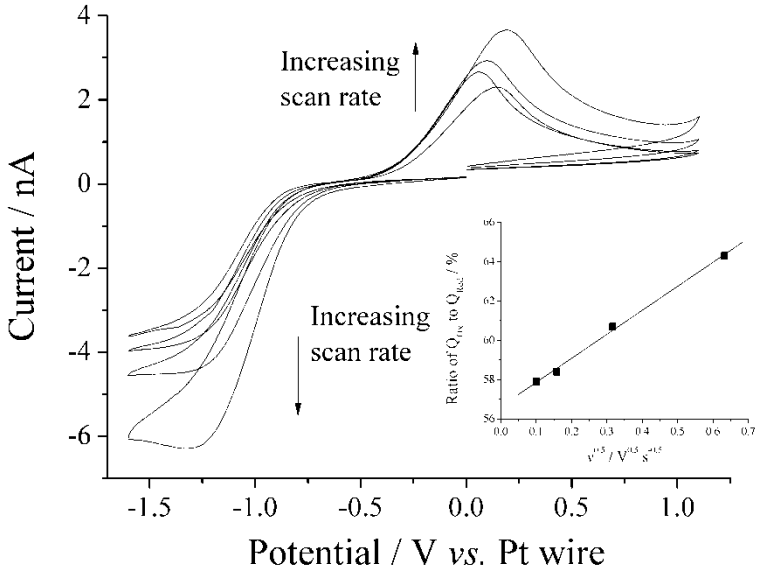

Figure 4.4 Scan rate study (10, 25, 100 and 400 mV s^{-1}) for 40 mM Z-lys(Z)-OH and 200 mM HNTf2 in [C_2mim][NTf_2] at a 4.7 µm Pd microelectrode

By performing this hydrogenolysis at a microelectrode, the electrochemical processes and chemical reaction occur at a well-defined system, and subsequent simulation of these results could yield fundamental parameters regarding the chemical reaction occurring at the Pd/H-RTIL interface.

It should be noted that the experiments were carried out *in vacuo*. This was necessary as H_2O-contamination of RTILs is rapid, and results in a dramatic reduction of the electrochemical window due to the facile electrolysis of the H_2O.[13] The electrolysis of trace H_2O in RTILs has been demonstrated to proceed smoothly with the production of H_2 and O_2 at the cathode and anode, respectively.[14] In this work it was noted that the dissolved H_2O omnipresent in RTIL samples before vacuum drying could be readily reduced to form Pd/H. Such a system could potentially be employed for green hydrogenation and hydrogenolysis reactions, with H_2O as the hydrogen source, RTIL as the recyclable electrolyte (with unique solvation capabilities) and O_2 as the only by-product.

4.3 Conclusions

By demonstrating the rapid hydrogenolysis, proof-of-concept has been achieved indicating that Room Temperature Ionic Liquids can be used for electrochemical hydrogenolysis. Hydrogenolysis of N,N'-bis(benzyloxycarbonyl)-L-lysine (Z-lys(Z)-OH) was achieved by the electrochemical reduction of a labile proton, at a Pd microelectrode, and the hydrogenolysis monitored by the change in ratio of oxidation charge to reduction charge for various concentrations, Z-lys(Z)-OH. The extension of this system to hydrogenation reactions should present no great problems.

References

1 Y. Meng, L. Aldous, R. G. Compton, *Green Chemistry* 2010, *12*, 1926-1928.

2 V. I. Parvulescu, C. Hardacre, *Chemical Reviews* 2007, *107*, 2615-2665.

3 J. Dupont, R. F. de Souza, P. A. Z. Suarez, *Chemical Reviews* 2002, *102*, 3667-3691.

4 D. S. Silvester, R. G. Compton, *Zeitschrift Fur Physikalische Chemie-International Journal of Research in Physical Chemistry & Chemical Physics* 2006, *220*, 1247-1274.

5 D. A. Fort, R. C. Remsing, R. P. Swatloski, P. Moyna, G. Moyna, R. D. Rogers, *Green Chemistry* 2007, *9*, 63-69.

6 I. A. Ignatyev, C. Van Doorslaer, P. G. N. Mertens, K. Binnemans, D. E. De Vos, *Chemsuschem* 2010, *3*, 91-96.

7 J. Julis, M. Hölscher, W. Leitner, *Green Chemistry* 2010, *DOI: 10.1039/c004751a*.

8 H. N. Zhang, X. Y. Zhang, D. M. Xie, D. H. Liu, Z. H. Li, *Canadian Journal of Chemical Engineering* 2002, *80*, 769-773.

9 L. Aldous, D. S. Silvester, W. R. Pitner, R. G. Compton, M. C. Lagunas, C. Hardacre, *Journal of Physical Chemistry C* 2007, *111*, 8496-8503.

10 D. S. Silvester, L. Aldous, C. Hardacre, R. G. Compton, *Journal of Physical Chemistry B* 2007, *111*, 5000-5007.

11 Y. Li, G. Manickam, A. Ghoshal, P. Subramaniam, *Synthetic Communications* 2006, *36*, 925-928.

12 P. K. Mandal, J. S. McMurray, *Journal of Organic Chemistry* 2007, *72*, 6599-6601 Doi 10.1021/Jo0706123.

13 A. M. O'Mahony, D. S. Silvester, L. Aldous, C. Hardacre, R. G. Compton, *Journal of Chemical and Engineering Data* 2008, *53*, 2884-2891.

14 M. M. Islam, T. Okajima, S. Kojima, T. Ohsaka, *Chemical Communications* 2008, 5330-5332.

Chapter 5 Palladium nanoparticle-modified carbon nanotubes for electrochemical hydrogenolysis in RTILs

The electrochemical hydrogenolysis of benzyl and carboxybenzyl protecting groups is described. Optimisation of a synthetic protocol afforded well-defined palladium (Pd) nanoparticles on the surface of multiwall carbon nanotubes (CNTs). The high surface area composite was investigated, and differences observed in the voltammetry for the same composite in aqueous and ionic liquid systems are discussed. When used to reduce acidic protons in the ionic liquid (IL) 1-Ethy-3-methylimidazolium bis(trifluoromethylsulfonyl)imide ([C_2mim][NTf_2]) reactive palladium hydride was formed efficiently, and which rapidly performed hydrogenolysis. The compounds 1-(3-(benzyloxy)propyl)-4-methoxybenzene, benzyl octyl carbonate, *N*,*N'*-bis(benzyloxycarbonyl)-L-lysine and *N*-benzyl-L-prolinol were investigated. Extended electrolysis of bis(trifluoromethylsulfonyl)imide (H[NTf_2]) in [C_2mim][NTf_2] containing alcohol groups protected with benzyl and carboxybenzyl groups afforded the alcohol product in high yield. Hydrogenolysis of the similarly protected amine groups is also reported.

Dr. Leigh Aldous, Ben S. Pilgrim and Prof. Timothy J. Donohoe have assisted this work presented in this chapter. The X-ray photoelectron spectroscopy experiments were performed by Dr. Leigh Aldous in the Compton Group and NMR spectroscopy was carried out by Ben S. Pilgrim in Chemistry Research Laboratory, University of Oxford. This work has been published in New Journal of Chemistry.[1]

5.1 Introduction

Ionic liquids (ILs) are salts with melting points below 373K, and are typically liquid at room temperature.[2] Their extremely low volatility[3] facilitates their recycle and minimises volatile organic pollution, the wide electrochemical windows available present numerous electrosynthetic opportunities, and their unique ability to solvate and stabilise certain

compounds opens new possibilities.[4] Large increases in reactivity and selectivity have been highlighted when moving to IL systems, as well as reactions unique to IL media.[5]

Nanoparticles possess large surface areas, in many cases enhancing their utility by several orders of magnitude above that of its bulk material (*e.g.* gram per gram).[6] This is of particular interest when using precious metals. Carbon substrates are attractive support materials, and in the case of carbon nanotubes (CNTs) numerous particles can be adhered securely to the surface of electrodes, acting as both support and molecular wire to provide large, active surface areas.[7]

Protecting groups are of paramount importance in organic chemistry, particularly in natural product synthesis, where sensitive moieties in polyfunctional organic molecules need to be carried through a synthetic sequence.[8] Benzyl groups have found widespread use in this respect for the protection of both alcohols and amines. Their utility stems from their orthogonality to many other protecting groups due to their relative stability to both acidic and basic conditions whilst being readily cleaved under hydrogenolytic conditions. Carboxybenzyl groups can also be cleaved by hydrogenolysis and are frequently used for amine protection. They can often be both introduced and removed under milder conditions than those required for a benzyl group, making them more suitable for sensitive substrates.

Palladium (Pd) is widely used as a catalyst for hydrogenation and hydrogenolysis reactions, adsorbing H_2 onto its surface to form reactive palladium hydride (denoted Pd/H).[9] This has been used for a variety of purposes, including the removal of protecting groups.[9] Hydrogenolysis reactions can be hindered by both substrate and hydrogen insolubility. The solubility of H_2 in ILs is similar to that found in aqueous systems, *e.g.* sub-millimolar levels at atmospheric temperature and pressure,[10] and there are safety implications concerning the use of large quantities of hydrogen gas, so new conditions for the removal of these groups are highly desirable.

The first electrochemical hydrogenolysis reaction using Pd in an IL was reported in the previous chapter, removing carboxybenzyl-protecting groups from *N*,*N*′-bis(benzyloxycarbonyl)-L-lysine.[11] Although electrochemical hydrogenolysis by passed the use of H_2 gas, the technique described utilised a Pd microelectrode and as such was unsuitable for the extended conversion of material, some hydrogen being lost into the body of the electrode.[11]

In this chapter, we report the synthesis of Pd-nanoparticle decorated CNTs, in order to provide a high surface area, highly active material for electrochemical hydrogenolysis. This material has been fully characterised, and successfully utilised in an IL in order to perform the electrochemical cleavage of both benzyl and carboxybenzyl groups. This has been demonstrated both voltammetrically, and by the isolation, identification and quantification of the hydrogenolysis products obtained in the IL environment.

5.2 Experimental

5.2.1 Ultrasonic modification of the CNT

The CNTs were sonicated in conc. $HClO_4$ and HNO_3 (3:7 v/v) for 7 h to oxidize their surfaces, before being centrifuged and washed until the eluent was pH 7. A suitable quantity of $PdCl_2$ and 0.1 g CNT were added to 80 mL acetonitrile, sonicated for 1 h, and then $NaBH_4$ added to the mixture. The reaction was allowed to proceed for 1 h under sonication at 338 K. Finally, the products were centrifuged, washed with deionised water several times, isolated and dried under vacuum for 24 h prior to use.

5.2.2 Modification of the GC electrode with CNTs

1 mg of CNTs were suspended in 1 mL of chloroform and the mixture sonicated until the CNT were uniformly suspended. 10 μL of the suspension was then carefully placed onto the polished surface of the GC electrode in order to form a droplet, and allowed to air dry.

5.2.3 Synthesis of the various organic compounds investigated

N,*N'*-bis(benzyloxycarbonyl)-L-lysine, *N*-benzyl-L-prolinol and octan-1-ol were used as supplied from Aldrich. All other organic compounds were synthesised and characterised in house, as detailed in the appendix to this chapter.

5.2.4 Measurements

Images of the samples were obtained by field emission scanning electron microscopy (FESEM, FEI SIRION). Sonication was carried out using a D-78224 Singen/Htw sonicator (50/60 Hz, 80 W, UK). Centrifugation was carried out using a Centrifuge 5702 (Eppendorf, UK). pH measurement was made using a pH213 pH meter (Hanna instrument, UK) calibrated using reference pH buffer solutions of pH 4.01 ± 0.01 and pH 7.01 ± 0.01 (Hanna instrument, UK). GC-MS samples were run on an Agilent 6890 Series GC System (Micromass GCT). Compounds were detected under conditions of Positive Chemical Ionisation (CI^+) and calibration was *via* the lock mass of amyl acetate. Column conditions used were: initial oven temperature 353 K; temperature ramp 293 K min^{-1}; final oven temperature 553 K. X-ray photoelectron spectroscopy (XPS) was performed on SAF VG 2 at the Chemical Research Laboratory, Department of Chemistry, University of Oxford, UK, using X-radiation from the Al Kα band. All XPS experiments were recorded using an analyzer energy of 50 eV for survey scans and 20 eV for detailed scans. The base pressure in the analysis chamber was maintained at not more than 1.0 x 10^{-6} mbar. The Pd-modified CNT were directly mounted onto double sided carbon adhesive tape (SPI supplies, PA, USA), attached onto a stainless steel stub and then placed in the ultra-high vacuum analysis chamber of the spectrometer. Analysis of the resulting spectra was performed using XPS Peak 4.1. The reported atomic composition values for each sample were corrected with the atomic sensitivity factors, and assignment of the peaks made according to an online database.[12]

Flash column chromatography was carried out on silica gel (60 Å, 0.033-0.070 mm, BDH) using Still's method, with head pressure provided by bellows. Reactions and columns were monitored by thin layer chromatography analysis on Merck DC-Keisegel 60 F_{254} 0.2 mm precoated plates. Spots were visualised by UV light (λ_{max} = 254 nm) and/or staining with basic potassium permanganate solution or acidic vanillin solution as deemed appropriate for the compound.

5.3. Results and Discussion

5.3.1 Synthesis of Pd-decorated CNTs

Decoration of the CNT surface with Pd nanoparticles was performed using a chemical reduction technique. Briefly, the CNT were sonicated in a 3:7 v/v mixture of concentrated $HClO_4$ and concentrated HNO_3 for 7 h. Oxidation in this media is known to introduce a variety of oxygen functional groups to carbon surfaces, and in particular significantly increase the quantity of RCOOH groups.[13] It also results in cutting of CNTs, producing shorter CNT with a corresponding increase in the number edge sites and defects.[14] The

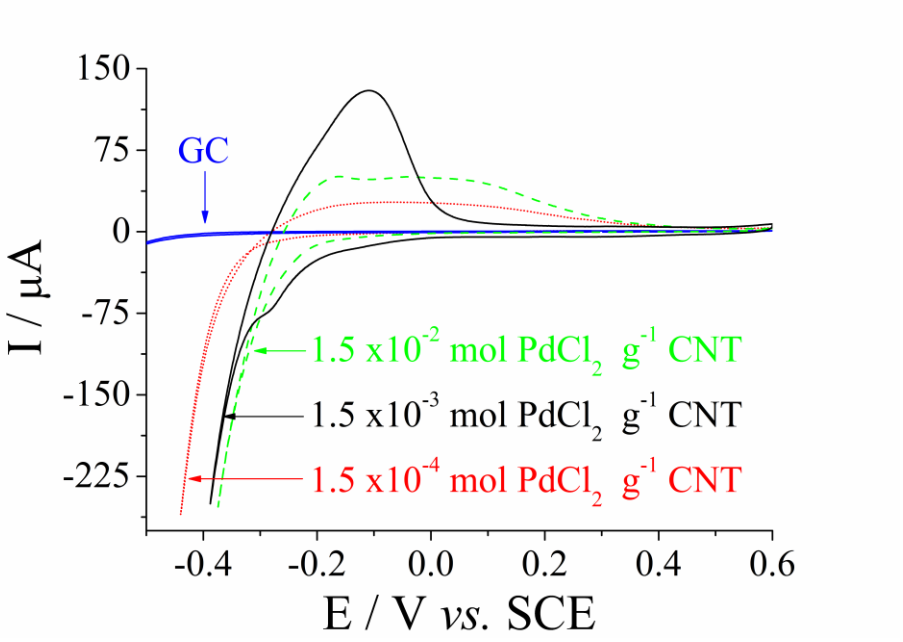

Figure 5.1 CVs (100 mV s^{-1}) recorded in 0.25 M H_2SO_4 for a GC electrode, as well as that electrode after being dropcast with CNT modified with three different concentrations of $PdCl_2$

various oxygen-containing functional groups are believed to interact with metal complexes in solution,[15, 16] and defect sites are expected to provide key sites for the nucleation of nanoparticles, prior modification of the CNT therefore ensuring numerous, well-adhered nanoparticles on the CNT surface. Palladium dichloride was introduced to a suspension of CNT in acetonitrile, sonicated for 1 h, reduced with $NaBH_4$ at 338 K and sonicated for a further hour. The Pd-modified CNT were centrifuged, isolated and washed thoroughly with water before characterisation.

5.3.2 Characterisation of the Pd-decorated CNTs

Three ratios of Pd:CNT were investigated, and the resulting Pd-modified CNT characterised by voltammetry, Scanning Electron Microscopy (SEM) and X-ray Photoelectron Spectroscopy (XPS). The three ratios were 1.5 $x10^{-2}$ mol, 1.5 $x10^{-3}$ mol and 1.5 $x10^{-4}$ mol $PdCl_2$ per g of CNT. Reduction of the Pd(II) species was afforded as described above.

Electrochemical proton reduction at Pd is known to first form a surface adsorbed hydrogen atom (denoted Pd/H), which can then diffuse into the Pd matrix. At higher overpotentials further reduction of protons results in their combination on the Pd surface and formation of H_2.[17] Figure 5.1 displays the scans recorded for a GC electrode in 0.25 M H_2SO_4, as well as scans for the GC electrode modified by dropcasting the three Pd-modified CNT samples onto the GC surface.

The potential corresponding to proton reduction (resulting in both adsorbed hydrogen at the Pd surface and absorbed hydrogen in the Pd bulk)[6] shifted cathodically as the quantity of Pd used in the synthesis decreased, consistent with the active quantity of Pd(0) decreasing. Under certain conditions a distinct voltammetric peak corresponding to the formation of only surface adsorbed hydrogen can be observed. For example, this feature can be discerned as a distinct peak (prior to bulk proton reduction) for 10 monolayers of Pd deposited on Au(111), but on 50 μm thick Pd foil the bulk reduction of protons dominates and only one reduction

feature can be observed.[18] Nanostructured Pd microdisks[19] and Pd nanoparticles electrodeposited on boron-doped diamond[5] have also allowed the distinct observation of this feature. In Figure 5.1, the Pd-modified CNT prepared using the middle quantity of Pd (1.5 $x10^{-3}$ mol $PdCl_2$ per g of CNT) displayed a small reduction feature at -0.285 V prior to the more significant reduction of protons from *ca.* -0.3 V onwards, indicating that that sample contained a high surface area and/or limited volume particles of Pd, both features consistent with a CNT modified with well-defined nanoparticles.

On the reverse scan the hydrogen adsorbed/absorbed into the Pd matrix is oxidised to regenerate protons in solution. Again, the Pd-modified CNT prepared using the middle quantity of Pd displayed the most well-defined voltammetry. The samples prepared using both more and less $PdCl_2$ displayed broader oxidation features, consistent with extremely heterogeneous Pd deposits.

The three Pd-modified CNT samples were also analysed by SEM. The sample utilising the highest ratio of Pd to CNT displayed several metallic features over a range of geometries and sizes (> 1 μm, not shown) consistent with the poorly defined voltammetery displayed in Figure 5.1. In the sample prepared using the lowest amount of Pd, no distinct metallic features could be observed on the CNT surfaces.

The sample utilising 1.5 $x10^{-3}$ mol $PdCl_2$ per g CNT (medium quantity) displayed numerous small, spherical, metallic features on the CNT surfaces, all consistently less than 100 nm in diameter (Figure 5.2), demonstrating that Pd nanoparticles had successfully been formed. The presence of Pd (and absence of other metals) was demonstrated by X-ray Photoelectron Spectroscopy (Figure 5.3), which gave a molecular composition of *ca.* 94.1 % C, 5.5 % O and 0.5 % Pd. As such the CNT modified with the medium quantity of Pd was used throughout the remainder of this charpter.

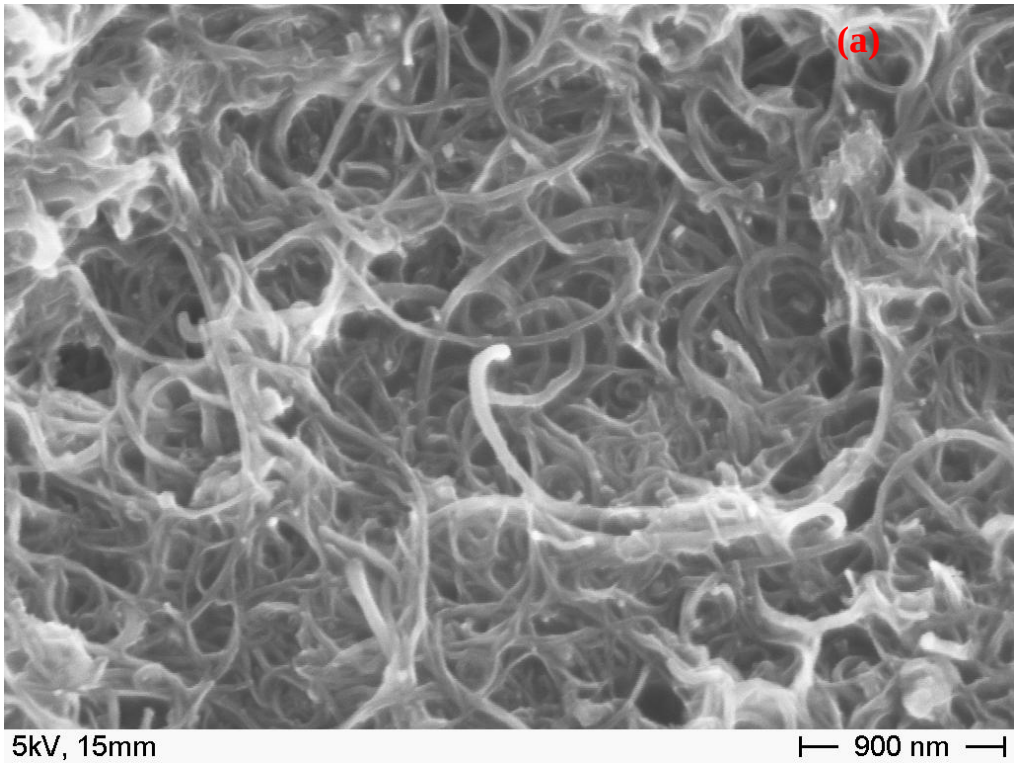

Figure 5.2 Characteristic SEM images recorded for (top) CNT oxidised by sonicating in 3:7 v/v $HClO_4$: HNO_3, and (b) oxidised CNT after modification with Pd nanoparticles

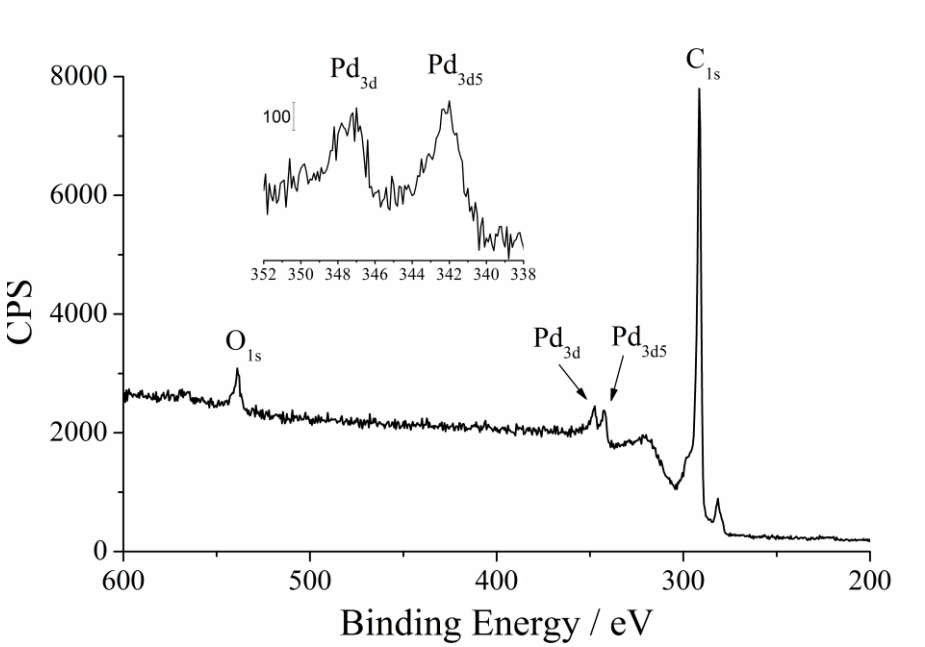

Figure 5.3 XPS spectra recorded for Pd-decorated CNT, displaying a survey scan and (inset) detailed scan over the Pd region

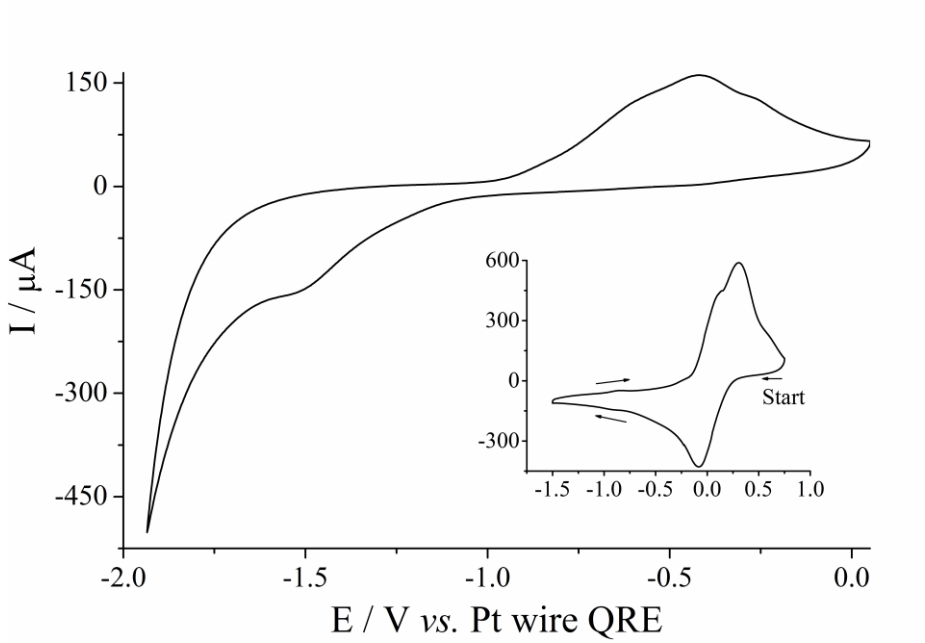

Figure 5.4 Scan recorded for 3 mm GC electrode modified by dropcasting Pd-decorated CNT, in N_2-degassed water-saturated [C_2mim][NTf_2], and (inset) after the addition of 40 mM H[NTf_2] and *in vacuo*. Both scans recorded at 100 mV s^{-1} and 298 K

5.3.3 CV for Pd-decorated CNTs in an ionic liquid

The reduction of bis(trifluoromethylsulfonyl)imide, $H[NTf_2]$, has previously been reported in 1-alkyl-3-methylimidazolium bis(trifluoromethylsulfonyl)imide ($[C_nmim][NTf_2]$) ionic liquids at GC, Au, Pt and Pd electrodes.[11, 20, 21] At Pd microelectrodes the reduction of the proton to form palladium hydride, followed by oxidation of the palladium hydride on the reverse sweep has been observed.[11] Reduction of water present in water-saturated $[C_2mim][NTf_2]$ was also observed to form palladium hydride.[11]

Figure 5.4 displays the CV recorded in N_2-degassed, water-saturated $[C_2mim][NTf_2]$ for Pd-decorated CNTs dropcast onto a GC surface. Water present in ILs is known to typically undergo more facile oxidation and reduction than that of the IL itself.[22] The reduction of water can be observed at *ca.* -1.5 V (*vs.* Pt wire *quasi*-reference), with the corresponding oxidation of palladium hydride at *ca.* -0.5 V.

To the solution $H[NTf_2]$ was added (40 mM), and the sample then placed under vacuum for *ca.* 30 min and investigated. After the addition of the acid a reduction peak was observed at *ca.* -0.1 V and oxidation peaks at *ca.* +0.3 V *vs.* Pt wire *quasi*-reference (inset in Figure 5.4). The shift in the oxidation features likely corresponds to a shift in the *quasi*-reference potential upon addition of the protons, rather than a shift in the thermodynamics of proton insertion/release from the Pd matrix. The electrochemical reduction and oxidation of the acidic proton at Pd is significantly more reversible, and reduction occurs at significantly more anodic potentials than those observed for water reduction, as would be expected due to the added difficulty of breaking the H-OH bond prior to Pd/H formation from H_2O.

A potential of -1 V (*vs.* Pt wire) was applied for 60 s in order to reduce $H[NTf_2]$, and a potential of +0.75 V then applied for 60 s in order to oxidise the resulting Pd/H. Comparison of the reduction and oxidation charge indicated a Q_{red}:Q_{ox} ratio of 0.91. The slight difference is attributed to protons that diffused into the Pd particles and were not released on the time

scale of the experiment. No indication of extensive H_2 bubble formation at a saturated Pd/H-electrolyte interface was therefore indicated. The absence of H_2 formation in a range of aprotic solvents has previously been noted,[23] although in the IL this lack of H_2 formation (on the time scale of the experiment) can also be attributed to the fact that the diffusion coefficient, D, of the proton in $[C_2mim][NTf_2]$ and the D of hydrogen inside the Pd matrix are of the same order of magnitude. The D value of $H[NTf_2]$ in $[C_2mim][NTf_2]$ has previously been found to be 3.2 x 10^{-11} m^2 s^{-1} (*ca.* 293 K);[21] the D value of hydrogen inside Pd is influenced by numerous factors (matrix defects, strain, phase, concentration, *etc.*) but is generally found in the range of 1 to 7 x 10^{-11} m^2 s^{-1} (293-298 K).[24-29] The D value of dissociated protons in aqueous systems has been reported as 8.2 x 10^{-9} m^2 s^{-1} (293 K).[30]

The oxidation of Pd/H in Figure 5.4 consists of approximately three overlapping oxidation processes (*e.g.* at -0.59, -0.41 and -0.27 V *vs.* Pt wire for the water-saturated IL in Figure 5.4). Similar features have been reported for nanostructured Pd, and different surface sites, place exchange mechanisms (requiring rearrangement of surface layers) or the direct oxidation of the more difficult to oxidise subsurface layers at higher overpotentials were all reported as possible causes.[19] The slow reorganisation of bulky IL cations and anions[31] would likely influence place exchange mechanisms, while faster diffusion of hydrogen inside Pd than in the IL would lead to enhanced oxidation of subsurface layers, if occurring. Both explanations could explain these multiple features being more distinct in the IL (Figure 5.4) than in aqueous H_2SO_4 (Figure 5.1).

5.3.4 Electrochemical hydrogenolysis of Z-lys(Z)-OH on the voltammetric timescale

To evaluate the ability of the Pd-decorated CNTs to perform rapid electrochemical hydrogenolysis, the behaviour of the system was investigated on the voltammetric timescale in the presence of *N*,*N'*-bis(benzyloxycarbonyl)-L-lysine (Z-Lys(Z)-OH). Voltammetry at a

Pd microelectrode has previously indicated that in $[C_2mim][NTf_2]$, the reduction of $H[NTf_2]$ to form Pd/H results in hydrogenolysis of the carboxybenzyl-protecting groups, as demonstrated by scan rate and concentration studies.[11] Figure 5.5 displays a scan rate study recorded for 40 mM $H[NTf_2]$ in $[C_2mim][NTf_2]$ at a GC electrode modified with Pd-decorated CNT, in the presence of 15 mM Z-Lys(Z)-OH. The reduction of $H[NTf_2]$ and oxidation of the resulting Pd/H are clearly observed, with the multiple oxidation features (at *ca.* -0.435 and +0.15 V *vs.* Pt wire) previously observed in Figure 5.4 more well resolved. The adsorption of crystal violet at Pd previously been demonstrated to alter proton insertion/release kinetics,[18] and in this case it likely corresponds to the adsorption of Z-Lys(Z)-OH or its hydrogenolysis product at the Pd nanoparticles surface.

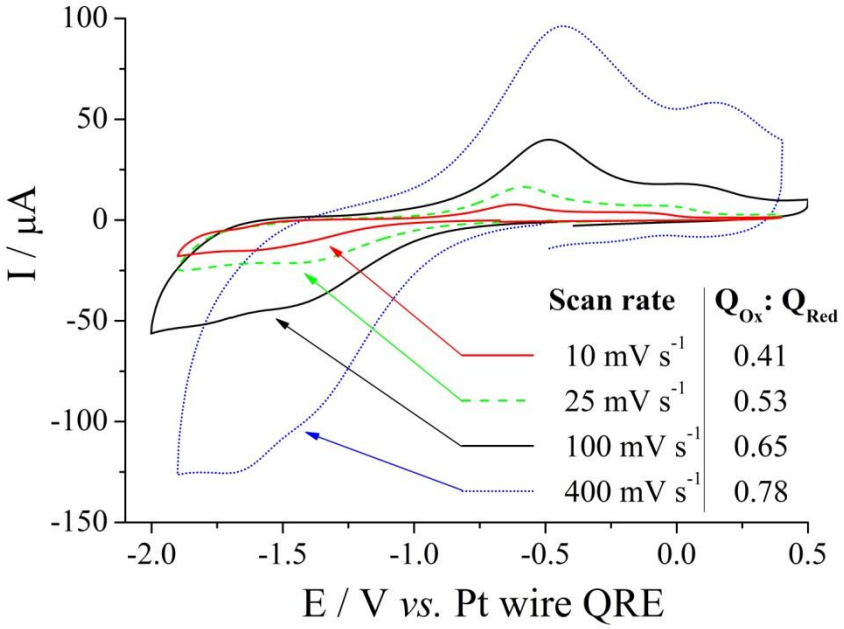

Figure 5.5 Scan rate study recorded *in vacuo* and at 298 K for a 3 mm GC electrode modified by dropcasting Pd-decorated CNT, in $[C_2mim][NTf_2]$ containing 40 mM $H[NTf_2]$ and 15 mM Z-lys(Z)-OH. The ratio of the oxidation charge (Q_{Ox}) to the reduction charge (Q_{Red}) is also displayed.

The 400 mV s^{-1} scan in Figure 5.5 took *ca.* 12 s to be completed; the 10 mV s^{-1} scan took *ca.* 500 s. The ratio of oxidation charge to reduction charge for the four scan rates is displayed in the Figure, and these values clearly demonstrate that at slower scans less Pd/H is oxidised on the reverse scan, due to its consumption in the hydrogenolysis of Z-Lys(Z)-OH on the time scale of the scan.

5.3.5 Bulk electrolysis for the electrochemical hydrogenolysis of various protecting groups

In order to conclusively demonstrate the ability of Pd-decorated CNT to achieve the hydrogenolysis of organic compounds in ILs, extended hydrogenolysis was performed and the resulting products analysed. Samples (all 200 mM) containing either a benzyl-protected alcohol (**1**), a benzyl-protected amine (**2**) or a carboxybenzyl-protected (Z-protected) alcohol (**3**) were dissolved in $[C_2mim][NTf_2]$ containing 250 mM $H[NTf_2]$. The structures of the species employed are displayed in Table 5.1. The IL sample (0.1 or 0.3 mL) was deposited on top of a 3 mm GC electrode modified by dropcasting 1.5 µg of Pd-decorated CNT, and a Pt

Table 5.1: Details of extended hydrogenolysis reactions (performed at -1.75 V, 298 K, passing 95-100 % of theoretical charge)

Entry	Starting Material	Isolated product	Isolated Yield
1	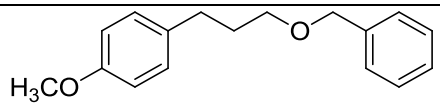	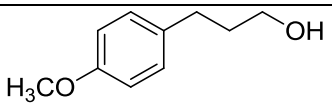	71 %
2	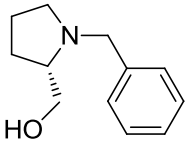	n/a[1]	n/a[1]
3	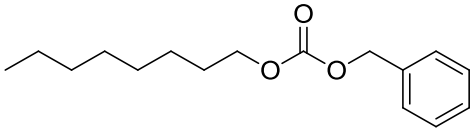	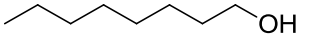	85 %[2]

[1] Only trace starting material isolated from the IL; converted material believed to remain in the IL phase

[2] Some benzyl octyl ether observed in the crude; see text for details

quasi-reference wire and Pt coil counter electrode immersed in the IL. Potentiostatic electrolysis was performed at -1.75 V (*vs.* Pt wire) until the charge passed was equivalent to 95-100 % of the theoretical charge required for the complete conversion of the starting material, assuming a 1 electron process. The 0.1 mL samples were run initially in order to confirm the products by TLC and GC-MS (CI^+) analysis, with the 0.3 mL samples run subsequently in order to isolate the products by flash column chromatography and allow characterisation by NMR.

Electrolysis of **1** was found to afford the alcohol as the anticipated hydrolysis product, as confirmed by NMR and GC-MS m/z trace (NMR displayed in the Appendix 5.5). Although electrolysis of **2** appeared to proceed smoothly, the resulting amine could not be extracted from the IL solution. Treatment with aqueous solutions of Na_2CO_3 or acetonitrile solutions of NMe_4OH in order to neutralise the anticipated protonated amine followed by extraction was found to isolate only small quantities of the starting material. Therefore it is likely that hydrogenolysis of **2** occurred, but resulted in a product that was difficult to isolate from IL. Due to the difficulty in isolating this amine product from the IL, the extended hydrogenolysis of Z-Lys(Z)-OH was not attempted as the results were expected to be similar.

Electrolysis of **3** was found to afford the expected hydrogenolysis product, octan-1-ol, in 85 % yield. A trace impurity was also observed in the GC-MS of the crude sample. The m/z trace of this impurity was consistent with that of benzyl octyl ether, and separate synthesis of this compound followed by GC-MS showed it had an identical retention time and m/z trace to the impurity. The impurity was not present in sufficient amounts to be detectable after flash column chromatography. Mixtures of $H[NTf_2]$ and **3** in $[C_2mim][NTf_2]$ were not observed to exhibit any degradation, even after a period of days. However, a mixture of $H[NTf_2]$ and equimolar quantities of **3** and octan-1-ol in $[C_2mim][NTf_2]$ demonstrated (by GC-MS of the crude sample) the presence of **3**, octan-1-ol and benzyl octyl ether after being left to stand for

Scheme 5.1: Suspected mechanism for the formation of benzyl octyl ether side product

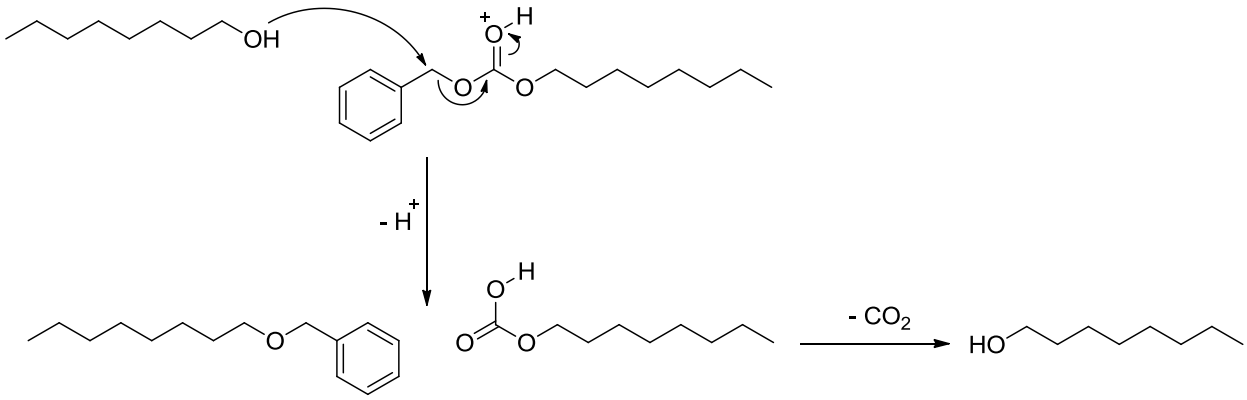

24 hr. It can therefore be inferred that protonation of the carbonyl group in **3** (Scheme 5.1) in $[C_2mim][NTf_2]$ facilitates attack by octan-1-ol, releasing CO_2, catalytically regenerating octan-1-ol and a proton and yielding benzyl octyl ether. It is likely that the trace benzyl octyl ether found after hydrogenolysis of **3** stemmed from residual starting material reacting in a *ca.* 24 hr gap between cease of electrolysis and GC-MS analysis. Extended electrolysis would clearly result in the full removal of the benzyl octyl ether to yield the pure product, as the structurally similar benzyl ether protected compound **1** underwent successful hydrogenolysisunder similar conditions. Alternatively, the use of weaker acids or even H_2O (as demonstrated in Figure 5.4) could be used to form reactive Pd/H in the absence of strongly acidic protons.

5.4. Conclusions

The decoration of carbon nanotubes with Pd nanoparticles has been demonstrated and the composite characterised. When dropcast on an inert glassy carbon electrode, the resulting Pd-modified substrate can be used for the efficient reduction of protons to Pd/H in an IL. No hydrogen gas evolution was demonstrated over short periods, due to the comparable diffusion coefficients of the proton in the IL media and the hydrogen atom in the Pd matrix.

Electrochemically formed Pd/H was demonstrated voltammetrically to perform hydrogenolysis of carboxybenzyl-protected lysine. Although amines containing benzyl- and carboxybenzyl-protecting groups are believed to have undergone electrolysis, the resulting products could not easily be isolated from the IL. Extended electrolysis of both carboxybenzyl-protected and benzyl-protected alcohols afforded the corresponding alcohol after flash column chromatography. The acidic proton was found to encourage reaction between benzyl octyl carbonate and octan-1-ol to afford benzyl octyl ether, if not electrolysed to completion. ILs are known to have unique solvating ability, and proof-of-principle has now been demonstrated that Pd nanoparticles can be used for clean, efficient, safe electrochemical hydrogenolysis in IL media.

5.5 Appendix

5.5.1 Experimental Techniques

^{1}H and ^{13}C NMR spectra were recorded on a Bruker Avance AV400 spectrometer (400 MHz and 100 MHz respectively) in $CDCl_3$ and referenced to residual solvent peaks or to tetramethylsilane as an internal standard. Chemical shifts δ are quoted in parts per million (ppm) to the nearest 0.01 for ^{1}H and 0.1 for ^{13}C, coupling constants *J* are quoted in Hz to the nearest 0.1 and splittings are recorded as singlet (s), doublet (d), triplet (t), quartet (q), quintet (quin.) and broad (br.). Assignments were based upon DEPT, COSY and HMQC experiments.

THF and CH_2Cl_2 were dried by purification through two activated alumina purification columns. Petrol refers to the petroleum ether fraction that boils in the range 40-60 ^{o}C. Reagents were obtained from Aldrich and were used as supplied. All non-aqueous reactions were carried out in flame-dried glassware under an atmosphere of argon, unless otherwise specified.

Flash column chromatography was carried out on silica gel (60 Å, 0.033-0.070 mm, BDH) using Still's method, with head pressure provided by bellows. The solvent system is quoted in parentheses. Reactions and columns were monitored by thin layer chromatography analysis on Merck DC-Keisegel 60 F_{254} 0.2 mm precoated plates. Spots were visualised by UV light (λ_{max} = 254 nm) and/or staining with basic potassium permanganate solution or acidic vanillin solution as deemed appropriate for the compound.

5.5.2 Experimental Procedures

1-(3-(Benzyloxy)propyl)-4-methoxybenzene reactant **1**

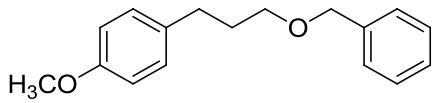

A solution of 3-(4-methoxyphenyl)propan-1-ol (347 mg, 2.09 mmol) in THF (21 mL) was stirred at 273 K. Sodium hydride (60 % dispersion in mineral oil, 125 mg, 3.14 mmol) was added portionwise and the mixture left to stir for 30 min. Benzyl bromide (428 mg, 2.50

mmol) and tetrabutylammonium iodide (39 mg, 0.105 mmol) were added and then the reaction was warmed to room temperature and then stirred at reflux for 18 h. The reaction was cooled to room temperature and then quenched by dropwise addition of saturated aqueous NH_4Cl (5 mL) and diluted with Et_2O (100 mL). The organic layer was washed with H_2O (2 × 25 mL) and brine (25 mL), dried over Na_2SO_4, filtered, and the solvent removed *in vacuo* to give the crude product. Purification by flash column chromatography [SiO_2, petrol/EtOAc, 9:1 to 4:1] furnished benzyl ether **1** (528 mg, 98 %) as an oil.

^{1}H NMR (400 MHz, $CDCl_3$) δ_H: 7.39 (4H, m, 4 × *H*C(Ar)), 7.33 (1H, m, *H*C(Ar)), 7.13 (2H, d, *J* 8.6, 2 × *H*C(Ar)), 6.86 (2H, d, *J* 8.6, 2 × *H*C(Ar)), 4.54 (2H, s, C*H*$_2$OR), 3.81 (3H, s, OC*H*$_3$), 3.52 (2H, t, *J* 6.4, CH_2CH_2OR), 2.70 (2H, t, *J* 8.1, C*H*$_2$), 1.94 (2H, tt, *J* 8.1, 6.4, C*H*$_2$$CH_2$OR); **^{13}C NMR** (100 MHz, $CDCl_3$) δ_C: 157.8, 138.6, 134.1 (3 × *C*(Ar)), 129.4, 128.4, 127.7, 127.5, 113.7 (5 × H*C*(Ar)), 72.9 (*C*H_2OR), 69.5 (CH_2*C*H_2OR), 55.3 (O*C*H_3), 31.6 (*C*H_2), 31.5 (*C*H_2). Data were consistent with those previously reported.[32]

3-(4-Methoxyphenyl)propan-1-ol **product 1**

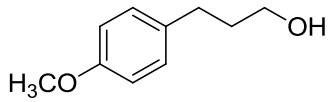

A solution of benzyl ether **1** (17.3 mg, 0.0675 mmol) in ionic liquid (340 μL) was subjected to hydrogenolysis. The reaction mixture was purified by flash column chromatography [SiO_2, petrol/EtOAc, 9:1 to 3:1] to furnish alcohol **product 1** (8.0 mg, 71 %) as an oil.

^{1}H NMR (400 MHz, $CDCl_3$) δ_H: 7.13 (2H, d, *J* 8.6, 2 × *H*C(Ar)), 6.85 (2H, d, *J* 8.6, 2 × *H*C(Ar)), 3.80 (3H, s, OC*H*$_3$), 3.66 (2H, t, *J* 5.8, C*H*$_2$OH), 2.66 (2H, t, *J* 7.3, C*H*$_2$), 1.87 (2H, tt, *J* 7.3, 5.8, C*H*$_2$$CH_2$OH), 1.30 (1H, br. s, O*H*); **^{13}C NMR** (100 MHz, $CDCl_3$) δ_C: 157.8, 134.0 (2 × *C*(Ar)), 129.3, 113.8 (2 × H*C*(Ar)), 62.1 (*C*H_2OH), 55.3 (O*C*H_3), 34.4 (*C*H_2), 31.2 (*C*H_2). Data were consistent with those previously reported.[33]

Benzyl octyl carbonate reactant **3**

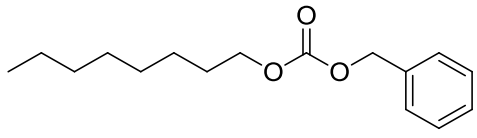

Octan-1-ol (261 mg, 2.00 mmol) was added dropwise to a stirred solution of benzyl chloroformate (409 mg, 2.40 mmol), pyridine (237 mg, 3.00 mmol) and 4-dimethylaminopyridine (2 mg, 0.02 mmol) in CH_2Cl_2 (20 mL) at 273 K. The reaction was warmed to room temperature and stirred for a further 18 h. The mixture was concentrated *in vacuo* to give the crude product which was purified by flash column chromatography [SiO_2, petrol/EtOAc, 24:1 to 9:1] to furnish carbonate **3** (433 mg, 82 %) as an oil.

^{1}H NMR (400 MHz, $CDCl_3$) δ_H: 7.41-7.33 (5H, m, 5 × *H*C(Ar)), 5.17 (2H, s, PhC*H*$_2$OR)), 4.16 (2H, t, *J* 6.9, C*H*$_2$OR), 1.67 (2H, quin, *J* 7.5, C*H*$_2$CH$_2$OR), 1.39-1.26 (10H, m, 5 × C*H*$_2$), 0.89 (3H, t, *J* 6.9, C*H*$_3$); **^{13}C NMR** (100 MHz, $CDCl_3$) δ_C: 155.3 (*C*=O), 135.4 (*C*(Ar)), 128.6, 128.5, 128.3, (3 × H*C*(Ar)), 69.4 (Ph*C*H$_2$OR), 68.3 (*C*H$_2$OR), 31.7, 29.2 (2 × *C*H$_2$), 29.1 (*C*H$_2$CH$_2$OR), 28.6, 25.7, 22.6 (3 × *C*H$_2$), 14.1 (*C*H$_3$). Data were consistent with those previously reported.[34]

Octan-1-ol **product 3**

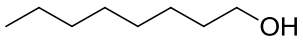

A solution of carbonate **3** (31.0 mg, 0.117 mmol) in ionic liquid (620 μL) was subjected to hydrogenolysis. The reaction mixture was purified by flash column chromatography [SiO_2, petrol/EtOAc, 19:1 to 9:1] to furnish alcohol **product 3** (13.0 mg, 85 %) as an oil.

^{1}H NMR (400 MHz, $CDCl_3$) δ_H: 3.59 (2H, q, *J* 5.4, C*H*$_2$OH), 1.53 (2H, quin, *J* 7.0, C*H*$_2$CH$_2$OH), 1.33-1.23 (11H, m, 5 × C*H*$_2$ + OH), 0.86 (3H, t, *J* 6.8, C*H*$_3$); **^{13}C NMR** (100 MHz, $CDCl_3$) δ_C: 62.8 (*C*H$_2$OH), 32.7, 31.8, 29.4, 29.3, 25.7, 22.6 (6 × *C*H$_2$), 14.0 (*C*H$_3$).

5.5.3 Copies of ^{1}H and ^{13}C NMR spectra

Reactant 1 (^{1}H)

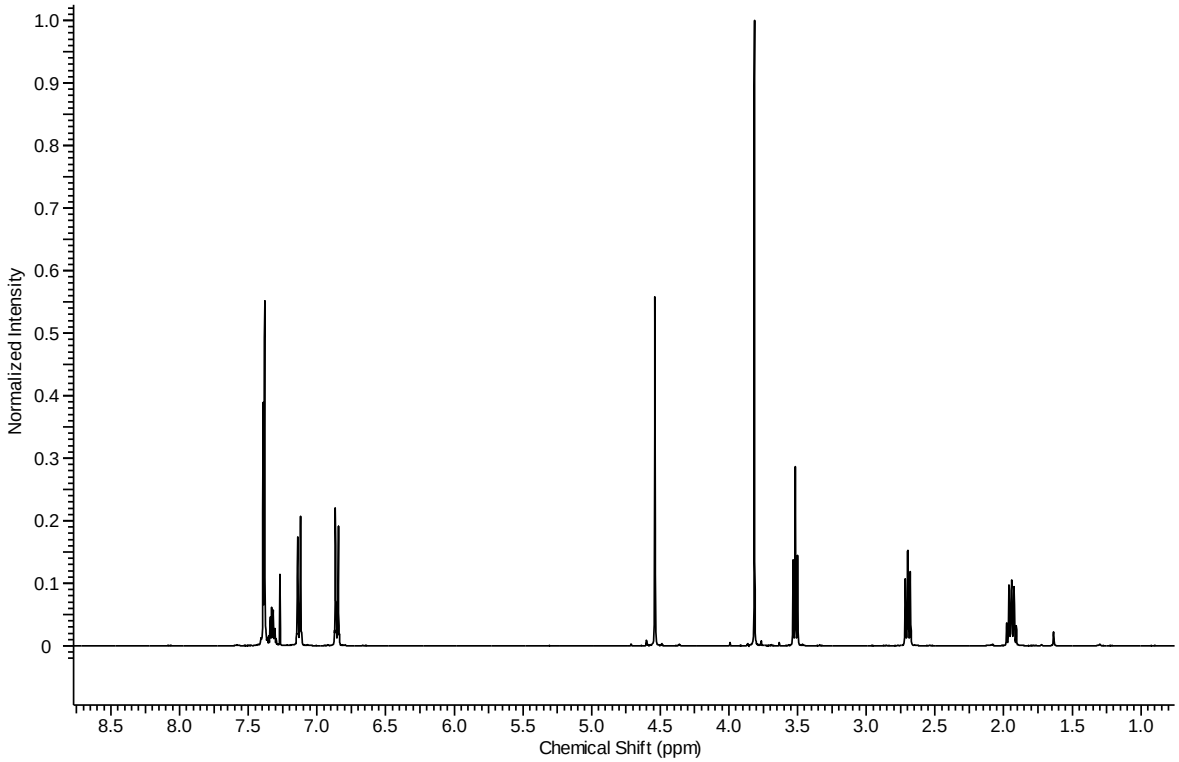

Reactant 1 (^{13}C)

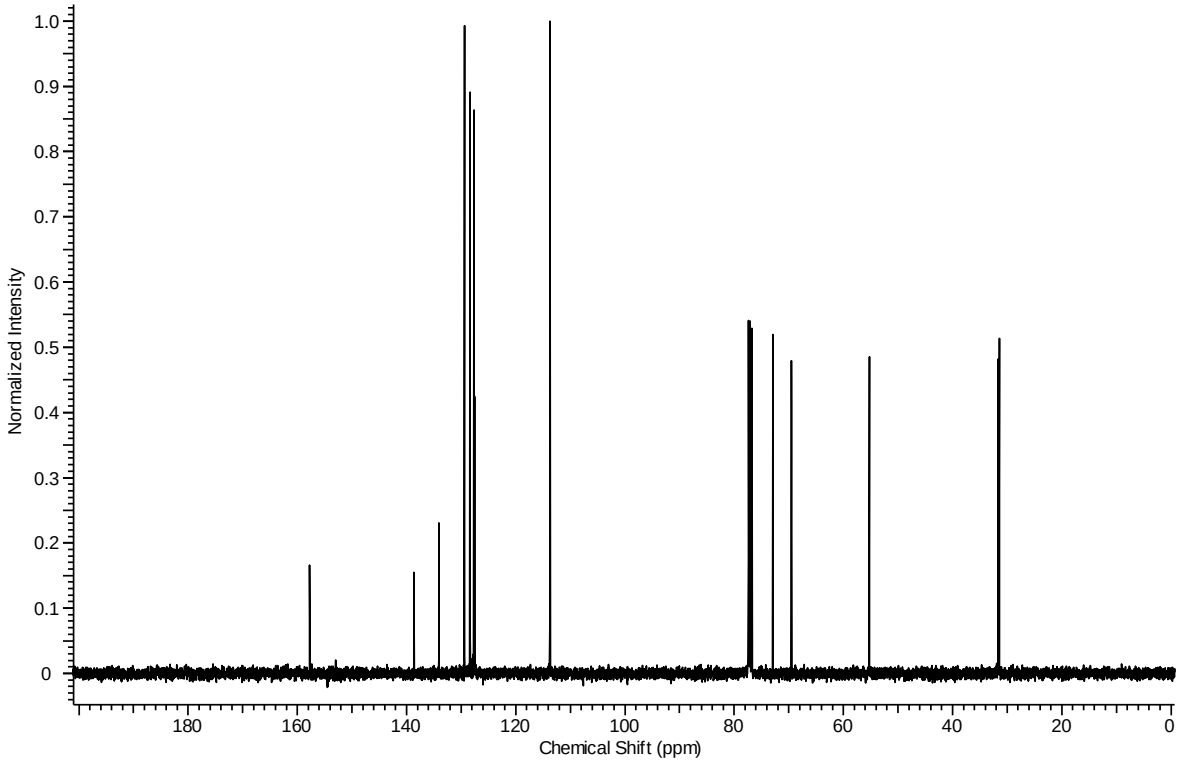

Product1 (^{1}H)

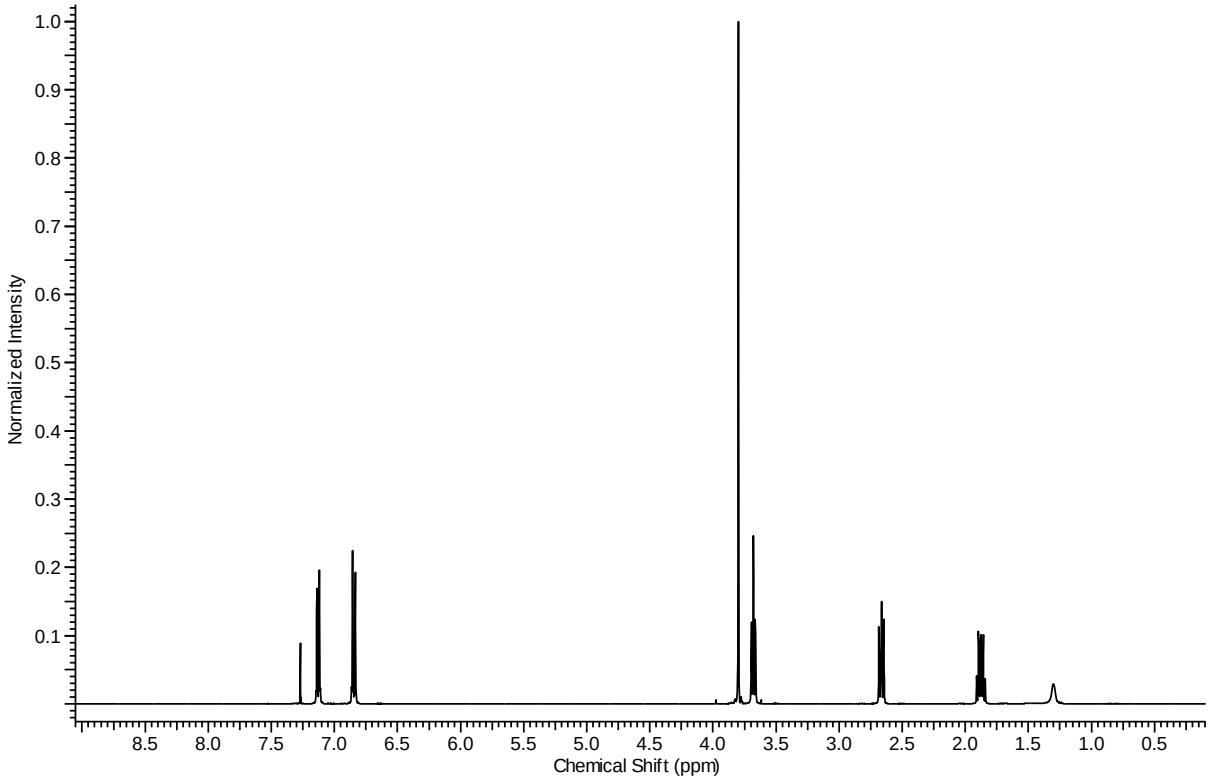

Product1 (^{13}C)

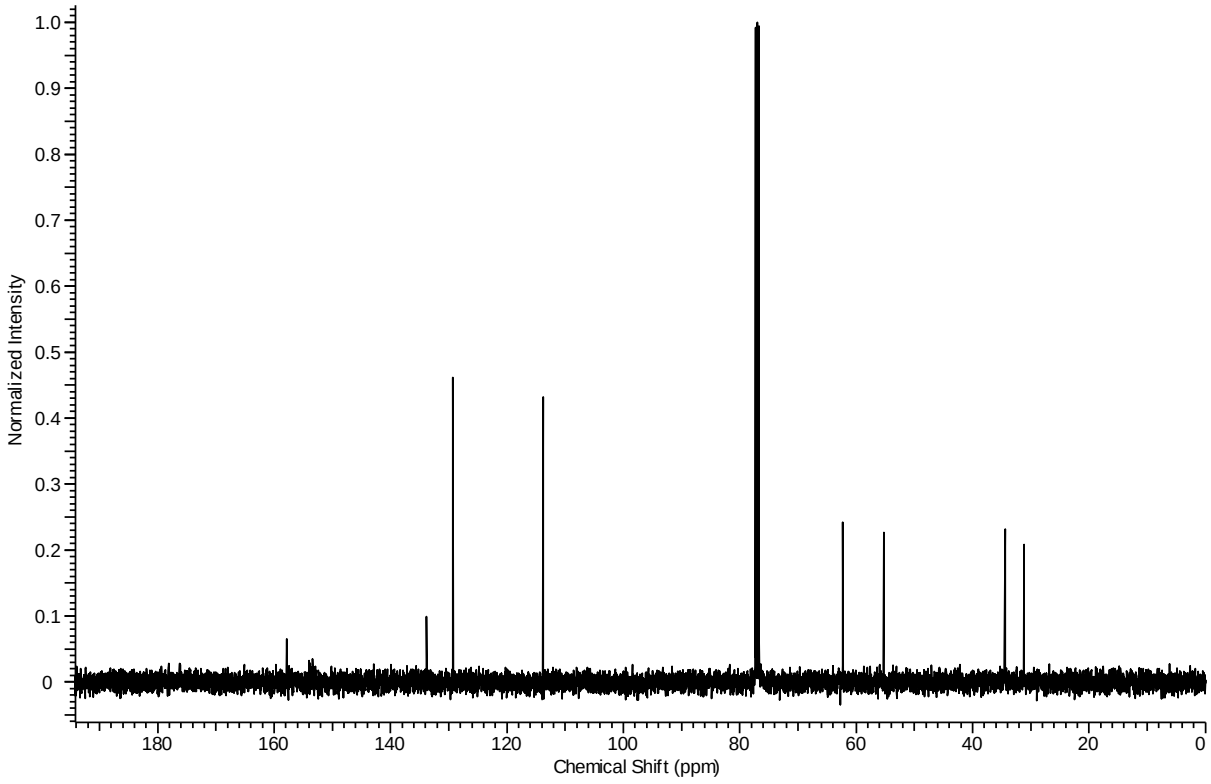

Reactant 3 (^{1}H)

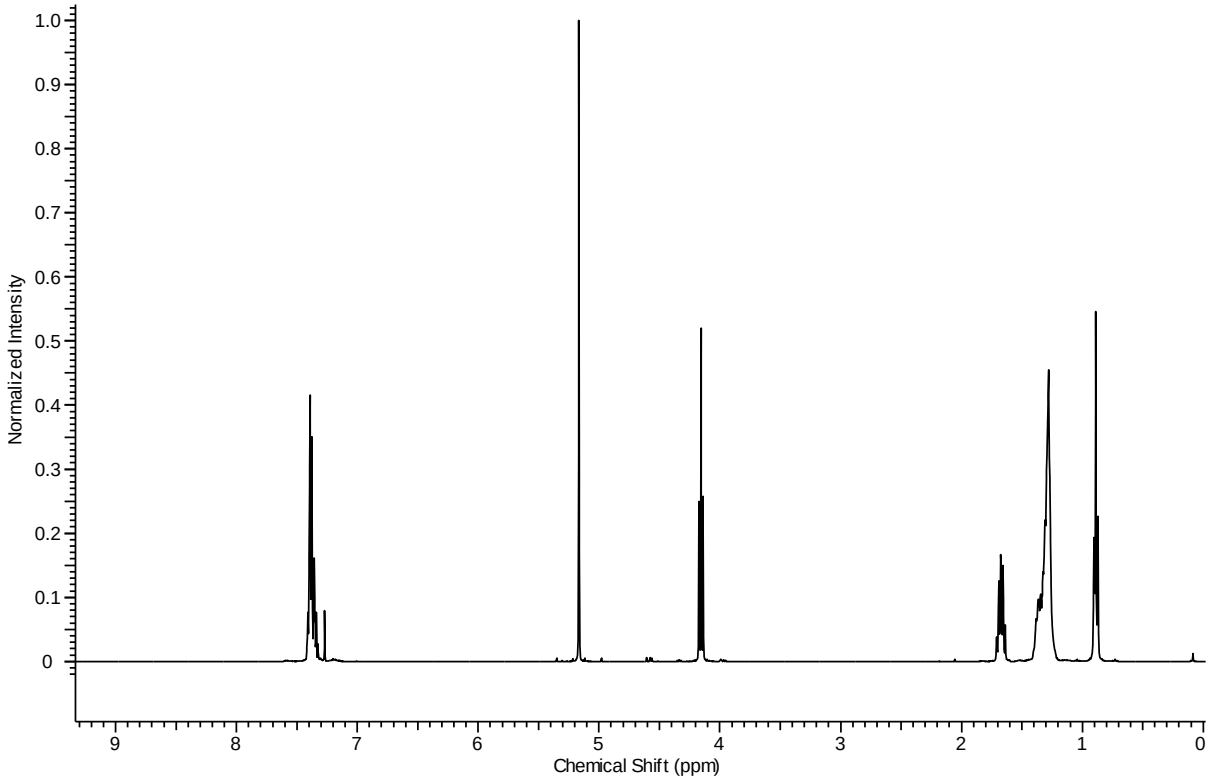

Reactant 3 (^{13}C)

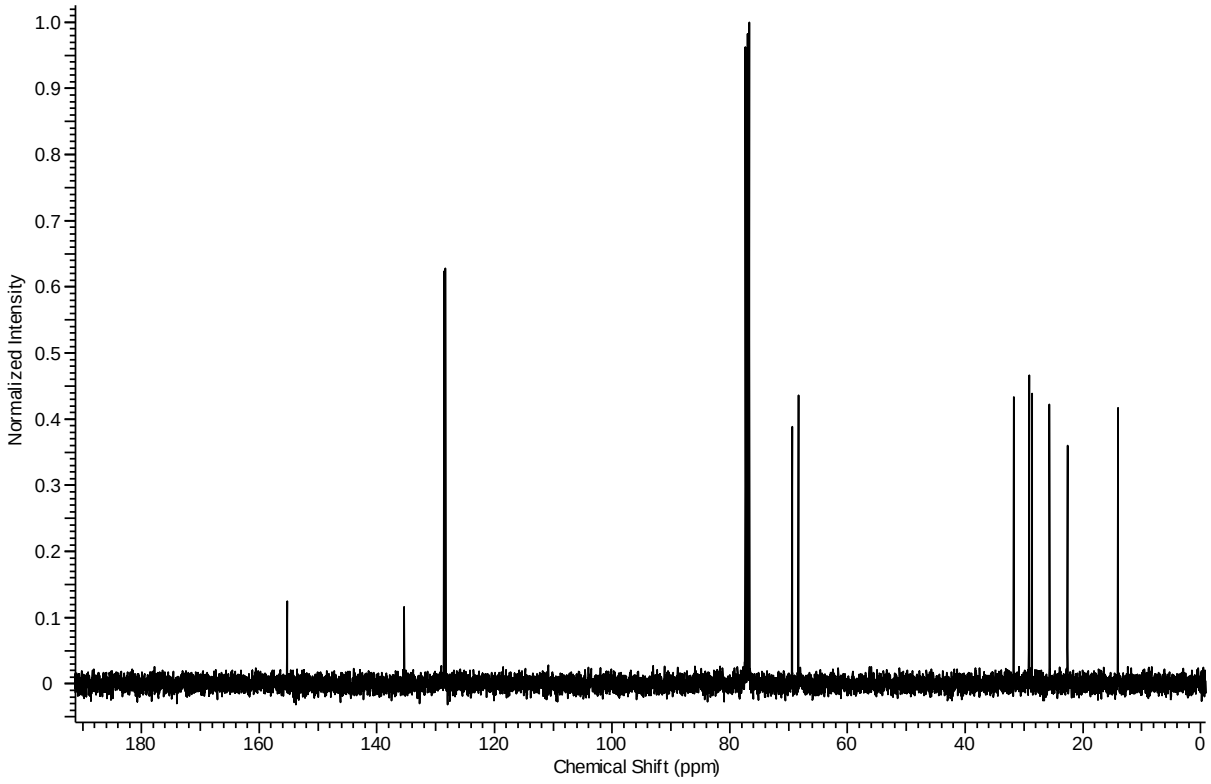

Product 3 (^{1}H)

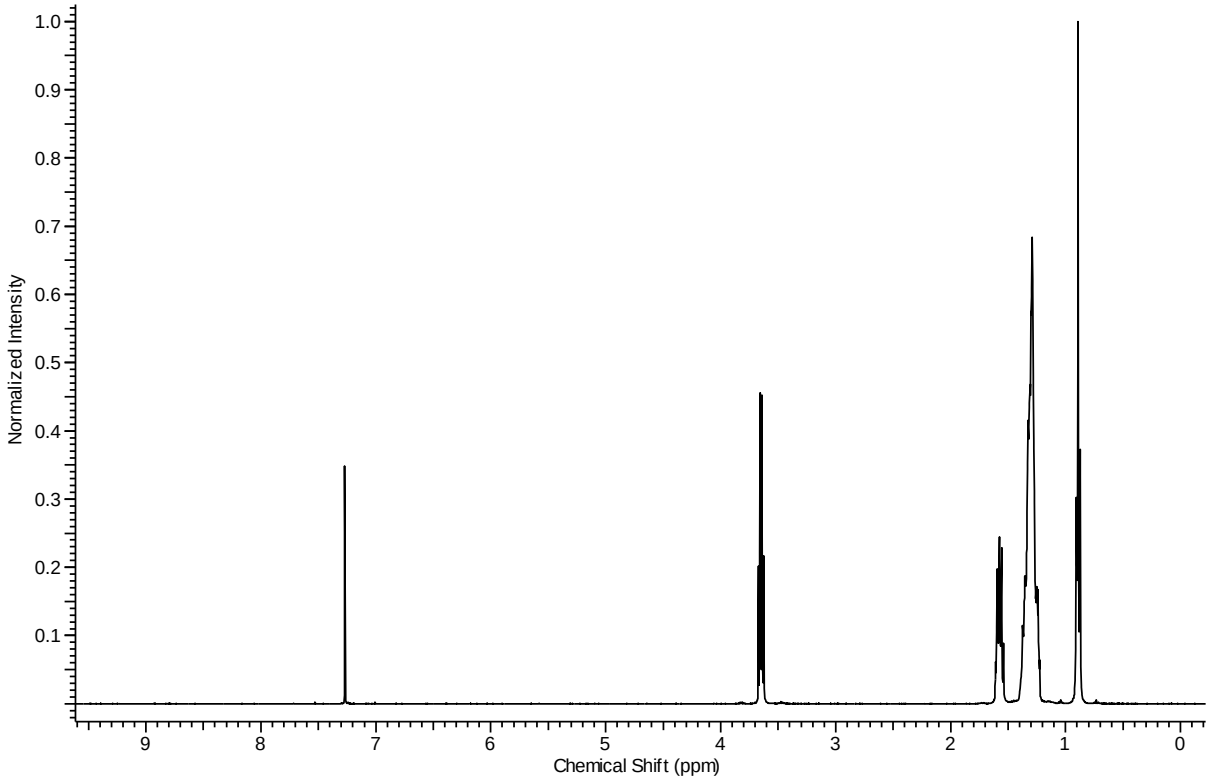

Product 3 (^{13}C)

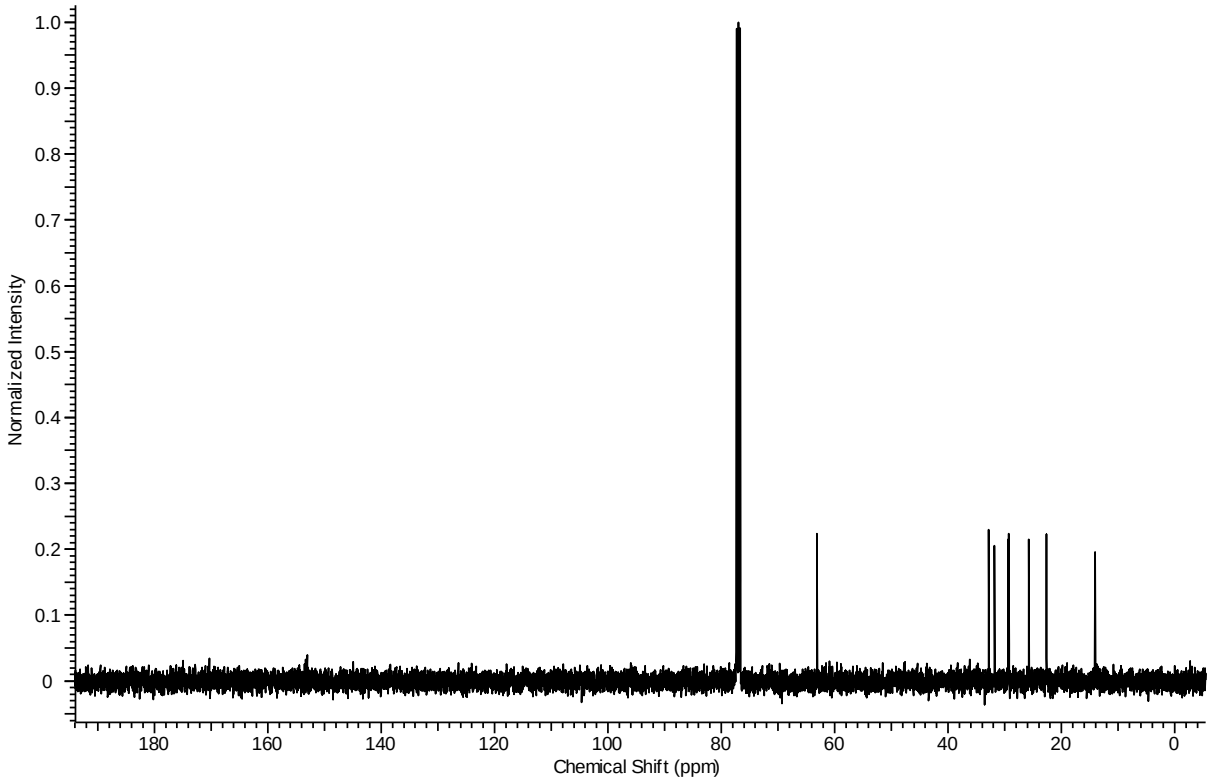

References

1. Y. Meng, L. Aldous, B. S. Pilgrim, T. J. Donohoe and R. G. Compton, New J. Chem, 2011, 35, 7, 1369-1375.
2. D. S. Silvester and R. G. Compton, *Z Phys Chem*, 2006, 220, 1247-1274.
3. J. M. S. S. Esperanca, J. N. C. Lopes, M. Tariq, L. M. N. B. F. Santos, J. W. Magee and L. P. N. Rebelo, *J Chem Eng Data*, 2010, 55, 3-12.
4. H. T. Liu, Y. Liu and J. H. Li, *Phys Chem Chem Phys*, 2010, 12, 1685-1697.
5. V. I. Parvulescu and C. Hardacre, *Chem Rev*, 2007, 107, 2615-2665.
6. C. Batchelor-McAuley, C. E. Banks, A. O. Simm, T. G. J. Jones and R. G. Compton, *Chemphyschem*, 2006, 7, 1081-1085.
7. J. Panchompoo, L. Aldous, L. Xiao and R. G. Compton, *Electroanal*, 2010, 22, 912-917.
8. M. Schelhaas and H. Waldmann, *Angewandte Chemie-International Edition in English*, 1996, 35, 2056-2083.
9. Y. Li, G. Manickam, A. Ghoshal and P. Subramaniam, *Synthetic Commun*, 2006, 36, 925-928.
10. D. S. Silvester, K. R. Ward, L. Aldous, C. Hardacre and R. G. Compton, *J Electroanal Chem*, 2008, 618, 53-60.
11. Y. Meng, L. Aldous and R. G. Compton, *Green Chem*, 2010, 12, 1926-1928.
12. S. Morton, "UK Surface Analysis Forum", to be found under http://www.uksaf.org/.
13. A. T. Masheter, L. Xiao, G. G. Wildgoose, A. Crossley, H. J. C. John and R. G. Compton, *J Mater Chem*, 2007, 17, 3515-3524.
14. J. Liu, A. G. Rinzler, H. J. Dai, J. H. Hafner, R. K. Bradley, P. J. Boul, A. Lu, T. Iverson, K. Shelimov, C. B. Huffman, F. Rodriguez-Macias, Y. S. Shon, T. R. Lee, D. T. Colbert and R. E. Smalley, *Science*, 1998, 280, 1253-1256.
15. D. J. Guo and H. L. Li, *J Colloid Interf Sci*, 2005, 286, 274-279.
16. G. P. Jin, R. Baron, N. V. Rees, L. Xiao and R. G. Compton, *New J Chem*, 2009, 33, 107-111.
17. R. G. Compton and C. E. Banks, *Understanding voltammetry, 2nd ed.*, World Scientific, Singapore, 2010.
18. L. Birry and A. Lasia, *Electrochim Acta*, 2006, 51, 3356-3364.
19. G. Denuault, C. Milhano and D. Pletcher, *Phys Chem Chem Phys*, 2005, 7, 3545-3551.
20. L. Aldous, D. S. Silvester, W. R. Pitner, R. G. Compton, M. C. Lagunas and C. Hardacre, *J Phys Chem C*, 2007, 111, 8496-8503.
21. D. S. Silvester, L. Aldous, C. Hardacre and R. G. Compton, *J Phys Chem B*, 2007, 111, 5000-5007.
22. A. M. O'Mahony, D. S. Silvester, L. Aldous, C. Hardacre and R. G. Compton, *J Chem Eng Data*, 2008, 53, 2884-2891.
23. R. Mihajlovic, Z. Simic, L. Mihajlovic, A. Jokic, M. Vukasinovic and N. Rakicevic, *Anal Chim Acta*, 1996, 318, 287-295.
24. A. Adrover, M. Giona, L. Capobianco and V. Violante, *J Alloy Compd*, 2004, 368, 287-297.
25. R. V. Bucur and I. Covaci, *Electrochim Acta*, 1985, 30, 1237-1241.

26. C. P. Chang, J. K. Wu, Y. D. Yao, C. W. Wang and E. K. Lin, *Int J Hydrogen Energ*, 1991, 16, 491-497.

27. J. G. Early, *Acta Metall Mater*, 1978, 26, 1215-1223.

28. P. Millet, C. Lebouin, C. Decaux, R. Ngameni, A. Ranjbari and M. Guymont, *Int J Hydrogen Energ*, 2009, 34, 4990-4996.

29. Y. Sakamoto, X. Q. Tong and F. A. Lewis, *Scripta Metall Mater*, 1991, 25, 1629-1634.

30. R. Mills and V. M. M. Lobo, *Self-diffusion in electrolyte solutions : a critical examination of data compiled from the literature*, Elsevier, Amsterdam, 1989.

31. Y. Yasui, Y. Kitazumi, H. Mizunuma, N. Nishi and T. Kakiuchi, *Electrochem Commun*, 2010, 12, 1479-1482.

32 R. H. Burnell, C. Côté and M, Girard, J. Nat. Prod., 1993, 56, 4, 461-472

33 B. S. Bodnar and P. F. Vogt, J. Org. Chem. 2009, 74, 6, 2598–2600

34 Tetrahedron, 1992, 48 (31), 6477-6484

Chapter 6 Electrochemistry of Hydrogen in the RTIL $[C_2mim][NTf_2]$: Dissolved Hydrogen 'Lubricates' Diffusional Transport

In this chapter, the electrochemical characterization of bis(trifluoromethylsulfonyl)imide ($H[NTf_2]$) and ferrocene in the Room Temperature Ionic Liquid (RTIL) 1-ethyl-3-methylimidazolium bis(trifluoromethylsulfonyl)imide ($[C_2mim][NTf_2]$) was undertaken in the presence of various concentrations of dissolved hydrogen (H_2). Chronoamperometric measurements in the presence of varying levels of H_2 were used to determine the diffusion coefficients of $H[NTf_2]$ and ferrocene at 298 K in $[C_2mim][NTf_2]$. Upon saturation with H_2 at 298 K these were found to increase from 2.5 (± 0.1) × 10^{-11} m^2 s^{-1} and 4.7 (± 0.1) × 10^{-11} m^2 s^{-1} to 2.8 (± 0.1) × 10^{-11} and 5.1 (± 0.1) × 10^{-11} m^2 s^{-1}, respectively. It is believed that the physicochemical changes correspond to the H_2 occupying the interstices and therefore resulting in a change in the permittivity of the space between ions of the RTIL, resulting in diminished Coulombic interactions and a net reduction in the RTIL viscosity. Even more significant changes were observed at 308 K, despite the saturated dissolved H_2 concentration being lower (4.4 mM H_2 at 298 K, 4.0 mM H_2 at 308 K). Arrhenius plots of the diffusion coefficient of ferrocene in the RTIL displayed a decrease in the diffusion activation energy from 29.5 kJ mol^{-1} in the absence of H_2 to 20.5 kJ mol^{-1} upon saturation with H_2. The activation energy of diffusion of H_2 was also determined in an RTIL for the first time (13.7 kJ mol^{-1}), and deviation of the mass transport of the small H_2 molecule from the Stokes-Einstein relationship was confirmed. This work presented in this chapter has been published in the Journal of Physical Chemistry C with the assistance of Dr. Leigh Aldous.[1]

6.1 Introduction

Room temperature ionic liquids (RTILs) are salts that characteristically possess high lattice enthalpies and relatively weak Coulombic interactions between bulky unsymmetrical cations and weakly coordinating inorganic anions, resulting in the liquid state being attained at room temperature and pressure.[2] Their low volatility[3] facilitates their recycle and minimises volatile organic pollution, leading to the term 'green solvents' in this respect.[4] Their wide electrochemical windows and unique ability to solvate and stabilise certain compounds presents numerous electrosynthetic opportunities.[5, 6] Large increases in reactivity and selectivity have been highlighted when moving to RTIL systems, as well as reactions unique to RTIL media.[7] Their low volatility over a large range of temperatures also makes them strong potential electrolytes for gas sensors, where traditional solvents in sensors are prone to dry out or to degrade over time.[8] RTILs have been successfully utilised as media for hydrogenation[7, 9] and hydrogenolysis[10, 11] reactions (see chapters 4 and 5).

Although van der Waals' forces and hydrogen bonding play a role in dictating the viscosity of ionic liquids, the most dominant effect is Coulombic interactions.[12, 13] As a result, RTILs typically possess viscosities which are two or three order of magnitude higher than traditional molecular solvents, and are typically in the range of *ca.* 20 - 7500 cP at ambient temperature.[6, 14, 15] The high viscosity of RTILs slows down the mass transport properties of electroactive species, and has a significant influence on the rate of diffusion controlled electrochemical reactions.[6] Coulombic interactions (*e.g.* with charged solutes) can also be significant.[6, 14] When studying cyclic voltammetry in RTILs, the high viscosity of the solvent must be taken into account, as it has significant consequences for interpreting voltammetric behaviour. This situation can be further complicated as the viscosity of RTILs are also highly influenced by the presence of other species, such as water and halides, even at low concentrations. [2, 6, 16, 17]

Barrosse-Antle has reported that dissolved sulphur dioxide, SO_2,[18] and carbon dioxide, CO_2,[19] to 1-ethyl-3-methylimidazlium bis(trifluoromethansulfonyl)imide ($[C_2mim][NTf_2]$) results in a significant change on the voltammetry of the ferrocene/ferrocenium redox couple. In both cases, the voltammery revealed an increase in the limiting current of the redox couple on increasing the concentration of dissolved gas; increases in the diffusion coefficients were quantified by chronoamperometry. These two gases, particularly SO_2, decrease the viscosity of the ionic liquid and increase both rotational and translational diffusion rates in the solution.[19-21] Changes in RTIL viscosity after being placed in contact with the gas hydrogen sulphide, H_2S, has also been noted.[22] Strong interactions such as ion-pairing between these solutes and the RTIL (particularly with the RTIL anions) are believed to result in a disruption of the long-range structure and introduce charge shielding, resulting in a net reduction in viscosity.[23-26]

The Stokes-Einstein equation predicts an inverse relationship between solute diffusion coefficients and solution viscosity; deviation from this relationship has been found in RTILs for solutes that are significantly smaller than the ions that compose the RTIL, such as H_2,[15] O_2 [27] and SO_2.[18]

A detailed, systematic investigation on the physiochemical influence of dissolved H_2 on the RTIL 1-ethyl-3-methylimidazolium bis(trifluoromethylsulfonyl)imide, $[C_2mim][NTf_2]$ is reported in this chapter. The significant influence of H_2 gas on the diffusion coefficient of dissolved protons and ferrocene, as well as its influence on the viscosity of the RTIL has been quantified. This study provides new insights into the solvation of H_2 in ionic liquids, as well as the corresponding changes that result in the structure of the ionic liquid itself. Confirmation of been provided for the non-Stokes Einstein transport behaviour of H_2 in RTILs, and the activation energy of diffusion of H_2 has also been quantified in an RTIL for the first time.

6.2 Results and Discussion

6.2.1 Electrochemical behaviour of $H[NTf_2]$ in $[C_2mim][NTf_2]$ in the presence and absence of hydrogen

Figure 6.1 displays the reduction of 100 mM $H[NTf_2]$ at an Au microelectrode (diameter 9.2 µm) in $[C_2mim][NTf_2]$ at a scan rate of 100 mV s^{-1} at 298 K. This voltammetry was recorded under vacuum, in order to remove the influences of other solutes such as O_2, CO_2 and H_2O.[14, 28] A reduction feature is clearly observed from *ca.* -1.0 V *vs.* Pt, corresponding to the reduction of $H[NTf_2]$ to form H_2.[29, 30] On the reverse sweep the oxidation of H_2 was not observed at any potential in the electrochemical window of the RTIL (as apparent in the inset in Figure 6.1). At high anodic potentials some evidence of Au oxidation was observed overlapping with the breakdown of the RTIL, as previously noted at bulk Au electrodes in the presence of $H[NTf_2]$ in $[C_4mim][NTf_2]$.[30] Au is known to be relatively inactive with respect to the electro-oxidation of H_2.[31]

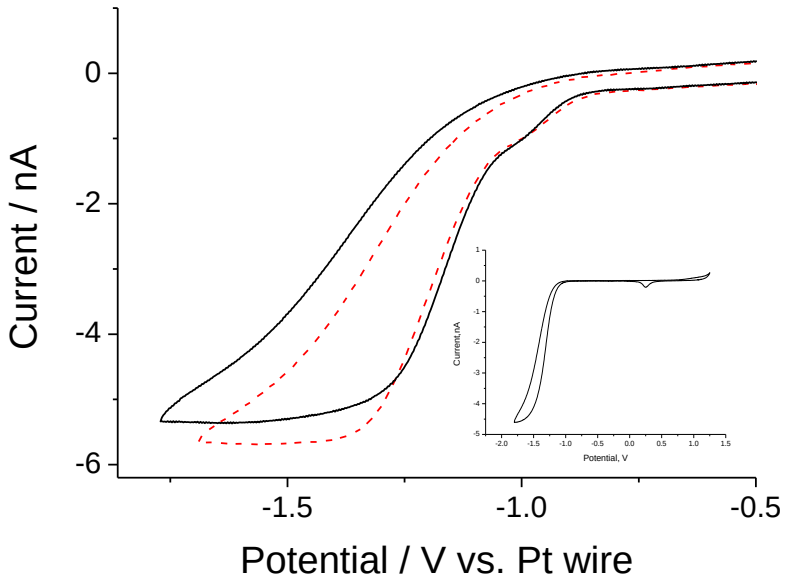

Figure 6.1 Cyclic voltammetry for the reduction of *ca.* 100 mM $H[NTf_2]$ on an Au microelectrode (diameter 9.2 µm) in $[C_2mim][NTf_2]$ at a scan rate of 100 mV s^{-1} at 298 K, under vacuum (solid line) and after being saturated with H_2 (---). The inset is a cyclic voltammogram recorded between -1.6 V and +1.25 V.

Chronoamperometric transients were recorded for the reduction of 100 mM H[NTf_2] in [C_2mim][NTf_2] at an Au microelectrode under 298 K. The potential was stepped from 0 V (no Faradaic current passed) to -1.75 V *vs.* Pt (diffusion-limited reduction), and the corresponding transient simulated using the Shoup and Szabo equation.[32, 33] The diffusion coefficient of H[NTf_2] in [C_2mim][NTf_2] was calculated to be 2.5 (± 0.1) × 10^{-11} m^2 s^{-1}, which is in good agreement with the previous literature value.[15] The product of the concentration and number of electrons passed (*nc* value) indicated a one electron process, namely

$$2\mathrm{H}[\mathrm{NTf_2}] + 2e^- \rightleftharpoons H_2 + 2[NTf_2]^- \qquad (6.1)$$

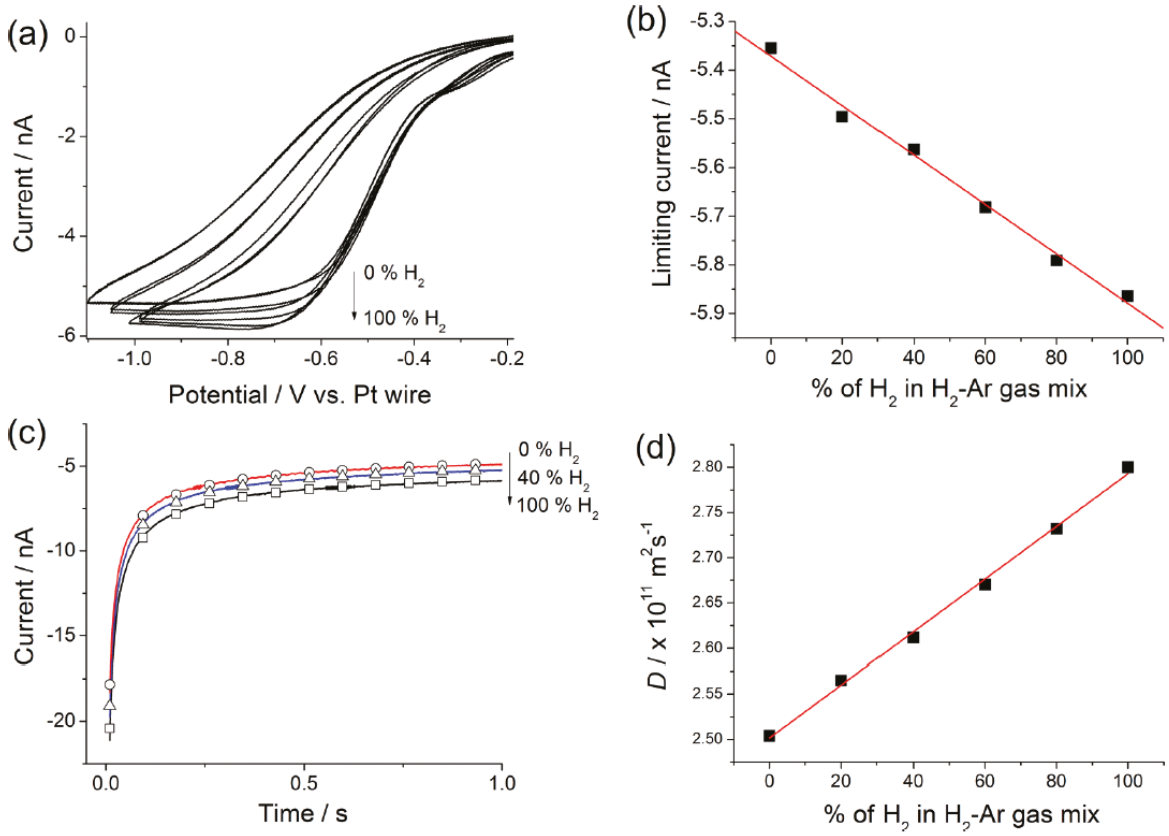

Figure 6.2. (a) Cyclic voltammetry for the reduction of ca. 100 mMH[NTf_2] on a Au microelectrode (diameter 9.2 μm) in [C_2mim][NTf_2] at a scan rate of 100 mV s^{-1} at 298 K, in the presence of increasing v/v % H_2 (0, 20, 40, 60, 80 and 100% H_2 in an Ar / H_2 mixture), (b) plot of the limiting current of reduction wave versusH_2 proportion, (c) experimental chronoamperometry (solid) and Shoup-Szabo fitting (symbols) at 0, 40, and 100% H_2, and (d) plot of the diffusion coefficient of H[NTf_2] in [C_2mim][NTf_2] versus H_2 proportion.

Solutions containing both acidic protons and hydrogen (H_2) are of significant fundamental interest with regards to the development of hydrogen-based reference scales in RTILs. After analysing the sample *in vacuo*, the vacuum was broken with a constant stream of dry hydrogen (H_2) and the gas was flowed for at least 30 min in order to equilibrate the system. After equilibration a 9.6% increase in the reduction wave of H[NTf_2] was noted (dashed line in Figure 6.1). A minor shift in the reduction potential was also observed, although this is attributed to a shift in the potential of platinum *quasi*-reference electrode. The change upon addition of H_2 was seen to be reversible, *e.g.* if the H_2-saturated RTIL was put under vacuum, the limiting current rapidly returned to its original value.

If the experiment was repeated except dry argon (Ar) introduced to the cell instead of H_2 gas then no related increase in the reduction wave was observed. Thus the change was specifically related to the addition of dry H_2 to the system (and not for example moisture contamination)[28]. Ar gas was also used to dilute the H_2 in order to better characterize the effect of the H_2 gas concentration on the observed voltammetry in RTIL. Figure 6.2(a) shows cyclic voltammetry for the reduction of *ca.* 100 mM H[NTf_2] on an Au microelectrode (diameter 9.2 μm) in [C_2mim][NTf_2] at a scan rate of 100 mV s^{-1} at 298 K, in the presence of increasing volume percentages of H_2 (0, 20, 40, 60, 80 and 100% v/v H_2 in a H_2 / Ar gas mixture). The limiting current increased with H_2 concentration, as shown by Figure 6.2(b).

Chronoamperometric transients were measured on the reduction wave in order to obtain the diffusion coefficient of each species in the presence of varying concentrations of H_2 in Ar. The potential was stepped from 0 V to a potential corresponding to the steady state current, and the current transient was recorded for 2 s. The transients were analysed using the Shoup and Szabo equation (Figure 6.2(c)),[33] and it was found that the diffusion coefficient of H[NTf_2] in [C_2mim][NTf_2] increased in a linear manner with the increasing proportion of H_2 in the gas flow.(Figure 6.2(d)) The diffusion coefficient of H[NTf_2] was found to increase

from 2.5 (± 0.1) × 10^{-11} m^2 s^{-1} (RTIL *in vacuo*) to 2.8 (± 0.1) × 10^{-11} m^2 s^{-1} (H_2-saturated RTIL), consistent with the observed voltammetry.

The Stokes-Einstein equation highlights the influence of viscosity on the diffusion coefficient of solutes, which can be applied qualitatively to many RTIL systems.[14] The increase in limiting current and diffusion coefficient suggests the addition of H_2 caused a physical change in the RTIL, thus decreasing the viscosity of RTIL. Similar changes upon the dissolution of other gases, such as CO_2 and SO_2, have been reported in the literature.[19, 21-26] In these cases interaction with the anion was dominant, for example SO_2 dissolved in [C_4mim]Br encouraged formation of short-range [C_4mim]Br-SO_2 ion pairs while disrupting long range ionic interactions, producing a 'charge screening' effect which resulted in a significant decrease in viscosity.[24]

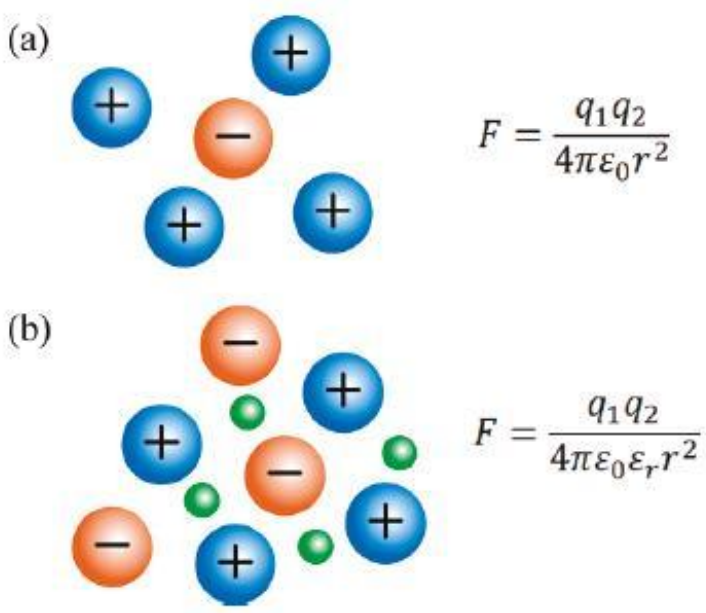

Figure 6.3. Cartoon depicting the relative molecular environments in (a) pure [C_2mim][NTf_2] and (b) [C_2mim][NTf_2] saturated with H_2. Also shown are the corresponding equations expressing Coulomb's Law for the Coulombic interactions, F, between (a) ionic species, and (b) ionic species separated by H_2 molecules.

Unlike the other gases previously noted, H_2 is a non-polar, non-ionic molecule and no strong interactions between H_2 and either the anion or cation are to be expected. In conventional RTILs the anion[34] is typically observed to be more significant in dictating dissolve gas saturation values than the cation,[35] although H_2 solubility has been observed to vary as a function of both RTIL anion and cation.[15, 34] Therefore in the case of H_2-saturated $[C_2mim][NTf_2]$ it is likely that dissolved H_2 resides within the holes or interstices of the RTIL, and the presence of H_2 can be seen as 'lubricating' transport within the RTIL by a change in permittivity. Figure 6.3 displays a simplified cartoon demonstrating (a) the environment in the RTIL *in vacuo*, and (b) after being saturated with H_2. Coulombic interactions can be calculated using Coulomb's Law, and the relevant equations have been included in the Figure. The presence of H_2 molecules are expected to weaken the Coulombic interactions between adjacent charged species due to the H_2 molecules higher relative permittivity (ε_r) with respect to the vacuum permittivity (ε_0), producing a net reduction in RTIL viscosity, as demonstrated by enhanced mass transport of $H[NTf_2]$.

6.2.2 The influence of temperature

The electrochemistry of $H[NTf_2]$ in the presence of H_2 was investigated after increasing the temperature of the system from 298 K to 308 K, using a temperature-controlled Faraday cage accurate to within ± 0.1 K.[36] The resulting voltammetry is shown in Figure 6.4(a), which displays the reduction of *ca.* 100 mM $H[NTf_2]$ on an Au microelectrode (diameter 9.2 μm) in $[C_2mim][NTf_2]$ at a scan rate of 100 mV s^{-1}, in the presence of increasing v/v % of H_2 (0, 25, 50, 75 and 100 % H_2 in H_2 / Ar gas mixture). As observed at 298 K, the limiting current increased as the percentage of H_2 increased. (Figure 6.4(b))

Potential step measurements were used to calculate the value of the diffusion coefficient of $H[NTf_2]$, as shown in Figure 6.4(c). RTIL viscosity drops rapidly with increasing temperature,

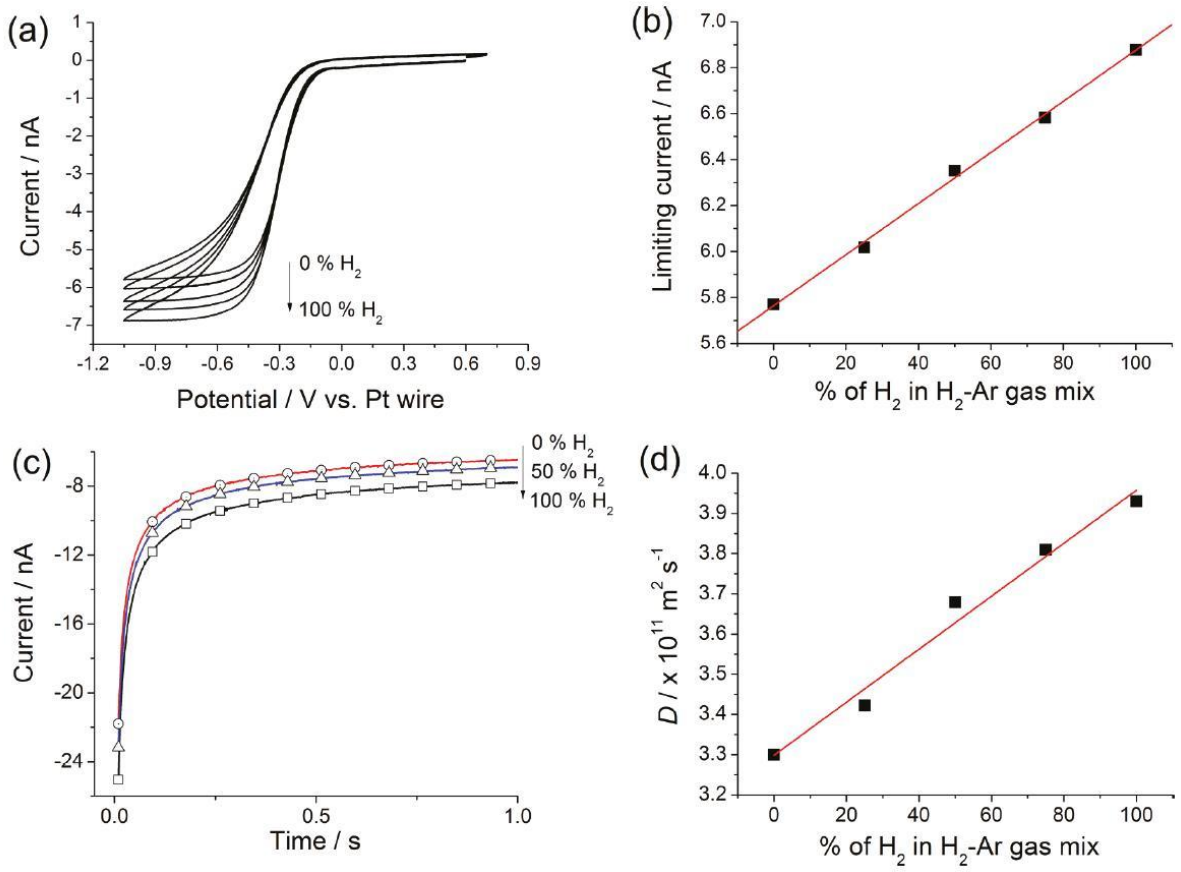

Figure 6.4. (a) Cyclic voltammetry for the reduction of ca. 100 mMH[NTf_2] on a Au microelectrode (diameter 9.2 μm) in [C_2mim][NTf_2] at a scan rate of 100 mV s^{-1} at 308 K, in the presence of increasing v/v % H_2 (0, 20, 40, 60, 80 and 100% H_2 in an Ar / H_2 mixture), (b) plot of the limiting current of reduction wave versusH_2 proportion, (c) experimental chronoamperometry (solid) and Shoup-Szabo fitting (symbols) at 0, 50, and 100% H_2, and (d) plot of the diffusion coefficient of H[NTf_2] in [C_2mim][NTf_2] versus H_2 proportion.

and the diffusion coefficient of H[NTf_2] in [C_2mim][NTf_2] correspondingly increased from 2.5 (± 0.1) × 10^{-11} m^2 s^{-1} (298 K, under Ar) to 3.3 (± 0.1) × 10^{-11} m^2 s^{-1} (308 K, under Ar). A linear relationship between the diffusion coefficient and the proportion of H_2 in Ar was also found and is shown in Figure 6.4(d). When 100% H_2 was added to the T-cell, the value reached to 3.96 (± 0.1) × 10^{-11} m^2 s^{-1}, an approximately 20 % increase from the original value, compared to a 12 % increase at 298 K. This highlights that the influence of dissolved H_2 on RTIL viscosity is more significant at elevated temperatures, despite the dissolved H_2 concentration decreasing with increasing temperature, *e.g.* the dissolved H_2 concentration in

$[C_2mim][NTf_2]$ at 1 bar has been reported as *ca.* 7.6 mM at 293.4 K and *ca.* 6.7 mM at 303.4 K.[35] This result is of particular significance with respect to mass-transport controlled catalytic hydrogenation reactions, where the elevated pressure and temperature conditions frequently encountered are likely to result in a significant decrease in viscosity and significant increase in mass transport of reactants, compared to that expected (*i.e.* if the physiochemical influence of dissolved H_2 is not considered).

6.2.3 Voltammetry of Ferrocene in $[C_2mim][NTf_2]$ in the presence of H_2 at an Au microelectrode

To support the assumption that a physical change occurs in the RTIL rather than any chemical interaction with $H[NTf_2]$, 30 mM ferrocene was studied in $[C_2mim][NTf_2]$ instead of $H[NTf_2]$. The corresponding oxidation peak can be seen in Figure 6.5. Saturating the system with 100 % Ar or 100 % H_2 resulted in a 0.7 % decrease and 10.2 % increase of limiting current, respectively. The 10.2 % increase upon H_2 addition mirrors the 12 %

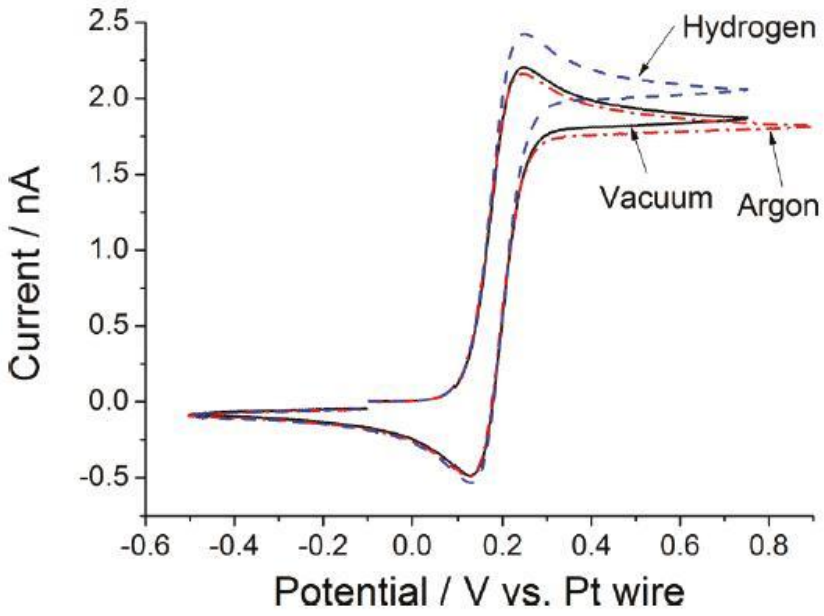

Figure 6.5 Oxidation of 30 mM Ferrocene on an Au microelectrode (diameter 9.2 µm) in $[C_2mim][NTf_2]$ at a scan rate of 100 mV s^{-1} at 298 K under vacuum (**—**), in the presence of H_2 (---) and Ar (**….**)

Table 6.1 Solubility of various gases in $[C_2mim][NTf_2]$ and diffusion coefficient of ferrocene in gas-saturated $[C_2mim][NTf_2]$ at 298 K.

Gas	Solubility of gas / mM	D_{Fc} / $\times 10^{11}$ m^2 s^{-1}
Vacuum	n/a	4.65 (± 0.1)
H_2	4.43	5.1 (± 0.1)
CO_2	90-100	6.0 (± 0.2)
SO_2	230	16 (± 1.0)

increase in diffusion coefficient of $H[NTf_2]$ under the same conditions, highlighting that this phenomena is generally independent of the diffusing species. Table 6.1 summarizes the diffusion coefficient of ferrocene in $[C_2mim][NTf_2]$ when equilibrated with various gases at 1 bar, including the saturated dissolved gas concentration. Correlation is observed between the diffusion coefficient of ferrocene and the concentration of dissolved gas, as could be expected based upon the assumption that all gases increase the diffusion coefficient of ferrocene by participating in charge screening within the RTIL.[24]

6.2.4. Quantification of the activation energy of diffusion of ferrocene in the presence of hydrogen

A heated Faraday cage was applied to vary the temperature of the system in order to study ferrocene in $[C_2mim][NTf_2]$ between 293 and 321 K. The inset of Figure 6.6(a) displays the relative change in voltammetry over the range of temperatures. Chronoamperometry was also recorded as a function of temperature, in order to quantify the diffusion coefficient of ferrocene (inset of Figure 6.6(b)); this could not be achieved by monitoring the limiting current obtained from the steady-state waves obtained in the cyclic voltammetry, due to the volatilisation of ferrocene from the system during the time required for thermal equilibration of the system (*ca.* 1 hr). The volatilisation of ferrocene from this RTIL has recently been described in detail.[37, 38] Chronoamperometry was used to simultaneously obtain the diffusion

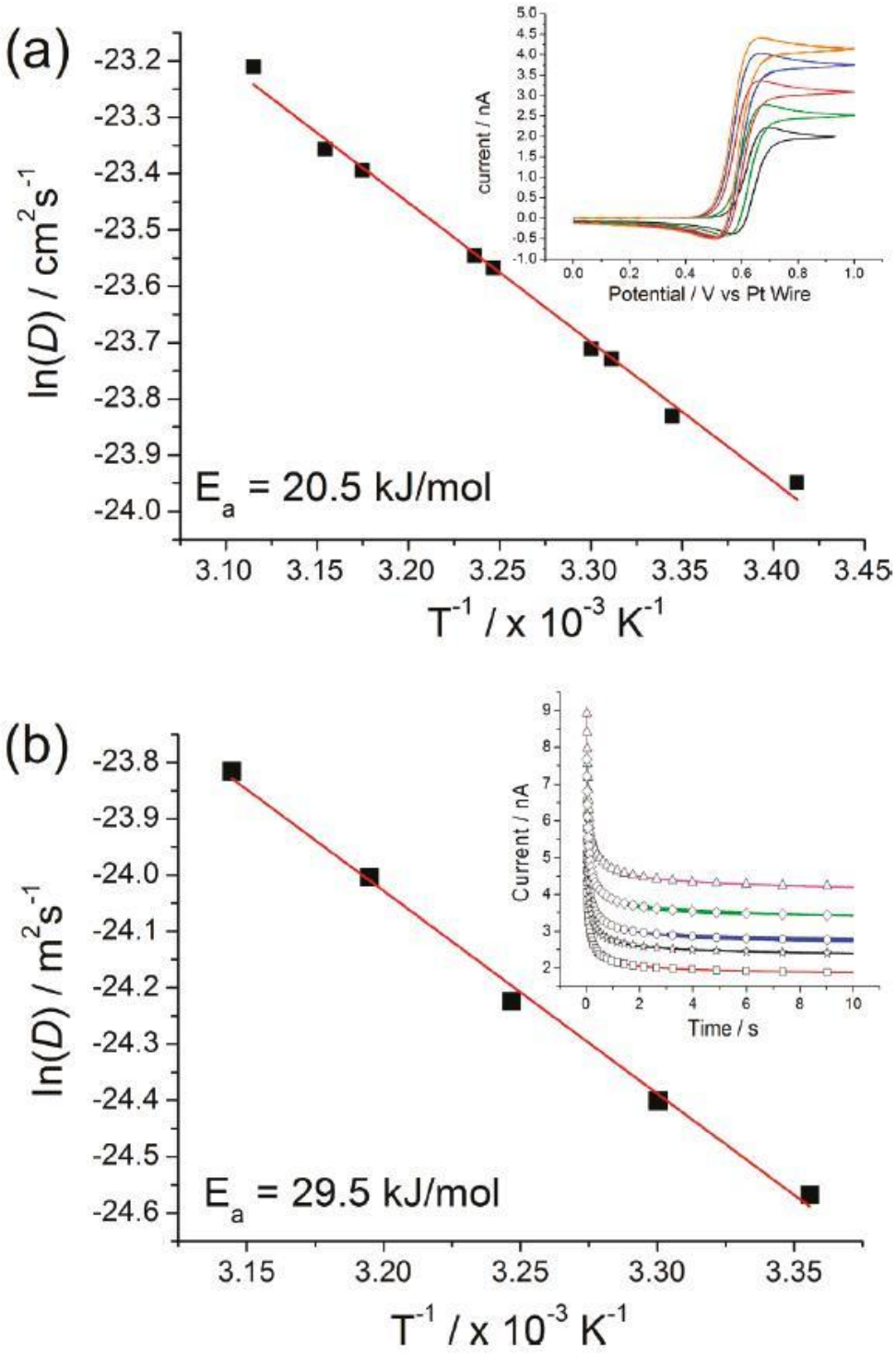

Figure 6.6. (a) Arrhenius plot obtained by measuring the diffusion coefficient of ferrocene at a range of temperature (293-321 K) using chronoamperometry in H_2-saturated $[C_2mim][NTf_2]$. Inset is the corresponding voltammetry of ferrocene under the same conditions. (b) Arrhenius plot obtained by measuring the diffusion coefficient of ferrocene at a range of temperature (298-318 K) using chronoamperometry in $[C_2mim][NTf_2]$ under vacuum. Inset is the corresponding experimental chronoamperometry (solid) and Shoup-Szabo fitting (symbols) under the same conditions.

coefficient, *D*, and concentration, *c*, and the resulting Arrhenius plot of ln(*D*) and 1/*T* is shown in Figure 6.6(a), corresponding to a diffusion activation energy of ferrocene of 20.5 ± 0.6 kJ mol^{-1} in $[C_2mim][NTf_2]$ in the presence of H_2. Figure 6.6(b) displays a similar plot for data obtained *in vacuo* between 298 and 318 K for ferrocene in $[C_2mim][NTf_2]$. The corresponding diffusion activation energy of ferrocene was calculated to be 29.5 ± 1.0 kJ mol^{-1}, in excellent agreement with the previous literature values of 28.2 ± 0.7 kJ mol^{-1} [37] and 29.0 ± 0.5 kJ mol^{-1} [21] obtained in the same RTIL.

As ferrocene is known to follow the Stokes-Einstein relation in conventional RTILs[14, 39] the decrease in the activation energy of diffusion for ferrocene upon introduction of H_2 indicates a significant decrease in the activation energy of viscosity occurred relative to that of the pure RTIL (24.9 kJ mol^{-1} [39]).

6.2.5 Voltammetry of hydrogen on a Pt microelectrode as a function of temperature

Silvester *et al.* previously investigated the oxidation of H_2 at 298 K in ten H_2-saturated RTILs.[15, 29] Chronoamperometry allowed the quantification of the diffusion coefficient of dissolved H_2, and a plot of the diffusion coefficient *vs.* literature values for the viscosity of the pure RTILs did not display an obvious linear relationship, *i.e.* diffusion of H_2 was independent of the (pure) solvent viscosity, and therefore deviated from the Stokes-Einstein equation.[15] Fukuta et *al.* have also reported an electrochemical investigation using three H_2-saturated RTILs and reported similar observation.[40] However, the results presented herein have demonstrated that the presence of H_2 dissolved in $[C_2mim][NTf_2]$ changes the viscosity of the RTIL relative to its viscosity when pure. The diffusion of H_2 in $[C_2mim][NTf_2]$ was therefore investigated with reference to a suitable probe molecule (in this case ferrocene) in H_2-saturated $[C_2mim][NTf_2]$ in order to evaluate the prior preliminary observation of non-Stokes Einstein transport behaviour of H_2 by Silvester *et al.*[15] and Fukuta et *al.*[40]

The analysis of ferrocene could be conducted in the presence of H_2 by virtue of the poor electrocatalytic ability of Au with respect to H_2 oxidation. Alternatively, platinum (Pt) is an excellent substrate for the electrocatalytic oxidation of H_2.[15, 29, 41] However, due to blocking or adsorptive effects, activation is required in order to obtain reproducible results.[15, 29, 41] Figure 6.7(a) displays scans recorded for the oxidation of H_2 in H_2-saturated $[C_2mim][NTf_2]$ at a Pt microelectrode in the temperature range 294 to 308 K. On the forward sweep a poorly resolved wave was observed before current dropped nearly to zero, corresponding to adsorptive blocking of the Pt surface followed by Pt oxide formation.[41] On the reverse sweep the Pt oxide is reduced, a pristine Pt surface is generated, and a significantly more resolved H_2 oxidative wave was observed.[15, 29, 41] The voltammetry at this 'activated' Pt surface is now representative of the dissolved H_2 concentration.[41]

Chronoamperometry was performed as a function of temperature using an 'activated' Pt microelectrode (by oxidising for 10 s, as described in detail in references[15, 29]) in order to determine the diffusion coefficient, *D*, of H_2 and is shown in Figure 6.7 (b). The obtained concentration c and *D* values as a function of temperature are shown in Table 6.2. The c was found to decrease with temperature, contrary to the observations of Fukuta et al.,[40] but in agreement with the observations of Jacquemin et al.[35] as well as the generally observed trends for other dissolved gases in RTILs.[34, 35] The c of H_2 in $[C_2mim][NTf_2]$ at 298 K was 4.43 mM, similar to the literature values (4.2,[15] 5.5,[40] and ca. 7.2[35] mM) reported for the same RTIL. An Arrhenius plot of ln(*D*) *vs*. 1/*T* (Figure 6.7(c)) was generated which gave the diffusion activation energy of H_2 as 13.7 ± 0.3 kJ mol^{-1} in H_2-saturated $[C_2mim][NTf_2]$. This value is significantly lower than the activation energy of diffusion for ferrocene (20.5 kJ mol^{-1}) under the same conditions.

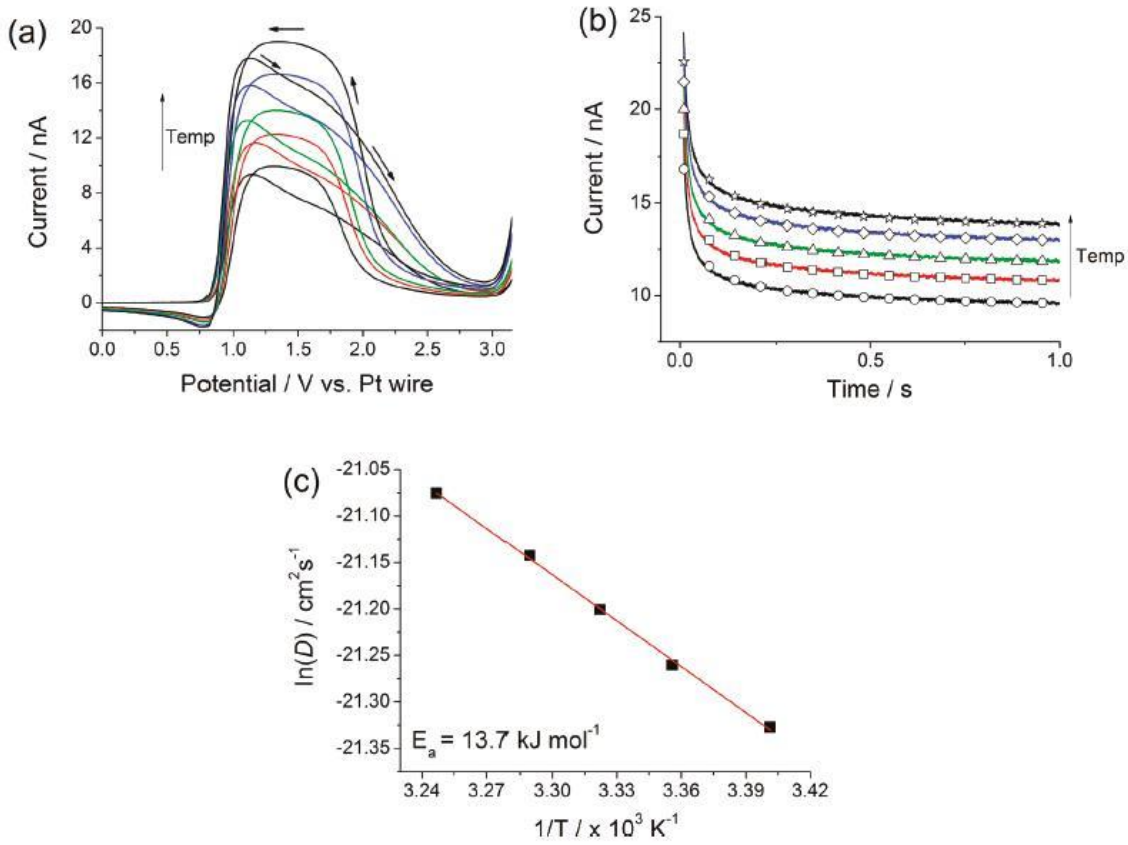

Figure 6.7. (a) Cyclic voltammetry for the oxidation of H_2 in H_2-saturated [C_2mim][NTf_2] at a Pt microelectrode (radius 5.2 μm) and 100 mV s^{-1} in the temperature range 298-318 K, (b) the corresponding experimental chronoamperometry (solid) and Shoup-Szabo fitting (symbols) under the same conditions, and (c) Arrhenius plot obtained by measuring the diffusion coefficient of H_2 by chronoamperometry in the temperature range 294-308 K.

Table 2 Concentration and diffusion coefficient of dissolved H_2 in H_2-saturated [C_2mim][NTf_2], obtained as a function of temperature by chronoamperometry.

Temperature / (± 0.1) K	Concentration of H_2 / (± 0.05) mM	D_{H^+} / (± 0.1) ×10^{10} m^2 s^{-1}
294.1	4.53	5.5
298.1	4.43	5.9
301.1	4.25	6.2
304.1	4.13	6.6
308.1	3.99	7.0

Given that ferrocene can be considered a reasonable measure of Stokes-Einstein type diffusion, the significant difference in activation energies between ferrocene and H_2 supports the preliminary claim [15] that H_2 deviates from the Stokes-Einstein relationship in RTILs. The small size of the dissolved H_2 molecules results in H_2 occupying the holes in the RTILs, with the result that (i) the H_2 molecule deviates from the Stokes-Einstein equation and experiences rapid and facile diffusion, and (ii) Coulombic interactions are decreased to some extent, decreasing viscosity and facilitating diffusion of other solutes. Therefore H_2 possesses a diffusion coefficient in RTILs which is a factor of ten faster than conventional solutes (such as H^+ and ferrocene), while also accelerating mass transport of other solutes by up to 20 % under standard conditions (with even more drastic changes anticipated at elevated temperature and pressures). This must therefore be considered in fundamental thermodynamic and physiochemical investigations, (electrochemical) gas sensors based upon RTILs and during kinetic analysis of the many chemical reactions that utilise H_2 gas.[7]

6.3 Conclusions

It has been demonstrated that when the RTIL $[C_2mim][NTf_2]$ is saturated with H_2 there is a significant decrease in the viscosity of the solution. This results in an increase in the diffusivity of the solutes $H[NTf_2]$ and ferrocene, as characterised by increases in their diffusion coefficients and a decrease in the activation energy of diffusion (E_a for ferrocene = 29.5 ± 1.0 kJ mol^{-1} in $[C_2mim][NTf_2]$ under vacuum, E_a = 20.5 ± 0.6 kJ mol^{-1} in H_2-saturated $[C_2mim][NTf_2]$). This effect is more pronounced at elevated temperatures. The diffusion of H_2 was also analysed in detail, with the activation energy of diffusion (E_a = 13.7 ± 0.3 kJ mol^{-1} in H_2-saturated $[C_2mim][NTf_2]$) being found to be significantly lower than that of the typical probe molecule ferrocene under the same conditions, hence confirming the non-Stokes-Einstein behaviour of dissolved H_2 in RTILs. These observations are attributed to H_2 dissolving into the interstices or holes inherent in the RTIL structure, whereby diffusion is

more facile, and the H_2 results in reduced Coulombic interactions with a concurrent net reduction in RTIL viscosity.

References

1 Y. Meng, L. Aldous, R. G. Compton, *Journal of Physical Chemistry C* 2011, *115*, 14334-14340.

2 D. S. Silvester, L. Aldous, M. C. Lagunas, C. Hardacre, R. G. Compton, *Journal of Physical Chemistry B* 2006, *110*, 22035-22042.

3 J. M. S. S. Esperanca, J. N. C. Lopes, M. Tariq, L. M. N. B. F. Santos, J. W. Magee, L. P. N. Rebelo, *Journal of Chemical and Engineering Data* 2010, *55*, 3-12.

4 A. Vidis, G. Laurenczy, E. Kusters, G. Sedelmeier, P. J. Dyson, *Journal of Physical Organic Chemistry* 2007, *20*, 109-114.

5 H. T. Liu, Y. Liu, J. H. Li, *Physical Chemistry Chemical Physics* 2010, *12*, 1685-1697 Doi 10.1039/B921469k.

6 M. C. Buzzeo, R. G. Evans, R. G. Compton, *Chemphyschem* 2004, *5*, 1106-1120.

7 V. I. Parvulescu, C. Hardacre, *Chemical Reviews* 2007, *107*, 2615-2665.

8 M. C. Buzzeo, C. Hardacre, R. G. Compton, *Analytical Chemistry* 2004, *76*, 4583-4588.

9 P. J. Dyson, G. Laurenczy, C. A. Ohlin, J. Vallance, T. Welton, *Chemical Communications* 2003, 2418-2419.

10 Y. Meng, L. Aldous, R. G. Compton, *Green Chemistry* 2010, *12*, 1926-1928.

11 Y. Meng, L. Aldous, B. S. Pilgrim, T. J. Donohoe, R. G. Compton, *New Journal of Chemistry* 2011.

12 F. Endres, S. Z. El Abedin, *Physical Chemistry Chemical Physics* 2006, *8*, 2101-2116.

13 P. Wasserscheid, W. Keim, *Angewandte Chemie-International Edition* 2000, *39*, 3772-3789.

14 L. E. Barrosse-Antle, A. M. Bond, R. G. Compton, A. M. O'Mahony, E. I. Rogers, D. S. Silvester, *Chemistry-an Asian Journal* 2010, *5*, 202-230.

15 D. S. Silvester, K. R. Ward, L. Aldous, C. Hardacre, R. G. Compton, *Journal of Electroanalytical Chemistry* 2008, *618*, 53-60.

16 J. A. Widegren, E. M. Saurer, K. N. Marsh, J. W. Magee, *Journal of Chemical Thermodynamics* 2005, *37*, 569-575.

17 K. R. Seddon, A. Stark, M. J. Torres, *Pure and Applied Chemistry* 2000, *72*, 2275-2287.

18 L. E. Barrosse-Antle, C. Hardacre, R. G. Compton, *Journal of Physical Chemistry B* 2009, *113*, 1007-1011.

19 L. E. Barrosse-Antle, C. Hardacre, R. G. Compton, *Journal of Physical Chemistry B* 2009, *113*, 2805-2809.

20 L. E. Barrosse-Antle, L. Aldous, C. Hardacre, A. M. Bond, R. G. Compton, *Journal of Physical Chemistry C* 2009, *113*, 7750-7754.

21 L. E. Barrosse-Antlle, C. Hardacre, R. G. Compton, *Journal of Physical Chemistry B* 2009, *113*, 1007-1011.

22 A. M. O'Mahony, R. G. Compton, *Electroanalysis* 2010, *22*, 2313-2322.

23 R. A. Ando, L. J. A. Siqueira, F. C. Bazito, R. M. Torresi, P. S. Santos, *Journal of Physical Chemistry B* 2007, *111*, 8717-8719.

24 L. J. A. Siqueira, R. A. Ando, F. F. C. Bazito, R. M. Torresi, P. S. Santos, M. C. C. Ribeiro, *Journal of Physical Chemistry B* 2008, *112*, 6430-6435.

25 Z. M. Liu, W. Z. Wu, B. X. Han, Z. X. Dong, G. Y. Zhao, J. Q. Wang, T. Jiang, G. Y. Yang, *Chemistry-a European Journal* 2003, *9*, 3897-3903.

26 S. H. Ren, Y. C. Hou, W. Z. Wu, Q. Y. Liu, Y. F. Xiao, X. T. Chen, *Journal of Physical Chemistry B* 2010, *114*, 2175-2179.

27 R. G. Evans, O. V. Klymenko, S. A. Saddoughi, C. Hardacre, R. G. Compton, *Journal of Physical Chemistry B* 2004, *108*, 7878-7886.

28 A. M. O'Mahony, D. S. Silvester, L. Aldous, C. Hardacre, R. G. Compton, *Journal of Chemical and Engineering Data* 2008, *53*, 2884-2891.

29 D. S. Silvester, L. Aldous, C. Hardacre, R. G. Compton, *Journal of Physical Chemistry B* 2007, *111*, 5000-5007.

30 L. Aldous, D. S. Silvester, W. R. Pitner, R. G. Compton, M. C. Lagunas, C. Hardacre, *Journal of Physical Chemistry C* 2007, *111*, 8496-8503.

31 Y. H. Xu, *International Journal of Hydrogen Energy* 2009, *34*, 77-83.

32 C. A. Paddon, D. S. Silvester, F. L. Bhatti, T. J. Donohoe, R. G. Compton, *Electroanalysis* 2007, *19*, 11-22.

33 D. Shoup, A. Szabo, *Journal of Electroanalytical Chemistry* 1982, *140*, 237-245.

34 J. L. Anthony, J. L. Anderson, E. J. Maginn, J. F. Brennecke, *Journal of Physical Chemistry B* 2005, *109*, 6366-6374.

35 J. Jacquemin, P. Husson, V. Majer, M. F. C. Gomes, *Journal of Solution Chemistry* 2007, *36*, 967-979.

36 U. Schröder, J. D. Wadhawan, R. G. Compton, F. Marken, P. A. Z. Suarez, C. S. Consorti, R. F. de Souza, J. Dupont, *New Journal of Chemistry* 2000, *24*, 1009-1015.

37 C. Fu, L. Aldous, E. J. F. Dickinson, N. S. A. Manan, R. G. Compton, *ChemPhysChem* 2011.

38 C. Fu, L. Aldous, E. J. F. Dickinson, N. S. A. Manan, R. G. Compton, *Chemical Communications* 2011.

39 E. I. Rogers, D. S. Silvester, D. L. Poole, L. Aldous, C. Hardacre, R. G. Compton, *Journal of Physical Chemistry C* 2008, *112*, 2729-2735.

40 R. Fukuta, Y. Katayama, T. Miura, *ECS Transactions* 2007, *3*, 567-576.

41 W. C. Barrette, D. T. Sawyer, *Analytical Chemistry* 1984, *56*, 653-657.

Chapter 7 The Hydrogen Evolution Reaction in a Room Temperature Ionic Liquid: Mechanism and Electrocatalyst Trends

In this Chapter, the kinetics and mechanism of the proton reduction reaction in the room temperature ionic liquid 1-ethyl-3-methylimidazolium bis(trifluoromethylsulfonyl)imide ($[C_2mim]$ $[NTf_2]$) is studied at gold, molybdenum, nickel, titanium and platinum electrodes. Significant differences in electrochemical rate constants were observed between the different metals and with the corresponding processes in aqueous solution. The hydrogen evolution mechanism was consistent at all five metals in the ionic liquid, in stark contrast to the known behaviour in aqueous systems. This work has been carried out with the collaboration of Dr. Leigh Aldous and D.Phil candidate Mr. Stephen R. Belding and has been published in the Journal of Physical Chemistry Chemistry Physics.[1] The computer program of cyclic voltammetry simulation was written by Mr. Belding.

7.1 Introduction

The proton reduction mechanism to form dihydrogen (H^+ to H_2) is of extensive fundamental importance, and has been the subject of a vast number of studies, predominately in aqueous solution.[2-4] In electrochemistry the H^+/H_2 redox couple forms the basis of fundamental reference scales, such as the standard hydrogen electrode (SHE)[5] and the reversible hydrogen electrode (RHE).[6] Generally the proton reduction is site specific whether in enzymes[7] or, as in electrochemistry, on bulk metals such as Fe or Pt,[2] and the nature of the site determines the rate of reaction. Accordingly the proton reduction reaction is exquisitely sensitive to the chemical nature of the electrode in general, and to the exact reaction site (of H-atom adsorption) in particular. Different metal surfaces therefore show very different levels of electrocatalysis towards the proton reduction reaction.[3]

One measurement of the rate of 'electrocatalysis' of the hydrogen evolution reaction (HER) at an electrode surface is the exchange current density (j_0),[5] and which has been observed in aqueous solutions to cover several orders of magnitude from 'poor' electrocatalysts such as Hg and Pb to 'good' electrocatalysts such as Pt.[2] Another (related) measure which is more widely employed across electrochemical studies in general is the standard electrochemical rate constant, k^0, a measure of the rate of electron transfer at the formal potential of the redox couple, E_f^0.[8]

Tafel plots can be used to derive mechanistic information from multistep electrochemical processes,[9] and in strongly acidic solution three mechanisms are widespread in the hydrogen evolution reaction. The Volmer reaction constitutes the first step (equation (7.1)) followed by either dimerisation of adsorbed hydrogen atoms by the Tafel reaction (equation (7.2)) or by the electrochemical Heyrovsky reaction (equation (7.3)).[2, 5, 8]

$$H^+ + e^- \rightarrow H_{ads} \qquad (7.1)$$

$$2H_{ads} \rightarrow H_2 \qquad (7.2)$$

$$H_{ads} + H^+ + e^- \rightarrow H_2 \qquad (7.3)$$

It has been observed that for certain metals in acidic aqueous solution (*i.e.* Pt, Au, Mo), M-H formation by reduction of H^+ is facile, H_{ads} migration is relatively slow, and subsequently the Heyrovsky reaction is the primary mechanism for H_2 discharge. Tafel plots in these systems yield an observed transfer coefficient, α, of 1.5.[2, 8, 9] For other metals (*i.e.* Ni, Fe, Hg) the formation of the H_{ads} is the rate limiting step and $\alpha = 0.5$ is observed.[2, 8, 9]

Despite its importance, both fundamentally in terms of electrode kinetics and application in areas such as synthetic hydrogenation and dihydrogen gas sensing, the kinetics of proton reduction in room temperature ionic liquids are essentially unexplored. Ionic liquids are

composed nearly entirely of ions, possess melting points below 373 K and inherent ionic conductivity, and have numerous applications with respect to electrochemistry and other areas,[10] although significant fundamental knowledge is still lacking, as exemplified by the lack of a standard reference scale based upon a hydrogen-based reference electrode.

Studies have investigated proton reduction in ionic liquids, such as studies of $H[NTf_2]$ at various electrodes.[11-15] The oxidation of hydrogen has also been investigated.[6, 15-17] The thermodynamics of proton reduction and hydrogen oxidation have also been recently investigated in a sub-family of ionic liquids; protic ionic liquids.[6] However, the kinetics and mechanism of proton reduction have not received detailed investigation. This is despite ionic liquids having been demonstrated to accelerate the rate of hydrogen evolution by ammonia borane dehydrogenation,[18] and act as efficient electrolytes for hydrogen evolution *via* water electrolysis.[19, 20]

In this chapter the proton reduction reaction (or hydrogen evolution reaction) has been investigated in detail at five different electrocatalytic metals, platinum, gold, molybdenum, nickel and titanium, in the room temperature ionic liquid $[C_2mim][NTf_2]$. Careful and detailed investigation of the H^+/H_2 redox couple at platinum gave a reference potential of -0.078 ± 0.004 V *vs.* Fc / Fc^+ (298 K). Using this reference point, quantitative analysis of proton reduction kinetics is performed in an ionic liquid for the first time. Both mechanism and kinetics of the process are investigated, and compared and contrasted with the existing literature available for aqueous systems.

7.2. Results & Discussion

7.2.1 The Ag/Ag^+ reference couple in $[C_2mim][NTf_2]$

In order to quantitatively explore the kinetics and mechanism of the reduction of $H[NTf_2]$ across a range of electrode materials, it was necessary to first develop a stable reference

electrode. *In situ* redox probes such as ferrocene[21] were found to react with $H[NTf_2]$, various other common aprotic reference couples such as TMPD[22] would likely have undergone protonation leading to chemical instability in the media of interest, while the cobaltocenium reduction wave[23] overlapped with the voltammetric features of interest. A micro-Ag/Ag^+ reference electrode was therefore developed that could be incorporated into existing experimental equipment[24] designed for rigorously thermostated experiments performed *in vacuo* on the µL scale, thus ensuring the removal of adventitious gases and moisture.[25] Huber and Roling recently described a micro-Ag/Ag^+ reference electrode for ionic liquid studies,[26] while the reference electrode employed in this study was constructed of different material. The reference electrode consisted of a Ag wire immersed in $[C_2mim][NTf_2]$ containing 10 mM Ag[OTf] and yielded a stable reference potential for $\geq$ 1 week; the full preparation details of this reference electrode are included in the Section 3.4.

The Ag/Ag reference electrode was frequently compared with the ferrocene/ferrocenium (Fc / Fc^+) redox couple in $[C_2mim][NTf_2]$. The $E_{1/2}$ potential was identified by cyclic voltammetry, and after careful correction[27] to account of the known non-equal diffusion coefficients between Fc and Fc^+[5, 20] the E_f^0 of ferrocene in $[C_2mim][NTf_2]$ was found to be -0.273 ± 0.003 V (*vs.* Ag / Ag^+, Ag^+ = 10 mM Ag[OTf]) at 298 K.

7.2.2 Proton reduction in $[C_2mim][NTf_2]$

The proton reduction feature has previously been semi-quantitatively investigated in $[C_nmim][NTf_2]$ (n = 2, 4) ILs at Au,[11] Pt,[11, 12, 15] Pd[13, 14] and GC[11] electrodes. The present study seeks to perform a quantitative investigation of the proton reduction feature at five microelectrodes consisting of metals with varying electrocatalytic ability with respect to the hydrogen evolution reaction, as previously investigated in depth in aqueous systems.[2, 3, 5, 8]

Figure 7.1 displays the cyclic voltammetry of solutions of $H[NTf_2]$ in $[C_2mim][NTf_2]$ (*in vacuo*, 298 ± 0.5 K) at platinum, molybdenum, gold, nickel and titanium microelectrodes

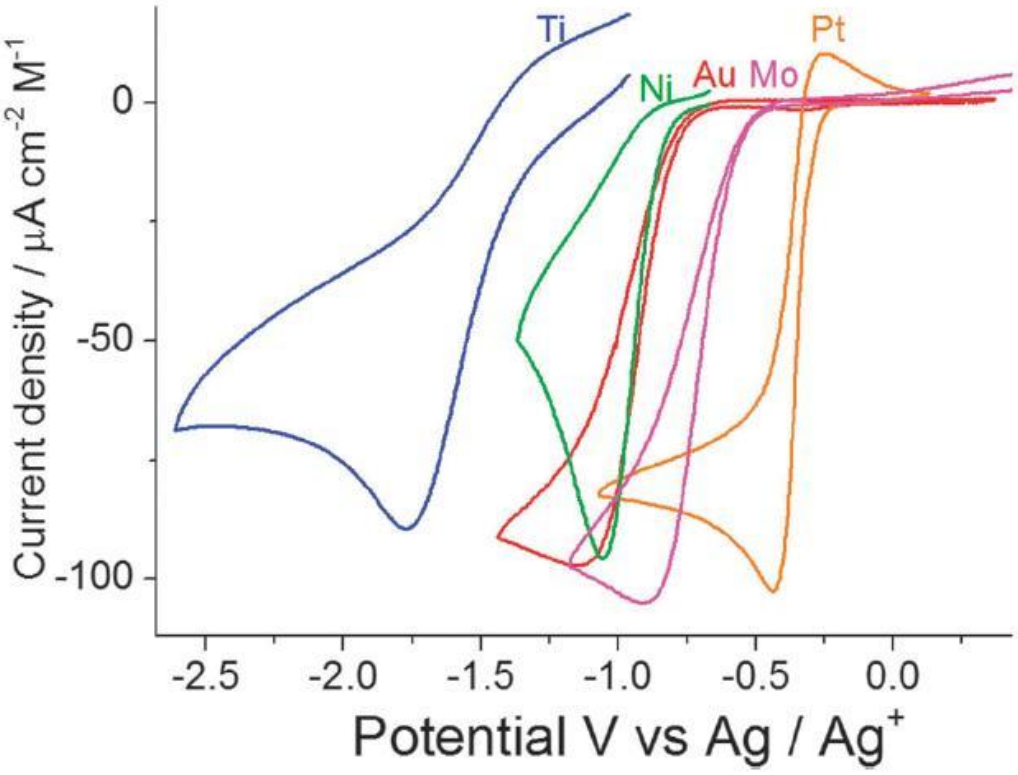

Figure 7.1 Normalised cyclic voltammograms recorded for $H[NTf_2]$ reduction in $[C_2mim][NTf_2]$ at 400mV s^{-1} on a range of electrode metals. Experiments were performed on multiple $H[NTf_2]$ concentrations between 12 and 95 mM; full data available in the appendix 7.4.

recorded at 400 mV s^{-1} *vs.* Ag/Ag^+ reference electrode. The data has been normalised with respect to the calibrated electrode surface area and the precise experimentally determined $H[NTf_2]$ concentration (by chronoamperometry followed by Shoup & Szabo simulation,[28, 29] as outlined in the section3.5.2).

Pt displayed *quasi*-reversible voltammetry, with the oxidation of H_2 clearly observed on the reverse sweep, while the other metals demonstrated irreversible proton reduction. Figure 7.2 displays overlaid scan rate studies for Pt and Mo to highlight the difference responses, while the raw data for Ti, Mo, Ni, Pt and Mo over a range of scan rates can be found in the appendix to this chapter.

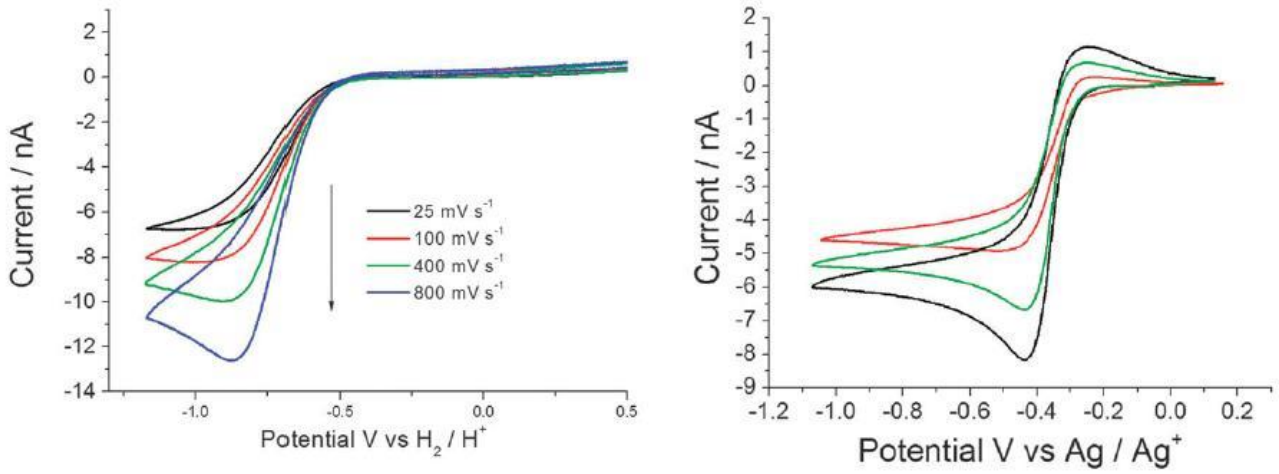

Figure.7.2 Scan rate studies recorded for (left) 95mM H[NTf_2] in [C_2mim][NTf_2] at a 13 mm diameter Mo microelectrode, and (right) 75mM H[NTf_2] in [C_2mim][NTf_2] at a 10 mm diameter Pt microelectrode.

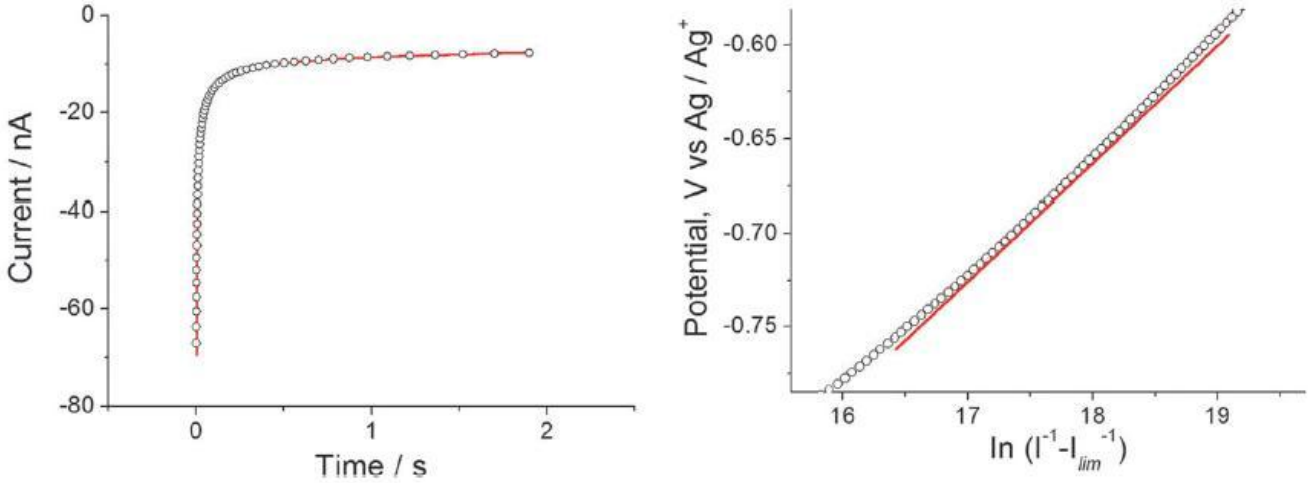

Figure. 7.3 Data for 95 mM H[NTf_2] in [C_2mim][NTf_2] at a 10 mm diameter Mo microelectrode, displaying (left) experimental chronoamperogram (–) and simulated data using the Shoup & Szabo equation[29] (O), and (right) a mass-transport corrected Tafel plot,[36] where individual experimental data points are represented by O.

Chronoamperometric experiments were performed at all five electrodes and simulated using the Shoup and Szabo equation.[12, 15, 16, 28, 29] Figure 7.3(a) displays the chronoamperometric transients recorded at Mo, as well as the resulting Shoup and Szabo simulated data; the

diffusion coefficient of $H[NTf_2]$ in $[C_2mim][NTf_2]$ was found to be 2.5 (± 0.1) × 10^{-11} m^2 s^{-1} at all five metals, in agreement with the literature,[12, 16] while the diffusion coefficient of H_2 in $[C_2mim][NTf_2]$ has previously been reported to be 5.5 (± 0.1) × 10^{-10} m^2 s^{-1}.[12]

Mass-transport corrected Tafel plots[30] were obtained for all metals, and transfer coefficient (α) values were found to be between 0.2 and 0.5. Figure 7.3(b) displays the mass-transport corrected Tafel plot obtained at Mo, while the α values for all five metals have been summarised in Table 7.1. The $\alpha \leq 0.5$ values indicate that the first electron transfer is rate limiting at all five metal surfaces in the IL,[2] in stark contrast to aqueous solution, where the observed α values for Au, Mo and Pt are 1.3, 1.5 and 1.5, respectively.[2] Therefore in aqueous solution the hydrogen evolution reaction is anticipated to occur at Au, Mo and Pt by the Heyrovsky reaction, while in the IL the limiting step in H_2 evolution at all metals is the Volmer reaction.

The $E_{1/2}$ values at the five metals are spread over a range in excess of a volt, indicating that that the electrocatalytic nature of the substrate is highly influential, and also that a solution-phase dissociation step of $H[NTf_2]$ is unlikely to be a limiting factor in comparison. The adsorption energetics are therefore likely responsible for the observed change in hydrogen evolution mechanism when moving from strongly acidic aqueous solution to strong acidic ionic liquid solution.

7.2.3 Referencing the Ag / Ag^+ couple to the H_2 / H^+ couple

The voltammetry at all of the metals contains kinetic information. In order to extract this the *quasi*-reversible voltammetry of the $H_2/H[NTf_2]$ redox couple at Pt was investigated in more detail so as to quantify the E_f^0 of this couple in $[C_2mim][NTf_2]$ and allow determination of the standard electrochemical rate constant (k_c^0) on platinum.

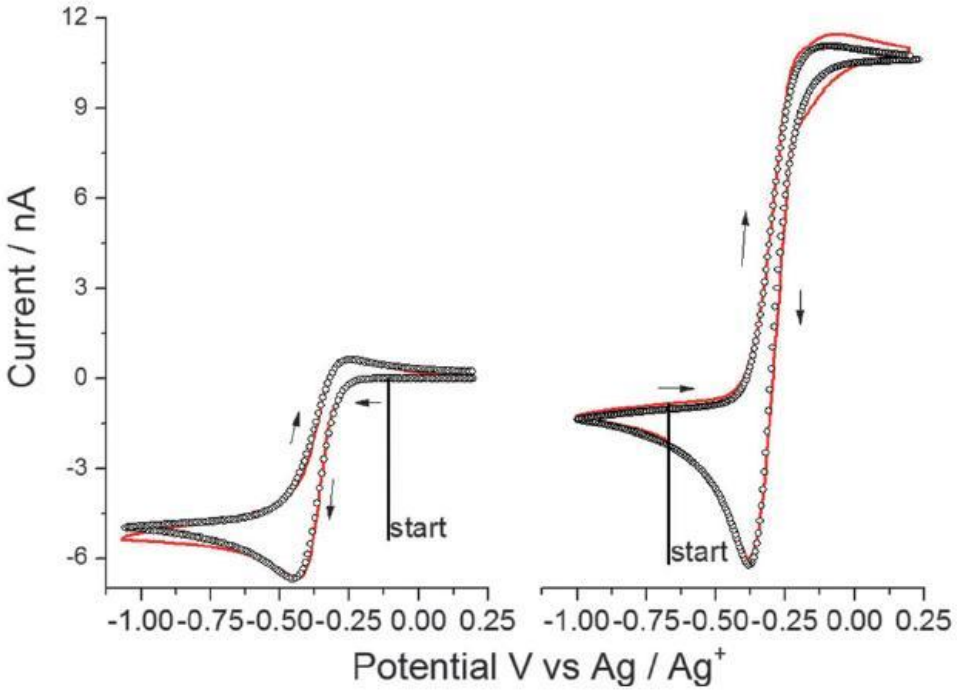

Figure 7.4 Cyclic voltammetry experimental data (-) and optimised of simulated curve (o) for 75 mM H[NTf_2] (left) and 4.55 mM H_2 hydrogen (right) on a 10 µm Pt electrode in [C_2mim][NTf_2] at 400 mV s^{-1}.The line indicates start potential and arrows indicate scan direction.

As the proton reduction[11, 12, 15] and hydrogen oxidation[6, 12, 15-17] mechanisms in ILs occur at different potentials and so do not necessarily have a common transition state, the proton reduction and hydrogen oxidation processes were initially investigated separately and simulated in order to give kinetic and mechanistic data.

Figure 7.4(a) displays a CV recorded at a Pt microelectrode in [C_2mim][NTf_2] containing 75 mM H[NTf_2], while Figure 7.4(b) displays a CV recorded in H_2-saturated [C_2mim][NTf_2] (H_2 concentration = 4.55 mM). Despite significantly different concentrations, the H[NTf_2] reduction wave in Figure 7.4(a) and hydrogen oxidation wave in Figure 7.4(b) are of a similar magnitude. In addition the H_2 oxidation peak in Figure 7.4(a) is relatively small and the H^+ reduction peak in Figure 7.4(b) is relatively large. These features relate to the order of

magnitude difference in the $H[NTf_2]$ and H_2 diffusion coefficients, and emphasises the need for full simulation in order to accurately pinpoint the E_f^0 value for the couple.

Simulation was performed for the data displayed in Figures 7.4(a) and (b) (as well as a wide range of scan rates) using the computational model outlined in Section 2.8, in order to obtain the physical parameters corresponding to the cathodic (equation (7.4)) and anodic (equation (7.5)) processes.

$$j = k_c^0[H^+]\exp(-\frac{\alpha F}{RT}(E - E_{f,c}^0))$$

$$= k_c^0 \exp(\frac{\alpha F E_{f,c}^0}{RT})[H^+]\exp(-\frac{\alpha FE}{RT}) \qquad (7.4)$$

$$= k_c^{'}[H^+]\exp(-\frac{\alpha FE}{RT})$$

$$j = k_a^0[H_2]\exp(\frac{\beta F}{RT}(E - E_{f,a}^0))$$

$$= k_a^0 \exp(-\frac{\beta F E_{f,a}^0}{RT})[H_2]\exp(\frac{\beta FE}{RT}) \qquad (7.5)$$

$$= k_a^{'}[H_2]\exp(\frac{\beta FE}{RT})$$

The concentration values, diffusion coefficients and α and β values were kept within 5 % of the values determined by chronoamperometry and Tafel plots, with only k'_c and k'_a varied in order to obtain the best fit. The best fit simulation data is overlaid in Figure 7.4, and the obtained physical parameters have been collected in Table 7.2.

A further six experiments were performed in $[C_2mim][NTf_2]$; three experiments containing a fixed concentration of H_2 with three different concentrations of $H[NTf_2]$, and three

Table 7.1 Electrochemical parameters for the hydrogen evolution reaction in $H[NTf_2]/[C_2mim][NTf_2]$ at a range of different electrode metals

	$D_{(HNTf2)}$ ($cm^2\ s^{-1}$)	$D_{(H2)}$ ($cm^2\ s^{-1}$)	Radius (cm)	α	E_f^o (V *vs.* Ag/Ag^+)	k_c^0 ($cm\ s^{-1}$)
Pt	2.5×10^{-7}	5.5×10^{-6}	5.25×10^{-4}	0.5	-0.338 (± 0.004)	1.3×10^{-3}
Mo	2.5×10^{-7}	5.5×10^{-6}	6.5×10^{-4}	0.3	-0.338 (± 0.004)	5×10^{-6}
Au	2.5×10^{-7}	5.5×10^{-6}	4.6×10^{-4}	0.35	-0.338 (± 0.004)	1.7×10^{-7}
Ni	2.5×10^{-7}	5.5×10^{-6}	5×10^{-3}	0.35	-0.338 (± 0.004)	1.3×10^{-7}
Ti	2.5×10^{-7}	5.5×10^{-6}	2.5×10^{-3}	0.2	-0.338 (± 0.004)	2.6×10^{-8}

Table 7.2 Parameters used in the cyclic voltammetric simulation for proton reduction and hydrogen oxidation (Figure 7.4) on Pt in $[C_2mim][NTf_2]$

	Cathodic reaction	Anodic reaction
C (mM)	75	9.1
k' **($cm\ s^{-1}$)**	4×10^{-6}	6.5×10^{-5}
α	0.5	-
β	-	0.5

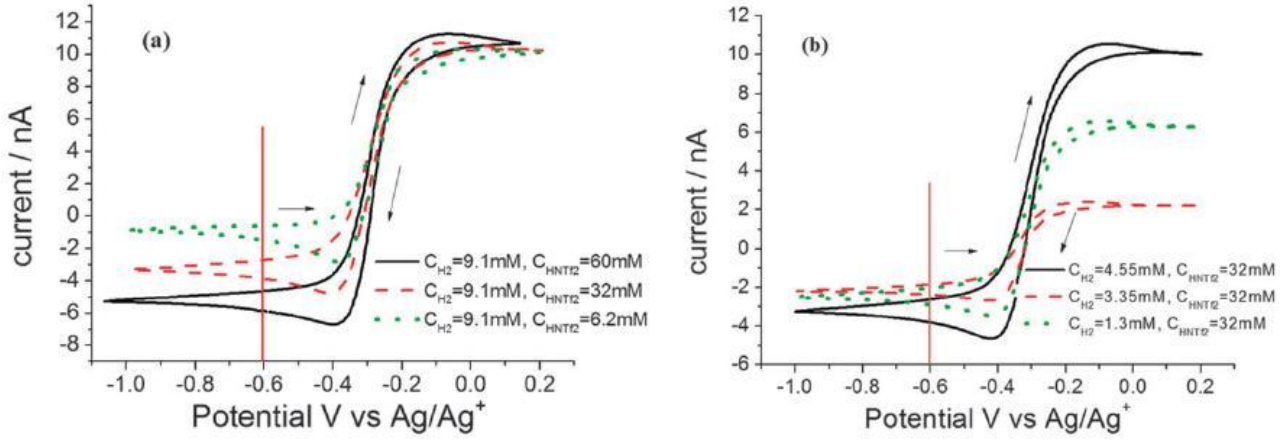

Figure. 7.5 Proton reduction and hydrogen oxidation at a Pt microelectode (10 mm diameter) at 400 mV s^{-1}, (a) for a range of concentrations of $H[NTf_2]$ (60, 32 and 6.2 mM) in the presence of a fixed concentration of H_2 (4.55 mM), and (b) for a range of concentrations of H_2 (4.55, 3.35 and 1.3 mM) in the presence of a fixed concentration of $H[NTf_2]$ (36 mM). The line indicates start potential and arrows indicate scan direction.

experiments containing a fixed concentration of $H[NTf_2]$ with three different concentrations of H_2. The resulting data at one scan rate is displayed in Figure 7.5. The influence of H_2 concentration of the viscosity of $[C_2mim][NTf_2]$ (and therefore $H[NTf_2]$ diffusion coefficient)[12] was accounted for throughout. Due to the order of magnitude discrepancy in diffusion coefficients between H_2 and $HNTf_2$, H_2 oxidation resulted in accumulation of $H[NTf_2]$ near the electrode surface (*cf.* Fig 7.4). Scans were therefore started at -0.6 V and scanned anodically, as this was found to result in the minimum initial disruption to the concentration gradient at the surface of the electrode at the starting of the scan.

In these systems the current density, *j*, close to the formal potential can be expressed by the Butler-Volmer equation,

$$j = k_c^{'}[H^+]\exp(-\frac{\alpha FE}{RT}) - k_a^{'}[H_2]\exp(\frac{\beta FE}{RT}) \qquad (7.6)$$

where k'_c, k'_a α and β (Table 7.2) were obtained from the separate investigations on $H[NTf_2]$ and H_2 described above, while the various concentrations of $H[NTf_2]$ and H_2 were determined accurately by chronoamperometry. When $j = 0$ then E is equal to the equilibrium potential, E_e, and the E_e can be related to the formal potential, E_f^0, by the Nernst Equation, (7.7),

$$E_e = E_f^0 + \frac{RT}{F} In(\frac{[H^+]}{[H_2]^{\frac{1}{2}}}) \qquad (7.7)$$

where $[H^+]$ and $[H_2]$ are already known. Although the kinetics of equation (7.4) were found to operate within ±4mV of E_f^0, consistency with equation (7.5) would require them to alter at a potential closer to E_f^0. However, from the obtained data six E_f^0 values were calculated from the six different experiments, and the E_f^0 of the $H_2/H[NTf_2]$ redox couple at Pt was found to be -0.338 ± 0.004 V *vs.* Ag/Ag^+ (or -0.065 ± 0.004 V at 298 K *vs.* Fc / Fc^+) in *all* six experiments.

7.2.4 Simulation of the proton reduction features with respect to the H_2/H^+ couple

Using the obtained E_f^0 value for the H_2/H^+ couple, the voltammetry recorded for $H[NTf_2]$ at Pt, Au, Ni, Mo and Ti electrodes were simulated using the same program used previously to simulate the proton reduction feature at Pt. All physical parameters were experimentally determined and fixed, and only k^0_c varied in order to obtain a fit. This was successful for all metals, over a range of scan rates and concentrations, and the resulting simulation is overlaid with the experimental results in Figure 7.6. It should be noted that concentration studies were performed at several of the metals, and it was determined that the mechanism presented in the Theory section was applicable over a wide range of concentrations, highlighting that the proton reduction process was first order as opposed to alternative mechanisms such as second order reduction pathways.

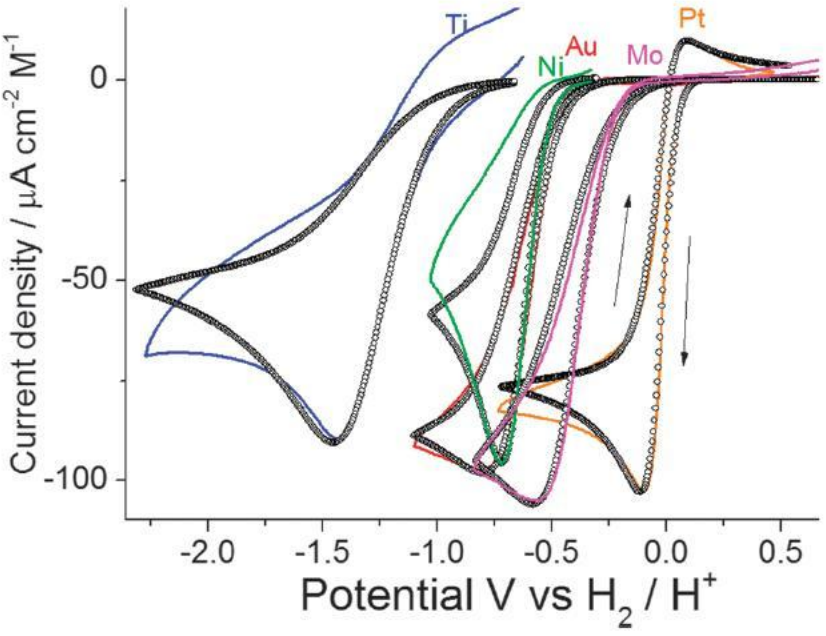

Figure 7.6 Normalised voltammetry, comparing the experiment data (−) and optimised simulation data (o) for $H[NTf_2]$ reduction in $[C_2mim][NTf_2]$ at 400 mV s^{-1} on a range of electrode metals.

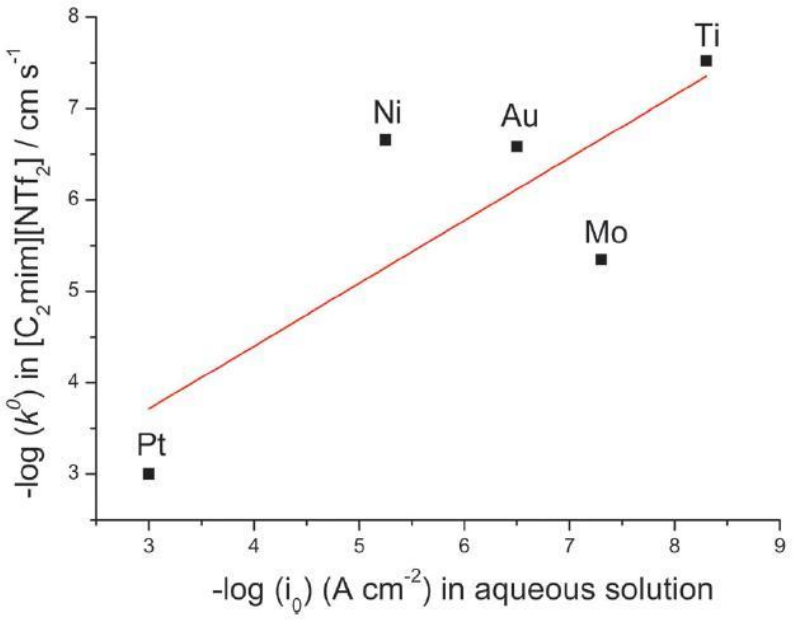

Figure. 7.7 Plot of the k^0 values obtained in this work for the reduction of H[NTf_2] in [C_2mim][NTf_2] at five electrode materials, in comparison with the j_0 values for hydrogen evolution from acidic aqueous solution at the same metals. The j_0 values were taken from reference.[4] The best fit linear plot has been included to guide the eye.

From the simulation the rate constant of proton reduction (k^0_c) was obtained, and it was instructive to compare this value with the known hydrogen evolution reaction trends in aqueous systems.[2-4] Figure 7.7 displays a plot of the obtained k^0_c values for the five metals in [C_2mim][NTf_2] *vs.* the exchange current densities, j_0, reported for aqueous systems.[4]

Despite the mechanism for hydrogen evolution from the five metals in [C_2mim][NTf_2] differing in mechanism from those reported in aqueous systems (as discussed in Section 7.4.2), the electrocatalytic trends follow approximately the same order in both systems. It is noted that if Pt, Au and Ti are taken as centre-points of a linear trend, then Ni displays relatively sluggish hydrogen evolution kinetics in [C_2mim][NTf_2], while Mo displays relatively fast hydrogen evolution kinetics. It is noted that de Souza *et al.* have previously highlighted that Mo is more effective for hydrogen evolution by water electrolysis in the presence of 10 % v/v [C_4mim][BF_4] than Pt.[19] Although our results for H[NTf_2] in dry

$[C_2mim][NTf_2]$ highlight Mo is relatively more effective than expected when extrapolated from classical aqueous solutions, our observations demonstrate Pt to be by far the most active metal for hydrogen evolution from $H[NTf_2]$.

7.3. Conclusions

Electrochemical proton reduction to form dihydrogen has been quantitatively investigated over a range of different metals in an ionic liquid for the first time. Using $H[NTf_2]$ as the proton source, careful analysis of proton reduction and H_2 oxidation at platinum in the ionic liquid $[C_2mim][NTf_2]$ allowed the formal potential of the H^+/H_2 redox couple in this ionic liquid to be quantified as -0.065 ± 0.004 V at 298 K *vs.* Fc / Fc^+ (or -0.338 ± 0.004 V *vs.* Ag/Ag^+).

Using this formal potential value, the standard electrochemical rate constant for proton reduction was determined at platinum, gold, molybdenum, titanium and nickel. Comparison with the known values from aqueous systems indicated approximately similar trends in electrocatalytic tendencies towards the hydrogen evolution reaction, although nickel and molybdenum were outliers, with the kinetics at nickel slower than might be expected in the ionic liquid, while molybdenum was faster, in partial agreement with prior work performed in water/ionic liquid mixtures.

Interestingly, on moving to the ionic liquid system the hydrogen evolution reaction mechanism at the metal surfaces were observed to change from those demonstrated by previous studies in aqueous systems. platinum, gold and molybdenum are known to evolve hydrogen by the Heyrovsky reaction in acidic aqueous solution, while the Volmer reaction was the rate limiting step at all five investigated metals in $[C_2mim][NTf_2]$.

7.4 Appendix- Simulated voltammograms

The details of voltammetry over a range of $H[NTf_2]$ concentration, metals and scan rate studies (Experiment data (-) and optimization of theoretical curve (o)) vs Ag/Ag^+ reference redox couple

7.4.1. $H[NTf_2]$ reduction only on Pt electrode in $[C_2mim][NTf_2]$

ν= 100, 400, 800mV s^{-1}

E_f=-0.335 V

D_c=2.5e-7 cm^2s^{-1}

D_a=5.5e-6 cm^2s^{-1}

C_c=75mM

k^0_c=4e-4 cm s^{-1}

r=5.25e-4 cm

α=0.5

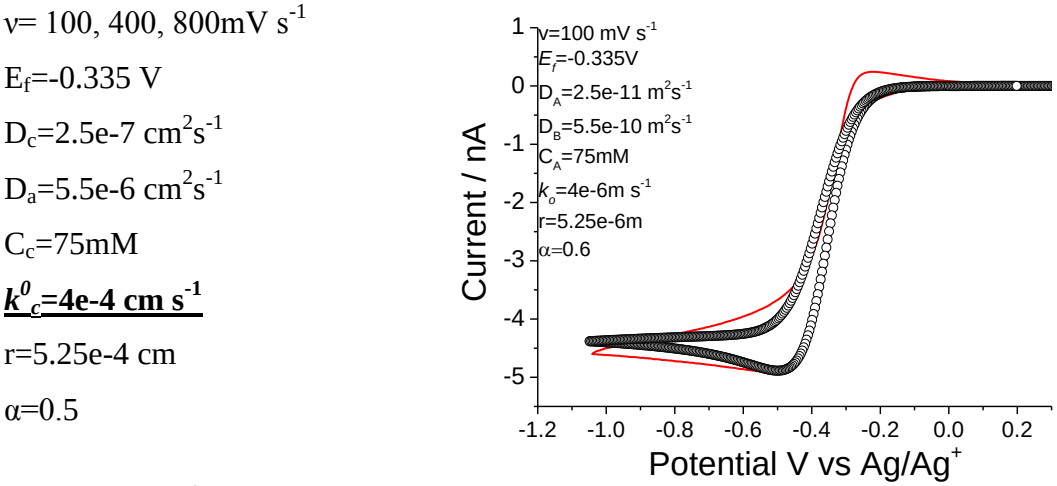

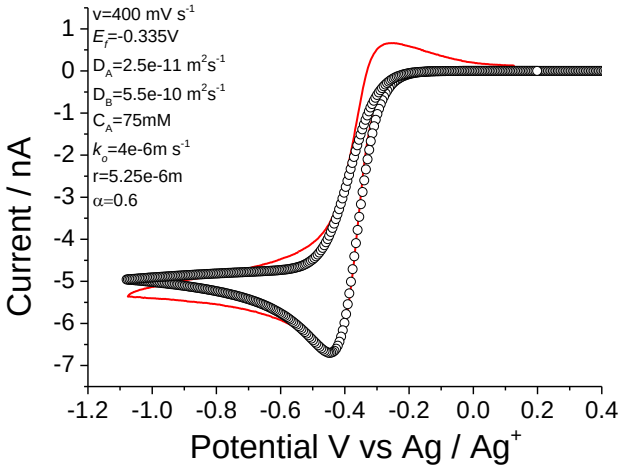

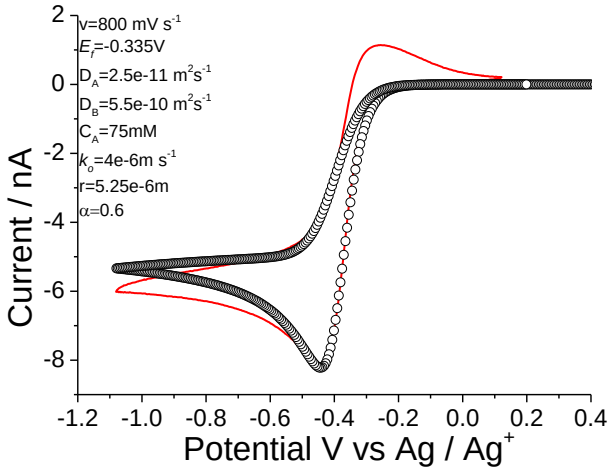

7.4.2. Hydrogen oxidation only on Pt electrode in $[C_2mim][NTf_2]$

ν= 100, 400, 800mV s^{-1}

E_f=-0.335V

D_c=5.5e-6 cm^2s^{-1}

D_a=2.5e-7 cm^2s^{-1}

C_c=4.55mM

$\underline{k^0_a}$=6.5e-3 cm s^{-1}

r=5.25e-4 cm

β=0.5

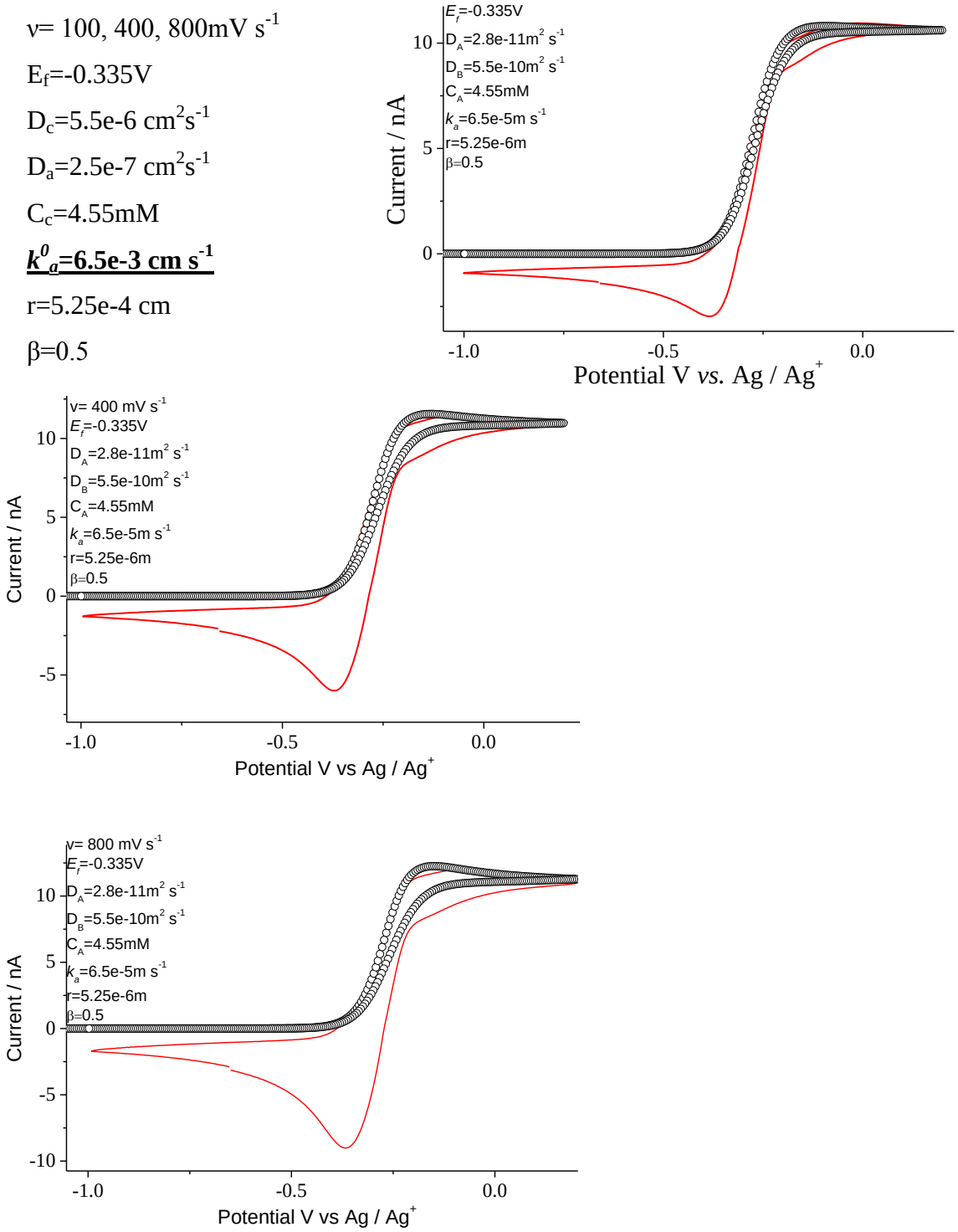

7.4.3 H[NTf_2] concentration study on gold in [C_2mim][NTf_2])

(a). 89mM H[NTf_2] on gold in [C_2mim][NTf_2])

Au
Scan rate: 100mV/s
Potential window (V): (-1.45, 0.25)
D (HNTf2): 2.5e-7 cm^2s^{-1}
D (H_2): 5.5e-6 cm^2s^{-1}
r_{Au}: 4.6e-4 cm
α: 0.35
k^o : 1.7e-7 cm s^{-1}
C: 89 mM
E_f : -0.338 V

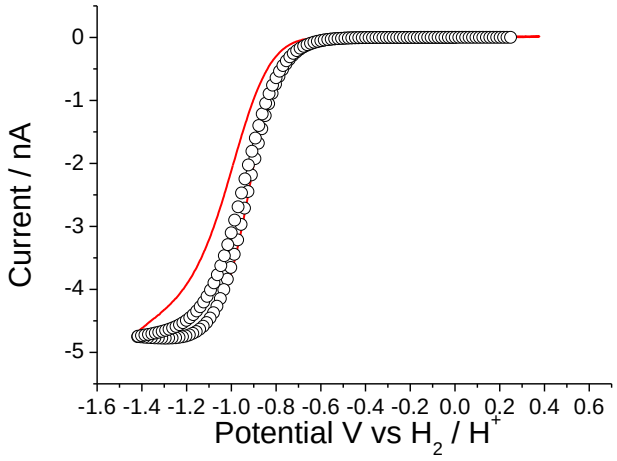

Au
Scan rate: 400mV/s
Potential window (V): (-1.45, 0.25)
D (HNTf2): 2.5e-7 cm^2s^{-1}
D (H_2): 5.5e-6 cm^2s^{-1}
r_{Au}: 4.6e-4 cm
α: 0.35
k^o: 1.7e-7 cm s^{-1}
C: 89 mM
E_f : -0.338 V

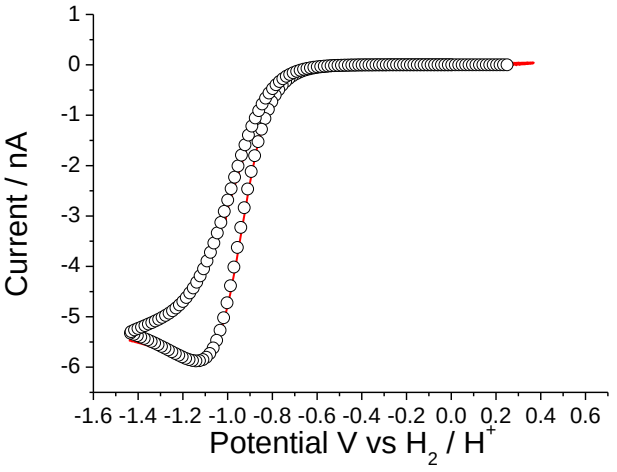

Au
Scan rate: 1V/s
Potential window (V): (-1.45, 0.25)
D (HNTf2): 2.5e-7 cm^2s^{-1}
D (H_2): 5.5e-6 cm^2s^{-1}
r_{Au}: 4.6e-4 cm
α: 0.35
k^o: 1.7e-7 cm s^{-1}
C: 89 mM
E_f : -0.338 V

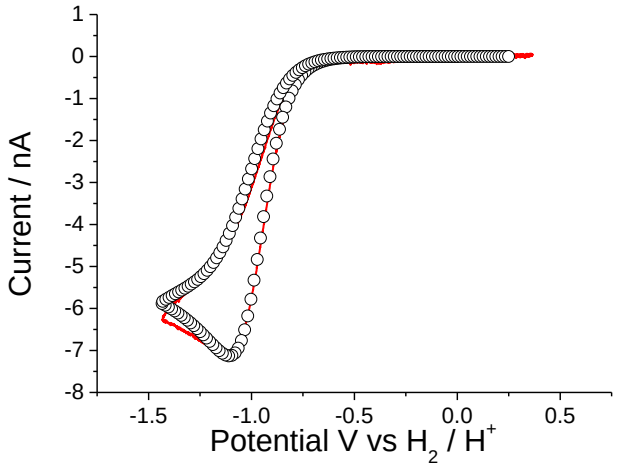

(b). 33mM H[NTf_2] on gold in [C_2mim][NTf_2])

Au
Scan rate: 100mV/s
Potential window (V): (-1.55, 0.25)
D (HNTf2): 2.5e-7 cm^2s^{-1}
D (H_2): 5.5e-6 cm^2s^{-1}
r $_{Au}$: 4.6e-4 cm
α: 0.35
k^o : 1.7e-7 cm s^{-1}
C: 33 mM
E_f : -0.338 V

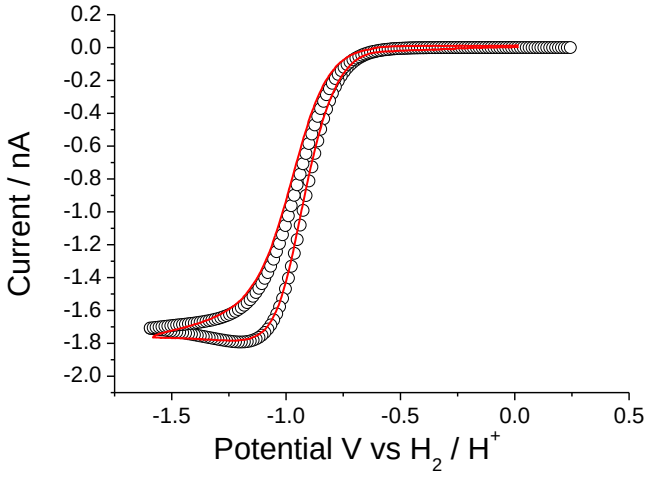

Au
Scan rate: 400mV/s
Potential window (V): (-1.55, 0.25)
D (HNTf2): 2.5e-7 cm^2s^{-1}
D (H_2): 5.5e-6 cm^2s^{-1}
r $_{Au}$: 4.6e-4 cm
α: 0.35
k^o : 1.7e-7 cm s^{-1}
C: 33 mM
E_f : -0.338 V

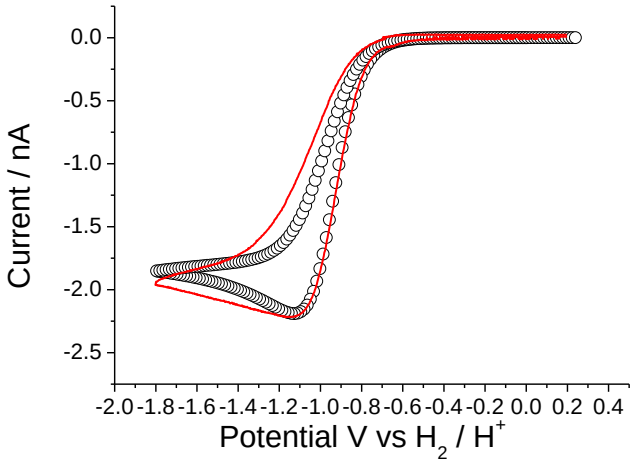

Au
Scan rate: 800mV/s
Potential window (V): (-1.55, 0.25)
D (HNTf2): 2.5e-7 cm^2s^{-1}
D (H_2): 5.5e-6 cm^2s^{-1}
r $_{Au}$: 4.6e-4 cm
α: 0.35
k^o: 1.7e-7 cm s^{-1}
C: 33 mM
E_f : -0.338 V

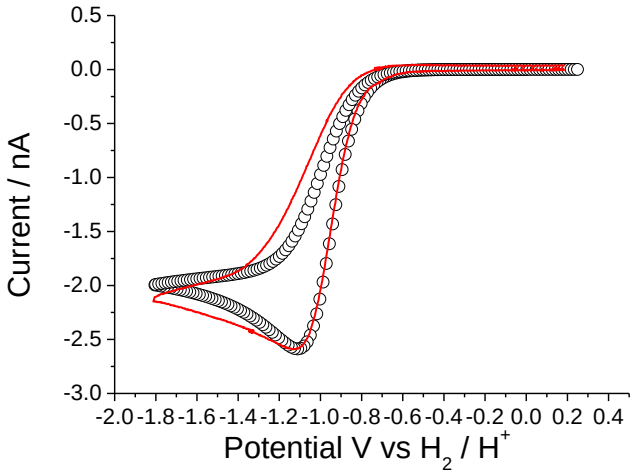

(c). 12mM H[NTf_2] on gold in [C_2mim][NTf_2])

Au
Scan rate: 100mV/s
Potential window (V): (-1.55, 0.25)
D (HNTf2): 2.5e-7 cm^2s^{-1}
D (H_2): 5.5e-6 cm^2s^{-1}
r $_{Au}$: 4.6e-4 cm
α: 0.35
k^o: 1.7e-7 cm s^{-1}
C: 12 mM
E_f : -0.338 V

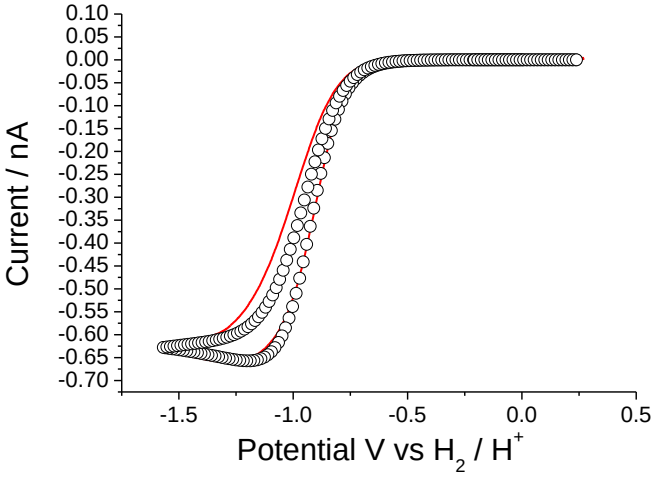

Au
Scan rate: 400mV/s
Potential window (V): (-1.55, 0.25)
D (HNTf2): 2.5e-7 cm^2s^{-1}
D (H_2): 5.5e-6 cm^2s^{-1}
r $_{Au}$: 4.6e-4 cm
α: 0.35
k^o : 1.7e-7 cm s^{-1}
C: 12 mM
E_f : -0.338 V

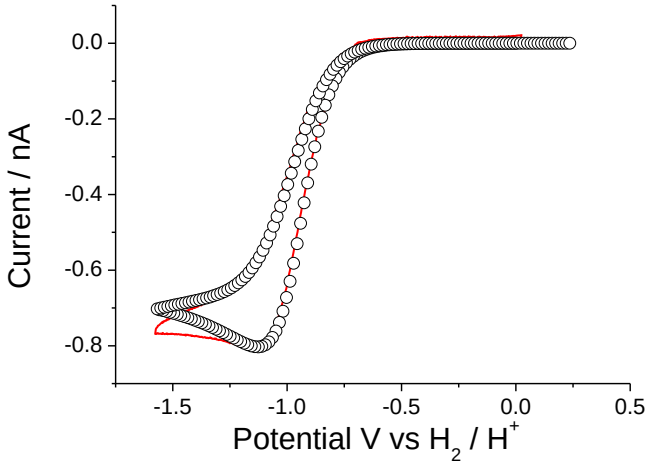

Au
Scan rate: 800mV/s
Potential window (V): (-1.55, 0.25)
D (HNTf2): 2.5e-7 cm^2s^{-1}
D (H_2): 5.5e-6 cm^2s^{-1}
r $_{Au}$: 4.6e-4 cm
α: 0.35
k^o : 1.7e-7 cm s^{-1}
C: 12 mM
E_f : -0.338 V

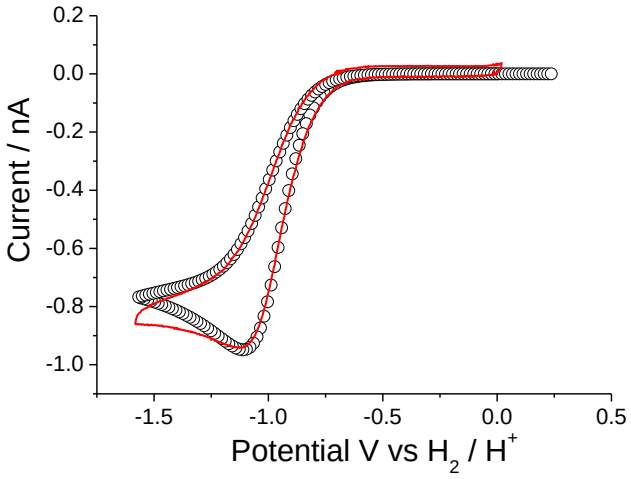

7.4.4 H[NTf_2] concentration study on molybdenum in [C_2mim][NTf_2])

(a). 95mM H[NTf_2] on molybdenum in [C_2mim][NTf_2])

Mo
Scan rate: 25mV/s
Potential window (V): (-1.2, 1)
D (HNTf2): 2.5e-7 cm^2s^{-1}
D (H_2): 5.5e-6 cm^2s^{-1}
r $_{Mo}$: 6.5e-4 cm
α: 0.35
k^o : 5e-6 cm s^{-1}
C: 95 mM
E_f : -0.338 V

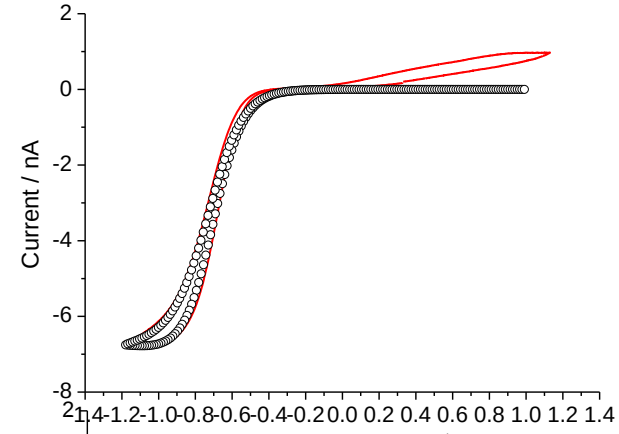

Mo
Scan rate: 100mV/s
Potential window (V): (-1.2, 1)
D (HNTf2): 2.5e-7 cm^2s^{-1}
D (H_2): 5.5e-6 cm^2s^{-1}
r $_{Mo}$: 6.5e-4 cm
α: 0.35
k^o : 5e-6 cm s^{-1}
C: 95 mM
E_f : -0.338 V

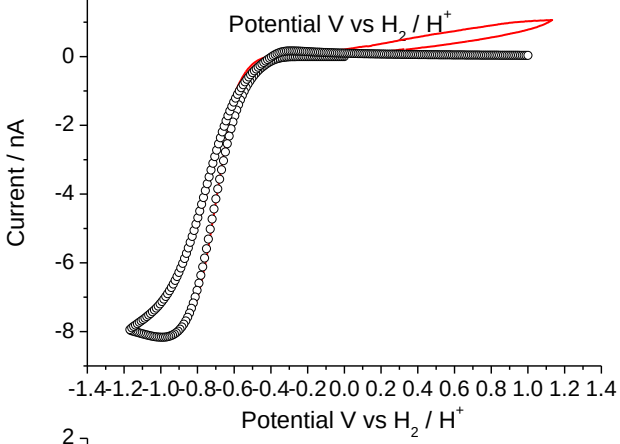

Mo
Scan rate: 400mV/s
Potential window (V): (-1.2, 1)
D (HNTf2): 2.5e-7 cm^2s^{-1}
D (H_2): 5.5e-6 cm^2s^{-1}
r $_{Mo}$: 6.5e-4 cm
α: 0.35
k^o : 5e-6 cm s^{-1}
C: 95 mM
E_f : -0.338 V

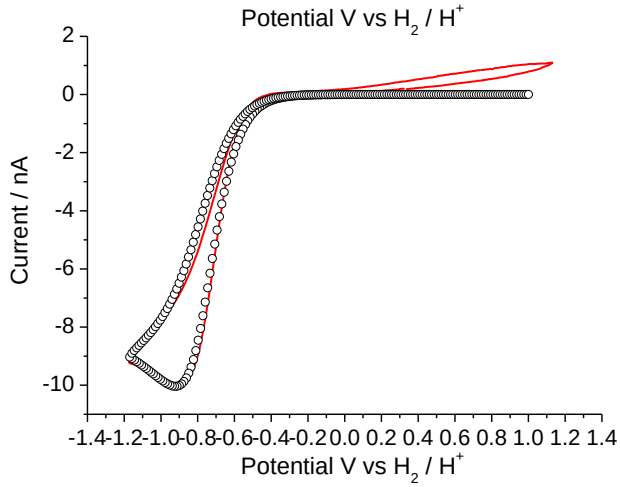

Mo
Scan rate: 800mV/s
Potential window (V): (-1.2, 1)
D (HNTf2): 2.5e-7 cm^2s^{-1}
D (H_2): 5.5e-6 cm^2s^{-1}
r $_{Mo}$: 6.5e-4 cm
α: 0.35
k^o : 5e-6 cm s^{-1}
C: 95 mM
E_f : -0.338 V

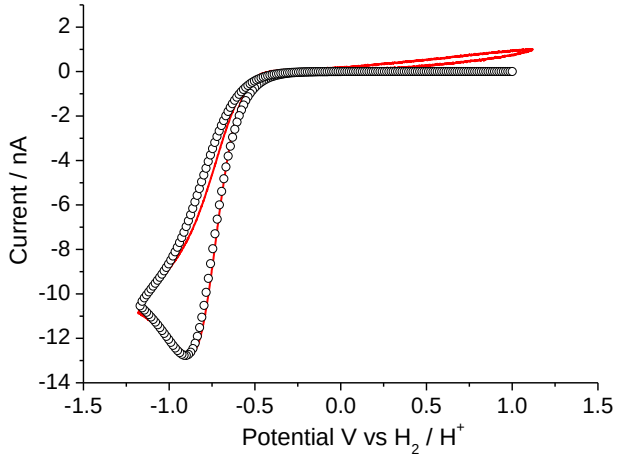

(b) 30mM H[NTf_2] on molybdenum in [C_2mim][NTf_2])

Mo
Scan rate: 25mV/s
Potential window (V): (-1.5, 1)
D (HNTf2): 2.5e-7 cm^2s^{-1}
D (H_2): 5.5e-6 cm^2s^{-1}
r $_{Mo}$: 6.5e-4 cm
α: 0.35
k^o : 5e-6 cm s^{-1}
C: 30 mM
E_f : -0.338 V

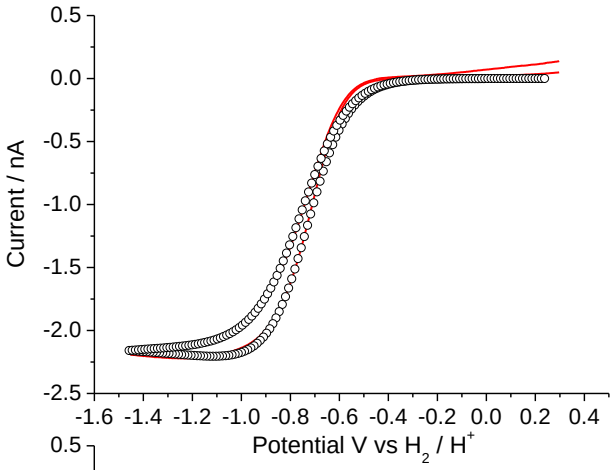

Mo
Scan rate: 100mV/s
Potential window (V): (-1.5, 1)
D (HNTf2): 2.5e-7 cm^2s^{-1}
D (H_2): 5.5e-6 cm^2s^{-1}
r $_{Mo}$: 6.5e-4 cm
α: 0.35
k^o: 5e-6 cm s^{-1}
C: 30 mM
E_f: -0.338 V

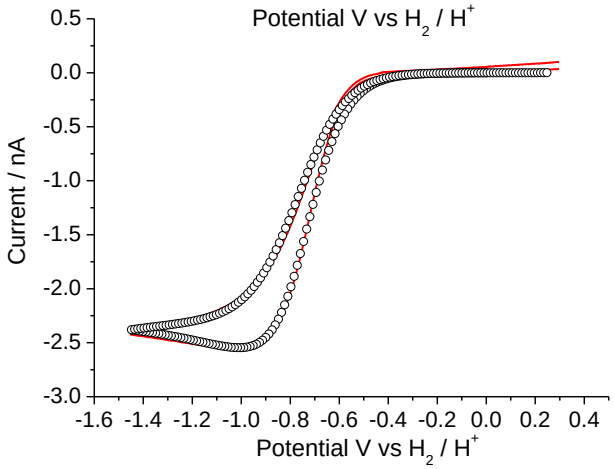

Mo
Scan rate: 400mV/s
Potential window (V): (-1.5, 1)
D (HNTf2): 2.5e-7 cm^2s^{-1}
D (H_2): 5.5e-6 cm^2s^{-1}
r $_{Mo}$: 6.5e-4 cm
α: 0.35
k^o : 5e-6 cm s^{-1}
C: 30 mM
E_f : -0.338 V

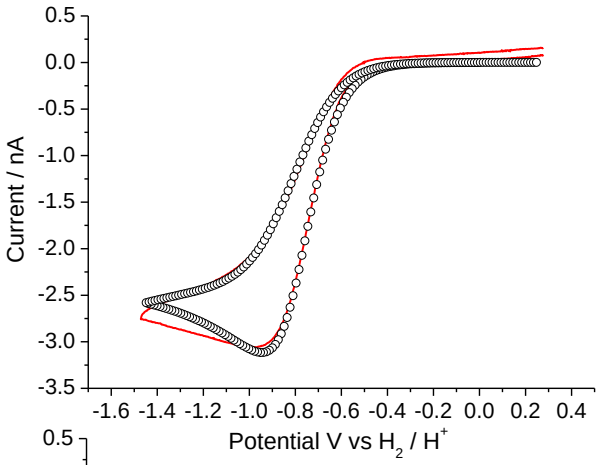

Mo
Scan rate: 800mV/s
Potential window (V): (-1.2, 1)
D (HNTf2): 2.5e-7 cm^2s^{-1}
D (H_2): 5.5e-6 cm^2s^{-1}
r $_{Mo}$: 5e-4 cm
α: 0.35
k^o : 6.5e-6 cm s^{-1}
C: 30 mM
E_f: -0.338 V

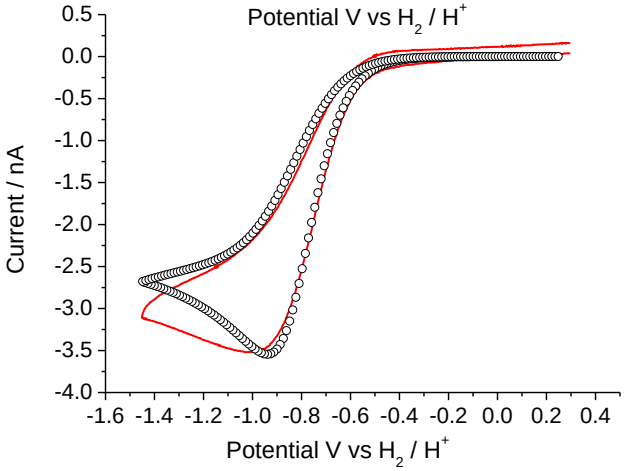

(c). 19mM H[NTf_2] on molybdenum in [C_2mim][NTf_2])

Mo
Scan rate: 25mV/s
Potential window (V): (-1.5, 1)
D (HNTf2): 2.5e-7 cm^2s^{-1}
D (H_2): 5.5e-6 cm^2s^{-1}
r $_{Mo}$: 6.5e-4 cm
α: 0.35
k^o : 5e-6 cm s^{-1}
C: 19 mM
E_f : -0.338 V

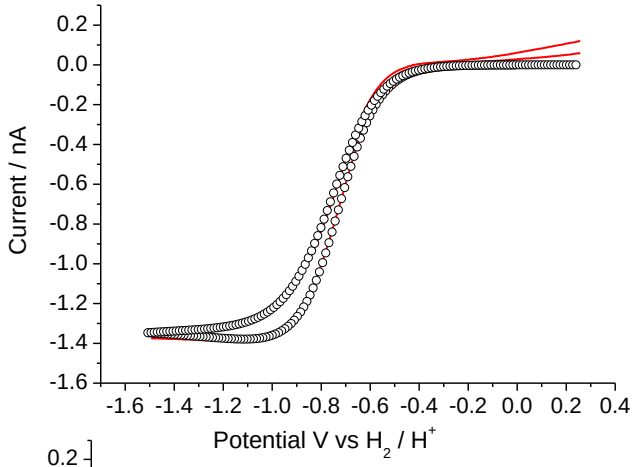

Mo
Scan rate: 100mV/s
Potential window (V): (-1.5, 1)
D (HNTf2): 2.5e-7 cm^2s^{-1}
D (H_2): 5.5e-6 cm^2s^{-1}
r $_{Mo}$: 6.5e-4 cm
α: 0.35
k^o : 5e-6 cm s^{-1}
C: 19 mM
E_f : -0.338 V

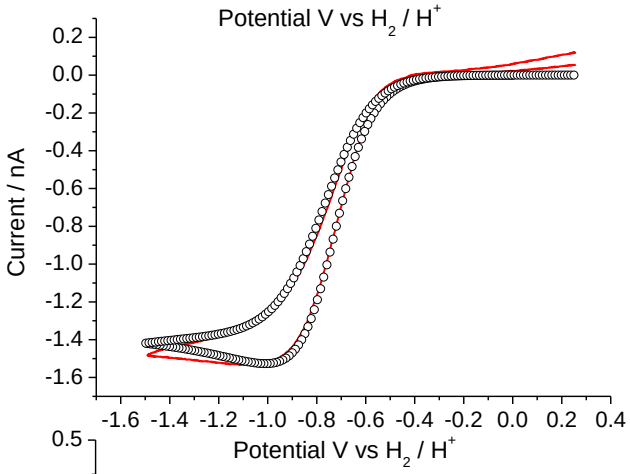

Mo
Scan rate: 400mV/s
Potential window (V): (-1.5, 1)
D (HNTf2): 2.5e-7 cm^2s^{-1}
D (H_2): 5.5e-6 cm^2s^{-1}
r $_{Mo}$: 6.5e-4 cm
α: 0.35
k^o : 5e-6 cm s^{-1}
C: 19 mM
E_f : -0.338 V

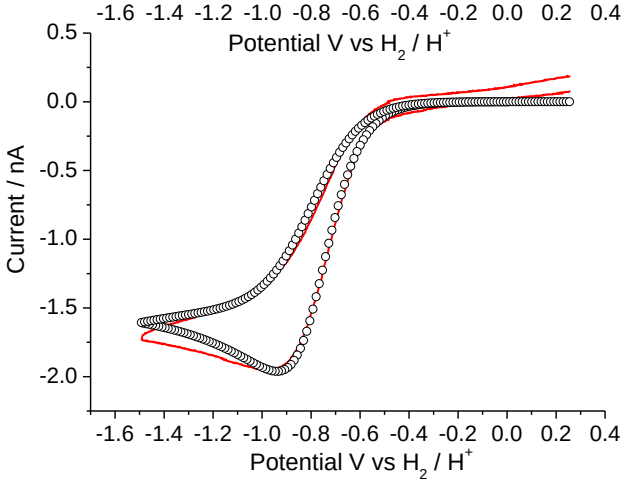

Mo
Scan rate: 800mV/s
Potential window (V): (-1.5, 1)
D (HNTf2): 2.5e-7 cm^2s^{-1}
D (H_2): 5.5e-6 cm^2s^{-1}
r $_{Mo}$: 6.5e-4 cm
α: 0.35
k^o : 5e-6 cm s^{-1}
C: 19 mM
E_f : -0.338 V

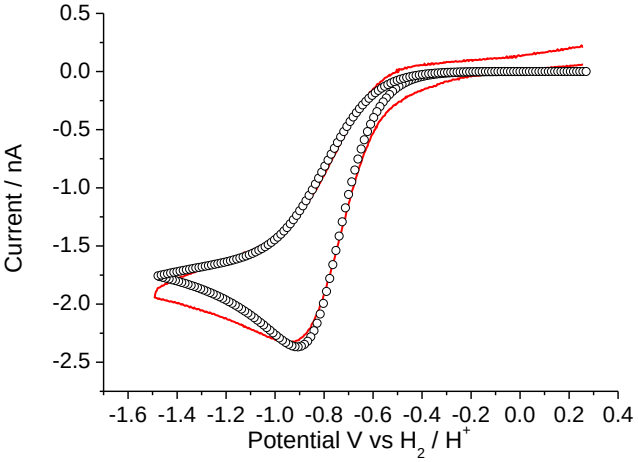

7.4.5. Scan rate study of H[NTf_2] reduction on Nickel in [C_2mim][NTf_2])

Ni
Scan rate: 100mV/s
Potential window (V): (-1.35, -0.5)
D (HNTf2): 2.5e-7 cm^2s^{-1}
D (H_2): 5.5e-6 cm^2s^{-1}
r $_{Ni}$: 5e-3 cm
α: 0.35
k^o : 1.3e-7 cm s^{-1}
C: 24 mM
E_f : -0.338 V

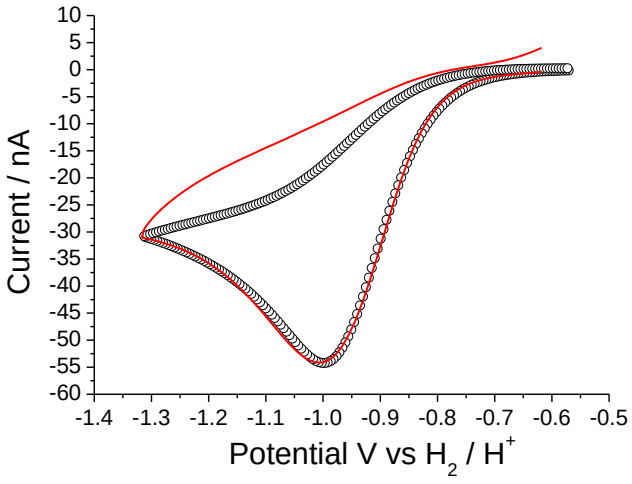

Ni
Scan rate: 200mV/s
Potential window (V): (-1.35, -0.5)
D (HNTf2): 2.5e-7 cm^2s^{-1}
D (H_2): 5.5e-6 cm^2s^{-1}
r $_{Ni}$: 5e-3 cm
α: 0.35
k^o : 1.3e-7 cm s^{-1}
C: 24 mM
E_f : -0.338 V

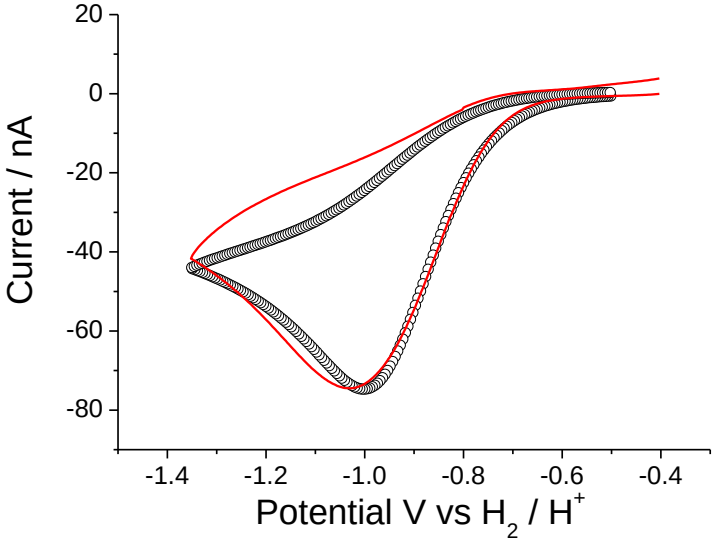

Ni
Scan rate: 400mV/s
Potential window (V): (-1.35, -0.5)
D (HNTf2): 2.5e-7 cm^2s^{-1}
D (H_2): 5.5e-6 cm^2s^{-1}
r $_{Ni}$: 5e-3 cm
α: 0.35
k^o : 1.3e-7 cm s^{-1}
C: 24 mM
E_f : -0.338 V

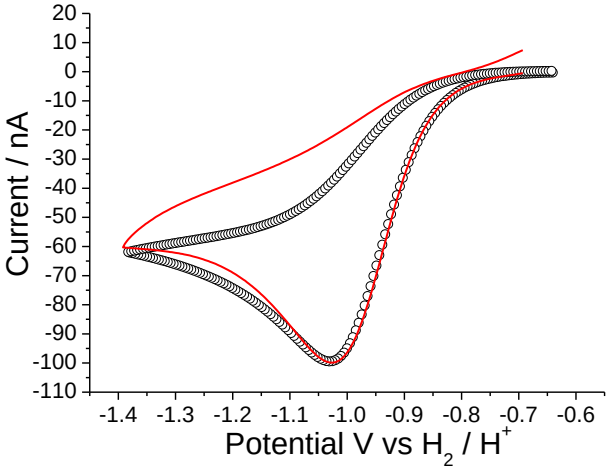

Ni
Scan rate: 600mV/s
Potential window (V): (-1.35, -0.5)
D (HNTf2): 2.5e-7 cm^2s^{-1}
D (H_2): 5.5e-6 cm^2s^{-1}
r $_{Ni}$: 5e-3 cm
α: 0.35
k^o : 1.3e-7 cm s^{-1}
C: 24 mM
E_f : -0.338 V

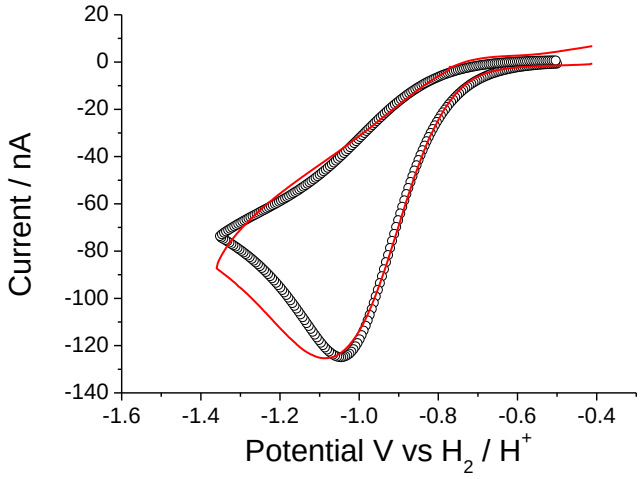

Ni
Scan rate: 800mV/s
Potential window (V): (-1.35, -0.5)
D (HNTf2): 2.5e-7 cm^2s^{-1}
D (H_2): 5.5e-6 cm^2s^{-1}
r $_{Ni}$: 5e-3 cm
α: 0.35
k^o : 1.3e-7 cm s^{-1}
C: 24 mM
E_f : -0.338 V

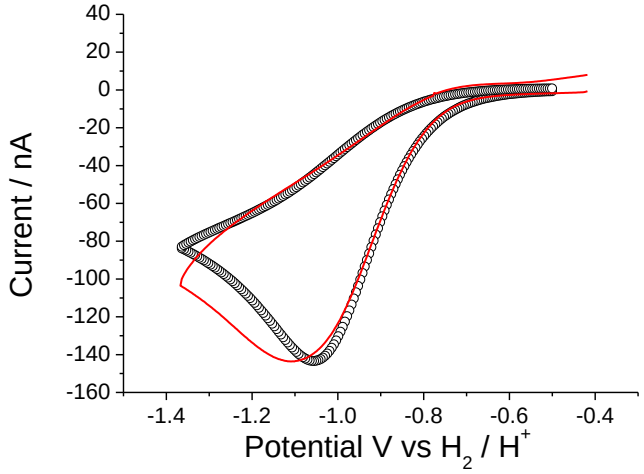

7.4.6. Scan rate study of H[NTf_2] reduction on Titanium in [C_2mim][NTf_2])

Ti
Scan rate: 100mV/s
Potential window (V): (-2.6, -0.6)
D (HNTf2): 2.5e-7 cm^2s^{-1}
D (H_2): 5.5e-6 cm^2s^{-1}
r $_{Ti}$: 2.5e-3 cm
α: 0.2
k^o : 2.6e-8 cm s^{-1}
C: 88 mM
E_f : -0.338 V

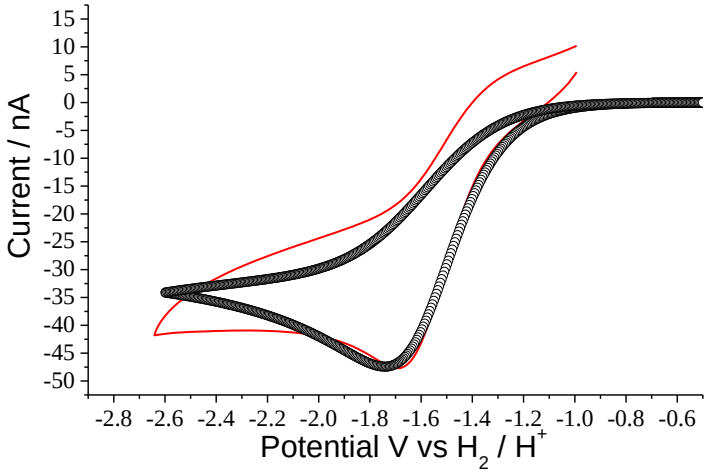

Ti
Scan rate: 200mV/s
Potential window (V): (-2.6, -0.6)
D (HNTf2): 2.5e-7 cm^2s^{-1}
D (H_2): 5.5e-6 cm^2s^{-1}
r $_{Ti}$: 2.5e-3 cm
α: 0.2
k^o : 2.6e-8 cm s^{-1}
C: 88 mM
E_f : -0.338 V

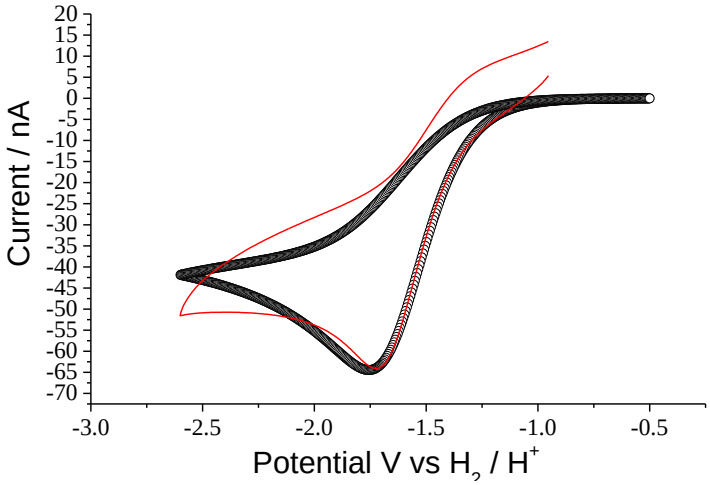

Ti
Scan rate: 400mV/s
Potential window (V): (-2.6, -0.6)
D (HNTf2): 2.5e-7 cm^2s^{-1}
D (H_2): 5.5e-6 cm^2s^{-1}
r $_{Ti}$: 2.5e-3 cm
α: 0.2
k^o : 2.6e-8 cm s^{-1}
C: 88 mM
E_f : -0.338 V

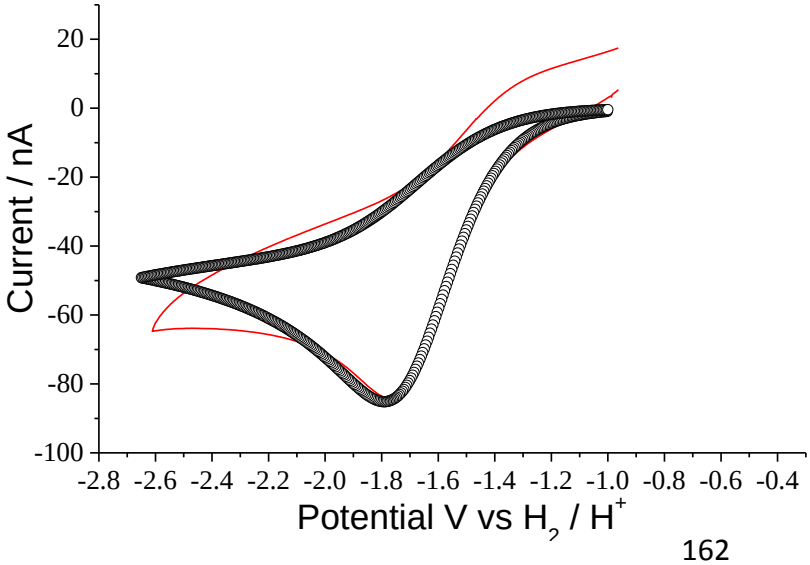

Ti
Scan rate: 600mV/s
Potential window (V): (-2.6, -0.6)
D (HNTf2): 2.5e-7 cm^2s^{-1}
D (H_2): 5.5e-6 cm^2s^{-1}
r $_{Ti}$: 2.5e-3 cm
α: 0.2
k^o : 2.6e-8 cm s^{-1}
C: 88 mM
E_f : -0.338 V

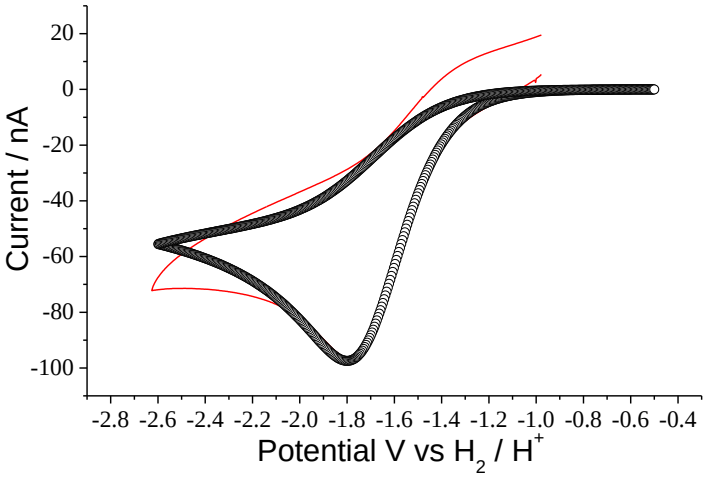

Ti
Scan rate: 800mV/s
Potential window (V): (-2.6, -0.6)
D (HNTf2): 2.5e-7 cm^2s^{-1}
D (H_2): 5.5e-6 cm^2s^{-1}
r $_{Ti}$: 2.5e-3 cm
α: 0.2
k^o : 2.6e-8 cm s^{-1}
C: 88 mM
E_f : -0.338 V

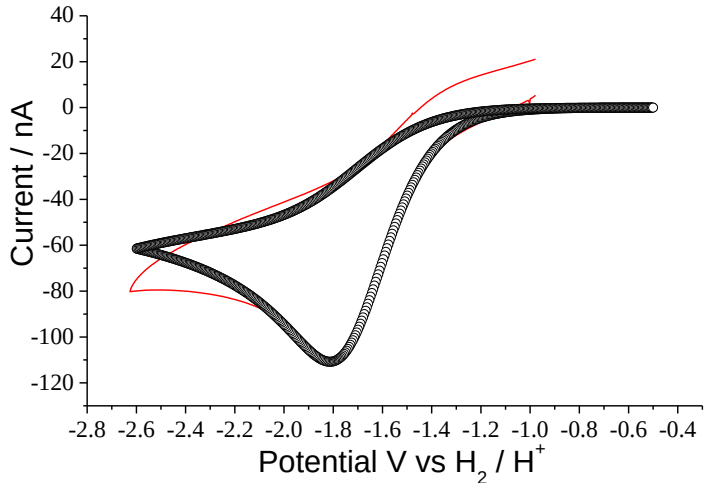

References

1 Y. Meng, L. Aldous, S. R. Belding, R. G. Compton, *Physical Chemistry Chemical Physics* 2012, *14*, 5222-5228.

2 P. H. Rieger, *Electrochemistry*. Editor, Prentice-Hall, Englewood Cliffs ; London, 1987, pp. xvii,508p.

3 B. E. Conway, J. O. Bockris, *Journal of Chemical Physics* 1957, *26*, 532-541.

4 S. Trasatti, *Journal of Electroanalytical Chemistry* 1972, *39*, 163-&.

5 L. A. Kibler, *Chemphyschem* 2006, *7*, 985-991.

6 J. A. Bautista-Martinez, L. Tang, J. P. Belieres, R. Zeller, C. A. Angell, C. Friesen, *Journal of Physical Chemistry C* 2009, *113*, 12586-12593.

7 F. A. Armstrong, N. A. Belsey, J. A. Cracknell, G. Goldet, A. Parkin, E. Reisner, K. A. Vincent, A. F. Wait, *Chemical Society Reviews* 2009, *38*, 36-51.

8 R. G. Compton, C. E. Banks, *Understanding voltammetry, 2nd ed.*, Editor, World Scientific, Singapore ; London, 2011, pp. xii, 371 p.

9 S. Fletcher, *Journal of Solid State Electrochemistry* 2009, *13*, 537-549.

10 F. Endres, S. Z. El Abedin, *Physical Chemistry Chemical Physics* 2006, *8*, 2101-2116.

11 L. Aldous, D. S. Silvester, W. R. Pitner, R. G. Compton, M. C. Lagunas, C. Hardacre, *Journal of Physical Chemistry C* 2007, *111*, 8496-8503.

12 Y. Meng, L. Aldous, R. G. Compton, *Journal of Physical Chemistry C* 2011, *115*, 14334-14340.

13 Y. Meng, L. Aldous, R. G. Compton, *Green Chemistry* 2010, *12*, 1926-1928.

14 Y. Meng, L. Aldous, B. S. Pilgrim, T. J. Donohoe, R. G. Compton, *New Journal of Chemistry* 2011, *35*, 1369-1375.

15 D. S. Silvester, L. Aldous, C. Hardacre, R. G. Compton, *Journal of Physical Chemistry B* 2007, *111*, 5000-5007.

16 D. S. Silvester, K. R. Ward, L. Aldous, C. Hardacre, R. G. Compton, *Journal of Electroanalytical Chemistry* 2008, *618*, 53-60.

17 R. Fukuta, Y. Katayama, T. Miura, *ECS Transactions* 2007, *3*, 567-576.

18 M. E. Bluhm, M. G. Bradley, R. Butterick, U. Kusari, L. G. Sneddon, *Journal of the American Chemical Society* 2006, *128*, 7748-7749.

19 R. F. de Souza, G. Loget, J. C. Padilha, E. M. A. Martini, M. O. de Souza, *Electrochemistry Communications* 2008, *10*, 1673-1675 10.1016/j.elecom.2008.08.029.

20 R. F. de Souza, J. C. Padilha, R. S. Goncalves, J. Rault-Berthelot, *Electrochemistry Communications* 2006, *8*, 211-216.

21 R. Wibowo, L. Aldous, S. E. W. Jones, R. G. Compton, *Chemical Physics Letters* 2010, *492*, 276-280.

22 E. I. Rogers, D. S. Silvester, S. E. W. Jones, L. Aldous, C. Hardacre, A. J. Russell, S. G. Davies, R. G. Compton, *Journal of Physical Chemistry C* 2007, *111*, 13957-13966.

23 E. I. Rogers, D. S. Silvester, D. L. Poole, L. Aldous, C. Hardacre, R. G. Compton, *Journal of Physical Chemistry C* 2008, *112*, 2729-2735.

24 U. Schröder, J. D. Wadhawan, R. G. Compton, F. Marken, P. A. Z. Suarez, C. S. Consorti, R. F. de Souza, J. Dupont, *New Journal of Chemistry* 2000, *24*, 1009-1015.

25 A. M. O'Mahony, D. S. Silvester, L. Aldous, C. Hardacre, R. G. Compton, *Journal of Chemical and Engineering Data* 2008, *53*, 2884-2891.

26 B. Huber, B. Roling, *Electrochimica Acta* 2011, *56*, 6569-6572 DOI 10.1016/j.electacta.2011.02.055.

27 R. Wibowo, L. Aldous, E. I. Rogers, S. E. W. Jones, R. G. Compton, *Journal of Physical Chemistry C* 2010, *114*, 3618-3626.

28 C. A. Paddon, D. S. Silvester, F. L. Bhatti, T. J. Donohoe, R. G. Compton, *Electroanalysis* 2007, *19*, 11-22.

29 D. Shoup, A. Szabo, *Journal of Electroanalytical Chemistry* 1982, *140*, 237-245.

30 A. J. Bard, L. R. Faulkner, *Electrochemical methods : fundamentals and applications*. 2nd ed. ed., Editor, John Wiley, New York ; Chichester, 2000, pp. xxi, 833 p.

Chapter 8 The Formal Potentials and Electrode Kinetics of the Proton / Hydrogen Couple in Various Room Temperature Ionic Liquids

In this chapter, the hydrogen evolution reaction is quantitatively investigated at a Pt electrode in series of room temperature ionic liquids vs Ag / Ag^+ redox couple, The measured formal potentials of the H_2 / H^+ ($HNTf_2$) redox couple in each RTIL reveals a dependence on the nature of anion, suggesting significant interaction between proton and anion. This work presented in this chapter was carried out with the assistance of Dr. Leigh Aldous and has been published in the Journal of Chemical Communications.[1] The theoretical models used including the programs for chronoamperometry and cyclic voltammetry simulation were reported in chapter 7,[2] and were written by D.Phil candidate Mr. Stephen R. Belding.

8.1 Introduction

Room temperature ionic liquids (RTILs) exist in the liquid state near room temperature, and are composed entirely of cations and anions. They have several characteristic properties, such as low volatility, high thermal stability, wide electrochemical potential windows and intrinsic conductivity,[3, 4] and RTILs are the subject of intense investigation relating to a vast number of fields such as gas sensors,[5] green synthesis and catalysis[6], electrodeposition,[7] batteries,[8] solar cells,[9] *etc.*

The high viscosity characteristic of the vast majority of RTILs results in a slowing down the mass diffusional transport and lowering the conductivity from what could be expected of a liquid composed entirely of ions. The high viscosity primarily derives from van der Waals forces and hydrogen bonding[7, 10] and is generally in the range of 30-450 cP at ambient temperatures.[4] While many solutes follow the Stokes-Einstein relationship,[11] namely that solute diffusivity is proportional to solvent viscosity, weakly-associating solutes which are

smaller than the RTIL ions can display significant deviation; examples are hydrogen[12] and sulphur dioxide[13].

Hydrogen (H_2) oxidation and proton reduction are seeming simple processes, but are of significant fundamental and practical relevance, particularly with regards to applications in fuel cells, gas sensors, pK_a determination and the establishment of a hydrogen reference electrode of the first kind. Semi-quantitative electrochemical investigations of proton reduction and hydrogen oxidation in RTILs have previously been reported at Au[14], Pt[15-18], Pd[19, 20] and GC[14] electrodes, as well as *ab initio* simulation of proton solvation dynamics.[21] Recently, the electrochemical proton reduction mechanism and kinetics were successfully determined in the RTIL $[C_2mim][NTf_2]$ at Pt, Ti, Ni, Mo and Ni electrodes.[2]

This chapter builds on the approach in chapter 7 and reports the first quantitative investigation probing both proton reduction and hydrogen evolution at a Pt electrode in a range of RTILs, and the observed proton/hydrogen redox couple is interpreted in light of features such as proton-anion interactions.

8.2 Results and discussions

Figure 8.1 displays cyclic voltammograms recorded at a Pt electrode for hydrogen bis(trifluoromethylsulfonyl)mide， $H[NTf_2]$, dissolved in three RTILs, $[C_4mim][NTf_2]$, $[C_4mim][OTf]$ and $[C_4mim][BF_4]$ *vs* the Ag/Ag^+ redox couple used throughout this work. The details of the Ag/Ag^+ reference electrode are listed in the previous chapter.[2] Clear reduction features can be observed for all three RTILs, relating to H^+ reduction to H_2, with an oxidation peak corresponding to accumulated H_2 present on the reverse sweep. A range of further scan rates, as well as data for the RTILs $[C_4mpyrr][NTf_2]$ and $[C_4dmim][NTf_2]$, is available in the appendix to this chapter. Well-defined, quasi-reversible features were observed for all RTILs except $[C_4mim][BF_4]$, which displayed broad, irreversible features.

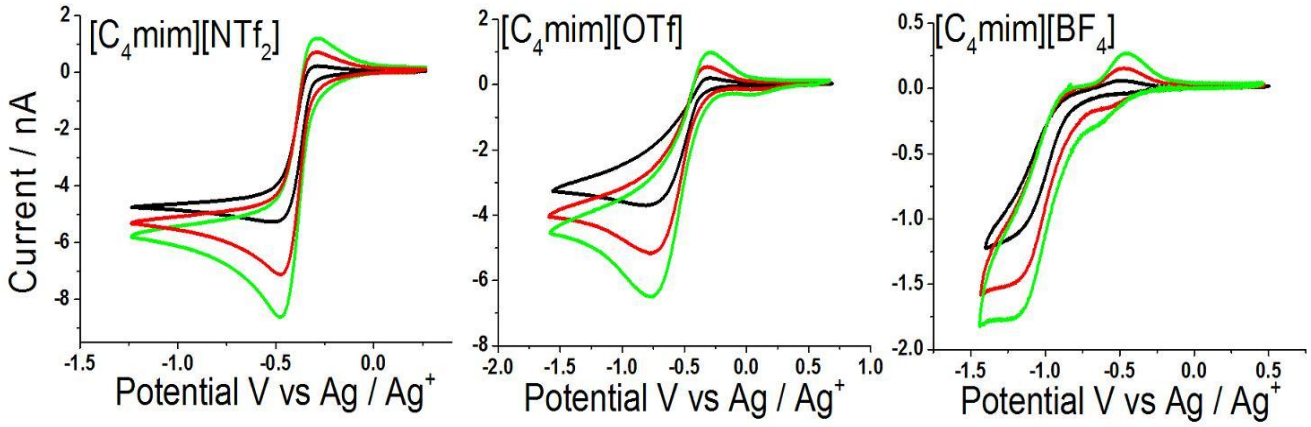

Figure 8.1 Voltammograms for $HNTf_2$ reduction at a Pt electrode (radius 10 µm) in $[C_4mim][NTf_2]$, $[C_4mim][OTf]$ and $[C_4mim][BF_4]$ vs Ag / Ag^+ couple at a range of scan rate 0.1, 0.4 and 0.8 V s^{-1}

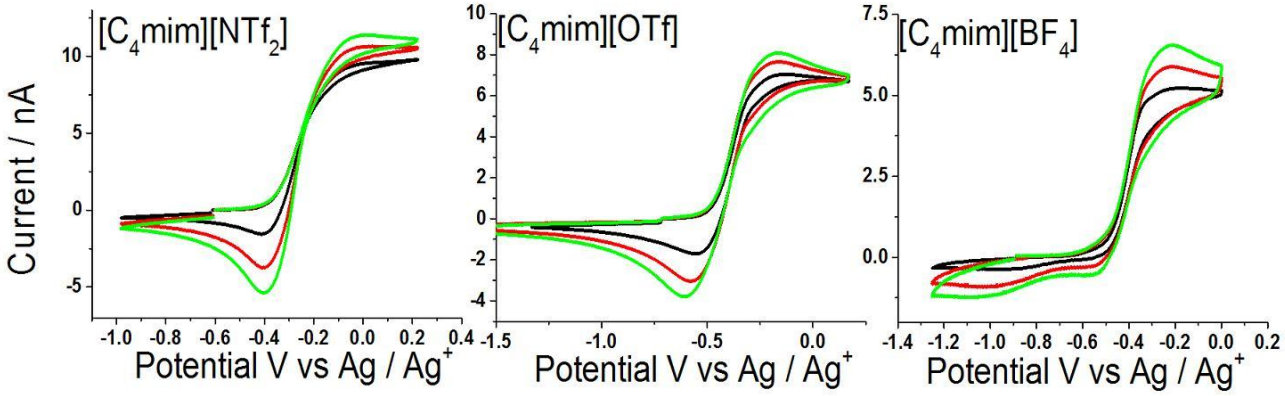

Figure 8.2 Voltammograms for H_2 oxidation at a Pt electrode (radius 10 µm) in $[C_4mim][NTf_2]$, $[C_4mim][OTf]$ and $[C_4mim][BF_4]$ vs Ag / Ag^+ couple at a range of scan rate 0.1, 0.4 and 0.8 V s^{-1}

The mass transport-corrected Tafel equation[22] was applied and the heterogeneous charge transfer coefficient, α, was found to be 0.25 in$[C_4mim][OTf]$, 0.27 in $[C_4mim][BF_4]$ andbetween 0.45-0.55 in the three $[NTf_2]^-$-based RTILs, which indicates that the first electron transfer is rate determining step in all of these RTILs. This is in contrast to aqueous solution, where the α value calculated by Tafel analysis is 1.5 at a Pt surface showing that the second electron transfer in the formation of H_2 from $2H^+$ is rate limiting.[23] Therefore, the

electrochemical kinetics and mechanism show significant differences in RTILs from what is commonly observed in aqueous electrolytes.[23]

Potential step measurements were carried out in all five RTILs to measure the proton diffusion coefficient using the Shoup and Szabo expression;[24] the best fits for simulated data for all the RTILs are displayed in the SI. The Shoup and Szabo simulated data gave the diffusion coefficients (D) for the protonic species, which are listed in Table 8.1, as well as the known viscosities for the RTILs.[4]

Figure 8.2 displays CVs recorded for the oxidation of H_2 in H_2-saturated $[C_4mim][NTf_2]$, $[C_4mim][OTf]$ and $[C_4mim][BF_4]$.at a Pt electrode *vs.* Ag/Ag^+ reference electrode at 298 K. Voltammograms obtained over a range of scan rates, as well as scans recorded in $[C_4dmim][NTf_2]$ and $[C_4mpyrr][NTf_2]$ are shown in the appendix. *Quasi*-reversible voltammetry was observed in $[C_4mim][OTf]$ and all three $[NTf_2]^-$-based RTILs, with irreversible voltammetry in $[C_4mim][BF_4]$. A reduction peak associated with protons formed by hydrogen oxidation was observed on the reverse scan in all RTILs.

Chronoamperometric experiments were performed in order to determine both the concentration (c) and D of H_2 in the five H_2-saturated RTILs. All experimental data and the best fit results using the Shoup and Szabo expression[24] are displayed in the appendix, while the c and D values are displayed in Table 8.1.

The Stokes-Einstein relationship predicts that for analytes of similar dimensions to the solvent, a linear relationship is observed between the D of solutes and the inverse of solvent viscosity, η. Figure 8.3 displays plots of (a) the D of the proton and (b) D of H_2 *vs.* η^{-1}. The linear relationship for the proton indicates that its diffusion is proportional to RTIL viscosity, and likely diffuses as $H[A]_x$, where A is the RTIL anion and $x \geq 1$. The scatter observed for

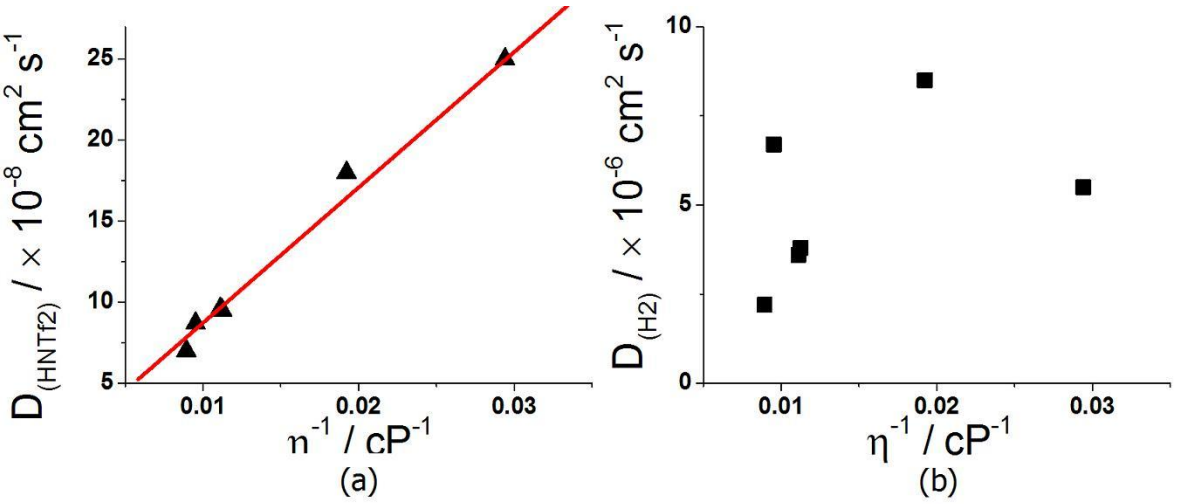

Figure 8.3 plot of diffusion coefficient (D) of both (a) $HNTf_2$ and (b) H_2 at 298 K against the inverse of viscosity (η) of RTIL in table 8.1

H_2 indicates that that the weakly-associating H_2 molecule is independent of RTIL viscosity due to the extremely small solvatodynamic radii of the H_2 molecules when dissolved in the RTIL, allowing the H_2 to move around the ions, where possible, in preference to displacing them. This latter observation is in agreement with a similar plot obtained by Silvester *et al.*[16] and the relatively low activation energy of diffusion of H_2 observed in $[C_2mim][NTf_2]$.[12] Therefore as η increases an increasing discrepancy in *D* between that of protons and hydrogen is expected.

Finally, CVs were recorded in the five RTILs containing both $H[NTf_2]$ and H_2 simultaneously, with the concentration of $H[NTf_2]$ fixed and H_2 varied by varying the partial pressure of H_2. Figure 8.4 displays scans recorded in $[C_4mim][NTf_2]$, $[C_4mim][OTf]$ and $[C_4mim][BF_4]$, with data for $[C_4mpyrr][NTf_2]$ and $[C_4dmim][NTf_2]$ in the appendix 8.4. All CVs were recorded from the open circuit potential, scanning into the H_2 reduction feature first, and the H_2 reduction feature decreased as the H_2 partial pressure was decreased. The potential separation between oxidation and reduction features demonstrated reversible

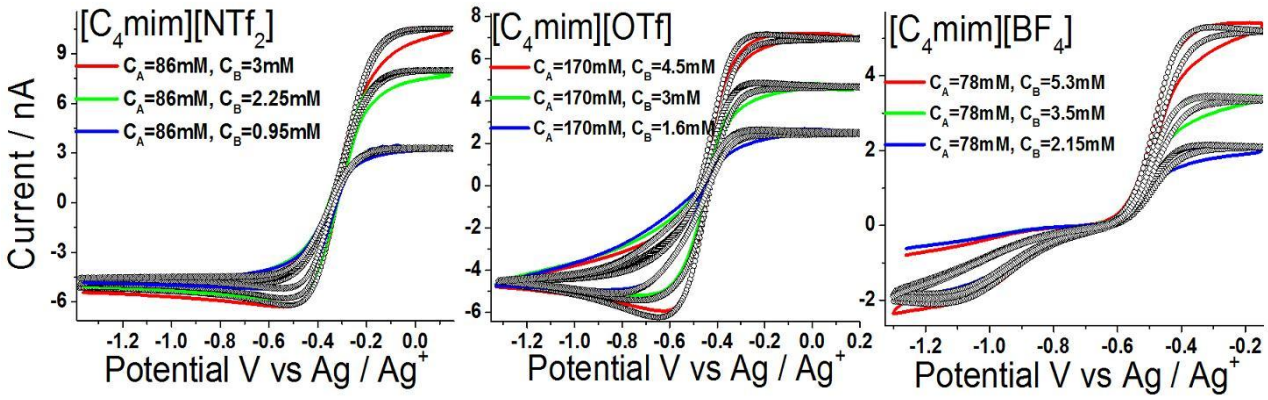

Figure 8.4 Concentration study of $HNTf_2$ and H_2 at a Pt electrode (radius 10 µm) in $[C_4mim][NTf_2]$, $[C_4mim][OTf]$ and $[C_4mim][BF_4]$ vs Ag / Ag^+ couple at 0.1 V s^{-1}. (Experimental data, line; simulated data, scatter.)

voltammetry for RTILs with the $[NTf_2]^-$ and $[OTf]^-$-anions, indicating weak interactions between the proton and solvating anions. In the case of $[C_4mim][BF_4]$, irreversible voltammetry was observed. The hydrolysis of $[C_4mim][BF_4]$, either in dilute solution[25] or in contact with water[26] is well-reported. However, the hydrolytic decomposition of $[BF_4]^-$ in contact with a proton in an RTIL in the absence of water (as in this study) is less well investigated. For example, Thomazeau *et al.* have successfully investigated anhydrous $[C_4mim][BF_4]$ containing $H[NTf_2]$, and found this system to possess a more acidic Hammett function than $[C_4mim][NTf_2]$ containing $H[NTf_2]$.[27]

Table 8.1 Electrochemical parameters determined for proton reduction and hydrogen oxidation on Pt over a range of different RTILs at 298 K

(a)

RTILs	η at 298K (cP)	$D_{(HNTf2)}$ / $\times10^{-8}$ ($cm^2\ s^{-1}$)[(a)]	$D_{(H2)}$ / $\times10^{-6}$ ($cm^2\ s^{-1}$)[(b)]	$C_{(H2)}$ (mM)
$[C_2mim][NTf_2]$	34	25	5.5	4.1
$[C_4mim][NTf_2]$	52	18	8.5	3
$[C_4mpyrr][NTf_2]$	89	9.5	3.8	5.9
$[C_4dmim][NTf_2]$	105	8.7	6.7	2.85
$[C_4mim][OTf]$	90	9.6	3.6	4.5
$[C_4mim][BF_4]$	112	7	2.2	5.3

(b)

RTILs	α	E_f^o (V *vs.* Ag/Ag$^+$)	k_c / × 10^{-6} (cm s^{-1})	k_a / × 10^{-5} (cm s^{-1})
[C_2mim][NTf_2]	0.5	-0.338±0.004	4.5	6.5
[C_4mim][NTf_2]	0.55	-0.346±0.004	5.5	6
[C_4mpyrr][NTf_2]	0.45	-0.35±0.004	4	6
[C_4dmim][NTf_2]	0.47	-0.352±0.004	2.75	7.55
[C_4mim][OTf]	0.27	-0.457±0.004	3	7.5
[C_4mim][BF_4]	0.25	-0.587±0.004	0.08	0.9

(a) D of proton in RTIL containing only $HNTf_2$ at a Pt electrode

(b) D of H2 in H2-saturated RTIL at a Pt electrode

Next, theoretical models were used to simulate the proton reduction and hydrogen oxidation steps in all five RTILs separately (*i.e.* solutions containing only H[NTf_2] or H_2), and the full theoretical model and simulation results are presented in full in section 2.8. This allowed the determination of the apparent rate constants (see previous chapter) for electron transfer, k'$_a$ and k'$_c$, while the *c*, *D*, α and β values were all kept within 5 % of their independently determined values by chronoamperometry and Tafel plots. These simulations yielded the equilibrium potential, E_e (when current density, j = 0, as described in the appendix), which was related to the formal potential, E_f^0, by the Nernst Equation,

$$E_e = E_f^0 + \frac{RT}{F} ln\left(\frac{[H^+]}{[H_2]^{\frac{1}{2}}}\right) \qquad (8.1)$$

where [H^+] and [H_2] are already known. The calculated formal potentials are recorded for each RTIL in Table 8.1. It can be observed that the [NTf_2]$^-$-based RTILs have a similar formal potential, equal to *ca.* -0.34 ± 0.01 V *vs.* Ag/Ag$^+$, indicating that the cations do not have an obvious influence on the formal potential of the H_2 / H^+ couple at a Pt electrode, and suggesting that a standard reference scale based upon the H_2 / H^+ couple could be developed for most [NTf_2]$^-$-based RTILs. However, the fundamental role of the anion can also be observed for the [OTf]$^-$ and [BF_4]$^-$-based ILs, with the formal potential changing by *ca.* 100 and 220 mV, respectively. The more negative formal potential value indicates easier

oxidation of the H_2 in these RTILs, indicative of stronger interactions between the protonic product and the $[OTf]^-$ and $[BF_4]^-$-anions.

Finally, using the obtained formal potential values, the voltammetry of the RTILs containing both H_2 and H^+ in the same solution (see Appendix 8.4) could be simulated in order to obtain the rate constants for electron transfer, k_a^0 and k_c^0. The best fit simulation data is overlaid in Figure 8.4, while the measured k_a^0 and k_c^0 values are summarised in Table 8.1. It is noted that the kinetic rate constants are approximately independent of the cation and similar for $[OTf]^-$ and $[NTf_2]^-$-based ILs, but are significantly slower in $[C_4mim][BF_4]$.

8.3 Conclusions

Proton reduction and hydrogen oxidation has been quantitatively investigated separately to give their independent kinetic and thermodynamic parameters, as well as mechanism, in addition to a series of fundamental electrochemical parameters. The measured diffusion coefficients of proton and hydrogen suggest that protons display Stokes-Einstein-like transport whereas H_2 does not.

Using the comprehensive analysis above, the H_2 / H^+ couple has been quantitatively studied at a Pt electrode over a range of different RTILs *vs.* an Ag / Ag^+ reference electrode for the first time. Changes in the formal potential of the H_2 / H^+ redox couple is almost entirely attributable to the anion rather than cation, which demonstrates the influence of the interaction between proton and anion, and changes both kinetic and thermodynamic parameters.

8.4 Appendix- Simulated voltammograms

The details of scan rate study of simulated datas (o) and experimental datas (-) for $H[NTf_2]$ reduction, hydrogen oxidation and hydrogen evolution reaction over a range of RTILs at a Pt electrode vs Ag/Ag^+ reference redox couple

8.4.1 Scan rate study of $HNTf_2$ reduction on a range of RTILs

(1) $[C_4mim][NTf_2]$ RTIL

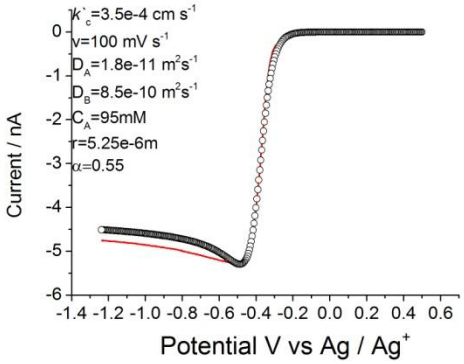

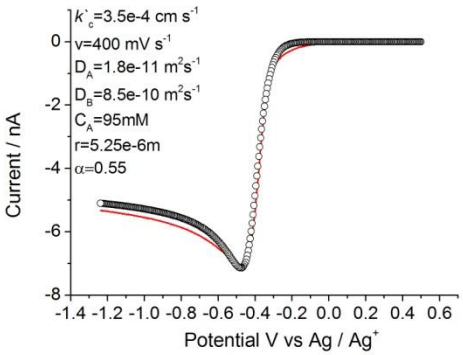

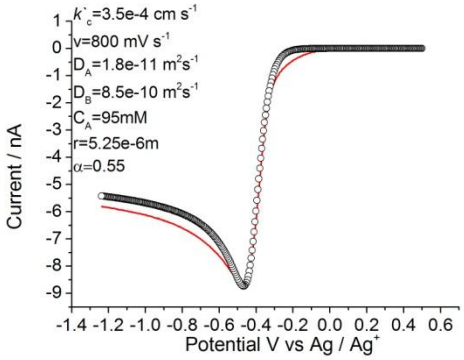

(2) $[C_4mpyrr][NTf_2]$ RTIL

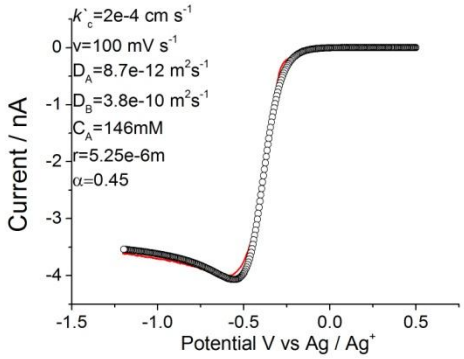

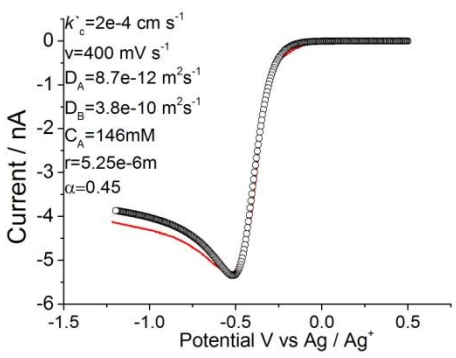

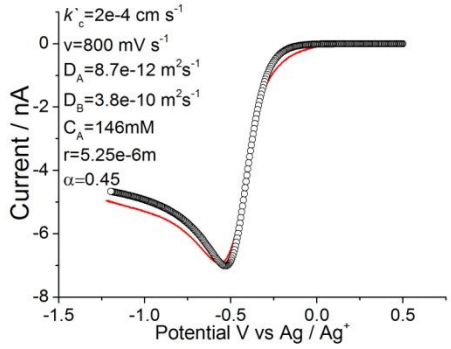

(3) [C4dmim][NTf2] RTIL

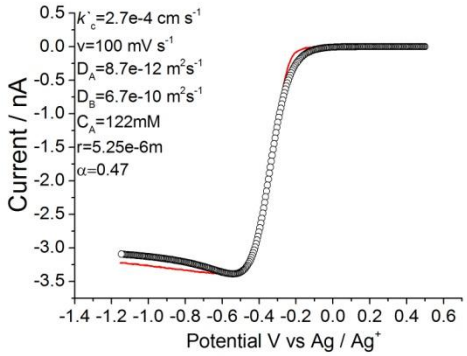

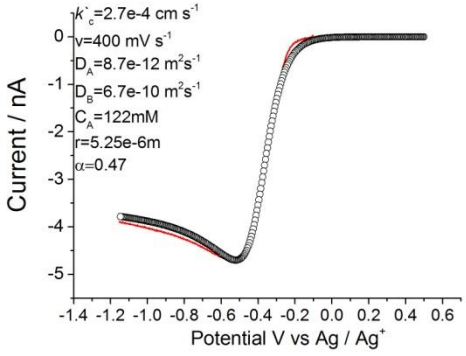

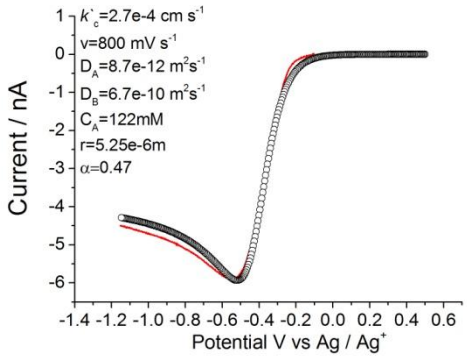

(4) [C4mim][OTf] RTIL

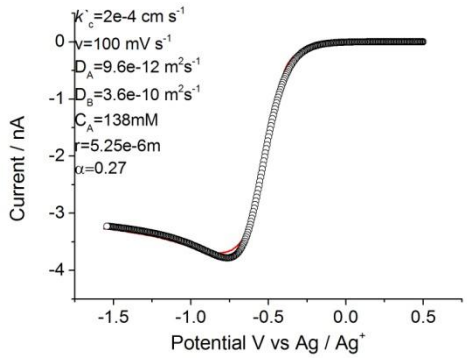

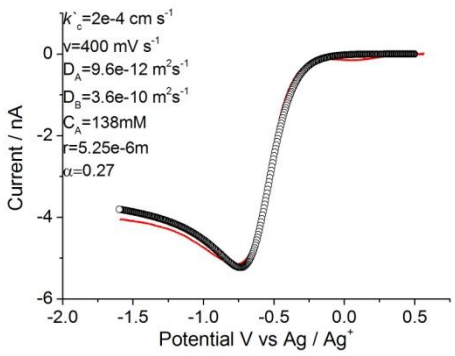

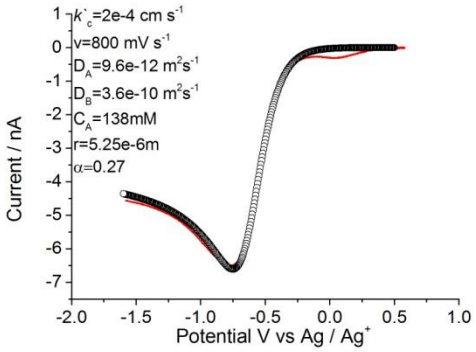

(5) [C_4mim][BF_4] RTIL

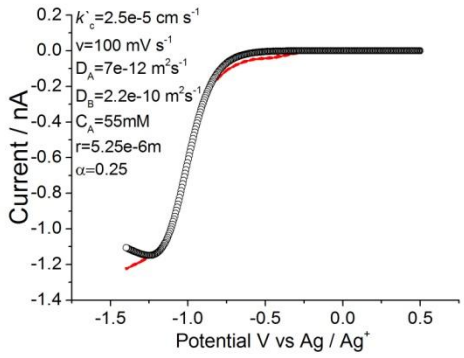

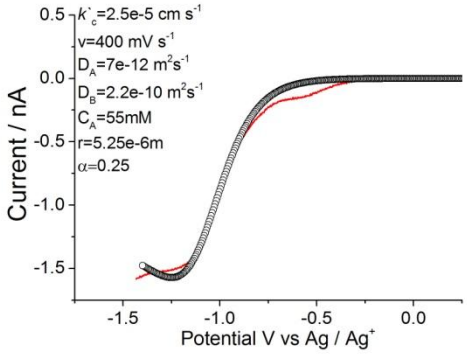

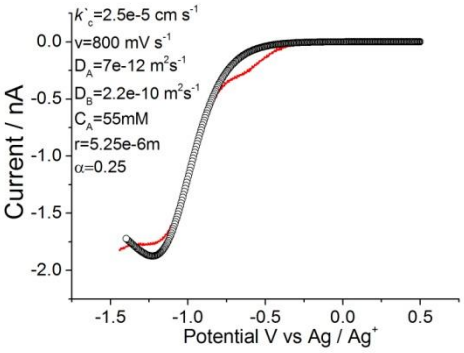

Comment: The small deviation between theory and experiment likely arises from non-Faradaic effects.

8.4.2 Scan rate study of hydrogen oxidation on a range of RTILs

(1) [C_4mim][NTf_2] RTIL

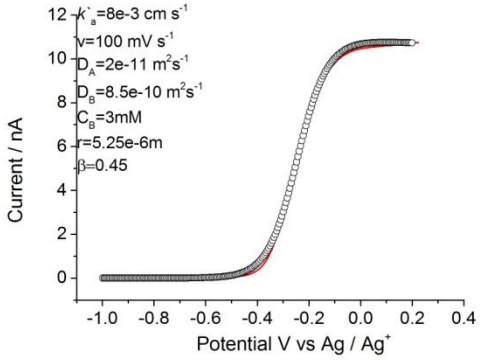

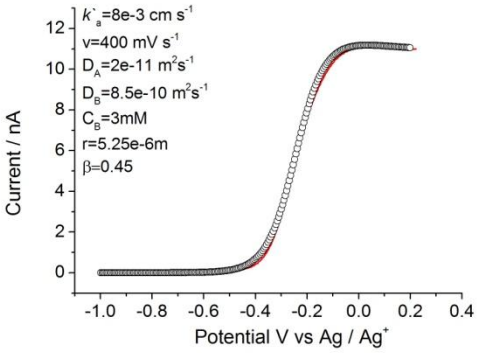

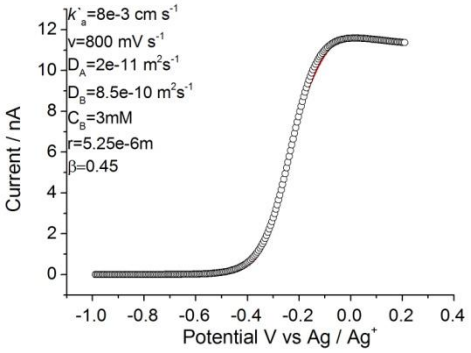

(2) [C_4mpyrr][NTf_2] RTIL

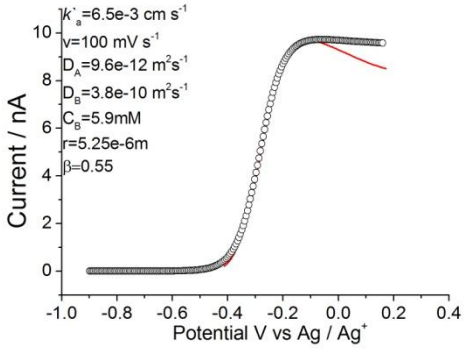

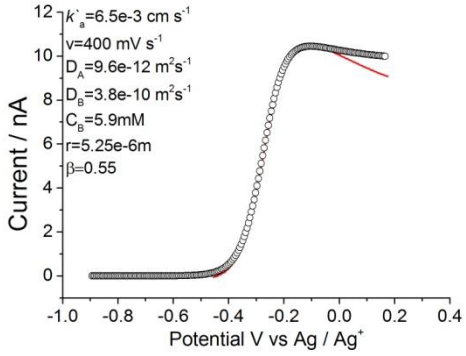

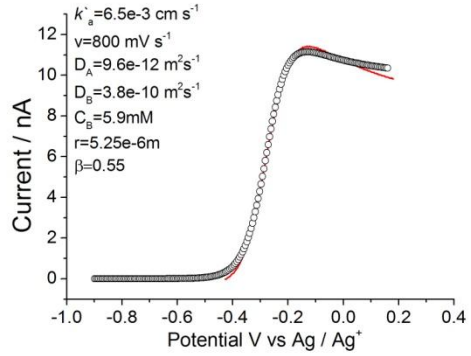

(3) *[C$_4$dmim][NTf$_2$] RTIL*

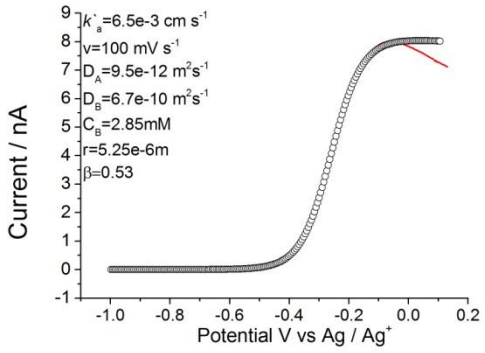

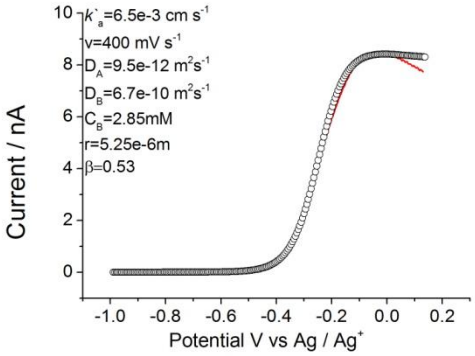

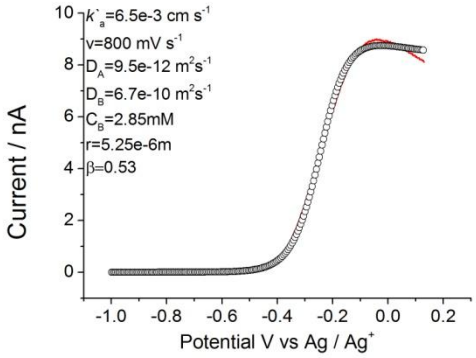

(4) *[C$_4$mim][OTf] RTIL*

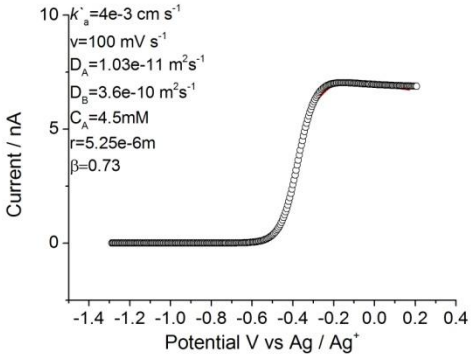

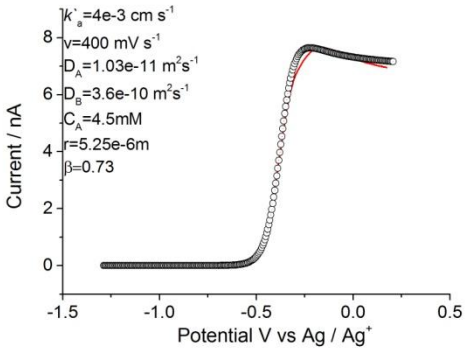

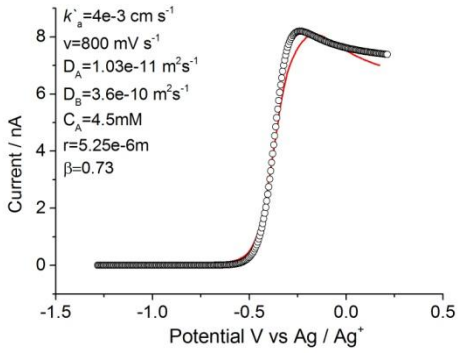

(5) *[C_4mim][BF_4] RTIL*

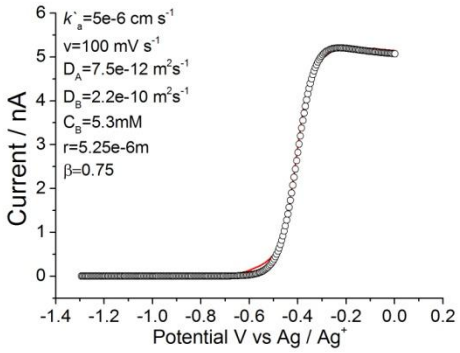

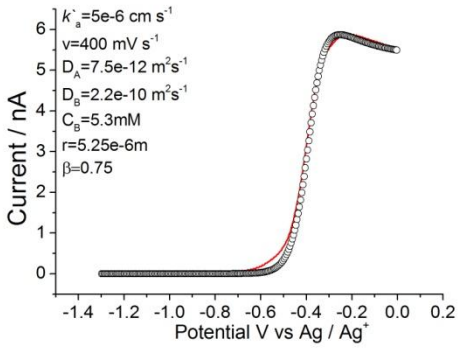

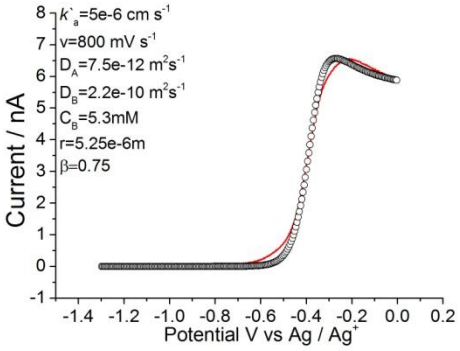

Comment: The small deviation between theory and experiment likely arises from non-Faradaic effects.

8.4.3 Hydrogen evolution reaction containing fixed concentration of $HNTf_2$ and various concentration of hydrogen, A= $HNTf_2$, B= H_2

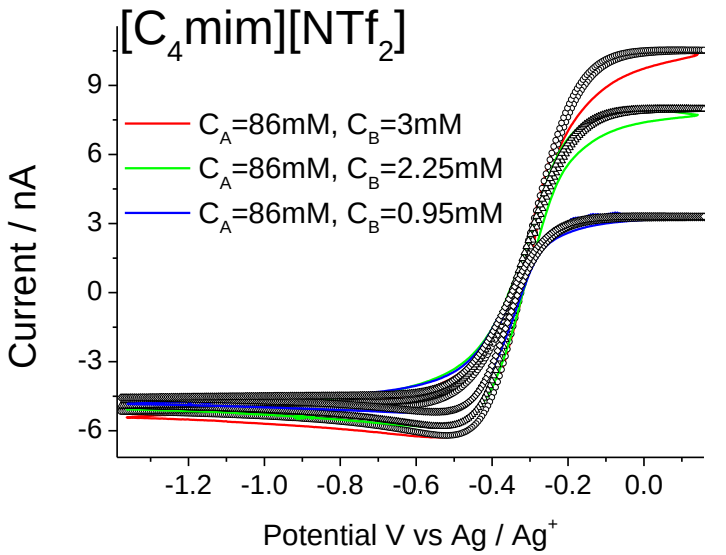

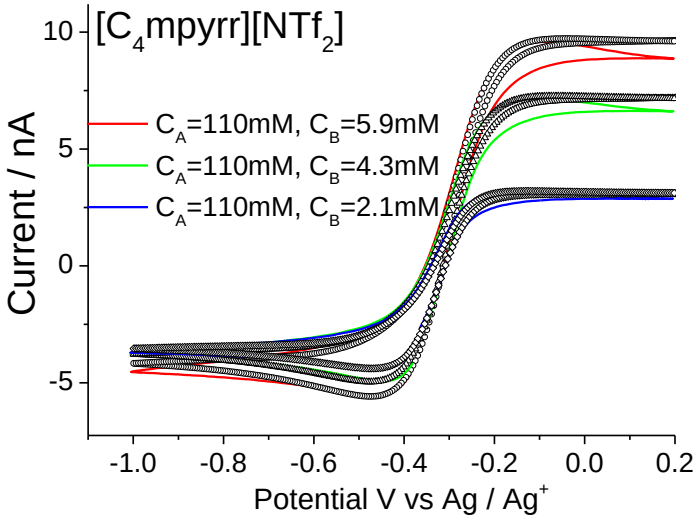

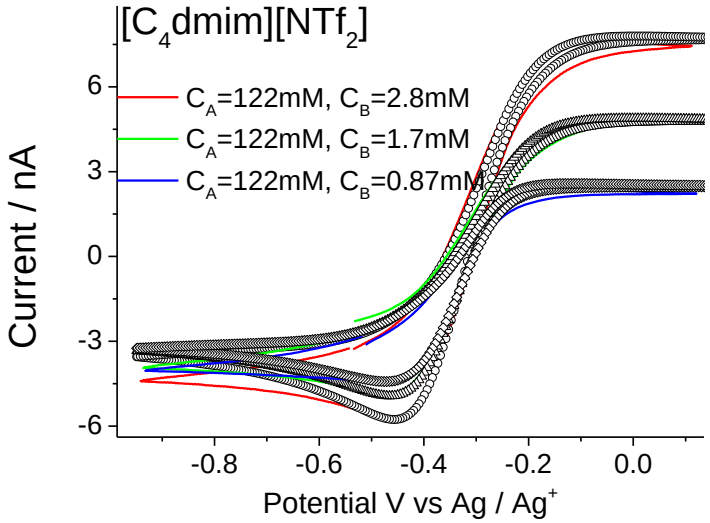
[C4dmim][NTf2]
CA=122mM, CB=2.8mM
CA=122mM, CB=1.7mM
CA=122mM, CB=0.87mM
Current / nA
Potential V vs Ag / Ag+

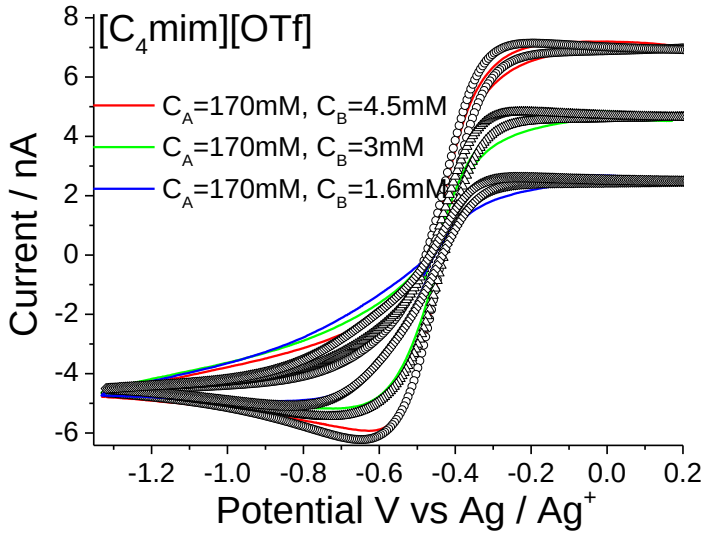
[C4mim][OTf]
CA=170mM, CB=4.5mM
CA=170mM, CB=3mM
CA=170mM, CB=1.6mM
Current / nA
Potential V vs Ag / Ag+

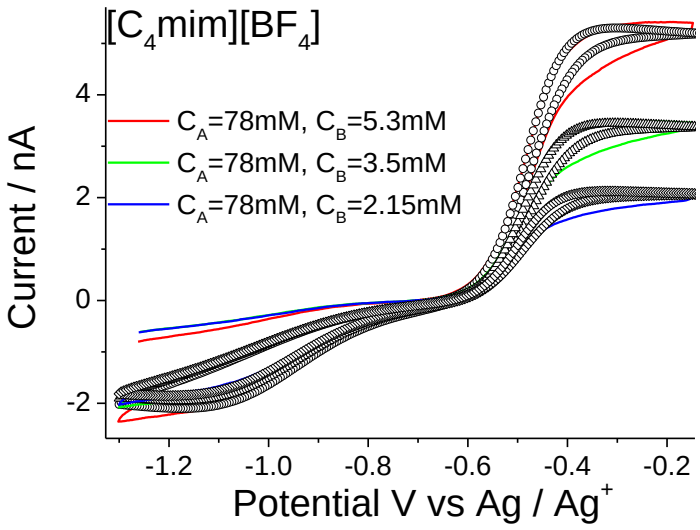
[C4mim][BF4]
CA=78mM, CB=5.3mM
CA=78mM, CB=3.5mM
CA=78mM, CB=2.15mM
Current / nA
Potential V vs Ag / Ag+

References

1 Y. Meng, L. Aldous, S. R. Belding, R. G. Compton, *Chemical Communications* 2012, *48*, 5572-5574.

2 Y. Meng, R. Stephen, R. G. Compton, *Phys. Chem. Chem. Phys* 2012, *14,* 5222-5228.

3 D. S. Silvester, R. G. Compton, *Zeitschrift Fur Physikalische Chemie-International Journal of Research in Physical Chemistry & Chemical Physics* 2006, *220*, 1247-1274.

4 L. E. Barrosse-Antle, A. M. Bond, R. G. Compton, A. M. O'Mahony, E. I. Rogers, D. S. Silvester, *Chem Asian J* 2010, *5*, 202-230.

5 X. J. Huang, L. Aldous, A. M. O'Mahony, F. J. del Campo, R. G. Compton, *Analytical Chemistry* 2010, *82*, 5238-5245.

6 D. Freudenmann, S. Wolf, M. Wolff, C. Feldmann, *Angewandte Chemie-International Edition* 2011, *50*, 11050-11060.

7 F. Endres, S. Z. El Abedin, *Physical Chemistry Chemical Physics* 2006, *8*, 2101-2116.

8 R. J. Chen, H. Q. Zhang, F. Wu, *Progress in Chemistry* 2011, *23*, 366-373.

9 C. Zafer, K. Ocakoglu, C. Ozsoy, S. Icli, *Electrochimica Acta* 2009, *54*, 5709-5714.

10 P. Wasserscheid, W. Keim, *Angewandte Chemie-International Edition* 2000, *39*, 3772-3789.

11 A. Einstein, Dover, New York*,* 1956.

12 Y. Meng, L. Aldous, R. G. Compton, *Journal of Physical Chemistry C* 2011, *115*, 14334-14340.

13 L. E. Barrosse-Antlle, C. Hardacre, R. G. Compton, *Journal of Physical Chemistry B* 2009, *113*, 1007-1011.

14 L. Aldous, D. S. Silvester, W. R. Pitner, R. G. Compton, M. C. Lagunas, C. Hardacre, *Journal of Physical Chemistry C* 2007, *111*, 8496-8503.

15 A. M. Navarro-Suarez, J. C. Hidalgo-Acosta, L. Fadini, J. M. Feliu, M. F. Suarez-Herrera, *Journal of Physical Chemistry C* 2011, *115*, 11147-11155.

16 D. S. Silvester, K. R. Ward, L. Aldous, C. Hardacre, R. G. Compton, *Journal of Electroanalytical Chemistry* 2008, *618*, 53-60.

17 R. Fukuta, Y. Katayama, T. Miura, *ECS Transactions* 2007, *3*, 567-576.

18 J. A. Bautista-Martinez, L. Tang, J. P. Belieres, R. Zeller, C. A. Angell, C. Friesen, *Journal of Physical Chemistry C* 2009, *113*, 12586-12593.

19 Y. Meng, L. Aldous, R. G. Compton, *Green Chemistry* 2010, *12*, 1926-1928.

20 Y. Meng, L. Aldous, B. S. Pilgrim, T. J. Donohoe, R. G. Compton, *New Journal of Chemistry* 2011, *35*, 1369-1375.

21 M. G. Del Popolo, J. Kohanoff, R. M. Lynden-Bell, *Journal of Physical Chemistry B* 2006, *110*, 8798-8803.

22 I. Streeter, R. G. Compton, *Electrochimica Acta* 2007, *52*, 4305-4311.

23 P. H. Rieger, *Prentice-Hall, Englewood Cliffs, London* 1987.

24 D. Shoup, A. Szabo, *Journal of Electroanalytical Chemistry* 1982, *140*, 237-245.

25 C. Villagran, C. E. Banks, C. Hardacre, R. G. Compton, *Analytical Chemistry* 2004, *76*, 1998-2003.

26 M. G. Freire, C. M. S. S. Neves, I. M. Marrucho, J. o. A. P. Coutinho, A. M. Fernandes, *The Journal of Physical Chemistry A* 2009, *114*, 3744-3749.

27 C. Thomazeau, H. Olivier-Bourbigou, L. Magna, S. Luts, B. Gilbert, *Journal of the American Chemical Society* 2003, *125*, 5264-5265.

Chapter 9 The electroreduction of benzoic acid: voltammetric observation of adsorbed hydrogen at a platinum microelectrode in room temperature ionic liquids

In this chapter, the electrochemical reduction of benzoic acid in the presence and absence of hydrogen (H_2) has been investigated on a 10 μm diameter platinum microelectrode in four different room temperature ionic liquids (RTILs) versus Ag / Ag^+ , namely $[C_4mim][NTf_2]$, $[C_4mpyrr][NTf_2]$, $[C_4mim][OTf]$ and $[C_4mim][BF_4]$. In all cases, reductive voltammetry is observed, and is suggested to occur via a CE mechanism in which dissociation of benzoic acid is followed by electron transfer to H^+ ultimately forming adsorbed hydrogen. Furthermore, the adsorbed H atoms formed from the reduction of benzoic acid, could be used to achieve the rapid hydrogenolysis of the organic compound (bis(benzyloxycarbonyl)-L-lysine) on the timescale of the voltammetric technique under moderate conditions (298 K). The work has been carried out with the collaboration of Mr. Sarah Norman and Prof. Christopher Hardacre who have synthesized the RTIL used in this work. It has been submitted to Journal of Physical Chemistry Chemistry Physics.

9.1 Introduction

The hydrogen evolution reaction (HER) and the associated H atom adsorption are some of the most widely studied fundamental electrochemical processes at a vast range of liquid / solid interfaces with very different behaviours seen at different electrode materials.[1-4] Research on the HER and H adsorption on metallic surfaces or metallic alloys or modified electrodes[5-9] as well as H absorption into the metals, such as Pd and Pd alloys[10, 11], is of great interest to electrochemical surface science, corrosion technology and new energy exploitation fields. For instance, the understanding of hydrogen-substrate interactions, of charge transfer, as well as the interactions between adsorbed species is of particular significance to the development of hydrogen-based fuel cells.[12, 13]

Room temperature ionic liquids (RTILs) have become progressively more available for electrochemical use due to helpful generic properties, such as extremely low saturated vapour pressures, large potential windows, high chemical and thermal stability, good electrical conductivity, although they do suffer from high viscosity.[14, 15] They are being widely used as solvents in many electrochemical experiments.[16, 17] It is of interest to explore the hydrogen absorption phenomenon in RTIL media, as addressed in this paper.

The dynamic dissociation constant, pK_a, of benzoic acid is found to be 9 ~ 10.5 in RTILs,[18] comparable to that of $HNTf_2$ to be -3.5 ~-5 in RTILs.[19] The electro-chemical reaction of benzoic acid has been reported in different solvents, such as RTILs, acidic media,[20, 21] dimethylformamide[22] and dimethyl sulfoxide,[23] giving the following generic CE mechanism:

$$C_6H_5COOH \rightleftarrows C_6H_5COO^- + H^+ \tag{9.1}$$

$$H^+ + M + e^- \rightarrow H - M \rightarrow \frac{1}{2}H_2 + M \tag{9.2}$$

where M is the metallic electrode. Electrochemically *quasi*-reversible or irreversible behaviour is typically seen in the corresponding voltammograms.[24] The diffusion coefficients of benzoic acid have been measured in RTILs, using potential-step chronoamperometric transients.[25] The dissociation constant of benzoic acid, pK_a, has been reported to reveal the higher acidity of benzoic acid in water solution than in RTILs.[26]

In the previous chapter we developed a stable Ag / Ag^+ reference electrode to allow us measure the formal potential of the H_2 / H^+ couple in RTILs.[27, 28] In the work presented in this chapter, we explore the electrochemical characteristics of underpotential deposition (UPD) H for the first time. In particular, the reduction of benzoic acid in the presence and absence of hydrogen, forming UPD H visible on the voltammetric reverse sweep, is investigated at a Pt microelectrode in four RTILs under well defined conditions. In addition, to the first observation of UPD H on Pt in RTIL media, we show the rapid hydrogenolysis of an organic

compound, displaying proof of concept that the UPD H can be used potentially synthetically for rapid hydrogenolysis.

9.2. Results and Discussions

9.2.1 The reduction of benzoic acid in RTILs

Typical voltammograms for the reduction of *ca.* 50mM benzoic acid at a 10 μm diameter Pt microelectrode in $[C_4mim][NTf_2]$, $[C_4mpyrr][NTf_2]$, $[C_4mim][OTf]$ and $[C_4mim][BF_4]$ over a range of scan rates (0.1, 0.4, 0.8, 2, 5, 10 and 20 V s^{-1}) *vs* Ag/ Ag^+ redox couple are displayed in figure 9.1, which shows similar overlapping reduction peaks and separated oxidation peaks over the range of RTILs studied: Peak Potentials: $[C_4mim][NTf_2]$, -1.37V; $[C_4mpyrr][NTf_2]$, -1.425V; $[C_4mim][OTf]$, -1.454V; $[C_4mim][BF_4]$), -1.335V for the cathodic sweep; $[C_4mim][NTf_2]$, -0.747V and -0.027V; $[C_4mpyrr][NTf_2]$, -0.988V and -0.134V; $[C_4mim][OTf]$, -0.754V and -0.189V; $[C_4mim][BF_4]$, -0.768V and -0.22V for the anodic sweep. It is believed that the main reduction waves can be assigned to the reduction of benzoic acid as follows.

$$C_6H_5COOH \rightleftarrows C_6H_5COO^- + H^+ \tag{9.3}$$

$$H^+ + e^- \rightleftarrows H_{ads}^{\cdot} \rightarrow \frac{1}{2}H_2 \tag{9.4}$$

The reduction waves at the more negative potential, especially obvious for $[C_4mim][OTf]$ may arise from direct reduction of benzoic acid. It is seen that near steady state voltammetry appears at the lower scan rate, whereas transient behaviour is seen at high scan rates in all four RTILs. Figure 9.2 displays plot of peak current of the proton reduction *vs* square root of scan rate in $[C_4mim][NTf_2]$ as a example. It tends to linearity at high scan rates corresponding

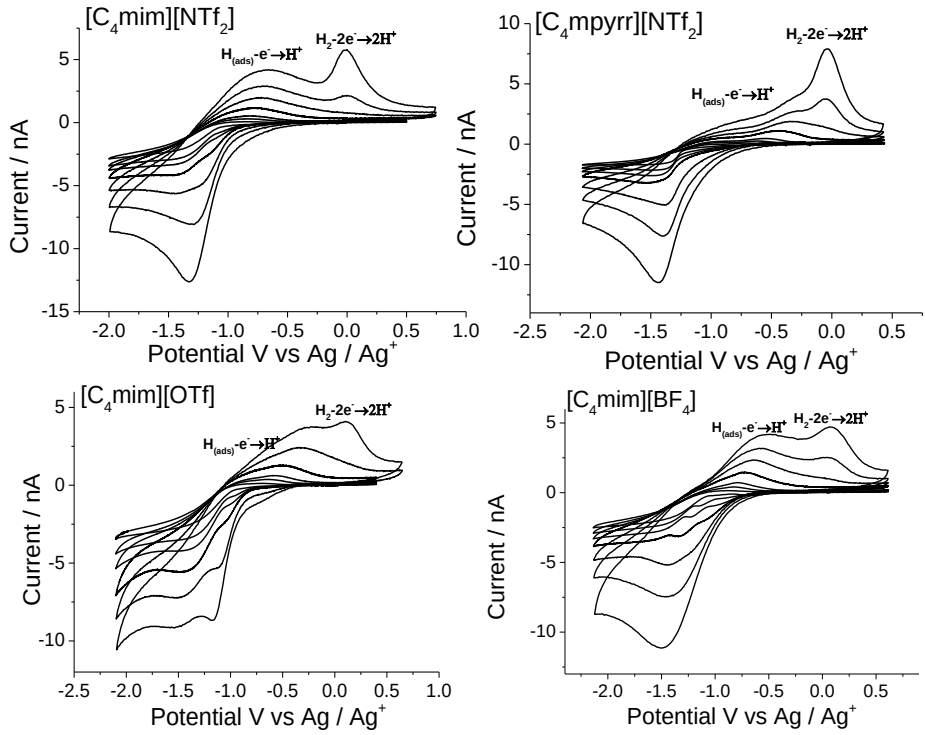

Figure. 9.1 Voltammograms recorded for ca. 50 mM benzoic acid at a 10 µm diameter Pt microelectrode in $[C_4mim][NTf_2]$ $[C_4mpyrr][NTf_2]$, $[C_4mim][OTf]$ and $[C_4mim][BF_4]$, over a range of scan rates (0.1, 0.4, 0.8, 2, 5, 10 and 20 V s^{-1}) at 298K *vs* Ag/ Ag^+ redox couple

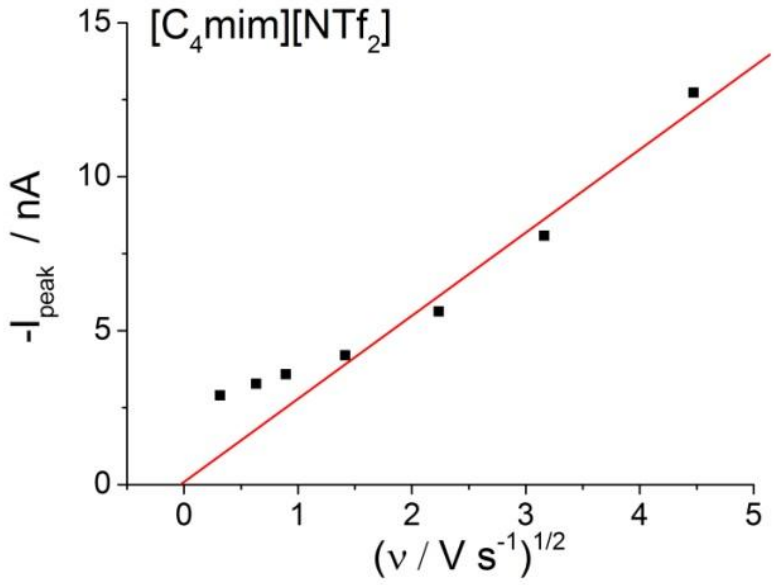

Figure. 9.2 Plot of peak current of benzoic acid reduction (from Fig.1) against the square root of the scan rate at a 10 µm diameter Pt microelectrode in $[C_4mim][NTf_2]$ *vs* Ag/ Ag^+ redox couple

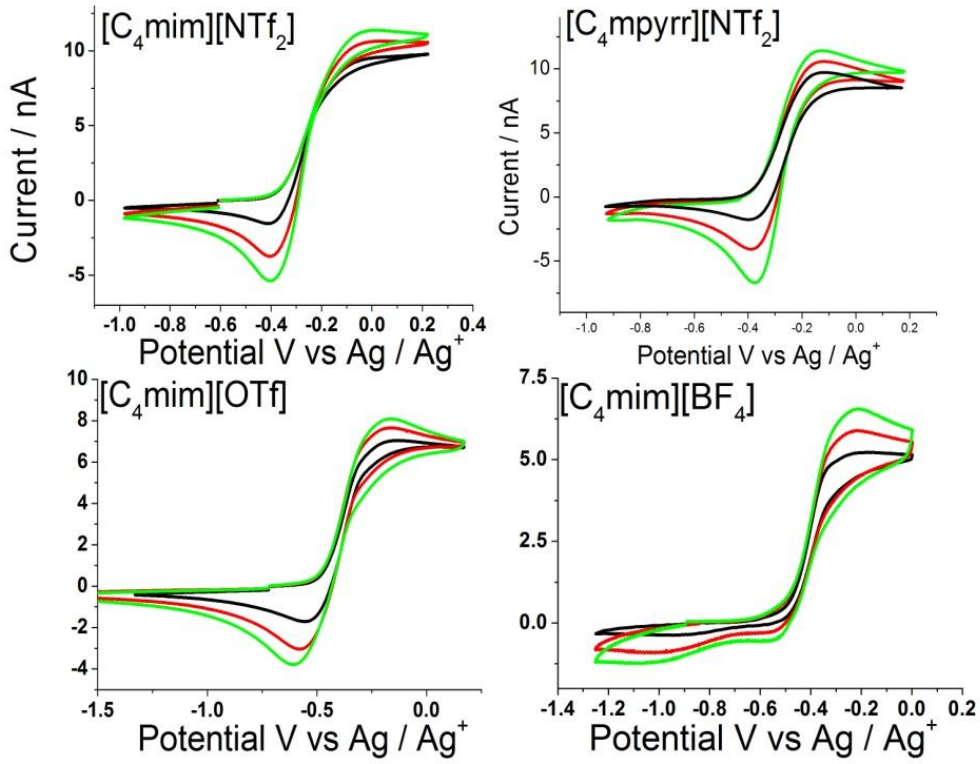

Figure. 9.3 Scan rate study recorded for saturated hydrogen at a 10 µm diameter Pt microelectrode in $[C_4mim][NTf_2]$ $[C_4mpyrr][NTf_2]$, $[C_4mim][OTf]$ and $[C_4mim][BF_4]$, over a range of scan rates (0.1, 0.4, 0.8 V s^{-1}) *vs* Ag/ Ag^+ redox couple

to Randles-Sevcik behaviour, but at lower values shows the characteristics intermediate to that of pure micro- and macroelectrode behaviour.A separate study was made of the oxidation of pure H_2 in the same RTIL media. Figure 9.3 shows a scan rate study at a 10 µm diameter Pt microelectrode recorded for saturated hydrogen in RTILs, *vs* Ag/ Ag^+ redox couple. *Quasi*-reversible voltammetry was observed for the H_2 oxidation in $[C_4mim][NTf_2]$, $[C_4mim][OTf]$ and $[C_4mpyrr][NTf_2]$ RTILs, with irreversible voltammetry in $[C_4mim][BF_4]$. The size of the oxidation waves in RTILs reflect the corresponding magnitude of the H_2 solubility, and their anodic potentials are used to assign to the nature of the $H_2 \rightarrow H^+$ peaks shown in figure 9.1, these corresponding in all cases to the oxidation waves at more positive potentials. The oxidation waves at more negative potentials are assigned to

$$H_{ads}^{\cdot} - e^- \rightarrow H^+ \qquad (9.5)$$

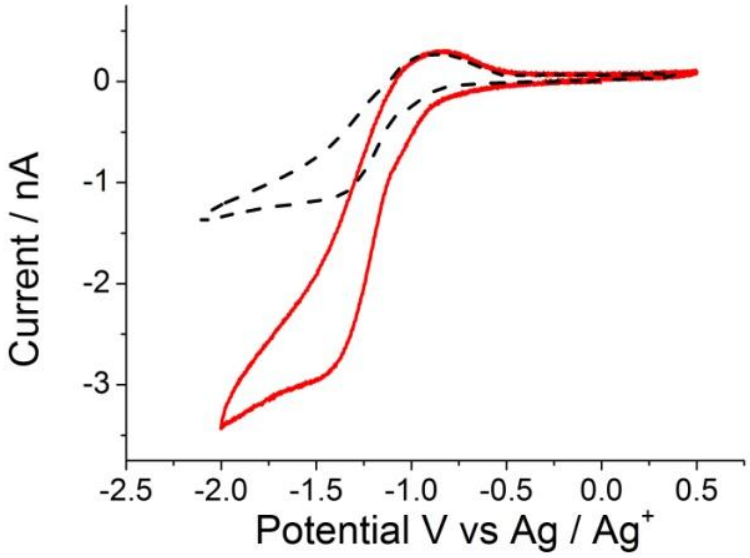

Figure. 9.4 Concentration study of benzoic acid (solid line, ca. 50 mM; dash line ca. 20 mM) at a 10 µm diameter Pt microelectrode in $[C_4mim][NTf_2]$ at 0.4 Vs^{-1} *vs* Ag/ Ag^+ redox couple

To confirm this the size of the oxidation wave was measured as a function of the concentration of benzoic acid. Figure 9.4 shows the data obtained at a 10 µm diameter Pt microelectrode in $[C_4mim][NTf_2]$ for benzoic acid concentration of 20 and 50mM at 0.4 V s^{-1} *vs* Ag/ Ag^+ redox couple. It is seen that although the reduction waves scale with concentration, the oxidation waves remain constant. The charge under the peak corresponds to 3.6×10^{-4} C cm^{-2} or 3.7×10^{-9} mol cm^{-2} corresponding to a UPD layer of adsorbed hydrogen atoms.[4, 29, 30] Note that for the reduction of benzoic acid at Au in RTIL, H(ads) is not seen as expected,[31] since H· is not stabilised on Au surface.

9.2.2 The voltammetry of benzoic acid in the presence of H_2 in RTILs

Figure 9.5 displays scan rate studies obtained for the voltammetry of benzoic acid at a Pt electrode in H_2 saturated RTILs, namely $[C_4mim][NTf_2]$, $[C_4mpyrr][NTf_2]$, $[C_4mim][OTf]$ and $[C_4mim][BF_4]$ over a range of scan rates (0.1, 0.4, 0.8, 2, 5, 10, 20, 30, 40 and 50 V s^{-1}) *vs* Ag/ Ag^+ redox couple. The hydrogen oxidation occurs near the beginning of the forward

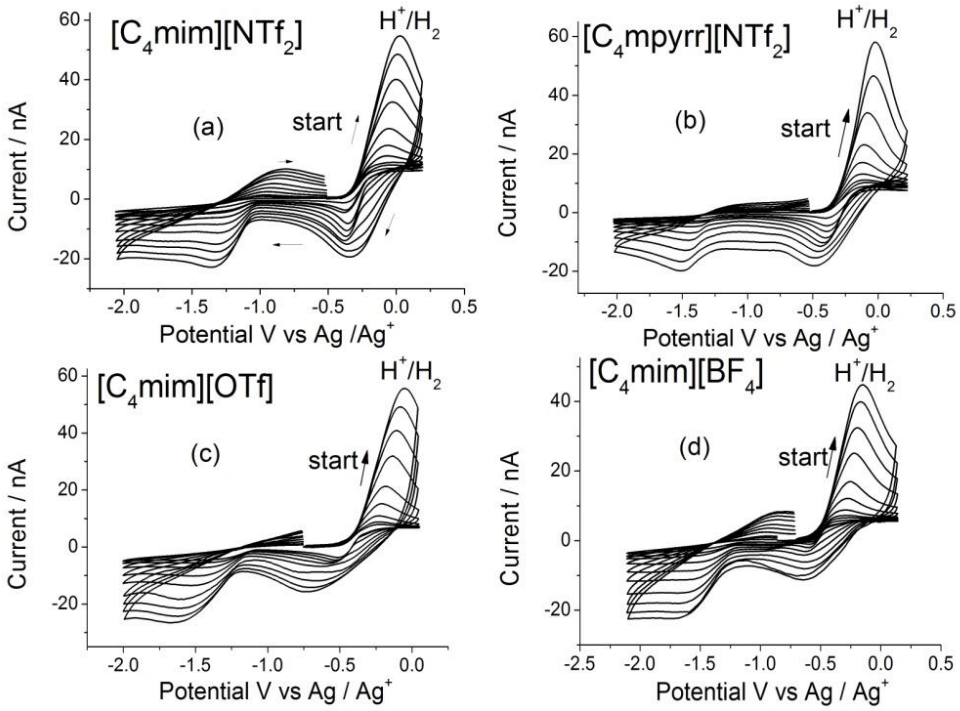

Figure. 9.5 Scan rate study obtained for the reduction of benzoic acid at a Pt electrode in H_2 saturated RTILs, including $[C_4mim][NTf_2]$, $[C_4mpyrr][NTf_2]$, $[C_4mim][OTf]$ and $[C_4mim][BF_4]$ over a range of scan rates (0.1, 0.4, 0.8, 2, 5, 10, 20, 30, 40 and 50 V s^{-1}) at 298K *vs* Ag/ Ag^+ redox couple

and the half wave potentials of oxidative wave coincide with reported values[27] from potentials is assigned to the electrolytically generated protons from H_2, which are strongly solvated by anions. Thus the specific properties of these reductive waves in each RTIL mirror these reported for H_2 / H^+ in the same RTILs, the reduction wave at more negative potential is that of benzoic acid as discussed above.[26, 32] The exact potential of the second reduction reflects the interaction of H^+ with anions in the RTIL and the pre-equilibrium, equation 9.1. Finally, the identity of reverse oxidative peak is, as discussed above, the UPD H on the platinum surface. The potential of UPD H oxidation is related to ions of the different RTILs, which form the double layer on the surface.

$$H_2 - e^- \xrightarrow{slow} H^{\bullet}_{(ads)} + H^+ \qquad (9.6)$$

$$H^{\bullet} - e^- \xrightarrow{fast} H^+ \qquad (9.7)$$

consistent with a transfer coefficient of β ~0.5. Note that the data in figure 9.5 shows explicitly the relative ease of oxidation of H(ads) compared to H_2.

9.2.3 The hydrogenolysis of bis(benzyloxycarbonyl)-L-lysine (Z-lys(Z)-OH), using adsorbed hydrogen atoms

It is of interest to explore the possible use of the adsorbed hydrogen atoms for hydrogenolysis. A variety of organic compound have been investigated on Pd microelectrodes and Pd / C nanostructures in RTILs but the use of Pt electrode is unexplored.[33-35] Z-lys(Z)-OH was selected as a candidate molecule for the rapid hydrogenolysis. Note that the amine groups in the chemical structure of Z-lys(Z)-OH, are protonated in the presence of protons and thus decrease the available concentration of protons. Therefore, the experiment uses *ca.* 100 mM benzoic acid and *ca.* 25 mM Z-lys(Z)-OH to obtain an approximate available concentration of 50mM benzoic acid and 50mM benzoate ions to compare with a solvent of *ca.* 50mM pure benzoic acid. Figure 6 displays the decrease in the size of oxidative wave on the reverse scan at a 10 µm diameter Pt microelectrode in $[C_4mim][NTf_2]$ at 0.4 Vs^{-1} *vs* Ag/ Ag^+ redox couple

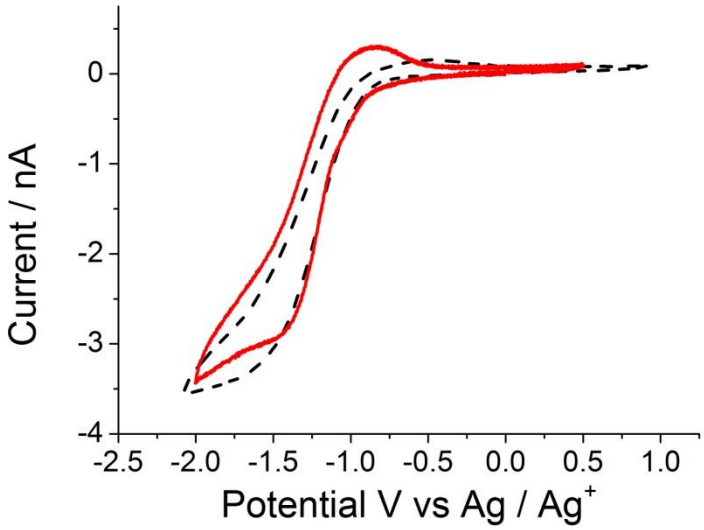

Figure.9.6 Voltammograms for the reduction of benzoic acid in the presence and absence of Z-lys(Z)-OH at a 10 µm diameter Pt microelectrode in $[C_4mim][NTf_2]$ at 0.4 Vs^{-1} *vs* Ag/ Ag^+ redox couple (solid line, ca. 50 mM benzoic acid; dash line, ca. 100 mM benzoic acid and ca. 25 mM Z-lys(Z)-OH)

in the presence of Z-lys(Z)-OH. Note that in contrast the reduction waves are comparable in size. In comparison with tradition hydrogenolysis or hydrogenation,[36] which usually require high temperature, high pressure and long time, as well as high flammable H_2. The electrochemical use of adsorbed H on Pt electrode under moderate conditions would be an efficient and practical technique.

9.3 Conclusions

The electrochemical reaction of benzoic acid has been investigated at a Pt electrode in four RTILs in the presence and absence of hydrogen, using a stable reference electrode. The half wave potential of bulk hydrogen oxidation coincides with the studies of HER with H_2 / H^+ ($HNTf_2$), relating to the measured formal potential of H_2 / H^+ redox couple. The corresponding potentials in each RTIL have been determined for the associated UPD H oxidation, which is dependent on the nature of the anion in the RTIL. Additionally, the UPD H have been successfully utilised to achieve a rapid hydrogenolysis for the organic compound, Z-lys(Z)-OH, at a Pt microelectrode on the timescale of cyclic voltammetry.

Reference

1 P. H. Rieger, *Prentice-Hall, Englewood Cliffs, London* 1987.

2 B. E. Conway, J. O. Bockris, *Journal of Chemical Physics* 1957, *26*, 532-541.

3 S. Trasatti, *Journal of Electroanalytical Chemistry* 1972, *39*, 163-&.

4 G. Jerkiewicz, *Progress in Surface Science* 1998, *57*, 137-186.

5 D. S. Silvester, L. Aldous, C. Hardacre, R. G. Compton, *Journal of Physical Chemistry B* 2007, *111*, 5000-5007.

6 Y. Meng, L. Aldous, R. G. Compton, *Journal of Physical Chemistry C* 2011, *115*, 14334-14340.

7 H. S. Mohran, A. R. El-Sayed, H. M. Abd El-Lateef, *Journal of Solid State Electrochemistry* 2009, *13*, 1147-1155.

8 I. Danaee, S. Noori, *International Journal of Hydrogen Energy* 2011, *36*, 12102-12111.

9 D. P. Zhan, J. Velmurugan, M. V. Mirkin, *Journal of the American Chemical Society* 2009, *131*, 14756-14760.

10 S. A. Chen, B. D. Adams, A. C. Chen, *Electrochimica Acta* 2010, *56*, 61-67.

11 N. V. Korovin, B. N. Yanchuk, *Electrochimica Acta* 1970, *15*, 569-&.

12 A. Veziroglu, R. Macario, *International Journal of Hydrogen Energy* 2011, *36*, 25-43.

13 I. Cumalioglu, A. Ertas, Y. Ma, T. Maxwell, *Journal of Fuel Cell Science and Technology* 2008, *5*, Artn 034001.

14 D. S. Silvester, R. G. Compton, *Zeitschrift Fur Physikalische Chemie-International Journal of Research in Physical Chemistry & Chemical Physics* 2006, *220*, 1247-1274.

15 L. E. Barrosse-Antle, A. M. Bond, R. G. Compton, A. M. O'Mahony, E. I. Rogers, D. S. Silvester, *Chemistry-an Asian Journal* 2010, *5*, 202-230.

16 D. Freudenmann, S. Wolf, M. Wolff, C. Feldmann, *Angewandte Chemie-International Edition* 2011, *50*, 11050-11060.

17 C. Zafer, K. Ocakoglu, C. Ozsoy, S. Icli, *Electrochimica Acta* 2009, *54*, 5709-5714.

18 M. Vaher, M. Borissova, M. Koel and M. Kaljurand, *Proc. Estonian Acad. Sci. Chem* 2007, *56*, 187–198.

19 T. Robert, L. Magna, H. Olivier-Bourbigou, B. Gilbert, *Journal of the Electrochemical Society* 2009, *156*, F115-F121.

20 W. Vielstich, D. Jahn, *Zeitschrift Fur Elektrochemie* 1960, *64*, 43-44.

21 R. G. Barradas, O. Kutowy, Shoesmit.Dw, *Electrochimica Acta* 1974, *19*, 49-56.

22 W. C. Barrette, D. T. Sawyer, *Analytical Chemistry* 1984, *56*, 653-657.

23 S. E. Treimer, D. H. Evans, *Journal of Electroanalytical Chemistry* 1998, *455*, 19-28.

24 D. S. Silvester, W. S. He, L. Aldous, C. Hardacre, R. G. Compton, *Journal of Physical Chemistry C* 2008, *112*, 12966-12973.

25 W. He, D. S. Silvester, I. Streeter, L. Aldous, C. Hardacre, R. G. Compton, *Journal of Physical Organic Chemistry* 2009, *22*, 69-76.

26 F. D'Anna, S. Marullo, P. Vitale, R. Noto, *J Org Chem* 2010, *75*, 4828-4834.

27 Y. Meng, L. Aldous, S. R. Belding, R. G. Compton, *Physical Chemistry Chemical Physics* 2012, *14*, 5222-5228.

28 Y. Meng, L. Aldous, S. R. Belding, R. G. Compton, *Chemical Communications* 2012, *48*, 5572-5574.

29 T. C. Franklin, R. Graves, *Surface Technology* 1978, *6*, 347-359.

30 X. B. Ji, D. S. Silvester, L. Aldous, C. Hardacre, R. G. Compton, *Journal of Physical Chemistry C* 2007, *111*, 9562-9572.

31 L. A. Khanova, L. I. Krishtalik, *Journal of Electroanalytical Chemistry* 2011, *660*, 224-229.

32 D. R. MacFarlane, J. M. Pringle, K. M. Johansson, S. A. Forsyth, M. Forsyth, *Chemical Communications* 2006, 1905-1917.

33 V. I. Parvulescu, C. Hardacre, *Chemical Reviews* 2007, *107*, 2615-2665 Doi 10.1021/Cr050948h.

34 Y. Meng, L. Aldous, B. S. Pilgrim, T. J. Donohoe, R. G. Compton, *New Journal of Chemistry* 2011, *35*, 1369-1375.

35 Y. Meng, L. Aldous, R. G. Compton, *Green Chemistry* 2010, *12*, 1926-1928.

36 R. Kramer, M. Fischbacher, H. L. Gruber, *Applied Catalysis* 1988, *42*, 337-350.

Summary

First, this thesis has looked at the electrochemical behaviour of the H_2 /H^+ redox couple, as well as the voltammetry of adsorbed hydrogen atoms, in room temperature ionic liquids. Using H[NTf_2] as the proton source, the results show remarkably different mechanistic behaviour of the hydrogen evolution reaction as compared to traditional solvents at a range of different electrode metals, notably Platinum, Gold, Molybdenum, Titanium and Nickel. Platinum, Gold and Molybdenum are known to evolve hydrogen by the Heyrovsky reaction in acidic aqueous solution, while the Volmer reaction is the rate limiting step at all five investigated metals in [C_2mim][NTf_2]. The values of the formal potentials and the standard electrochemical rates of H^+/H_2 redox couple have been determined *versus* a stable Ag / Ag^+ reference couple. It has also been shown that the nature of the RTIL anion has a very strong aspect of the electrode reaction interaction with protons, and this changes both kinetic and thermodynamic mechanisms.

In other experiments, benzoic acid was used as the proton source and a CE mechanism is observed on a Pt microelectrode in four RTILs *versus* Ag / Ag^+ redox couple in which dissociation of benzoic acid is followed by electron transfer to H^+ ultimately forming adsorbed hydrogen. In addition, the measured diffusion coefficients of proton and hydrogen suggested that (anion solvated) protons display Stokes-Einstein-like transport whereas H_2 does not.

Dissolved hydrogen gas in RTILs was found to result in an increase in the diffusivity of the solutes H[NTf_2] and ferrocene, as characterised by their diffusion coefficients and a decrease in the activation energy for diffusion. It was inferred that the H_2 results in reduced Coulombic interactions between the ions of the RTIL with a concurrent net reduction in RTIL viscosity.

Last, electrochemically formed adsorbed hydrogen atoms at a Pt or Pd microelectrode, or on Pd nanoparticles on the surface of CNTs in RTILs were demonstrated voltammetrically to perform hydrogenolysis of bis(benzyloxycarbonyl)-L-lysine, as well as react with other organic compounds. The hydrogenolysis products obtained in the IL environment were observed both voltammetrically, and isolated, identified and quantified. In particular, Pd nanoparticles can be used for clean, efficient, safe electrochemical hydrogenolysis in IL media without the need for H_2 gas.